Investigation of the Interaction between Nanoparticles, Asphaltenes, and Silica Surfaces for Inhibition and Remediation of Formation Damage

Montoya, Leidy Tatiana

UNIVERSITY OF CALGARY

Investigation of the Interaction between Nanoparticles, Asphaltenes, and Silica Surfaces for Inhibition and Remediation of Formation Damage

by

Leidy Tatiana Montoya

A THESIS

SUBMITTED TO THE FACULTY OF GRADUATE STUDIES

IN PARTIAL FULFILMENT OF THE REQUIREMENTS FOR THE

DEGREE OF DOCTOR OF PHILOSOPHY

GRADUATE PROGRAM IN CHEMICAL AND PETROLEUM ENGINEERING

CALGARY, ALBERTA

JULY, 2021

Abstract

World population growth, increment in industrialization and motorization of the world, increment in technical development and living standards are some factors that keep contributing to the increasing of the global energy demand. Therefore, it is necessary to find alternative sources to meet these demands. Considering renewable and non-renewable energies, there is still an interest in enhancing the oil and gas recovery, because its reserves are considerable in terms of the energy supply. Nevertheless, there are several challenges facing the oil production related with asphaltenes, and it requires a knowledge on the deposition mechanism of this fraction of oil and the factors influencing it, since they are important in many parts of the production processes, and refinery catalyst deactivation, causing significant production losses. Accordingly, appropriate mitigation techniques, for surfaces exposed to asphaltenes or operating conditions, can be identified. It has been demonstrated that the use of nanoparticles may improve the mobility of oil. This is because nanoparticles may enhance wettability alteration or disaggregation of asphaltene aggregates. Accordingly, this study will help to understand the interactions between asphaltenes and nanoparticles, at the beginning using computational modeling and model molecules for resins and asphaltenes. It is important to consider that asphaltenes are not the only component in the oil and the adsorbent affinity is affected for it. Then, naturally derived silicate-based nanoparticles were used to investigate their performance on wettability alteration and what is the mechanism involved in continuous flow over pre-adsorbed/deposited asphaltene SiO_2 sensors; this was achieved using a QCM-D, contact angle measurements and AFM images. The results showed that depending on the asphaltenes aggregation stage, the nanoparticles interact differently with them. Finally, basic silicate-based nanofluids were tested at reservoir conditions. The main results indicated that low salinity was the most promising formulation for inhibiting/remediating formation damage caused by asphaltene precipitation/deposition. Relative permeability curves showed a shift to right after the injection of nanoparticles, confirming the role of nanoparticles on wettability alteration. Oil recovery factor was also increased when using nanoparticles to inhibit/remediate the damage. Therefore, silicate-based nanoparticles are good candidates to use as treatment for asphaltene formation damage.

Keywords: Formation damage, asphaltenes, nanofluids, wettability, relative permeability.

.

Acknowledgements

I would like to express my deepest gratitude to my supervisor Dr. Nashaat N. Nassar for giving me the opportunity to join his research group Dr. Nassar Nanotechnology Research Group, for his guidance throughout this journey, for his support not only academically with his knowledge, connections and advices, but also personally, giving spaces to make a pause and think critically to improve the performance, for his patience and recommendations. I would like to thank Dr. Nancy Chen, Dr. Hassan Hassanzadeh, Dr. Robert Gordon Moore, Dr. Rahil Khoshnazar and Dr. Morteza Dejam for being part of my examination committee.

I would also like to thank Dr. Pedro Pereira-Almao for being there when I needed advice and support, for always being available to discuss my work, his help and his recommendations during this journey are highly appreciated.

I would like to thank the following people: Dr. Gerardo Vitale, for his guidance and knowledge in nanoparticles, Mr. Lante Carbognani and Dr. Carlos Scott for being available to discuss about asphaltenes, Dr. Monica Bartollini for her help, support and knowledge in characterization. All your advices motivated me to continue with this work.

I would like to thank the Department of Chemical and Petroleum Engineering for their financial support as well to the graduate program coordinators Arthur de Vera and Suha Abusalim. Also, thanks to Natural Sciences and Engineering Research Council of Canada (NSERC) for their financial support. Financial support was also provided by the Ursula and Herbert Zandmer Graduate Scholarship, the Engineering Graduate Excellence Scholarship Award from the Department of Chemical & Petroleum Engineering, Nova Chemicals Scholarship and Alberta Graduate Excellence Scholarship (AGES) – International.

I wish to thank to Fahad Sagala for his help, collaboration during the last part of this research, to Abdallah, Dr. Azfar Hassan for the collaboration. Also, special thanks to all the members of the Dr. Nassar Nanotechnology Research Group and CAFE group, all his comments, questions and advices helped me to improve my knowledge and develop a better research, enjoying the process. I also wish to thank the following people Sukhdeep Gill, Violeta Wills, Alejandro Coy who have been a great source of support. Thanks to my all my friends, specially Daniela and John for all the support and love, Karen, Jairo, Silvia, Diana, Jeymy e Ivan, for always being there. Thanks to Yoshi, for all the love, patience, support and understanding during this journey.

From the bottom of my heart thanks to my family, my mother Cristina, my father Martin and my brother Alejandro, despite the distance and the time zone, you were always supporting me and encouraging me all this time, without your love, patience and support this would not be possible.

Dedication

Dedicated with love to my family for their continuous support and encouragement during this journey.

Table of Contents

List of Tables

List of Figures and Illustrations

List of Symbols, Abbreviations and Nomenclature

Abbreviation

AFM	=	Atomic force microscopy
AN	=	Acid nanoparticles
BN	=	Basic nanoparticles
BPD	=	Barrels per day
D	=	Dissipation
DLS	=	Dynamic light scattering
EOR	=	Enhanced oil recovery
EROI	=	Energy return on investment
F	=	Frequency (Hz)
FTIR	=	Fourier-transformed infrared spectroscopy
FWHM	=	Full width high maximum
Ha	=	Hartree
HO	=	Heavy oil
HRTEM	=	High-resolution transmission electron spectroscopy
ICDD	=	International Centre for Diffraction Data
IFT	=	Interfacial tension
nf	=	Nanofluid
NLDFT	=	Non-local density functional theory
NN	=	Neutral nanoparticles
PAH	=	Polyaromatic hydrocarbon
PVI	=	Pore volume injected

QCM-D = Quartz crystal microbalance with dissipation

Q-65 = Quinolin 65

R_p = Profile residual

R_{wp} = Weighted profile residual

SA = Surface area

SEM = Scanning electron microscopy

TC = Taylor-Couette

TPD = Temperature programmed desorption

V-79 = Violanthrone 79

XRD = X-ray diffraction

XPS = X-ray photoelectron spectroscopy

Symbol

K Absolute permeability

K_{rw} Relative permeability to water

K_{ro} Relative permeability to oil

K_w Water effective permeability

K_o Oil affective permeability

P_c Capillary pressure

r Pore Radius

S_w Water saturation

S_{wc} Connate water saturation

n-C_7 Heptane

N_A	Avogadro's constant
C_0	Initial concentration
C_e	Equilibrium concentration
Q_{max}	Maximum adsorbed amount
K_L	Langmuir constant
d	Particle diameter
Q	Adsorbed amount in equilibrium
$\Delta G°_{ads}$	Gibbs free energy change

Greek symbols

$\emptyset$	Porosity
μ	Viscosity
σ	Interfacial tension
θ	Contact angle
λ	Wavelength
α_{ij}	Selectivity
χ^2	Chi-square
ρ	Density
ζ	Zeta potential

Epigraph

"If we knew what it was, we were doing, it would not be called research, would it?"

Albert Einstein

Chapter One: Introduction

1.1. Background

The production of fossil fuels can be affected by several sources of damage at subsurface and surface conditions that reduce the oil recovery (Bennion, 2002; Gill, Tsolakis, Dearn, & Rodríguez-Fernández, 2011). Heavy compounds of the crude oil like asphaltenes have potential to be a source of damage in light, medium and heavy oils. Precipitation and adsorption/deposition of asphaltenes and other organic components on the rock surface cause formation damage and reduction of the effective hydrocarbon mobility by reducing pore cross-sections and blocking pore throats; altering formation wettability from water-wet to oil-wet (Al-Maamari & Buckley, 2003; Majid Mohammadi, Dadvar, & Dabir, 2017), and decreasing effective hydrocarbon mobility by stabilizing water-oil emulsions. Some of the consequences of asphaltene damage are reduction in oil productivity and noneconomic operation of the reservoir (Eskin, Mohammadzadeh, Akbarzadeh, Taylor, & Ratulowski, 2016), related with problems after the production such as plugging flow lines because of asphaltene deposit build-up (Creek, 2005), and refinery catalyst deactivation because of asphaltene adsorption at active sites (Trimm, 1996). Depending on the type of oil the damage will be different, it means, in the case of light crude oils with low content of asphaltenes, the damage is related with the precipitation, deposition and adsorption of asphaltenes in the porous media (Adams, 2014). On the other hand, in crude oils with high asphaltenes content, the damage is associated with high viscosities that results in the reduction of the oil mobility possibly leading to interdigitation problems (Adams, 2014).

Asphaltenes are considered the heaviest, most aromatic and most surface-active fraction of crude oil (Acevedo et al., 2007; Adams, 2014; Andersen, 1995) being insoluble in light paraffins like n-pentane, n-hexane and n-heptane, but soluble in light aromatics like benzene, toluene or pyridine (Adams, 2014; Mullins, 2011; Mullins et al., 2012). Some characteristics associated with asphaltenes are polarizability, amphiphilic behavior that promotes self-association of asphaltenes molecules resulting in the formation of large aggregates (Yarranton, 2005) that also could increase the crude oil viscosity (Ghanavati, Shojaei, & SA, 2013; Leontaritis, Amaefule, & Charles, 1994); complex chemical structures composed mainly of cores of polycyclic aromatic hydrocarbons (PAH), naphthenic groups, heteroatoms such as nitrogen, oxygen, and sulfur and metals such as vanadium, nickel and iron (Qiao et al., 2017; Schuler, Meyer, Peña, Mullins, & Gross, 2015). It has been reported that the aggregation behaviour of asphaltenes is enhanced by decreasing the aromaticity of the solvent (Qiao et al., 2017; Zhang, Shi, Lu, Liu, & Zeng, 2016). On the other hand, changes in reservoir temperature, pressure and oil composition are parameters that can highly contribute to asphaltene precipitation in the reservoir (Nasrabadi, Moortgat, & Firoozabadi, 2016).

Common techniques for damage inhibition involve destabilization and deposition of asphaltenes or fractionating the chemical structure of the heaviest compounds present in the crude oil, but these fractioning processes usually lead to low energy return on investment (EROI) and a higher emission of greenhouse gas (Adams, 2014). Accordingly, other methods have been proposed to avoid asphaltene precipitation and deposition, mainly in places close to wells (Leontaritis et al., 1994). Some of these methods are periodic intervention via solvent soaking or constant chemical injection (Betancur, Carmona, Nassar, Franco, & Cortés, 2016; Mansoori, 2010); chemical injection such as antiflocculants, coagulants, flocculants and non-polar solvents (Ghloum, Al-Qahtani, & Al-Rashid, 2010; Mansoori, 2010). Besides the environmental impact, conventional methods to treat asphaltene precipitation can require additional staff and equipment on location, increasing their price (Betancur et al., 2016; Mansoori, 2010). Additionally, these asphaltene treatments can have low durability, change fluids compositions and do not guarantee prevention of asphaltene redeposition (Betancur et al., 2016; Mansoori, 2010).

Consequently, the use of nanoparticles have become an area of interest for the oil and gas industries like enhancing oil recovery (Franco, Nassar, Ruiz, Pereira-Almao, & Cortés, 2013; Hashemi, Nassar, & Pereira Almao, 2013a, 2013b, 2014). Additionally, due to exceptional properties of nanoparticles such as high ratio of surface area/volume, nanoparticles can act as adsorbents and/or catalysts toward heavy polar compounds in crude oils like asphaltenes (Franco, Montoya, Nassar, Pereira-Almao, & Cortés, 2013; Hassan, Carbognani, & Pereira-Almao, 2008; Nassar, Hassan, Carbognani, Lopez-Linares, & Pereira-Almao, 2012; Nassar, Hassan, Luna, & Pereira-Almao, 2013; Nassar, Hassan, & Pereira-Almao, 2011, 2013). Nanoparticles are defined as particles with size between 1 and 100 nm, allowing the particle smooth traveling and good dispersion through the porous media without risk of pore blocking when stable (Hashemi, Nassar, & Pereira-Almao, 2012). Therefore, the interaction of asphaltenes with solid surfaces has taken the attention of researchers studying the adsorption of asphaltenes onto several substrates, including silica (Dudášová, Silset, & Sjöblom, 2008; Zahabi, Gray, & Dabros, 2012), alumina (Dudášová, Silset, et al., 2008; González, Stull, López-Linares, & Pereira-Almao, 2007), iron oxide (Carbognani, 2000), gold (Goual & Abudu, 2009; Harbottle et al., 2014; Rudrake, Karan, & Horton, 2009; Sedghi, Goual, Welch, & Kubelka, 2013; Zahabi et al., 2012), stainless steel (Xie & Karan, 2005), glass (Acevedo, Castillo, Fernández, Goncalves, & Ranaudo, 1998), and clay minerals (Dudášová, Simon, Hemmingsen, & Sjöblom, 2008; Jada & Debih, 2009; Jada, Debih, & Khodja, 2006; Klein, Kim, Rodgers, Marshall, & Yen, 2006; Pernyeszi, Patzko, Berkesi, & Dékány, 1998; Tu et al., 2006).

In addition, studies have demonstrated that the presence of nanoparticles like alumina (nano-sized), silica, magnetite, ZrO_2 and TiO_2 affect the kinetics of asphaltene aggregation/fragmentation, demonstrating the effects of nanoparticles on the inhibition of asphaltene aggregation (Guzmán et al., 2016; Mohsen Mohammadi et al., 2011; Nassar, Betancur, Acevedo, Franco, & Cortés, 2015). Further, a model on population balance accounted for the effects of nanoparticles on inhibition of asphaltene aggregate growth has been reported (Nassar et al., 2015). The authors demonstrated that the used of nanoparticles could reduce the hydrodynamic ratio of the asphaltene aggregates and cause asphaltene flocs to disaggregate.

Besides, nanoparticles have been presented as alternatives for inhibiting the formation damage caused by asphaltene precipitation and for in-situ enhancement of oil recovery (Li et al., 2016; Mohsen Mohammadi et al., 2011; Rezvani, Khalilnezhad, Ganji, & Kazemzadeh, 2017). Nanoparticles specific chemical reactivity, active surfaces and dispersibility (Rezvani et al., 2017) facilitate the capture and removal of the asphaltenes present in a reservoir, impacting the enhancement of oil production, inhibiting formation damage and restoring wettability (Franco, Nassar, et al., 2013; Giraldo, Benjumea, Lopera, Cortés, & Ruiz, 2013; Moradi, Pourafshary, Jalali, Mohammadi, & Emadi, 2015). In addition, the usage of nanoparticles in enhanced oil recovery (EOR) processes have shown an important role in terms of wettability alteration and interfacial tension (IFT) reduction (Li et al., 2016; Negin, Ali, & Xie, 2016; Rezvani et al., 2017). It has been shown that nanoparticles can improve oil production in EOR processes through different mechanism like viscosity/density alteration of the injected fluid (Moradi et al., 2015), improvement of emulsification process, improvement of thermal conductivity and specific heat capacity (Jang & Choi, 2004; Patel et al., 2003), improvement of rock-fluid interactions

(McElfresh, Holcomb, & Ector, 2012) and alteration of heat transfer coefficient (Mustafin, Manasrah, Vitale, Askari, & Nassar, 2020; Rezvani et al., 2017).

Accordingly, several nanoparticles have been tested with different types of surfactant and polymer solution to improve the performance of the EOR processes (Cheraghian & Khalilinezhad, 2015; Nezhad & Cheraghian, 2016; Sedaghat, Mohammadi, & Razmi, 2016), through integration with water-alternating gas injection (WAG) (Moradi et al., 2015), water flooding (Dehghan Monfared, Ghazanfari, Jamialahmadi, & Helalizadeh, 2016; Joonaki & Ghanaatian, 2014) and CO_2 flooding (Worthen, Bryant, Huh, & Johnston, 2013). Nanoparticle performance in these processes have been investigated in the laboratory, using interfacial tension (IFT) measurements, sessile-drop wettability tests, micromodel experiments, and core flooding experiments (Giraldo et al., 2013; Li et al., 2016; Rezvani et al., 2017). As a result, researchers have found that one of the main mechanism associated with the presence of nanoparticles in EOR processes is the disjoining pressure (Li et al., 2016; Moradi et al., 2015; Rezvani et al., 2017). In this mechanism, the nanoparticles form a self-assemble wedge-shaped film with the discontinuous fluid in the interface (Moradi et al., 2015; Rezvani et al., 2017), as it is shown in Figure 1.

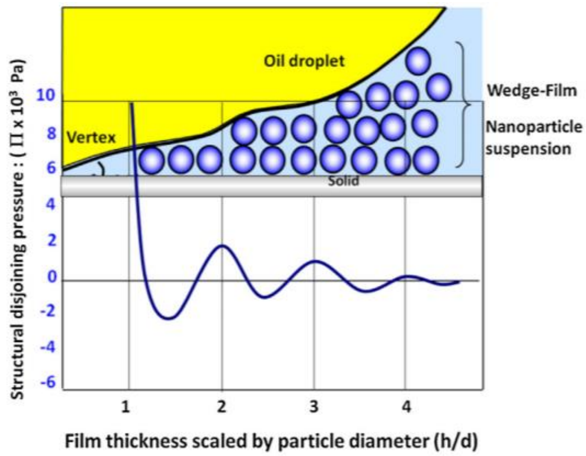

Figure 1.1. Schematic representation of the change in the disjoining pressure in the wedge film (Lim, Zhang, Wu, Nikolov, & Wasan, 2016).

Herein in this thesis, a new approach using computational modeling and model molecules for asphaltenes and resins are initially applied to understand the interaction between nanoparticle (NiO) and asphaltene model molecules. Then, naturally derived silicate-based nanoparticles are used for inhibiting and remediating formation damage caused by asphaltene precipitation/deposition. Silicate-based nanoparticles are chosen for this study because they are naturally derived material (Vitale, 2013). These nanoparticles are synthesized at low temperature (160 °C) and pressure which provides good scalability options (Vitale, 2013). This work will focus on the nanoparticle-asphaltene-surface interaction and how later, the nanoparticles injection have the ability to alter the surface wettability, varying chemical superficial properties of the nanoparticles, size, concentration and considering the composition of the surface with which they are going to interact, its mineral composition and its initial wetting nature. This gives an insight on the behavior of the silicate-based nanofluid with different surface chemistry in the inhibition of the formation damage by asphaltene precipitation, the mechanism behind the improvement in displacing the oil in the reservoir, more specifically in a sand-pack, mainly composed of silica. For this reason, the chemical composition of the selected nanoparticle was identical to the major mineral components present in the original reservoirs. It will be more focused on the nanofluid-induced structural effect on the sand/rock surface and the oil without the use of additional chemicals such as surfactants or polymers.

1.2. Motivation

In the current practice of oil recovery processes, small fraction (around 20%) is easily extractable and the remaining 80% are partially recovered through EOR methods (McEachern, 2009). Further, in most case, during the oil recovery formation damage is likely to occur (Betancur et al., 2016). This undesirable operational problem impact the recovery efficiency, limiting the reservoir productivity and causing inefficient operation (Franco, Montoya, et al., 2013; Maqbool, Balgoa, & Fogler, 2009). This problem is caused by interactions between the porous medium and reservoir fluids, resulting in other problems, such as fines migration (You, Badalyan, Bedrikovetsky, Hand, & Jenson, 2013), asphaltene precipitation/deposition (Adams, 2014; Mullins, 2011), condensate banks (Alzate et al., 2006), alteration of the rock wettability (Civan, 2015), among others. From those types of formation damage, precipitation and deposition of asphaltenes in the reservoir and in the production system (Leontaritis et al., 1994; Maqbool et al., 2009), are the most difficult issue to tackle.

It has been demonstrated that the use of nanoparticles provides great potential in improving the mobility of oil and alter the formation wettability (Nwidee, Lebedev, Barifcani, Sarmadivaleh, & Iglauer, 2017; Tavakkoli et al., 2013; Tratnyek & Johnson, 2006). This is because nanoparticles may enhance wettability alteration or disaggregation of asphaltene aggregates (Li et al., 2016). Therefore, the goals of this work are to inhibit the formation damage caused by asphaltene deposition and subsequently, to enhance oil recovery using silicate-based nanofluid flooding approach, varying nanoparticle surface chemistry, size and concentration. This is achieved to optimize the formulation and understand the factors related with those phenomena, through different experimental tests such as contact angle, QCM-D measurements, AFM and displacement tests. Also, to understand the interaction between asphaltenes and nanoparticles, computational modeling was carried.

In general terms, this research work will help to demonstrate and support the possibility of using basic/acidic silicate-based nanofluids to modify surface wettability, through modifying the layer of hydrocarbons adsorbed/deposited on inorganic solids (clays, sand, carbonate), and/or from pipelines, in order to improve oil recovery and transportation. In this way, by comparing with the most common technologies used nowadays, these nanofluids will represent a cost-effective alternative as they are naturally derived and could be prepared at low temperature and pressure conditions. Also, a naturally driven solution would be possible, as there would not be any type of contaminants released during the process, and the solvents to be used do not cause any alteration to the reservoir as the considered nanomaterials are naturally occurring.

1.3. Objectives

The main objective of this study is to investigate the interaction of nanoparticles, asphaltenes and surfaces for inhibiting/remediating formation damage caused by asphaltene precipitation in sandstone reservoirs. The specific objectives are:

- Carry out an extensive literature review on the application of nanomaterials as adsorbents for asphaltenes focusing on the recent progress and current challenges. This review includes high-quality information based on the nanoparticle types, factors affecting asphaltene adsorption, type of asphaltenes and adsorption method.

- Investigate the role of nanoparticle size on the interaction with heavy hydrocarbons, asphaltene model molecules, like quinoline 65 (Q-65) and, resin model molecule, like violanthrone 79 (V-79) using both experiments and computational modeling.
- Explore the role of surface acidity and basicity of silicate-based nanoparticles on interaction with asphaltene and silica surfaces using a QCM-D and subsequent asphaltene disaggregation and surface wettability alteration.
- Apply silicate-based nanofluids in water flooding processes for inhibiting/remediating formation damage caused by asphaltene precipitation in silica sand packs, varying nanoparticle concentration, pH and brine salinity.

1.4. Organization of the thesis

This thesis consists of six chapters and one appendix. The thesis is a collection of three articles, two published and one submitted, and one book chapter submitted. In **Chapter One**, background, motivation, objectives, and organization of the thesis are presented. A brief introduction has been included in this chapter since each chapter has a detailed introduction related to its subject.

Chapter Two provides a general overview and a background on asphaltene and formation damage. The chapter also highlighted the current practice of formation damage inhibition and remediation and its challenges. It also presents the recent progress on the use of nanoparticles as asphaltene adsorbents. Part of this research phase has been submitted as a book chapter to Springer Nature publisher titled **"Nanoparticles as Adsorbents for Asphaltenes"** in the book titled: *Nanotechnology for Enhancing In-Situ Recovery and Upgrading of Oil and Gas Processing*".

Chapter Three focuses on the use of violanthrone-79 (V-79) and Quinolin-65 (Q-65) as model heavy compounds to better mimic resin and asphaltenes molecules, respectively, in single and binary model oil solutions to understand their competitive and individual adsorption behaviors on different NiO nanoparticle sizes (5 and 40 nm). This chapter was included in a paper titled "**Size Effects of NiO Nanoparticles on the Competitive Adsorption of Quinolin-65 and Violanthrone-79: Implications for Oil Upgrading and Recovery",** by Tatiana Montoya, Azadeh Amrollahi, Gerardo Vitale, Negahdar Hosseinpour and Nashaat N. Nassar **published in ACS Applied Nano Materials, 2020, vol. 3, no 6, p. 5311-5326.** In this study, both experiments and computational modeling were performed with the Q-65 and V-79 to interact with different sizes of NiO nanoparticles to have an insight on which parts of these compounds get in contact with the nanoparticle surface and which site has more affinity with each compound. Also, molecular dynamic simulations were performed to have more insights on the mechanism involved in the adsorption process.

Chapter Four focuses on the use of the Quartz Crystal Microbalance with Dissipation (QCM-D) to study the asphaltenes adsorption/deposition and film formation over SiO_2 sensor surfaces, and the role of nanofluids on the formed asphaltene layer, in real time. This chapter is part of an article entitled **"Investigation of the Interaction between Nanoparticles, Asphaltenes, and Silica Surfaces by Real-Time Quartz Crystal Microbalance with Dissipation"** by Tatiana Montoya, Archana Jaiswal and Nashaat N. Nassar, published in **The Canadian Journal of Chemical engineering, 2021.** The aim of this study was to investigate the interaction between silicate-based nanofluids and asphaltene pre-adsorbed/deposited on silica surfaces.

Chapter Five focuses on the design and implementation of a core-flood (displacement) setup to work at reservoir conditions using silica sand packs to mimic the production process before and during a formation damage caused by asphaltene precipitation/deposition in the porous media. This chapter is part of an article entitled **"Silicate-Based Nanofluids for Inhibiting/Remediating**

Formation damage by Asphaltene in Sandstone Reservoirs" by Tatiana Montoya and Nashaat N. Nassar and submitted to **ACS Energy and Fuels, 2021.** The goal of this study was to test and understand the role of basic silicate-based nanofluids in the wettability alteration and the inhibition/remediation of the formation damage at reservoir conditions. The results from this study provide valuable findings on the use of silicate-based nanoparticles as formation damage inhibitor/remediator at reservoir conditions.

Finally, **Chapter Six** concludes the important aspects of this research and provides recommendations for future studies.

It should be noted that the present thesis is based on refereed papers that have already been submitted and published. Thus, unavoidably, there will be some repetitions between the chapters particularly in the introduction part or in the sections related with the experimental set-up and characterization analysis.

Appendix A provides Supporting Information for Chapter three.

1.5. References

Acevedo, S., Castillo, J., Fernández, A., Goncalves, S., & Ranaudo, M. A. (1998). A study of multilayer adsorption of asphaltenes on glass surfaces by photothermal surface deformation. Relation of this adsorption to aggregate formation in solution. *Energy & Fuels, 12*(2), 386-390.

Acevedo, S., Castro, A., Negrin, J. G., Fernández, A., Escobar, G., Piscitelli, V., Delolme, Frederic, & Dessalces, G. (2007). Relations between asphaltene structures and their physical and chemical properties: The rosary-type structure. *Energy & Fuels, 21*(4), 2165-2175.

Adams, J. J. (2014). Asphaltene adsorption, a literature review. *Energy & Fuels, 28*(5), 2831-2856.

Al-Maamari, R. S., & Buckley, J. S. (2003). Asphaltene precipitation and alteration of wetting: the potential for wettability changes during oil production. *SPE Reservoir Evaluation & Engineering, 6*(04), 210-214.

Alzate, G. A., Franco, C. A., Restrepo, A., Del Pino Castrillon, J. J., Barreto Alvares, D. L., Murillo, E., & Alberti, A. (2006). *Evaluation of alcohol-based treatments for condensate* *banking removal.* Paper presented at the SPE International Symposium and Exhibition on Formation Damage Control.

Andersen, S. I. (1995). Effect of precipitation temperature on the composition of n-heptane asphaltenes part 2. *Fuel science & technology international, 13*(5), 579-604.

Bennion, D. B. (2002). An overview of formation damage mechanisms causing a reduction in the productivity and injectivity of oil and gas producing formations. *Journal of Canadian Petroleum Technology, 41*(11).

Betancur, S., Carmona, J. C., Nassar, N. N., Franco, C. A., & Cortés, F. B. (2016). Role of particle size and surface acidity of silica gel nanoparticles in inhibition of formation damage by asphaltene in oil reservoirs. *Industrial & Engineering Chemistry Research, 55*(21), 6122-6132.

Carbognani, L. (2000). Effects of iron compounds on the retention of oil polar hydrocarbons over solid sorbents. *Petroleum science and technology, 18*(3-4), 335-360.

Cheraghian, G., & Khalilinezhad, S. (2015). Effect of nanoclay on heavy oil recovery during polymer flooding. *Petroleum science and technology, 33*(9), 999-1007.

Civan, F. (2015). *Reservoir formation damage*: Gulf Professional Publishing.

Creek, J. L. (2005). Freedom of action in the state of asphaltenes: Escape from conventional wisdom. *Energy & fuels, 19*(4), 1212-1224.

Dehghan Monfared, A., Ghazanfari, M. H., Jamialahmadi, M., & Helalizadeh, A. (2016). Potential Application of Silica Nanoparticles for Wettability Alteration of Oil–Wet Calcite: A Mechanistic Study. *Energy & fuels, 30*(5), 3947-3961.

Dudášová, D., Silset, A., & Sjöblom, J. (2008). Quartz crystal microbalance monitoring of asphaltene adsorption/deposition. *Journal of Dispersion Science and Technology, 29*(1), 139-146.

Dudášová, D., Simon, S., Hemmingsen, P. V., & Sjöblom, J. (2008). Study of asphaltenes adsorption onto different minerals and clays: Part 1. Experimental adsorption with UV depletion detection. *Colloids and Surfaces A: Physicochemical and Engineering Aspects, 317*(1-3), 1-9.

Eskin, D., Mohammadzadeh, O., Akbarzadeh, K., Taylor, S. D., & Ratulowski, J. (2016). Reservoir impairment by asphaltenes: A critical review. *The Canadian Journal of Chemical Engineering*.

Franco, C. A., Montoya, T., Nassar, N. N., Pereira-Almao, P., & Cortés, F. B. (2013). Adsorption and Subsequent Oxidation of Colombian Asphaltenes onto Nickel and/or Palladium Oxide Supported on Fumed Silica Nanoparticles. *Energy & fuels, 27*(12), 7336-7347.

Franco, C. A., Nassar, N. N., Ruiz, M. A., Pereira-Almao, P., & Cortés, F. B. (2013). Nanoparticles for inhibition of asphaltenes damage: adsorption study and displacement test on porous media. *Energy & Fuels, 27*(6), 2899-2907.

Ghanavati, M., Shojaei, M.-J., & SA, A. R. (2013). Effects of asphaltene content and temperature on viscosity of Iranian heavy crude oil: experimental and modeling study. *Energy & fuels, 27*(12), 7217-7232.

Ghloum, E. F., Al-Qahtani, M., & Al-Rashid, A. (2010). Effect of inhibitors on asphaltene precipitation for Marrat Kuwaiti reservoirs. *Journal of Petroleum Science and Engineering, 70*(1-2), 99-106.

Gill, S., Tsolakis, A., Dearn, K., & Rodríguez-Fernández, J. (2011). Combustion characteristics and emissions of Fischer–Tropsch diesel fuels in IC engines. *Progress in Energy and Combustion Science, 37*(4), 503-523.

Giraldo, J., Benjumea, P., Lopera, S., Cortés, F. B., & Ruiz, M. A. (2013). Wettability alteration of sandstone cores by alumina-based nanofluids. *Energy & Fuels, 27*(7), 3659-3665.

González, M. F., Stull, C. S., López-Linares, F., & Pereira-Almao, P. (2007). Comparing asphaltene adsorption with model heavy molecules over macroporous solid surfaces. *Energy & Fuels, 21*(1), 234-241.

Goual, L., & Abudu, A. (2009). Predicting the adsorption of asphaltenes from their electrical conductivity. *Energy & Fuels, 24*(1), 469-474.

Guzmán, J. D., Betancur, S., Carrasco-Marín, F., Franco, C. A., Nassar, N. N., & Cortés, F. B. (2016). Importance of the adsorption method used for obtaining the nanoparticle dosage for asphaltene-related treatments. *Energy & Fuels, 30*(3), 2052-2059.

Harbottle, D., Chen, Q., Moorthy, K., Wang, L., Xu, S., Liu, Q., Sjoblom, Johan, & Xu, Z. (2014). Problematic stabilizing films in petroleum emulsions: Shear rheological response of viscoelastic asphaltene films and the effect on drop coalescence. *Langmuir, 30*(23), 6730-6738.

Hashemi, R., Nassar, N. N., & Pereira-Almao, P. (2012). Transport behavior of multimetallic ultradispersed nanoparticles in an oil-sands-packed bed column at a high temperature and pressure. *Energy & fuels, 26*(3), 1645-1655.

Hashemi, R., Nassar, N. N., & Pereira Almao, P. (2013a). Enhanced heavy oil recovery by in situ prepared ultradispersed multimetallic nanoparticles: A study of hot fluid flooding for Athabasca bitumen recovery. *Energy & fuels, 27*(4), 2194-2201.

Hashemi, R., Nassar, N. N., & Pereira Almao, P. (2013b). In situ upgrading of athabasca bitumen using multimetallic ultradispersed nanocatalysts in an oil sands packed-bed column: Part 1. Produced liquid quality enhancement. *Energy & fuels, 28*(2), 1338-1350.

Hashemi, R., Nassar, N. N., & Pereira Almao, P. (2014). In situ upgrading of athabasca bitumen using multimetallic ultradispersed nanocatalysts in an oil sands packed-bed column: Part 2. Solid analysis and gaseous product distribution. *Energy & Fuels, 28*(2), 1351-1361.

Hassan, A., Carbognani, L., & Pereira-Almao, P. (2008). Development of an alternative setup for the estimation of microcarbon residue for heavy oil and fractions: Effects derived from air presence. *Fuel, 87*(17), 3631-3639.

Jada, A., & Debih, H. (2009). Hydrophobation of clay particles by asphaltenes adsorption. *Composite Interfaces, 16*(2-3), 219-235.

Jada, A., Debih, H., & Khodja, M. (2006). Montmorillonite surface properties modifications by asphaltenes adsorption. *Journal of Petroleum Science and Engineering, 52*(1-4), 305-316.

Jang, S. P., & Choi, S. U. (2004). Role of Brownian motion in the enhanced thermal conductivity of nanofluids. *Applied Physics Letters, 84*(21), 4316-4318.

Joonaki, E., & Ghanaatian, S. (2014). The application of nanofluids for enhanced oil recovery: effects on interfacial tension and coreflooding process. *Petroleum science and technology, 32*(21), 2599-2607.

Klein, G. C., Kim, S., Rodgers, R. P., Marshall, A. G., & Yen, A. (2006). Mass spectral analysis of asphaltenes. II. Detailed compositional comparison of asphaltenes deposit to its crude oil counterpart for two geographically different crude oils by ESI FT-ICR MS. *Energy & Fuels, 20*(5), 1973-1979.

Leontaritis, K., Amaefule, J., & Charles, R. (1994). A systematic approach for the prevention and treatment of formation damage caused by asphaltene deposition. *SPE Production & Facilities, 9*(03), 157-164.
Li, R., Jiang, P., Gao, C., Huang, F., Xu, R., & Chen, X. (2016). Experimental investigation of silica-based nanofluid enhanced oil recovery: The effect of wettability alteration. *Energy & Fuels, 31*(1), 188-197.
Lim, S., Zhang, H., Wu, P., Nikolov, A., & Wasan, D. (2016). The dynamic spreading of nanofluids on solid surfaces–Role of the nanofilm structural disjoining pressure. *Journal of colloid and interface science, 470*, 22-30.
Mansoori, G. A. (2010). Remediation of asphaltene and other heavy organic deposits in oil wells and in pipelines. *Socar proceedings, 2010*(4), 12-23.
Maqbool, T., Balgoa, A. T., & Fogler, H. S. (2009). Revisiting asphaltene precipitation from crude oils: A case of neglected kinetic effects. *Energy & Fuels, 23*(7), 3681-3686.
McEachern, P. (2009). Environmental management of Alberta's oil sands.
McElfresh, P. M., Holcomb, D. L., & Ector, D. (2012). *Application of nanofluid technology to improve recovery in oil and gas wells.* Paper presented at the SPE International Oilfield Nanotechnology Conference and Exhibition.
Mohammadi, M., Akbari, M., Fakhroueian, Z., Bahramian, A., Azin, R., & Arya, S. (2011). Inhibition of asphaltene precipitation by TiO2, SiO2, and ZrO2 nanofluids. *Energy & Fuels, 25*(7), 3150-3156.
Mohammadi, M., Dadvar, M., & Dabir, B. (2017). TiO2/SiO2 nanofluids as novel inhibitors for the stability of asphaltene particles in crude oil: Mechanistic understanding, screening, modeling, and optimization. *Journal of Molecular Liquids, 238*, 326-340.
Moradi, B., Pourafshary, P., Jalali, F., Mohammadi, M., & Emadi, M. (2015). Experimental study of water-based nanofluid alternating gas injection as a novel enhanced oil-recovery method in oil-wet carbonate reservoirs. *Journal of Natural Gas Science and Engineering, 27*, 64-73.
Mullins, O. C. (2011). The asphaltenes. *Annual Review of Analytical Chemistry, 4*, 393-418.
Mullins, O. C., Sabbah, H., Eyssautier, J. l., Pomerantz, A. E., Barré, L., Andrews, A. B., Ruiz-Morales, Yosadara, & Mostowfi, F., McFarlane, Richard, Goual, Lamia. (2012). Advances in asphaltene science and the Yen–Mullins model. *Energy & fuels, 26*(7), 3986-4003.
Mustafin, R., Manasrah, A. D., Vitale, G., Askari, R., & Nassar, N. N. (2020). Enhanced thermal conductivity and reduced viscosity of aegirine-based VR/VGO nanofluids for enhanced thermal oil recovery application. *Journal of Petroleum Science and Engineering, 185*, 106569.
Nasrabadi, H., Moortgat, J., & Firoozabadi, A. (2016). New three-phase multicomponent compositional model for asphaltene precipitation during CO2 injection using CPA-EOS. *Energy & fuels, 30*(4), 3306-3319.
Nassar, N. N., Betancur, S., Acevedo, S. c., Franco, C. A., & Cortés, F. B. (2015). Development of a population balance model to describe the influence of shear and nanoparticles on the aggregation and fragmentation of asphaltene aggregates. *Industrial & Engineering Chemistry Research, 54*(33), 8201-8211.

Nassar, N. N., Hassan, A., Carbognani, L., Lopez-Linares, F., & Pereira-Almao, P. (2012). Iron oxide nanoparticles for rapid adsorption and enhanced catalytic oxidation of thermally cracked asphaltenes. *Fuel, 95*, 257-262.

Nassar, N. N., Hassan, A., Luna, G., & Pereira-Almao, P. (2013). Kinetics of the catalytic thermo-oxidation of asphaltenes at isothermal conditions on different metal oxide nanoparticle surfaces. *Catalysis Today, 207*, 127-132.

Nassar, N. N., Hassan, A., & Pereira-Almao, P. (2011). Metal oxide nanoparticles for asphaltene adsorption and oxidation. *Energy & Fuels, 25*(3), 1017-1023.

Nassar, N. N., Hassan, A., & Pereira-Almao, P. (2013). Clarifying the catalytic role of NiO nanoparticles in the oxidation of asphaltenes. *Applied Catalysis A: General, 462*, 116-120.

Negin, C., Ali, S., & Xie, Q. (2016). Application of nanotechnology for enhancing oil recovery–A review. *Petroleum, 2*(4), 324-333.

Nezhad, S. S. K., & Cheraghian, G. (2016). Mechanisms behind injecting the combination of nano-clay particles and polymer solution for enhanced oil recovery. *Applied Nanoscience, 6*(6), 923-931.

Nwidee, L. N., Lebedev, M., Barifcani, A., Sarmadivaleh, M., & Iglauer, S. (2017). Wettability alteration of oil-wet limestone using surfactant-nanoparticle formulation. *Journal of colloid and interface science, 504*, 334-345.

Patel, H. E., Das, S. K., Sundararajan, T., Sreekumaran Nair, A., George, B., & Pradeep, T. (2003). Thermal conductivities of naked and monolayer protected metal nanoparticle based nanofluids: Manifestation of anomalous enhancement and chemical effects. *Applied Physics Letters, 83*(14), 2931-2933.

Pernyeszi, T., Patzko, A., Berkesi, O., & Dékány, I. (1998). Asphaltene adsorption on clays and crude oil reservoir rocks. *Colloids and Surfaces A: Physicochemical and Engineering Aspects, 137*(1-3), 373-384.

Qiao, P., Harbottle, D., Tchoukov, P., Masliyah, J., Sjoblom, J., Liu, Q., & Xu, Z. (2017). Fractionation of asphaltenes in understanding their role in petroleum emulsion stability and fouling. *Energy & Fuels, 31*(4), 3330-3337.

Rezvani, H., Khalilnezhad, A., Ganji, P., & Kazemzadeh, Y. (2017). How ZrO 2 nanoparticles improve the oil recovery by affecting the interfacial phenomena in the reservoir conditions? *Journal of Molecular Liquids*.

Rudrake, A., Karan, K., & Horton, J. H. (2009). A combined QCM and XPS investigation of asphaltene adsorption on metal surfaces. *Journal of colloid and interface science, 332*(1), 22-31.

Schuler, B., Meyer, G., Peña, D., Mullins, O. C., & Gross, L. (2015). Unraveling the molecular structures of asphaltenes by atomic force microscopy. *Journal of the American Chemical Society, 137*(31), 9870-9876.

Sedaghat, M., Mohammadi, H., & Razmi, R. (2016). Application of SiO2 and TiO2 nano particles to enhance the efficiency of polymer-surfactant floods. *Energy Sources, Part A: Recovery, Utilization, and Environmental Effects, 38*(1), 22-28.

Sedghi, M., Goual, L., Welch, W., & Kubelka, J. (2013). Effect of asphaltene structure on association and aggregation using molecular dynamics. *The Journal of Physical Chemistry B, 117*(18), 5765-5776.

Tavakkoli, M., Panuganti, S. R., Vargas, F. M., Taghikhani, V., Pishvaie, M. R., & Chapman, W. G. (2013). Asphaltene deposition in different depositing environments: part 1. Model oil. *Energy & fuels, 28*(3), 1617-1628.

Tratnyek, P. G., & Johnson, R. L. (2006). Nanotechnologies for environmental cleanup. *Nano today, 1*(2), 44-48.

Trimm, D. (1996). Catalytic deactivation *Studies in Surface Science and Catalysis* (Vol. 100, pp. 65-76): Elsevier.

Tu, Y., Woods, J., Kung, J., McCracken, T., Kotlyar, L., Sparks, B., & Dong, M. (2006). Adsorption of SARA Fractions from Heavy Oil and Bitumen on Kaolinite. *Clay Science, 12*(Supplement2), 183-187.

Vitale, G. (2013). Iron Silicate Nano-Crystals as Potential Catalysts or Adsorbents for Heavy Hydrocarbons Upgrading. *"Iron Silicate Nano-Crystals as Potential Catalysts or Adsorbents for Heavy Hydrocarbons Upgrading". PhD thesis, University of Calgary*.

Worthen, A. J., Bryant, S. L., Huh, C., & Johnston, K. P. (2013). Carbon dioxide-in-water foams stabilized with nanoparticles and surfactant acting in synergy. *AIChE Journal, 59*(9), 3490-3501.

Xie, K., & Karan, K. (2005). Kinetics and thermodynamics of asphaltene adsorption on metal surfaces: A preliminary study. *Energy & Fuels, 19*(4), 1252-1260.

Yarranton, H. W. (2005). Asphaltene self-association. *Journal of dispersion science and technology, 26*(1), 5-8.

You, Z., Badalyan, A., Bedrikovetsky, P., Hand, M., & Jenson, D. (2013). *Productivity Decline Due to Fines Migration (Modelling and Field Case).* Paper presented at the International Petroleum Technology Conference.

Zahabi, A., Gray, M. R., & Dabros, T. (2012). Kinetics and properties of asphaltene adsorption on surfaces. *Energy & Fuels*, *26*(2), 1009-1018.

Zhang, L., Shi, C., Lu, Q., Liu, Q., & Zeng, H. (2016). Probing Molecular Interactions of Asphaltenes in Heptol Using a Surface Forces Apparatus: Implications on Stability of Water-in-Oil Emulsions. *Langmuir, 32*(19), 4886-4895.

Chapter Two: Asphaltene Precipitation Fundamentals and Nanoparticle Application[1]

2.1. Abstract

Asphaltenes in crude oil, and consequently their adsorption and deposition on rock surfaces, affects rock properties. Therefore, in recent years, the oil industry has been using nanotechnology to solve problems caused by asphaltenes. Nanoparticles can rapidly remove asphaltenes from heavy oil, thus making the remaining oil transportable for conventional processing. Also, nanoparticles can be employed as catalysts to change asphaltenes into light usable distillates. This chapter describes asphaltenes in terms of their structure and behavior, which depend on several factors. Also, fundamentals of asphaltene precipitation in porous media and fluid flow in porous media are discussed. This chapter presents field reports on asphaltene deposition and conventional treatments used to remediate asphaltene deposition. In addition, this chapter presents some porous media studies and laboratory studies performed to determine asphaltene deposition. Finally, this chapter discusses the role of nanoparticles as asphaltene adsorbents, the types of nanoparticles used, and the application of nanoparticles to inhibit formation damage by asphaltene precipitation.
Keywords: Asphaltenes, formation damage, nanoparticles, inhibition

[1] Some of the information in this chapter is adapted from a book chapter to springer nature publisher titled **"Nanoparticles as Adsorbents for Asphaltenes"** by Abdallah Manasrah, **Tatiana Montoya** and Nashaat N. Nassar, and it is a subchapter of the book titled: "*Nanoparticles: An Emerging Technology for Oil Production and Processing Applications*" published by Springer Nature, 2021.

2.2. Introduction

Population growth and an increase in industrialization and living standards are factors that have caused a worldwide increase in total energy demand, and the demand is expected to increase a further 33% by 2035 (Rezvani, Khalilnezhad, Ganji, & Kazemzadeh, 2017). Therefore, it is necessary to find environmentally friendly, cost-effective, and sustainable sources of energy to meet this global demand. Various natural energy resources have been explored, including biomass, vegetable oils, and biodiesel (Perman, 2003). These resources are believed to be environmentally friendly fuels (Agarwal, 2007), but they are costly and insufficient in meeting energy demands. Further, usually these types of fuels need to be formulated to obtain similar properties of conventional fuels (Agarwal, 2007). Most importantly, they require advanced techniques to evaluate their advantages, disadvantages, and specific applications. These facts have led to an increased demand for upgrading and recovering unconventional oil to meet current and future energy needs. For instance, the oil sands reserves in Alberta are larger than the reserves of Iran, Iraq, or Russia, and are second only in size to those of Saudi Arabia (McEachern, 2009). However, only 20% of these reserves are easily extracted and the remaining 80% must be recovered using EOR methods (McEachern, 2009). In addition, formation damage has occurred in some reserves in the world (Betancur, Carmona, Nassar, Franco, & Cortés, 2016). This undesirable operational problem reduces oil and gas recovery, limits reservoir productivity, and causes inefficient operations (Franco, Montoya, Nassar, Pereira-Almao, & Cortés, 2013; Maqbool, Balgoa, & Fogler, 2009). Formation damage can be caused by several factors, including interactions between the porous medium and reservoir fluids, which can result in fine migration (You, Badalyan, Bedrikovetsky, Hand, & Jenson, 2013), asphaltene precipitation/deposition (Adams, 2014;

Mullins, 2011), condensate banks (Alzate et al., 2006), and alteration of rock wettability (Civan, 2015).

Another main challenge facing the oil industry is the presence of polar heavy hydrocarbons in an oil matrix. These molecules have caused major complications in pipelines and wellbores during the utilization and recovery of oil. A type of formation damage known as precipitation and deposition of asphaltenes in reservoirs and in production systems (K. Leontaritis, Amaefule, & Charles, 1994; Maqbool et al., 2009) is the most difficult to surpass. In addition, asphaltene deposition affects many different domains of the oil industry, such as altering reservoir rock wettability due to the potential of asphaltenes to be adsorbed on reservoir rock (Al-Maamari & Buckley, 2003; Majid Mohammadi, Dadvar, & Dabir, 2017), plugging flow lines because of asphaltene deposition (Creek, 2005), and refinery catalyst deactivation because of asphaltene adsorption at active sites (Trimm, 1996). Consequently, these asphaltene-related problems cause significant production losses and vastly increase operational costs.

Because there is a need to increase oil production, these problems mandate studies on removing asphaltenes from oil and bitumen. Hence, several techniques have been proposed to inhibit asphaltene deposition mainly in areas close to wells (K. Leontaritis et al., 1994). These methods include periodic intervention via solvent soaking or constant chemical injection (Betancur, Carmona, et al., 2016; Mansoori, 2010). There are also chemical treatments, including adding dispersants, anti-flocculants, coagulants, flocculants, and nonpolar solvents, which are mainly employed to control asphaltene precipitation and deposition (Ghloum, Al-Qahtani, & Al-Rashid, 2010; Mansoori, 2010). However, conventional methods, chemical treatments, and mechanical, thermal, and biological methods are expensive because, in most cases, they require complex equipment and additional staff on location (Betancur, Carmona, et al., 2016; Mansoori, 2010);

also, they have low durability, can cause changes in fluid composition and do not guarantee the prevention of asphaltene deposition after treatment, and are of environmental concern (Betancur, Carmona, et al., 2016; Mansoori, 2010).

In recent years, nanotechnology has been shown to have a significant impact on industrial applications. Nanoparticles and/or nanofluids are alternatives that can be used to reduce damage caused by asphaltene precipitation and for in situ enhancement of reservoir productivity (Li et al., 2016; Mohsen Mohammadi et al., 2011; Rezvani et al., 2017). Due to the unique properties of nanoparticles, such as high surface area/volume ratios, specific chemical reactivity, active surfaces and excellent dispersibility (Rezvani et al., 2017), they potentially offer an environmentally friendly and cost-effective approach for heavy oil recovery and upgrading.

Asphaltene adsorption has been studied extensively, but little has been done on the effect of nanoparticles on asphaltene precipitation in porous media. This chapter focuses on the problems related to asphaltenes in reservoirs, parameters affected by asphaltene precipitation/deposition, common treatments used to reduce formation damage by asphaltene precipitation and using nanoparticles to inhibit formation damage and improve oil recovery.

2.3. Asphaltenes

Asphaltenes are typically defined as the heaviest, most aromatic, and surface-active fraction of crude oil, and they are insoluble in light paraffins like *n*-pentane (n-C_5), *n*-hexane (n-C_6), and *n*-heptane (n-C_7) but soluble in light aromatics like benzene, toluene, or pyridine (Adams, 2014; Mullins, 2011; Mullins et al., 2012). Generally, asphaltenes have a polyaromatic structure that includes a few alkyl groups per aromatic ring, and their structure contains some heteroatoms, such as nitrogen, sulfur, oxygen, and several metallic heteroatoms, such as vanadium, iron and nickel

(Groenzin & Mullins, 2000). Thus, the presence of functional groups, such as carboxyl, ketones, aldehydes, benzothiophenes, dibenzothiophenes, naftenobenzotiophenes, alkyl sulfides, aryl alkyl sulfides, and aryl sulfides is likely to occur in asphaltene structures (Groenzin & Mullins, 1999; Mullins, 2011). Although the structure of asphaltenes is complex, basically, they have a nucleus composed of one or more cross-linked polyaromatic hydrocarbons (PAHs) (Acevedo, Castro, Negrin, Fernández, & Escobar, 2007; Mullins, 2011; Mullins et al., 2012). Several hypotheses on the chemical structures of asphaltenes are proposed in the literature, and these structures can be an island, archipelago, continental, or rosary-type (Acevedo et al., 2007; Durand et al., 2010; Mullins et al., 2012), as shown in **Figure 2.1** (a-d). Island architecture is composed of seven fused rings and one PAH, while archipelago architecture is composed of more than one PAH per asphaltene molecule and connected by alkyl chains (Mullins et al., 2012; Murgich, 2003). Continental architecture is composed of one or two PAHs, but it has more than seven fused rings (Durand et al., 2010; Murgich, 2003). Rosary architecture is very flexible and comprises two or more PAHs joined by flexible aliphatic chains. However, owing to their complex chemical structure, asphaltene architectures are being updated over time.

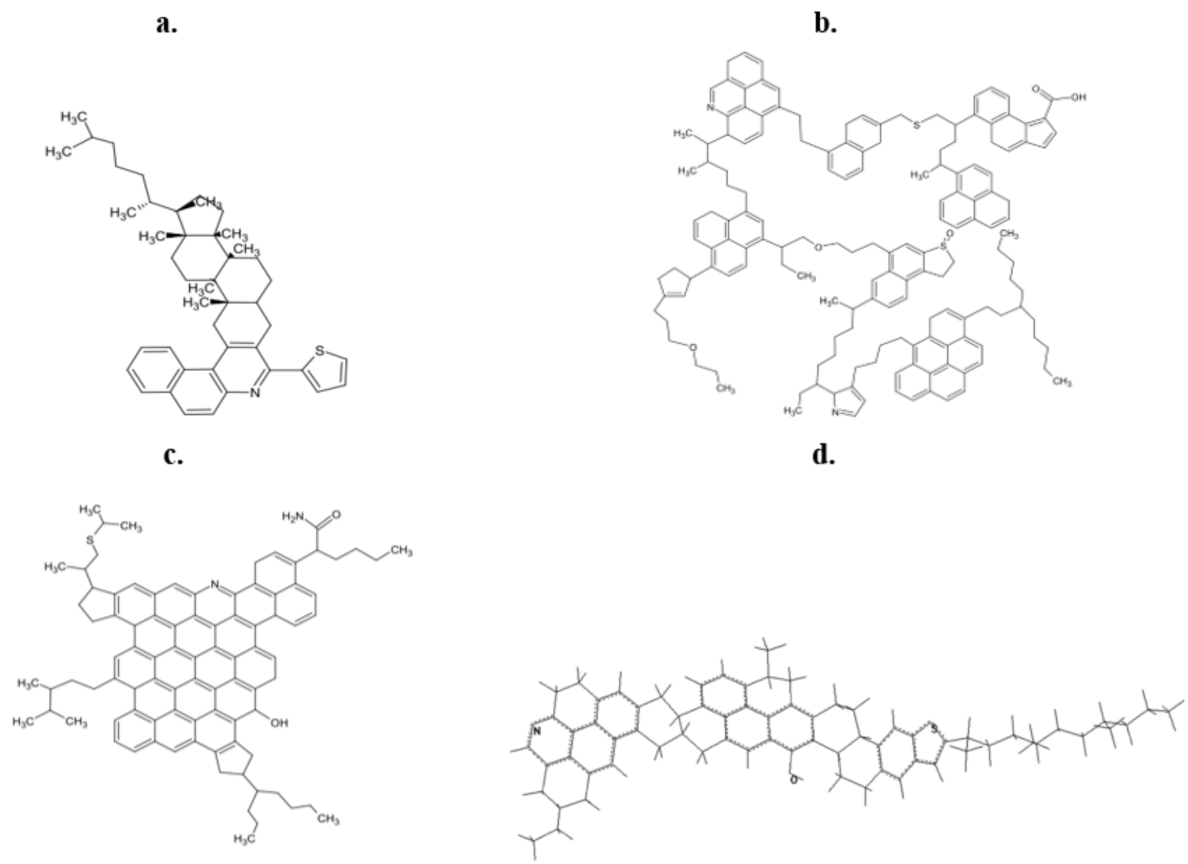

Figure 2.1. Schematic representations of different proposed molecular structures of asphaltenes: a) island structure, b) archipelago structure, c) continental structure, and d) rosary-type structure. Island, archipelago, continental, and rosary-type structures are reproduced from Mullins et al. (Mullins et al., 2012), Durand et al. (Durand et al., 2010), and Acevedo et al. (Acevedo et al., 2007), respectively.

The Yen-Mullis model is the most accepted model that describes the asphaltenes colloidal and molecular structure (Mullins, 2010, 2011; Mullins et al., 2012; Ruiz-Morales, 2009; Sabbah, Morrow, Pomerantz, & Zare, 2011; Yen, Erdman, & Pollack, 1961), as shown in **Figure 2.2**. This model considers island architecture to be the dominant molecular architecture of asphaltenes, and the structure has an average of seven fused rings in the PAH core and an asphaltene molecular weight of ~750 Da and a size of 1.5 nm (Figure 2.2, left). As asphaltene concentration increases, the self-associative nature of asphaltenes causes them to form nanoaggregates that have an average size of 2 nm (**Figure 2.2**, center). At higher asphaltene concentrations, the nanoaggregates form clusters that have an average size of 5 nm and aggregation numbers < 10 (**Figure 2.2**, right) (Mullins et al., 2012). Because of their amphiphilic behavior, asphaltenes tend to self-assemble and form large aggregates, which increase crude oil viscosity (Chianelli et al., 2007; Ghanavati, Shojaei, & SA, 2013; K. Leontaritis et al., 1994). In addition, asphaltenes that contain a high content of sulfur form strong C-S and C=S bonds and significantly increase crude oil viscosity (Chavan, Kini, & Ghosal, 2012; Chuan et al., 2010; Manasrah, Nassar, & Ortega, 2018). Further, large amounts of N and S in asphaltene structures produce SO_x, NO_x, and H_2S during processing. These characteristics of asphaltenes and their high content in heavy and extra heavy oil make it difficult to produce, transport, and process oil. Injecting naphtha or CO_2 to reduce viscosity are proven techniques for improving the production of crude oil. However, these techniques could lead to serious problems due to the possibility of modifying the flow and phase behavior of the oil under reservoir conditions, which leads to asphaltene precipitation and deposition in porous media and throughout the production system (K. Leontaritis et al., 1994; Oskui et al., 2011).

For sub-surface applications, if asphaltene precipitation and deposition occur in reservoir rock, it could reduce both porosity and permeability and negatively affect reservoir wettability changing it from a water-wet system to an oil-wet system that, together with high HO viscosities, result in the reduction of crude oil mobility (Al-Maamari & Buckley, 2003; K. Leontaritis et al., 1994). For on-surface applications, if asphaltene precipitation occurs throughout the production system, it could have a negative impact on pumps, pipelines, and surface facilities due to flow blocking and corrosion (Chavan et al., 2012). In both cases, these adverse effects reduce production and, hence, the energy return on investment (EROI), and in the worst scenario, the effects could cause the operation to be abandoned (Gharfeh, Yen, Asomaning, & Blumer, 2004).

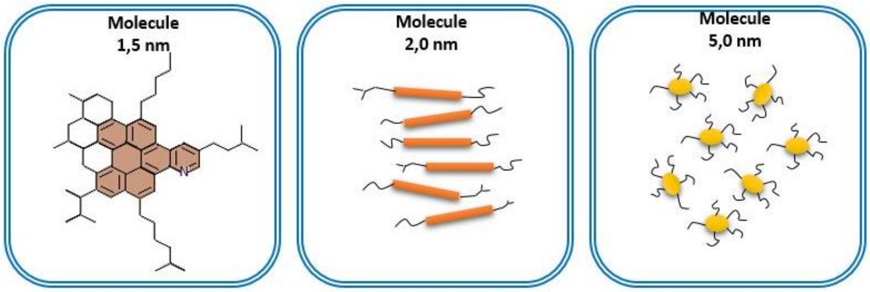

Figure 2.2. Yen-Mullins model (Mullins, 2010, 2011; Ruiz-Morales, 2009; Sabbah et al., 2011)

2.4. Fundamentals of Asphaltene Precipitation and Flow in Porous Media

Asphaltenes are present in oil and pass several phases depending on their stability and how well they remain in solution under the thermodynamic and operational conditions at which the oil is produced (Nghiem & Coombe, 1997). Initially, in the thermodynamic conditions of the reservoir, asphaltenes are stable and soluble in the oil; they remain soluble until any change in the conditions or in the equilibrium occurs (Fakher, Ahdaya, Elturki, & Imqam, 2020). After a change, the asphaltenes start to form solid particles in the crude oil solution (Fakher et al., 2020). The formation of solid particles in crude oil is called precipitation, and it involves asphaltene solids coming out of solution and forming visible asphaltene particles suspended in the oil. While these asphaltenes are suspended in oil, they do not present a threat because they move with the oil as long as precipitation does not keep increasing (Fakher et al., 2020).

2.4.1. Factors Affecting Asphaltene Precipitation

Asphaltene stability can be affected by several factors (Rogel, Leon, Espidel, & Gonzalez, 2001), which can be classified as operational and reservoir factors as shown in **Figure 2.3** (Fakher et al., 2020). Operational factors are related to external processes applied during oil production to alter oil properties; for example, solvents, such as CO_2, steam, surfactants, nitrogen, and methane, can be injected (Al-Maamari & Buckley, 2003; Fakher et al., 2020). As a solvent starts to interact with the oil, asphaltenes might be destabilized in the crude oil due to a change in the equilibrium conditions; this situation can occur slowly or quickly depending on the solvent type and concentration (Fakher et al., 2020). In contrast, reservoir factors, such as pressure, start to have influence above the bubble point (Moghanloo, Davudov, & Akita, 2018). If pressure is above the bubble point and decreases, asphaltene solubility decreases until reaching the minimum at bubble point pressure (Moghanloo et al., 2018); however, it has been reported that asphaltene solubility increases when decreasing pressure below the bubble point (Burke, Hobbs, & Kashou, 1990). Temperature influences asphaltene precipitation as well. Asphaltene solubility changes with temperature depending on the reservoir temperature (K. J. Leontaritis, 1996): asphaltene solubility increases if the temperature remains below reservoir temperature, and if the temperature is above reservoir temperature, asphaltene solubility decreases (Moghanloo et al., 2018). Finally, asphaltene solubility decreases when the amount of gas in solution increases (Burke et al., 1990; Moghanloo et al., 2018).

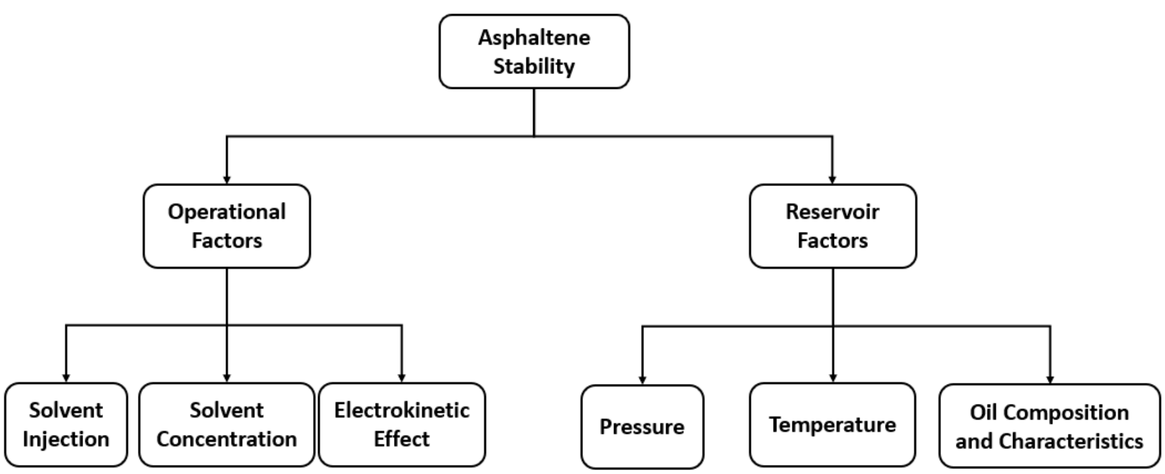

Figure 2.3. Factors that affect asphaltenes stability in crude oils (adapted from (Fakher et al., 2020)).

If asphaltene precipitation keeps increasing, asphaltene particles form larger asphaltene flocs that have a higher density than the previously precipitated particles. If asphaltene flocculation is noticed early, it can be remediated. In remediation processes, a stabilizing chemical agent is used, and asphaltene flocs are broken down into smaller precipitated particles and homogenized back into the crude oil (Fakher et al., 2020). Otherwise, if asphaltene flocculation continues, asphaltenes start to deposit. If a large volume of asphaltenes is deposited, it can plug pores in the reservoir and clog wellbores and pipelines (Fakher et al., 2020). Asphaltene deposition/adsorption on rock surfaces has a negative impact in reservoirs and can alter wettability and reduce permeability and oil recovery (Al-Maamari & Buckley, 2003; Majid Mohammadi et al., 2017). **Figure 2.4** illustrates some of the problems related with asphaltenes precipitation/deposition.

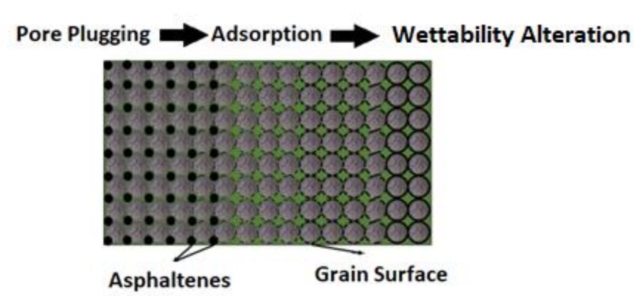

Figure 2.4. Asphaltene impact on porous medium (Fakher et al., 2020).

2.4.2. Fluid Flow in Porous Media

Hydrocarbon reservoirs are systems mainly consisting of reservoir rock and reservoir fluids (Civan, 2015). Porosity and permeability are the most important pore structure properties used in the discussion of hydrocarbon-reservoir-rock systems (Moghanloo et al., 2018). Due to multiphase flow behavior under varying pressure and temperature conditions, hydrocarbon systems are typically complex (Ahmed, 2018). Understanding reservoir and fluid properties is essential to understand oil recovery processes and the conditions needed to avoid problems such formation damage by organic precipitation.

2.4.3. Porosity

Porosity refers to the measure of void spaces in a certain material. Porosity is defined as the pore fraction of the rock volume over the total rock volume, which means the ratio of pore space volume to bulk rock volume. Porosity is usually expressed as a percentage varying from 0 to 100 % and can be expressed mathematically as follows:

$$\emptyset = \frac{V_p}{V_b} = \frac{V_b - V_g}{V_b} \qquad (2.1)$$

Where V_p is pore volume (m^3), V_b is bulk volume (m^3), V_g is grain volume (m^3), and $\emptyset$ is porosity (%). Porosity can be classified as primary and secondary porosity. Primary porosity results from deposited sediments, while secondary porosity occurs after post-depositional processes, such as dissolution, reprecipitation, and fracturing. Fractures, root channels, and animal burrows are some examples of secondary porosity, also, after geological events such as underground stresses, water movement, or geological activities that occur after sediment formation. From an engineering perspective, porosity can be classified as total and effective porosity. Total porosity considers connected and isolated pore spaces, which is irrelevant to fluid flow. In contrast, effective porosity corresponds to interconnected pores that allow fluid to flow through a formation.

2.4.4. Permeability

Permeability is defined as the ability of porous medium (rock) to transmit fluids under an applied pressure gradient. It is also considered as rock conductivity for flow. Typically, permeability is defined by Darcy's law, which states that the apparent velocity of a fluid flowing through a porous medium is directly proportional to the pressure gradient (dP/dx) and inversely proportional to fluid viscosity. The constant of proportionality, K, is called the permeability of a porous medium. Darcy's law, used to determine K, assumes flow is linear, laminar, and steady state and the porous medium is homogenous, as shown in equation 2.2, for flow in one direction:

$$v = \frac{q}{A} = -\frac{K}{\mu}\frac{dP}{dx} \qquad (2.2)$$

Where v is the apparent flow velocity (cm/s), q is the volumetric flow rate (cm^3/s), A is the cross-sectional area (cm^2), μ is the fluid viscosity (cP), $\frac{dP}{dx}$ is the pressure gradient atm/cm, and K is the permeability in Darcy's law. Rock permeability can be determined in the laboratory by measuring the pressure drop across a sample at different flow rates. This permeability is known as absolute permeability since it refers to a total saturation of the sample using one phase fluid. Darcy's law should be modified to account for more than one fluid. When flow is more than one phase, the term effective permeability of the phase K_{phase} is used; this term refers to the permeability of a given fluid when another fluid occupies some part of the pore space; due to this occupancy by other fluid, effective permeability is commonly lower than absolute permeability. Therefore, for flows of more than one fluid, the term relative permeability, $K_{r,phase}$, is used; this term is the ratio of the effective permeability of a phase to absolute permeability, as shown in equation 2.3:

$$K_{r,phase} = \frac{K_{phase}}{K} \qquad (2.3)$$

Where the phases can be oil, water, and/or gas, $K_{r,phase}$ is the relative permeability of a phase, K_{phase} is the effective permeability of a phase, and K is absolute permeability. Therefore, when two or more phases are present in the pores, flow of each phase is restricted by the other phases.

As the saturation of the water or gas phases is increased and the oil saturation decreases, the resistance for oil to flow increases until oil no longer flows at its residual oil saturation.

Relative permeability makes it possible to extend Darcy's law to immiscible three-phase flow in the porous media, such as water oil-gas systems. For a system were water is linearly displacing oil in a thin tube of porous media, where ρ is the phase density, g is the gravitational constant and α the inclination angle, Darcy's law can be expressed by the volumetric flux, q, for each phase as follows:

$$q_o = -A\frac{KK_{ro}}{\mu_o}\left(\frac{\partial P_o}{\partial x} \pm \rho_o g sin\alpha\right) \quad (2.4)$$

$$q_w = -A\frac{KK_{rw}}{\mu_w}\left(\frac{\partial P_w}{\partial x} \pm \rho_w g sin\alpha\right) \quad (2.5)$$

$$q_g = -A\frac{KK_{rg}}{\mu_g}\left(\frac{\partial P_g}{\partial x} \pm \rho_g g sin\alpha\right) \quad (2.6)$$

2.4.5. Capillary Pressure

Fluid-fluid interfaces occur in small pores in porous media, and these interfaces are highly curved. Due to interfacial tension, fluid pressure is not the same on both sides of the curved interface. Capillary pressure P_c is defined as the difference in pressure across an interface between two phases at equilibrium. Capillary pressure is directly proportional to interfacial tension and the wetting angle as shown in equation 2.7:

$$P_c = P_{nw} - P_w = \frac{2\sigma cos\theta}{r} \quad (2.7)$$

Where P_c is capillary pressure, P_{nw} is the non-wetting phase pressure, P_w is the wetting phase pressure, σ is the interfacial tension, θ is the wetting angle, and r is the pore radius. In reservoir engineering, capillary pressure is usually defined as the difference between oil pressure and water pressure, and it does not consider the wetting phase, which means that the capillary pressure becomes negative when oil is in the wetting phase.

2.4.6. Saturation

Saturation is defined as the ratio of a given phase volume contained in rock divided by the total pore volume of the rock. It is necessary to determine saturation at different points in the reservoir to approximate hydrocarbon volumes within a reservoir satisfactorily. Equation 2.8 denotes saturation for water (w), oil(o), and gas (g):

$$S_w = \frac{V_w}{V_p}; S_o = \frac{V_o}{V_p};\ S_g = \frac{V_g}{V_p} \qquad (2.8)$$

Where V_p is the pore volume of a sample; V_g, V_w, V_o are the volumes of gas, water, and oil, respectively; S_g, S_w, S_o are the saturations of gas, water and oil, respectively. When several fluids are present in a porous medium, each pore contains one or more of the other fluids. Therefore, the sum of the fluid saturation values is always equal to one as shown in equation 2.9 for a reservoir with oil, water, and gas:

$$S_o + S_w + S_g = 1 \qquad (2.9)$$

2.5. Asphaltene Formation Damage and Field Reports

As mentioned, asphaltene deposition can cause problems during oil production. Leontaritis et al. (K. Leontaritis et al., 1994) reported that there were four forms of formation damage induced by asphaltene deposition: (1) physical blockage or reduced permeability, (2) wettability alteration, (3) decreased crude oil viscosity, and (4) formation of a water-in oil emulsion. However, reduced permeability is the dominant form of formation damage. Adsorption of asphaltenes on rock surfaces is the first step in asphaltene deposition; then, hydrodynamic retention and/or trapping of the particles in the pore throat occurs, which eventually reduces effective oil mobility (Al-Maamari & Buckley, 2003; Moghanloo et al., 2018; Nghiem, Coombe, & Ali, 1998).

Some field cases report asphaltene precipitation during reservoir production and in the inside of reservoirs. However, there are no field cases, reports, nor investigations on asphaltenes in unconventional reservoirs. Most of the reported reservoirs are at high temperatures and moderately high pressures, which are two parameters that significantly affect asphaltene stability. (Moghanloo et al., 2018) reported that in Hassi Messaud, an Algerian field that had deposits of asphaltenes on the production tubing, the oil was light and had an asphaltene content of 0.062% because the wellhead pressure was close to the oil saturation pressure. Thomas et al. (Thomas, Becker, & Del Real Soria, 1995) reported on three fields: 1) a sandstone field in Mexico that had reduced oil production after nine months from 4700 to 436 barrels per day (BPD) because of asphaltene precipitation in the tubing, 2) a field in Louisiana that had reduced oil production from 406 to 56 BPD, and 3) a field in Mexico that was completely blocked by asphaltene deposition. Kalantari-Dahagi et al. (Kalantari-Dahaghi, Moghadasi, Gholami, & Abdi, 2006) reported a carbonate field, Kupal in Iran, which had reduced permeability of 45-90% due to asphaltene deposition after CO_2 injection. Also, Al-Ghazi and Lawson (Al-Ghazi & Lawson, 2007) reported a complete blockage due to asphaltene precipitation in a limestone formation in a field called Ghawar in Saudi Arabia. In contrast, Uetani (Uetani, 2014) reported altered wettability by asphaltene deposition in a field located in Japan.

2.6. Mitigation of Asphaltene Deposition in Oil Fields

Asphaltene mitigation is extremely complex since many of the chemicals used to remedy asphaltene problems have several drawbacks, including being incompatible with reservoir fluids, costly, environmentally unfriendly, unstable at reservoir conditions, and causing adverse health effects (Moghanloo et al., 2018). The conventional way to treat asphaltene deposition problems has been to use xylene, toluene, or other aromatic solvents (Thomas et al., 1995). This method requires using large amounts of an aromatic solvent and several treatments (Thomas et al., 1995). If reservoir production is decreased by asphaltene deposition, a clean-up treatment is required, which involves wellbore and formation cleanup, formation squeeze, or continuous injection to prevent more deposition. For the solvent treatment to be effective, the solvent must keep asphaltenes in solution throughout the production system; if this is not achieved, re-precipitation may occur (Thomas et al., 1995).

Some of the conventional treatments for asphaltene precipitation have been modified using additives to enhance performance; however, the new formulations are not reported. For example, Schantz and Stephenson (Schantz & Stephenson, 1991) chemically treated a field located in North Dakota. They first injected xylene, and production increased from 42 to 60 BPD. Also, they used a mixture of dispersant A and a paraffin/solid dispersant to remediate suspended entrapped solids in a field located in Wyoming. After this treatment, oil recovery increased by 33%. Thomas et al. (Thomas et al., 1995) reported using a mixture of 90 % xylene and 10 % “product 1” in a field located in Mexico to remediate asphaltene deposition in tubing. They also used a mutual solvent followed by a mixture of 90% “product 3” and 10% xylene to treat the formation; after these treatments, production increased from 436 to 4800 BPD. Also, (Thomas et al., 1995) used xylene and “product 2” with a mutual solvent pre-flush for a field located in Louisiana, and after the xylene treatment, production increased from 53 to 101 BPD, but later decreased to 66 BPD; after the second treatment, production increased to 152 and then stabilized at 91 BPD. In addition, Al-Ghazi and Lawson (Al-Ghazi & Lawson, 2007) reported using bullhead water to treat asphaltene precipitation in tubing in a field in Saudi Arabia. Bullhead xylene was supposed to be used, but the rate of penetration was not sufficient to break up asphaltenes; therefore, workover was considered the best option for this scenario. Finally, Uetani (Uetani, 2014) used xylene in a field in Japan, and after treatment, productivity increased and water cut decreased from 10-15% to 2-3%.

2.7. Porous Media Studies

As previously discussed, asphaltene deposition problems in rock reservoirs are difficult to remediate compared to remediating production tubing deposition issues, which are typically the focus of several asphaltene studies. Therefore, in this section, experimental studies conducted in laboratories on asphaltene deposition in porous media are discussed. Also, some theoretical aspects related to wettability are presented.

2.7.1. Asphaltene Deposition Measurement

Asphaltene deposition is the process where asphaltenes aggregate and attach to a surface. Asphaltenes can be adsorbed on a surface, which depends on the interaction between the surface and asphaltenes (Alian, Omar, Alta’ee, & Hani, 2011). Asphaltene deposition studies are mainly performed using microfluidics or capillary flow, Taylor-Couette (TC) cells, or core flooding experiments through porous media. Microfluidics study different phenomena, such as colloidal dynamics at very low Reynolds numbers (Mitra & Chakraborty, 2011). The Taylor-Couette device has the advantage of studying deposition under reservoir temperature and pressure conditions. Lastly, Rouzbeh G. Moghanloo et al. (Moghanloo et al., 2018) performed core flood experiments using surface chemical techniques, such as scanning electron microscope (SEM) with energy dispersive X-ray spectroscopy (SEM-EDS) and X-ray computed microtomography, to study crude oil volumes at the pore scale to quantify residual oil and wettability alteration (Seifried, 2016). In subsequent sections of this chapter, some studies on determining asphaltene deposition in a laboratory are presented.

2.7.2. Wettability

Wettability is defined as the tendency of a fluid to adhere or spread onto a solid surface in the presence of other immiscible fluids such as water, oil, and air. In a reservoir, the wetting phase can be oil, water, or gas, and the solid phase is the rock. In petroleum engineering, wettability is usually defined as the measurement of the reservoir rock's affinity for water or oil in a typical rock-fluid-oil system. Understanding rock wetting preference is important because it shows the mechanisms behind fluid flow in porous media, and ultimately promotes oil recovery efficiency (WG Anderson, 1986). Reservoir wettability can be classified as water-wet, oil-wet, mixed wet, fraction wet, and intermediate wet, being water-wet and oil-wet the most used. For a water-wet reservoir, there is a high affinity for water, and water predominantly occupies small rock pores and covers the surface of the formation rock. In contrast, oil-wet reservoir rock has a high affinity for oil, which occupies small rock pores. Usually, in a laboratory, core samples are cleaned and modified to provide a preferential wetting state for oil, water, or intermediate. The modifications in wettability expose a core sample to oil under certain conditions during a long period of time. The initial wettability preference of the sample can be determined using an imbibition test. Lastly, fractional wetting is where each section of the rock exhibits different wetting preferences (WG Anderson, 1986).

Wettability can be calculated using Young's equation; however, this equation was initially proposed for ideal surfaces. Other models, such as the Wenzel model where liquid wets rock pores that are directly under the droplet, and the Cassie-Baxter model where liquid droplets are partly buoyed by rock and air without the liquid penetrating the rock pores, have been developed over time to improve the contact angle description on surfaces with several variables (Gambaryan-Roisman, 2014).

2.7.3. Determining Wettability

There are various methods used to determine the wettability of rock on various fluids. The methods are classified as quantitative and qualitative (William Anderson, 1986). The quantitative methods are microscopic observation (such as contact angle), Amott wettability measurements, and the US Bureau of Mines (USBM) method. The qualitative methods include imbibition, relative permeability methods, flotation methods, glass slide method, capillary pressure curves, nuclear magnetic resonance (NMR) longitudinal relaxation, and dye desorption. In this thesis, only the most common used methods are discussed.

2.7.4. Contact Angle

This method involves direct observation and measurement of wetting angles on small rock samples or substrate and is one of the best wettability measurement techniques that can be used when artificial cores and pure fluids are applied since there is no possibility of wettability alteration due to surfactants or any other compounds. Contact angle can be used to determine whether crude oil can alter wettability and to examine the effects of parameters, such as temperature, pressure, and brine chemistry, on the wettability of the rock surface. Some methods used to determine contact angle include the tilting plate method, sessile drops or bubbles, vertical rod method, tensiometer method, cylinder method, and capillary rise method (William Anderson, 1986), and the sessile drop method is the most common technique in petroleum applications. In this method, a single or two flat, polished mineral crystals or substrates mounted parallel to each other are used. When measuring the contact angle using a single substrate, the angle is measured between the solid surface and the tangent to the drop profile at the drop edge. There are several issues that affect contact angle measurements, such as rock-fluid interaction (e.g., solubility), pH, ions in the aqueous phase, polar groups in crude oil, polished solids (quartz in sandstone, calcite in limestone), which is why single substrate may not be representative of solid surfaces in porous media. Also, the time needed to reach equilibrium (if the contact angle is independent of time) can differ from seconds to days or years. Therefore, the contact angle obtained in a laboratory may not represent the actual wettability of the system under examination.

2.7.5. Amott Measurements

The Amott method gives the average macroscopic wettability of a rock for a given fluid. It combines the measurements of the fluids that spontaneously and forcibly imbibe a rock sample. This method uses reservoir cores and fluids and assumes that the wetting phase imbibes spontaneously into the core, displacing the non-wetting phase. Also, the ratio of spontaneous imbibition to forced imbibition is used to decrease the effect of other factors, such as relative permeability, viscosity, and initial saturation of the rock. This method has no validity as an absolute measurement, but it is an industry standard for comparing the wettability of various core plugs.

2.7.6. U.S. Bureau of Mines (USBM) Method

USBM measures the mean macroscopic wettability of a rock for a given fluid. It is similar to the Amott method, but USBM considers the work required to displace fluids. This method also does not have validity as an absolute measurement, but it is an industry standard for comparing the wettability of various core plugs. Unlike the Amott wettability test, the major advantage of the USBM is that it is more sensitive to near-neutral wettability. Its minor disadvantage is that the USBM wettability index can only be measured on plug-size samples because the samples must be spun in a centrifuge.

2.7.7. Relative Permeability

Some methods to determine relative permeability curves are based on the effects of wettability on relative permeability. However, these methods are only useful to differentiate between strongly water-wet and strongly oil-wet core samples. A small change in wettability between strongly and moderately water-wet may not be noticed by these methods. Ehrlich et al. (Ehrlich & Wygal Jr, 1977) developed a relative permeability method based on the rules given by Craig (Craig, 1971) to differentiate between strongly water-wet and strongly oil-wet cores. Craig's rules are presented in **Table 2.1. Figure 2.5** shows an example of relative permeability curves for oil-wet and water-wet systems.

Table 2.1. Craig’s rules (Craig, 1971).

Water-wet system	**Oil-wet system**
$K_{rw} = K_{ro}$ at S_w>50	$K_{rw} = K_{ro}$ at S_w <50
K_{rw} (relative permeability to water) at max S_w< 30%	K_{rw} (relative permeability to water) at max $S_w >$ 50% (can be 100%)
S_{wc}(connate water saturation)>20-25 % PV	S_{wc}(connate water saturation) <10-15 % PV

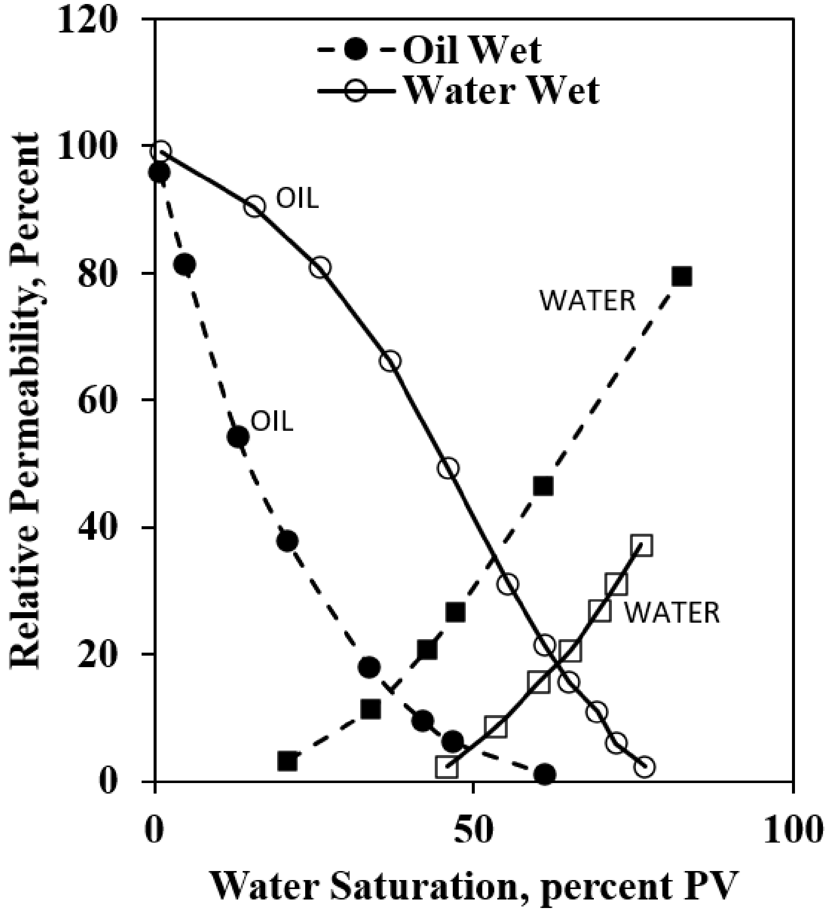

Figure 2.5. Relative permeability curves in water-wet and oil wet reservoirs (Jennings Jr, 1957).

Relative permeability data can be obtained by direct measurement in a laboratory using a steady-state flow process, an unsteady-state flow process, calculations of relative permeability from capillary pressure data, calculations from field performance data, and theoretical or empirical correlations. A steady-state flow process implies that values of relative permeability are not measured until the tested sample has achieved a steady-state behavior. Steady-state techniques of estimating relative permeability are often considered the most reliable sources of relative permeability data. For this method, Darcy’s law can be used to determine the effective permeability for each phase at a given saturation. The procedure for this method involves injecting two fluids into the core samples simultaneously at constant injection rates and pressure. When pressure drop across the core remains relatively constant, the system is assumed to be in a steady state. The outlet flow rate of each phase and the pressure drop is measured, and the obtained values are used in Darcy’s law to calculate the effective permeability of the fluid at that given saturation. In contrast, the unsteady state method is more complicated. For this method, one phase is injected into the core, and equilibrium is not achieved during the test. The experimental procedure involves displacing in-situ fluids with other fluids at a constant rate and pressure. The outlet fluid composition and flow rate are measured and used for relative permeability calculations. The main advantages of using the unsteady state method are cost and time.

After obtaining the experimental data, the Johnson, Bossler, and Naumann (JBN) method is used to calculate water-oil relative permeability curves. This method yields reliable results that agree with direct measurements of relative permeabilities obtained in steady-state flow test. Furthermore, relative permeability values can be calculated from displacement data obtained from short cores (Johnson, Bossler, & Bossler, 1959). This method involves numerical differentiation, and it is important to have good quality data. This method is based on data collected during the post-breakthrough part of a flood. However, this method neglects the effect of capillary pressure and gravity. When using this method, the relative permeability points are typically scattered, and it is sometimes desirable to fit a smooth curve through these points using fitting analytical relationships, such as the least square. Some parameters that affect relative permeability and/or effective permeability characteristics include capillary number, pore geometry, heterogeneity of the system, anisotropy of the system, fluid viscosity, interfacial tension (IFT), flow rate, and wettability.

2.7.8. Experimental Studies on Asphaltene Deposition

As previously mentioned, studies on asphaltene deposition are conducted using microfluidic experiments (capillary), Taylor-Couette cells, or core flooding experiments through porous media. Since precipitation of asphaltenes is necessary to induce deposition, two different methods have been widely used to destabilize asphaltenes in laboratories. One method requires the addition of n-alkanes to precipitate asphaltenes from the dead oil samples, and the other method induces asphaltene deposition by depressurizing live crude oil samples (Kuang et al., 2018). Wang et al. (J. Wang, Buckley, & Creek, 2004) studied asphaltene deposition in a stainless-steel capillary, representing tubing, for two different crude oils. They found a higher deposition rate in samples that had higher molecular weight precipitants, such as n-pentadecane, than in those that had lower molecular weight precipitants, such as n-heptane. Also, they did not find that flow rate influenced deposition rate. Boek et al. (Boek, Wilson, Padding, Headen, & Crawshaw, 2010) studied asphaltene deposition using whole crude oil in capillary flow. They observed a deposition-erosion/entrainment cycle for higher flow rates and higher-pressure fluctuations compared to experiments at lower flow rates. Broseta et al. (Broseta et al., 2000) investigated the onset point and deposition rate with respect to pressure, temperature, and varying fluid compositions.

In addition, Mozafari et al. (Mozaffari et al., 2017) studied heavy oil rheology and flow behavior in capillary experiments, and they found that solvent-to-bitumen ratios had an effect in pore plugging. Lin et al. (Lin et al., 2016) studied the effect of asphaltene solubility on deposition in microchannels, and they concluded that the deposition dynamics of asphaltene varied significantly with n-heptane concentration, increasing asphaltene deposition with increasing in n-heptane concentration. Sieben et al. (Sieben, Tharanivasan, Andersen, & Mostowfi, 2016) used a microfluidic approach to measure the solubility of asphaltenes in crude oil. They proposed a model that reduced the required time for analysis of asphaltene solubility. In contrast, Rahmani et al. (Rahmani, Masliyah, & Dabros, 2003) studied asphaltene floc size distributions in a Couette device for Athabasca bitumen (Alberta, Canada). This distribution studied the effect of varying shear rates on aggregation in Couette flows. They found that the frequency of collision and sticking probability control particle aggregation rate.

For core flood experiments, Minssieux (Minssieux, 1997) studied core samples that had different rock characteristics, it meant, different porous media. He concluded that porous sample plugging only occurred after enough oil had flowed through the sample and that damage at earlier stages was only observed in samples with a lower initial permeability. Pak et al. (Pak, Kharrat, Bagheri, Khalili, & Hematfar, 2011) studied asphaltene deposition in a sandstone core for three processes: recycled gas injection, which caused the most damage, CO_2 injection, and natural depletion (least damage). In these processes, asphaltene depositions were evaluated using pressure drop measurements across the vessel. The amount of deposited asphaltenes within a core was determined by the difference of asphaltene content between the inlet and outlet stream. This indirect method was applied to study asphaltene deposition caused by three processes. Pak et al. (Pak et al., 2011) also observed that reduced porosity occurred mostly in the core inlet. Shen and Sheng (Shen & Sheng, 2018) studied permeability reduction by asphaltene precipitation in shale porous media during the CO_2 huff-n-puff injection process. They found that asphaltene deposition mainly formed near the surface area of the core plug when CO_2 concentrations increased, and more oil was near the rock surface during the first cycle. Asphaltene precipitation and deposition were most significant during the huff period in the first cycle compared to subsequent cycles.

Ashoori et al. (Ashouri, Jami, Muller, & Ahmadi, 2006) used a slim tube to study the reversibility of asphaltene precipitation for Iranian oil; they used n-heptane as a precipitant, and they concluded that asphaltene precipitation was reversible for their conditions of varying composition and temperature. Wang et al. (S. Wang, Chen, & Li, 2016) studied asphaltene precipitation after miscible CO_2 flooding followed by a blowdown process in a sandstone core. They varied CO_2 injection pressure and temperature and found that asphaltene content in oil produced after the CO_2 breakthrough was lower than the oil samples collected before the CO_2 breakthrough. Soroush et al. (Soroush, Pourafshary, & Vafaie-Sefti, 2014) investigated asphaltene deposition from miscible and immiscible CO_2 injections in a sand pack, and they determined that asphaltene content of the produced oil decreased as pressure increased and that the amount of produced asphaltenes was higher when the pressure was below the minimum miscible pressure. Mendoza de la Cruz et al. (Mendoza de la Cruz, Arguelles-Vivas, Matias-Perez, Durán-Valencia, & Lopez-Ramirez, 2009) investigated asphaltene deposition in limestone cores to determine the effect of in-situ asphaltene precipitation and deposition caused by pressure depletion. They obtained a permeability reduction of 24-48%. In this section, some laboratory tests on asphaltene precipitation/deposition were presented. In the following sections, using nanoparticles to inhibit asphaltene precipitation and formation damage is discussed.

2.8. Role of Nanoparticles as Adsorbents

Adsorption of asphaltenes onto surfaces of nanoparticles is an attractive topic for the oil industry because conventional methods to treat asphaltene deposition have many drawbacks as previously discussed. Because asphaltene precipitation might occur in both heavy and light oils, nanoparticles should remove asphaltenes rapidly, making the remaining fraction of oil transportable for conventional processing (Alian et al., 2011; Nashaat N Nassar, Hassan, Carbognani, Lopez-Linares, & Pereira-Almao, 2012). Additionally, nanoparticles can act as catalysts by integrating asphaltene adsorption and oxidation to upgrade asphaltenes into light, usable distillates. Consequently, increased energy efficiency, reduced capital costs, and enhanced performance and portability would result using nanoparticles as catalyst. Several types of adsorbents are used in the oil industry, and they can significantly affect the upgrading of oil as a considered alternative approach to green and cost-effective technology. These adsorbents can be categorized into clay minerals, rock minerals, minerals, glass, soils, silica, modified silica, alumina, silica-alumina, metals, metal oxides, various forms of carbon, and polymers (Adams, 2014; Rana, Samano, Ancheyta, & Diaz, 2007). The adsorption process is controlled by the chemical and physical structure of asphaltenes in addition to the physical and chemical characteristics of the adsorbent (Franco, Nassar, & Cortés, 2014). Also, the source of asphaltenes plays an important role in determining their chemical structure, while the physical properties of adsorbents, such as surface area, surface morphology, pore diameter, internal pore volume, and pore distribution, contribute to adsorption process efficiencies (Acevedo, Ranaudo, García, Castillo, & Fernández, 2003; Syunyaev, Balabin, Akhatov, & Safieva, 2009). In addition, diffusion problems and pore plugging can still occur if classical porous adsorbents are used to remove asphaltenes (Acevedo et al., 2003). These problems can be prevented by decreasing particle size, increasing adsorbent porosity, and increasing surface area and pore diameter of the adsorbent (Adams, 2014).

Nanotechnology has emerged as an attractive area in heavy oil upgrading by asphaltene removal, air emission capture, energy and wastewater treatment (El-Qanni, Nassar, & Vitale, 2017;

Hethnawi, Manasrah, Vitale, & Nassar, 2018; Hmoudah, Nassar, Vitale, & El-Qanni, 2016; Manasrah, Almanassra, et al., 2018; Manasrah, Laoui, Zaidi, & Atieh, 2017; Marei et al., 2017). The interest in using nanotechnology interest is because the unique physical and chemical properties of nanoparticles, such as high surface area to volume ratio, excellent adsorption affinity, high degree of dispersion, and catalytic behaviors towards the removal of heavy hydrocarbon components (Hashemi, Nassar, & Almao, 2014).

Using nanoparticles as adsorbents and catalysts for asphaltene adsorption and subsequent oxidation and/or pyrolysis was first introduced by the Nassar group (Nashaat N. Nassar, 2010) and then followed by other research groups (Amrollahi Biyouki, Hosseinpour, & Nassar, 2018; Hosseinpour, Khodadadi, Bahramian, & Mortazavi, 2013; Setoodeh, Darvishi, & Lashanizadegan, 2018). This cost-effective and environmental approach has a positive impact on in-situ and ex-situ oil upgrading processes (Hashemi et al., 2014). Different studies conducted by our research group investigated new technologies for using nanoparticles in oil upgrading and recovery processes, particularly for asphaltene adsorptive removal and subsequent post-adsorption decomposition (Franco, Nassar, et al., 2014; Hashemi et al., 2014; Hassan, Lopez-Linares, Nassar, Carbognani-Arambarri, & Pereira-Almao, 2013). Recently, our research group confirmed that employing nanoparticles as inhibitors prevents or delays the precipitation of asphaltenes by in-situ adsorption of asphaltenes within wells (Franco, Nassar, Ruiz, Pereira-Almao, & Cortés, 2013; Guzmán et al., 2016). Moreover, nanoparticles' ability in dispersion and stabilization of asphaltene aggregates through adsorption and their small size has led to the idea of using them to prevent formation damage. Nanoparticles can adsorb asphaltenes quickly, which prevents asphaltene deposition by avoiding simultaneous flocculation and precipitation because the asphaltene content is stabilized within the oil medium, leading to better recovery. Furthermore, supported and unsupported nanoparticles can be employed to adsorb asphaltenes from an oil matrix followed by post-adsorption catalytic decomposition. In addition, asphaltene adsorption from crude oil onto nanoparticles delays asphaltene precipitation when changes in temperature, pressure, and composition occur, and alters surface wettability according to the wetting preference of the nanoparticles (Guzmán et al., 2016; Nashaat N Nassar, Betancur, Acevedo, Franco, & Cortés, 2015).

2.9. Types of Nanoparticles for Asphaltene Adsorption

The adsorption process generally begins by extracting asphaltenes from oil and resolubilizing them in a model solvent, such as toluene or heptol (heptane + toluene). Batch adsorption usually occurs using a ratio of 1:10 (L/g) model oil solution to nanoparticle mass at 298 K. The adsorption of asphaltenes onto nanoparticles is determined by changing the concentration of asphaltenes in the model oil solution before and after mixing with the nanoparticles. The adsorption of asphaltenes onto the surfaces of nanoparticles depends on the type and strength of interactions between the asphaltenes and the solid surfaces (Groenzin & Mullins, 2000). A number of interparticle forces, individually or collectively, are responsible for successful interactions between asphaltenes and surfaces that result from functionalized groups on the asphaltenes, including carboxylic, pyrrolic, pyridininc, thiophenic, and sulfite groups (Castro, de la Cruz, Buenrostro-Gonzalez, López-Ramírez, & Gil-Villegas, 2009; Strausz, Peng, & Murgich, 2002). The major forces that contribute to these interactions are van der Waals, electrostatic, charge transfer, hydrogen bonding, and steric interactions (Strausz et al., 2002).

Nassar et al. (2012) investigated the adsorption of Athabasca asphaltenes using different types of nanoparticles. During the adsorption process, the authors observed a monolayer of adsorbed asphaltenes on metal oxide nanoparticles (Nashaat N Nassar et al., 2012; Nashaat N Nassar, Hassan, & Pereira-Almao, 2011a, 2011d), alumina (Nashaat N Nassar, Hassan, & Pereira-Almao, 2011b), kaolin containing metal oxide nanoparticles (Hassan et al., 2013), and modified kaolin (Lopez-Linares et al., 2011). Nassar et al. (Nashaat N Nassar et al., 2012; Nashaat N Nassar et al., 2011a, 2011d) reported that adsorption of n-C_7 asphaltenes from Athabasca vacuum residue onto different types of metal oxide nanoparticles, such as NiO, Co_3O_4, Fe_3O_4, TiO_2, CaO, CeO_2, and ZrO_2 occurred. They determined that the adsorption of asphaltenes was strongly dependent on the type of nanoparticle. In similar studies using Iranian n-C_7 asphaltenes, Hosseinpour et al.(Hosseinpour et al., 2013) reported on the adsorption of asphaltenes onto different acid/base metal oxide nanoparticles, such as NiO, Fe_2O_3, WO_3, MgO, $CaCO_3$, and ZrO_2, and they found that the adsorption isotherms followed Langmuir-type behavior. In another study using palladium and nickel oxide incorporated into fumed silica nanoparticles, Franco et al. (Franco, Cortés, & Nassar, 2014) reported a significant enhancement in the adsorption of Colombian n-C_7 asphaltenes. The synergistic effect of these metal oxides on fumed silica might be achieved upon incorporation over the surface. The authors found that these types of supported nanoparticles (fumed silica with nickel and palladium oxides) allowed Type I adsorption isotherms to form, which facilitated later processes of asphaltenes, such as catalytic thermal cracking and the inhibition of formation damage. **Table 2.2** summarizes different types of nanoparticles used on different types of extracted asphaltenes for adsorption. The polar interactions, for example, are basically acid-base reactions that occur between adsorbate and adsorbent. From the presented results, it can be concluded that basic oxides, such as CaO and MgO, and amphoteric oxides, such as Fe_3O_4 and Co_3O_4, demonstrate higher adsorption capacity compared to acidic oxides, such as TiO_2 and NiO. However, adsorption affinity values were higher for acidic oxides, which suggests that strong interactions between adsorbate and adsorbent may increase the catalytic effect of solids with high-affinity values for various reactions. It can be concluded that the electrostatic and van der Waals attractions are the most dominant interactions between asphaltene aggregates and the surfaces of nanoparticles, and thus, acidic and basic metal oxide nanoparticles can be employed for adsorption and effective removal of asphaltene aggregates from reservoir oil as an approach for in-situ oil upgrading (Amrollahi Biyouki et al., 2018). Similar observations were reported by other research groups for adsorption of asphaltenes onto different minerals and clays (Alkafeef, Algharaib, & Alajmi, 2006; Angle, Long, Hamza, & Lue, 2006; Dean & Mcatee Jr, 1986; Rana et al., 2007). For example, Mohammadi et al. (Mohsen Mohammadi et al., 2011) used metal oxide nanoparticles, such as SiO_2, TiO_2, and ZrO_2, to improve the stability of asphaltene nanoaggregates by forming hydrogen bonds under acidic conditions. The authors confirmed that TiO_2 nanofluids, under strong acidic conditions, act as a dispersant, thereby enhancing the stability of asphaltenes and leading to a higher precipitation onset point.

Table 2.2. Adsorption of different extracted asphaltenes over different types of nanoparticles.

Type of Nanoparticle	**Type of Asphaltene**	**Oil source**	**Remarks**	**Ref.**
Co_3O_4	C_7-asphaltenes	Athabasca VR	Amphoteric effect, <50 nm particle size	(Nassar et al, 2011d)
NiO	C_7-asphaltenes	Athabasca VR	Acidic effect, <50 nm particle size	(Nassar et al, 2011d)

MgO	C_7-asphaltenes	Athabasca VR	Basic effect, <50 nm particle size	(Nassar et al, 2011d)
CaO	C_7-asphaltenes	Athabasca VR	Basic effect, <160 nm particle size	(Nassar et al, 2011d)
TiO_2	C_7-asphaltenes	Athabasca VR	Acidic effect, <25 nm particle size	(Nassar et al, 2011d)
Fe_3O_4	C_7-asphaltenes	Athabasca VR	Amphoteric effect, 20-30 nm particle size	(Nassar et al, 2011d)
nano-alumina	C_7-asphaltenes	Athabasca bitumen	Particle size <50 nm	(Nassar et al, 2011c)
micro-alumina	C_7-asphaltenes	Athabasca bitumen	Particle size 50-200 μm	(Nassar et al, 2011c)
γ-Al_2O_3	C_7-asphaltenes	Athabasca bitumen	Particle size <50 nm	(Nassar, 2010)
fumed silica (S)	C_7-asphaltenes	Colombian	BET 389 m^2/g	(Montoya et al, 2013)
SNi2	C_7-asphaltenes	Colombian	2wt%NiO supported-on-	(Montoya et al, 2013)

			silica (S), BET 233.63 m^2/g	
SPd2	C_7-asphaltenes	Colombian	2wt%PdO supported-on-silica (S), BET 205.15 m^2/g	(Montoya et al, 2013)
SNi	C_7-asphaltenes	Colombian	1wt%NiO supported-on-silica (S), BET 290.31 m^2/g	(Montoya et al, 2013)
SPd1	C_7-asphaltenes	Colombian	1wt%PdO supported-on-silica (S), BET 265.56 m^2/g	(Montoya et al, 2013)
SNi1Pd1	C_7-asphaltenes	Colombian	1wt%NiO and PdO supported-on-silica (S), BET 201.50 m^2/g	(Montoya et al, 2013)
SNi0.66Pd0.66	C_7-asphaltenes	Colombian	0.66 wt% of NiO and PdO supported-on-	(Montoya et al, 2013)

			silica (S), BET 220.79 m^2/g	
ZrO_2	C_7-asphaltenes	Athabasca Vacuum residue	Particle size 26 nm, BET 40 m^2/g	(Nassar et al, 2014)
CeO_2	C_7-asphaltenes	Athabasca Vacuum residue	Particle size 16 nm, BET 50 m^2/g	(Nassar et al, 2014)
TiO_2	C_7-asphaltenes	Athabasca Vacuum residue	Particle size 8nm, BET183 m^2/g	(Nassar et al, 2014)
NiO	C_7-asphaltenes	Iranian heavy oil	Acidic surface, 45 nm particle size	(Hosseinpour et al, 2013)
Fe_2O_3	C_7-asphaltenes	Iranian heavy oil	Amphoteric surface, 44 nm particle size	(Hosseinpour et al, 2013)
WO_3	C_7-asphaltenes	Iranian heavy oil	Acidic surface, 44 nm particle size	(Hosseinpour et al, 2013)
MgO	C_7-asphaltenes	Iranian heavy oil	Basic surface, 15 nm particle size	(Hosseinpour et al, 2013)

$CaCO_3$	C_7-asphaltenes	Iranian heavy oil	Basic surface, 15 nm particle size	(Hosseinpour et al, 2013)
ZrO_2	C_7-asphaltenes	Iranian heavy oil	Amphoteric surface, 20 nm particle size	(Hosseinpour et al, 2013)
Zeolite	C_7-asphaltenes	Colombia crude oil	16 nm particle size	(Nassar et al, 2013)
Silica gel	C_7-asphaltenes	Colombia crude oil	Amorphous	(Nassar et al, 2013)
Silica gel	C_7-asphaltenes	Colombia crude oil	Crystalline	(Nassar et al, 2013)
SNi5	C_7-asphaltenes	Colombia crude oil	Crystalline silica with 5 wt % $Ni(NO_3)_2$	(Nassar et al, 2013)
SNi15	C_7-asphaltenes	Colombia crude oil	Crystalline silica with 15 wt % $Ni(NO_3)_2$	(Nassar et al, 2013)

2.10. Using Nanoparticles to Inhibit Formation Damage Caused by Asphaltene Precipitation

As previously mentioned, conventional methods used to remediate asphaltene deposition in the oil and gas industry include injecting solvents, adding surfactants, conducting wireline cuttings, and many other mechanical treatments (Junior, Ferreira, & da Silva Ramos, 2006; K. J. Leontaritis & Mansoori, 1988). However, these methods are expensive and do not prevent asphaltene redeposition. As a result, researchers are looking for alternative materials and techniques that are more sustainable, efficient, and cost-effective.

Research on nanotechnology applications for asphaltene deposition prevention in the oil and gas industry has emerged (Betancur, Carmona, et al., 2016; Franco, Nassar, et al., 2013; Majid Mohammadi et al., 2017). Using nanoparticles to inhibit asphaltene deposition is being investigated because of the unique properties of nanoparticles, such as their high surface area to volume ratio, which is crucial for adsorption capability and for changing the asphaltene aggregation mechanism (Franco, Nassar, et al., 2013). Applications of nanotechnology in asphaltene precipitation/deposition inhibition have been reported in several studies, such as Mohammadi et al. (Mohsen Mohammadi et al., 2011). They investigated how TiO_2, ZrO_2, and SiO_2 nanoparticles can improve asphaltene stability. They found that because hydrogen bonds form under acidic conditions, TiO_2 nanofluids enhanced asphaltene stability. The opposite was observed for basic conditions because there were no hydrogen bonds. Therefore, the authors concluded that the surface acidity of the adsorbent enhanced asphaltene stability.

Additionally, Lu et al. (Lu, Li, Fan, Zhang, & Lv, 2016) evaluated the adsorption of asphaltenes onto Al_2O_3 nanoparticles during a CO_2 flooding. The influence of Al_2O_3 nanoparticles on asphaltene precipitation was investigated using the interfacial tension (IFT) behavior of the oil−CO_2 system. Coreflood tests were conducted to study the potential of nanoparticles to inhibit asphaltene damage during CO_2 flooding. Kazemzadeh et al. (Kazemzadeh et al., 2015) investigated the behavior of asphaltene adsorption onto SiO_2, NiO, and Fe_3O_4 nanoparticles on a micro-glass module to determine asphaltene adsorption and precipitation. The authors concluded that increasing n-heptane in the presence of the adsorbent resulted in more adsorption regardless of the type of nanomaterial used. However, the authors noted that the adsorption of asphaltenes followed the order SiO_2 > NiO > Fe_3O_4 (most to least adsorptive), which indicated that silica nanoparticles had more affinity to asphaltenes than did NiO or Fe_3O_4.

Franco et al. (Franco, Nassar, et al., 2013) studied the effect of the chemical natures of 12 types of nanoparticles on asphaltene adsorption on a porous medium at reservoir temperature and pressure. The displacement tests showed that damage from asphaltenes was inhibited by adding nanoparticles. They evaluated three systems, a blank system, a damaged system, and a treated system, and asphaltene damage was induced in the damage system by injecting n-heptane to an oil-containing porous medium. The treated system was simulated by simultaneously injecting both a defined number of nanoparticles and n-heptane. The authors observed that the oil relative permeability increased sharply after adding nanoparticles compared to what occurred in the damaged and blank (before induced damage and nanofluids) systems. This sharp increase was primarily attributed to the nanoparticles preventing asphaltene self-association and changes in the wettability of the porous medium. The authors concluded that due to the nanoparticles successfully adsorbed and stabilized the asphaltenes, and therefore, production was restored, which improvd oil recovery(Franco, Nassar, et al., 2013). Betancur et al. (Betancur, Carmona, et al., 2016) studied the role of nanoparticle size and surface acidity in inhibiting formation damage. In their study, the authors synthesized nanoparticles with sizes ranging from 11 to 240 nm. Additionally, they determined the kinetics of asphaltene aggregate growth in the presence and absence of nanoparticles using DLS measurements and different heptol (heptane + toluene) solutions. The authors found that the materials with the highest adsorptive capacity, higher total surface acidity, and lower mean particle size were most successful in inhibiting asphaltene aggregate growth. Additionally, the authors performed a displacement test using the best performance in batch-mode experiments to treat an asphaltene damaged core under flow conditions in a porous medium under typical reservoir conditions using the nanoparticles. A nanofluid treatment with silica nanoparticles increased the effective permeability of oil and enhanced oil recovery by 11% under the reported conditions. In another study, Betancur et al. (Betancur, Franco, & Cortés, 2016) determined that core-shell type nanoparticles composed of a magnetite core and a silica shell inhibited asphaltene formation damage and that the nanoparticles were recovered and regenerated using their magnetic properties.

In contrast, a successful field test was conducted by Zabala et al. (Zabala et al., 2014). They used commercial alumina-based nanofluids to prevent formation damage caused by asphaltene precipitation. First, they conducted a core flood test and then performed a field test by injecting alumina-based nanofluids to inhibit asphaltene deposition in the Cupiagua sur oil field in Colombia. They reported oil production of 150,000 barrels of oil after 271 days using alumina nanoparticle injection. The authors concluded that well-stabilized, alumina-based nanofluids were retained in the formation for longer than eight months. They suggested that these types of nanoparticles could be used in a reservoir that had very low permeability conditions (Zabala et al., 2014). Franco et al. (2015b) studied the competitive adsorption of n-C_7 asphaltenes and resin I on silica nanoparticles employing a method based on thermogravimetric analysis (TGA) and softening point (SP) measurements. They observed that when the number of adsorbed n-C_7 asphaltenes decreased, the amount of resin I increased, and adsorption was always higher for n-C_7 asphaltenes than for resin I for different asphaltene-to-resin ratios. The results suggested that silica nanoparticles could be used to treat asphaltene-related problems. Also, Guzman et al. (Guzmán et al., 2016) reported a methodology for designing asphaltene-related treatments using batch adsorption experiments. They evaluated nanoparticles that had different chemical natures and different physicochemical properties in adsorption tests using two methods: 1) exposing a certain mass of nanoparticles in a fixed volume of liquid and varying the initial concentration of asphaltenes and 2) exposing a given amount of asphaltenes in a fixed volume of liquid and varying the number of nanoparticles. They concluded that both methods led to different results in several applications.

Taborda et al. (Taborda, Franco, Lopera, Alvarado, & Cortés, 2016) used a sol-gel method SiO_2, acidified silica (SiO_2A), and Al_2O_3 nanoparticles to study their effects on asphaltene precipitation in a model oil solution. The authors found that the nanoparticles reduced the mean size of asphaltene aggregates, following the order in asphaltene aggregates reduction: $SiO_2A < SiO_2 < Al_2O_3$. Shojaati et al. (Shojaati, Riazi, Mousavi, & Derikvand, 2017) evaluated the inhibition capacity of metal oxide nanoparticles, such as Fe_3O_4, NiO, and Al_2O_3, to delay the onset of asphaltene precipitation for a synthetic oil sample. They concluded that the nanoparticles were effective in containing the onset point and reducing the amount of precipitated asphaltenes. Recently, López et al. (Lopez et al., 2020) investigated the effects of Cardanol/SiO_2 nanocomposites on formation damage using an asphaltene model solution. They found that adsorption of n-C_7 asphaltenes onto the surfaces of the Cardanol/SiO_2 nanocomposites decreased the amount of asphaltenes in the bulk solution and reduced the aggregation process. Alemi et al. (Mahmoudi Alemi, Mousavi Dehghani, Rashidi, Hosseinpour, & Mohammadi, 2021) synthesized Fe_2O_3 and functionalized SiO_2 nanoparticles to study their effect on asphaltene precipitation and aggregation in a light live oil that had a high asphaltene deposition risk during an isothermal depressurization process. Compared to the F-SiO_2 nanoparticles, the Fe_2O_3 nanoparticles reduced more asphaltene precipitation and aggregation. This result was attributed to the higher number of and stronger interactions between the acid/base functional groups of the asphaltenes and the surface sites of the Fe_2O_3 nanoparticles (Mahmoudi Alemi et al., 2021).

2.11. Conclusions

Using nanoparticles for asphaltene inhibition offers many benefits compared to using conventional methods because nanoparticles have unique chemical structures and surface functionality. However, most of the reported studies are mainly conducted in laboratories and under ambient conditions, and only a few field applications have been reported. Therefore, conducting field studies is important to understand better nanoparticle-asphaltene interactions and the mechanisms involved in inhibiting asphaltene precipitation/deposition and inhibiting aggregation processes under reservoir conditions in porous media. Therefore, more field experiments or experiments that more closely resemble field conditions must be conducted. These field studies must consider parameters, such as temperature, pressure, oil composition, asphaltene onset pressure, and solubility, to scale up the use of nanoparticles in oil reservoirs for formation damage remediation and to restore reservoir wettability without causing incompatibility reactions; these actions will optimize the amount and type of nanoparticle needed.

2.12. References

Acevedo, Sócrates, Castro, Alexandra, Negrin, Juan Gabriel, Fernández, Alberto, & Escobar, Gastón, Piscitelli, Vincent, Delolme, Frederic, Dessalces, Guy. (2007). Relations between asphaltene structures and their physical and chemical properties: The rosary-type structure. *Energy & fuels, 21*(4), 2165-2175.

Acevedo, Sócrates, Ranaudo, María A, García, Coromoto, Castillo, Jimmy, & Fernández, Alberto. (2003). Adsorption of asphaltenes at the toluene– silica interface: A kinetic study. *Energy & fuels, 17*(2), 257-261.

Adams, Jeramie J. (2014). Asphaltene adsorption, a literature review. *Energy & Fuels, 28*(5), 2831-2856.

Agarwal, Avinash Kumar. (2007). Biofuels (alcohols and biodiesel) applications as fuels for internal combustion engines. *Progress in energy and combustion science, 33*(3), 233-271.

Ahmed, Tarek. (2018). *Reservoir engineering handbook*: Gulf professional publishing.

Al-Ghazi, AS, & Lawson, Justin. (2007). *Asphaltene cleanout using VibraBlaster tool.* Paper presented at the SPE Saudi Arabia Section Technical Symposium.

Al-Maamari, Rashid SH, & Buckley, Jill S. (2003). Asphaltene precipitation and alteration of wetting: the potential for wettability changes during oil production. *SPE Reservoir Evaluation & Engineering, 6*(04), 210-214.

Alian, Sima Sh, Omar, Abdul Aziz, Alta'ee, Ali F, & Hani, Irzie. (2011). Study of asphaltene precipitation induced formation damage during CO2 injection for a Malaysian light oil. *International Journal of Chemical, Molecular, Nuclear, Materials and Metallurgical Engineering, 5*(6), 482-486.

Alkafeef, Saad F, Algharaib, Meshal K, & Alajmi, Abdullah F. (2006). Hydrodynamic thickness of petroleum oil adsorbed layers in the pores of reservoir rocks. *Journal of colloid and interface science, 298*(1), 13-19.

Alzate, Guillermo A, Franco, Carlos Alberto, Restrepo, Alejandro, Del Pino Castrillon, Jessica J, Barreto Alvares, Diogenes Laureano, Murillo, Escobar, & Alberti, Alfaro. (2006). *Evaluation of alcohol-based treatments for condensate banking removal.* Paper presented at the SPE International Symposium and Exhibition on Formation Damage Control.

Amrollahi Biyouki, Azadeh, Hosseinpour, Negahdar, & Nassar, Nashaat N. (2018). Pyrolysis and Oxidation of Asphaltene-Born Coke-like Residue Formed onto in Situ Prepared NiO Nanoparticles toward Advanced in Situ Combustion Enhanced Oil Recovery Processes. *Energy & Fuels, 32*(4), 5033-5044.

Anderson, WG. (1986). 1987, Wettability literature survey–part 1 to part 6. *J. Pet. Technol*, 1125-1144.

Anderson, William. (1986). Wettability literature survey-part 2: wettability measurement. *Journal of petroleum technology, 38*(11), 1246-1262.

Angle, Chandra W, Long, Yicheng, Hamza, Hassan, & Lue, Leo. (2006). Precipitation of asphaltenes from solvent-diluted heavy oil and thermodynamic properties of solvent-diluted heavy oil solutions. *Fuel, 85*(4), 492-506.

Ashouri, S, Jami, Alahmadi M, Muller, Steinhagen H, & Ahmadi, Kaveh. (2006). Investigation of reversibility of asphaltene precipitation and deposition for an Iranian crude oil.

Betancur, Stefanía, Carmona, Juan C, Nassar, Nashaat N, Franco, Camilo A, & Cortés, Farid B. (2016). Role of particle size and surface acidity of silica gel nanoparticles in inhibition of formation damage by asphaltene in oil reservoirs. *Industrial & Engineering Chemistry Research, 55*(21), 6122-6132.

Betancur, Stefanía, Franco, Camilo A, & Cortés, Farid B. (2016). Magnetite-silica nanoparticles with a core-shell structure for inhibiting the formation damage caused by the precipitation/deposition of asphaltene. *Journal of Magnetohydrodynamics and Plasma Research, 21*(3), 289-322.

Boek, Edo S, Wilson, Alexander D, Padding, Johan T, Headen, Thomas F, & Crawshaw, John P. (2010). Multi-scale simulation and experimental studies of asphaltene aggregation and deposition in capillary flow. *Energy & fuels, 24*(4), 2361-2368.

Broseta, D, Robin, M, Savvidis, T, Féjean, C, Durandeau, M, & Zhou, H. (2000). *Detection of asphaltene deposition by capillary flow measurements.* Paper presented at the SPE/DOE Improved Oil Recovery Symposium.

Burke, Nancy E, Hobbs, Ronald E, & Kashou, Samir F. (1990). Measurement and Modeling of Asphaltene Precipitation (includes associated paper 23831). *Journal of Petroleum Technology, 42*(11), 1,440-441,446.

Castro, Martín, de la Cruz, José L Mendoza, Buenrostro-Gonzalez, Eduardo, López-Ramírez, Simón, & Gil-Villegas, Alejandro. (2009). Predicting adsorption isotherms of asphaltenes in porous materials. *Fluid Phase Equilibria, 286*(2), 113-119.

Chavan, Sandeep, Kini, Harshad, & Ghosal, Ranjan. (2012). Process for Sulfur Reduction from High Viscosity Petroleum Oils. *International Journal of Environmental Science and Development, 3*(3), 228.

Chianelli, Russell R, Siadati, Mohammed, Mehta, Apurva, Pople, John, Ortega, Lante Carbognani, & Chiang, Long Y. (2007). Self-assembly of asphaltene aggregates: Synchrotron, simulation and chemical modeling techniques applied to problems in the structure and reactivity of asphaltenes *Asphaltenes, Heavy Oils, and Petroleomics* (pp. 375-400): Springer.

Chuan, Wu, Guang-Lun, Lei, Yao, Chuan-jin, Sun, Ke-ji, Gai, Ping-yuan, & Cao, Yan-bin. (2010). Mechanism for reducing the viscosity of extra-heavy oil by aquathermolysis with an amphiphilic catalyst. *Journal of Fuel Chemistry and Technology, 38*(6), 684-690.

Civan, Faruk. (2015). *Reservoir formation damage: fundamentals, modeling, assessment, and mitigation*: Gulf Professional Publishing.

Craig, Forrest F. (1971). *The reservoir engineering aspects of waterflooding* (Vol. 3): HL Doherty Memorial Fund of AIME New York.

Creek, Jefferson L. (2005). Freedom of action in the state of asphaltenes: Escape from conventional wisdom. *Energy & fuels, 19*(4), 1212-1224.

Dean, Kim Renea, & Mcatee Jr, James L. (1986). Asphaltene adsorption on clay. *Applied Clay Science, 1*(4), 313-319.

Durand, Emmanuelle, Clemancey, Martin, Lancelin, Jean-Marc, Verstraete, Jan, Espinat, Didier, & Quoineaud, Anne-Agathe. (2010). Effect of chemical composition on asphaltenes aggregation. *Energy & Fuels, 24*(2), 1051-1062.

Ehrlich, Robert, & Wygal Jr, Robert J. (1977). Interrelation of crude oil and rock properties with the recovery of oil by caustic waterflooding. *Society of Petroleum Engineers Journal, 17*(04), 263-270.

El-Qanni, Amjad, Nassar, Nashaat N, & Vitale, Gerardo. (2017). A combined experimental and computational modeling study on adsorption of propionic acid onto silica-embedded NiO/MgO nanoparticles. *Chemical Engineering Journal, 327*, 666-677.

Fakher, Sherif, Ahdaya, Mohamed, Elturki, Mukhtar, & Imqam, Abdulmohsin. (2020). Critical review of asphaltene properties and factors impacting its stability in crude oil. *Journal of Petroleum Exploration and Production Technology, 10*(3), 1183-1200.

Franco, Camilo A, Cortés, Farid B, & Nassar, Nashaat N. (2014). Adsorptive removal of oil spill from oil-in-fresh water emulsions by hydrophobic alumina nanoparticles functionalized with petroleum vacuum residue. *Journal of colloid and interface science, 425*, 168-177.

Franco, Camilo A, Montoya, Tatiana, Nassar, Nashaat N, Pereira-Almao, Pedro, & Cortés, Farid B. (2013). Adsorption and subsequent oxidation of colombian asphaltenes onto nickel and/or palladium oxide supported on fumed silica nanoparticles. *Energy & Fuels, 27*(12), 7336-7347.

Franco, Camilo A, Nassar, Nashaat N, & Cortés, Farid B. (2014). Removal of oil from oil-in-saltwater emulsions by adsorption onto nano-alumina functionalized with petroleum vacuum residue. *Journal of colloid and interface science, 433*, 58-67.

Franco, Camilo A, Nassar, Nashaat N, Ruiz, Marco A, Pereira-Almao, Pedro, & Cortés, Farid B. (2013). Nanoparticles for inhibition of asphaltenes damage: adsorption study and displacement test on porous media. *Energy & Fuels*, *27*(6), 2899-2907.

Gambaryan-Roisman, Tatiana. (2014). Liquids on porous layers: wetting, imbibition and transport processes. *Current opinion in colloid & interface science, 19*(4), 320-335.

Ghanavati, Mahdi, Shojaei, Mohammad-Javad, & SA, Ahmad Ramazani. (2013). Effects of asphaltene content and temperature on viscosity of Iranian heavy crude oil: experimental and modeling study. *Energy & Fuels, 27*(12), 7217-7232.

Gharfeh, Samir, Yen, Andrew, Asomaning, Sam, & Blumer, David. (2004). Asphaltene flocculation onset determinations for heavy crude oil and its implications. *Petroleum science and technology*, *22*(7-8), 1055-1072.

Ghloum, Ebtisam F, Al-Qahtani, Misfera, & Al-Rashid, Abeer. (2010). Effect of inhibitors on asphaltene precipitation for Marrat Kuwaiti reservoirs. *Journal of Petroleum Science and Engineering*, *70*(1-2), 99-106.

Groenzin, Henning, & Mullins, Oliver C. (1999). Asphaltene molecular size and structure. *The Journal of Physical Chemistry A, 103*(50), 11237-11245.

Groenzin, Henning, & Mullins, Oliver C. (2000). Molecular size and structure of asphaltenes from various sources. *Energy & Fuels*, *14*(3), 677-684.

Guzmán, Juan D, Betancur, Stefania, Carrasco-Marín, Francisco, Franco, Camilo A, Nassar, Nashaat N, & Cortés, Farid B. (2016). Importance of the adsorption method used for obtaining the nanoparticle dosage for asphaltene-related treatments. *Energy & Fuels, 30*(3), 2052-2059.

Hashemi, Rohallah, Nassar, Nashaat N, & Almao, Pedro Pereira. (2014). Nanoparticle technology for heavy oil in-situ upgrading and recovery enhancement: Opportunities and challenges. *Applied Energy, 133*, 374-387.

Hassan, Azfar, Lopez-Linares, Francisco, Nassar, Nashaat N, Carbognani-Arambarri, Lante, & Pereira-Almao, Pedro. (2013). Development of a support for a NiO catalyst for selective adsorption and post-adsorption catalytic steam gasification of thermally converted asphaltenes. *Catalysis today, 207,* 112-118.

Hethnawi, Afif, Manasrah, Abdallah D, Vitale, Gerardo, & Nassar, Nashaat N. (2018). Fixed-bed column studies of total organic carbon removal from industrial wastewater by use of diatomite decorated with polyethylenimine-functionalized pyroxene nanoparticles. *Journal of colloid and interface science, 513,* 28-42.

Hmoudah, Maryam, Nassar, Nashaat N, Vitale, Gerardo, & El-Qanni, Amjad. (2016). Effect of nanosized and surface-structural-modified nano-pyroxene on adsorption of violanthrone-79. *RSC advances, 6*(69), 64482-64493.

Hosseinpour, Negahdar, Khodadadi, Abbas Ali, Bahramian, Alireza, & Mortazavi, Yadollah. (2013). Asphaltene adsorption onto acidic/basic metal oxide nanoparticles toward in situ upgrading of reservoir oils by nanotechnology. *Langmuir, 29*(46), 14135-14146.

Jennings Jr, HY. (1957). Surface properties of natural and synthetic porous media. *Prod. Monthly, 21*(5), 20-24.

Johnson, EF, Bossler, DP, & Bossler, VO. (1959). Calculation of relative permeability from displacement experiments. *Transactions of the AIME, 216*(01), 370-372.

Junior, Luiz Carlos Rocha, Ferreira, Maira Silva, & da Silva Ramos, Antonio Carlos. (2006). Inhibition of asphaltene precipitation in Brazilian crude oils using new oil soluble amphiphiles. *Journal of Petroleum Science and Engineering, 51*(1-2), 26-36.

Kalantari-Dahaghi, Amir Masoud, Moghadasi, Jamshid, Gholami, Vida, & Abdi, Roohollah. (2006). *Formation damage due to asphaltene precipitation resulting from CO2 gas injection in Iranian carbonate reservoirs.* Paper presented at the SPE Europec/EAGE Annual Conference and Exhibition.

Kazemzadeh, Yousef, Eshraghi, S Ehsan, Kazemi, Keyvan, Sourani, Saeed, Mehrabi, Mehran, & Ahmadi, Yaser. (2015). Behavior of asphaltene adsorption onto the metal oxide nanoparticle surface and its effect on heavy oil recovery. *Industrial & Engineering Chemistry Research, 54*(1), 233-239.

Kuang, Jun, Tavakkoli, Mohammad, Yarbrough, Josiah, Wang, Jianxin, Jain, Shekhar, & Ashtekar, Sunil, Abdallah, Dalia S, Punnapala, Sameer, Vargas, Francisco M. (2018). Investigation of asphaltene deposition at high temperature and under dynamic conditions. *Energy & Fuels, 32*(12), 12405-12415.

Leontaritis, KJ, Amaefule, JO, & Charles, RE. (1994). A systematic approach for the prevention and treatment of formation damage caused by asphaltene deposition. *SPE Production & Facilities, 9*(03), 157-164.

Leontaritis, Kosta J. (1996). The asphaltene and wax deposition envelopes. *Fuel Science and Technology International, 14*(1-2), 13-39.

Leontaritis, Kosta J, & Mansoori, G Ali. (1988). Asphaltene deposition: a survey of field experiences and research approaches. *Journal of Petroleum Science and Engineering, 1*(3), 229-239.

Li, Rong, Jiang, Peixue, Gao, Cheng, Huang, Feng, Xu, Ruina, & Chen, Xue. (2016). Experimental investigation of silica-based nanofluid enhanced oil recovery: The effect of wettability alteration. *Energy & Fuels, 31*(1), 188-197.

Lin, Yu-Jiun, He, Peng, Tavakkoli, Mohammad, Mathew, Nevin Thunduvila, Fatt, Yap Yit, & Chai, John C, Goharzadeh, Afshin, Vargas, Francisco M, Biswal, Sibani Lisa. (2016). Examining asphaltene solubility on deposition in model porous media. *Langmuir, 32*(34), 8729-8734.

Lopez-Linares, Francisco, Carbognani, Lante, Hassan, Azfar, Pereira-Almao, Pedro, Rogel, Estrella, Ovalles, Cesar, . . . Zintsmaster, John. (2011). Adsorption of Athabasca vacuum residues and their visbroken products over macroporous solids: influence of their molecular characteristics. *Energy & Fuels, 25*(9), 4049-4054.

Lopez, Daniel, Giraldo, Lady J, Lucas, Elizabete F, Riazi, Masoud, Franco, Camilo A, & Cortes, Farid B. (2020). Cardanol/SiO2 Nanocomposites for Inhibition of Formation Damage by Asphaltene Precipitation/Deposition in Light Crude Oil Reservoirs. Part I: Novel Nanocomposite Design Based on SiO2–Cardanol Interactions. *Energy & Fuels, 34*(6), 7048-7057.

Lu, Teng, Li, Zhaomin, Fan, Weiyu, Zhang, Xinglu, & Lv, Qichao. (2016). Nanoparticles for Inhibition of Asphaltenes Deposition during CO2 Flooding. *Industrial & Engineering Chemistry Research*.

Mahmoudi Alemi, Fatemeh, Mousavi Dehghani, Seyed Ali, Rashidi, Ali, Hosseinpour, Negahdar, & Mohammadi, Saber. (2021). Potential Application of Fe2O3 and

Functionalized SiO2 Nanoparticles for Inhibiting Asphaltene Precipitation in Live Oil at Reservoir Conditions. *Energy & Fuels, 35*(7), 5908-5924.

Manasrah, Abdallah D, Almanassra, Ismail W, Marei, Nedal N, Al-Mubaiyedh, Usamah A, Laoui, Tahar, & Atieh, Muataz A. (2018). Surface modification of carbon nanotubes with copper oxide nanoparticles for heat transfer enhancement of nanofluids. *RSC Advances, 8*(4), 1791-1802.

Manasrah, Abdallah D, Laoui, Tahar, Zaidi, Syed Javaid, & Atieh, Muataz A. (2017). Effect of PEG functionalized carbon nanotubes on the enhancement of thermal and physical properties of nanofluids. *Experimental Thermal and Fluid Science, 84*, 231-241.

Manasrah, Abdallah D, Nassar, Nashaat N, & Ortega, Lante Carbognani. (2018). Conversion of petroleum coke into valuable products using oxy-cracking technique. *Fuel, 215*, 865-878.

Mansoori, G Ali. (2010). Remediation of asphaltene and other heavy organic deposits in oil wells and in pipelines. *Socar proceedings, 2010*(4), 12-23.

Maqbool, Tabish, Balgoa, Arjames T, & Fogler, H Scott. (2009). Revisiting asphaltene precipitation from crude oils: A case of neglected kinetic effects. *Energy & Fuels, 23*(7), 3681-3686.

Marei, Nedal N, Nassar, Nashaat N, Hmoudah, Maryam, El-Qanni, Amjad, Vitale, Gerardo, & Hassan, Azfar. (2017). Nanosize effects of NiO nanosorbcats on adsorption and catalytic thermo-oxidative decomposition of vacuum residue asphaltenes. *The Canadian Journal of Chemical Engineering, 95*(10), 1864-1874.

McEachern, Preston. (2009). Environmental management of Alberta's oil sands.

Mendoza de la Cruz, Jose L, Arguelles-Vivas, Francisco J, Matias-Perez, Victor, Durán-Valencia, Cecilia de los A, & Lopez-Ramirez, Simon. (2009). Asphaltene-induced precipitation and deposition during pressure depletion on a porous medium: an experimental investigation and modeling approach. *Energy & fuels, 23*(11), 5611-5625.

Minssieux, L. (1997). *Core damage from crude asphaltene deposition.* Paper presented at the International Symposium on Oilfield Chemistry.

Mitra, Sushanta K, & Chakraborty, Suman. (2011). *Microfluidics and Nanofluidics Handbook: Chemistry, physics, and life science principles*: CRC press.

Moghanloo, Rouzbeh G, Davudov, Davud, & Akita, Emmanuel. (2018). Formation damage by organic deposition. *Formation Damage During Improved Oil Recovery*, 243-273.

Mohammadi, Majid, Dadvar, Mitra, & Dabir, Bahram. (2017). TiO2/SiO2 nanofluids as novel inhibitors for the stability of asphaltene particles in crude oil: Mechanistic understanding, screening, modeling, and optimization. *Journal of Molecular Liquids, 238*, 326-340.

Mohammadi, Mohsen, Akbari, Mahdi, Fakhroueian, Zahra, Bahramian, Alireza, Azin, Reza, & Arya, Sharareh. (2011). Inhibition of asphaltene precipitation by TiO2, SiO2, and ZrO2 nanofluids. *Energy & Fuels, 25*(7), 3150-3156.

Mozaffari, Saeed, Tchoukov, Plamen, Mozaffari, Ali, Atias, Jesus, Czarnecki, Jan, & Nazemifard, Neda. (2017). Capillary driven flow in nanochannels–Application to heavy oil rheology studies. *Colloids and Surfaces A: Physicochemical and Engineering Aspects, 513*, 178-187.

Mullins, Oliver C. (2010). The Modified Yen Model†. *Energy & Fuels, 24*(4), 2179-2207.

Mullins, Oliver C. (2011). The asphaltenes. *Annual Review of Analytical Chemistry, 4*, 393-418.

Mullins, Oliver C, Sabbah, Hassan, Eyssautier, Joëlle, Pomerantz, Andrew E, Barré, Loïc, & Andrews, A Ballard, Ruiz-Morales, Yosadara, Mostowfi, Farshid, McFarlane, Richard,

Goual, Lamia. (2012). Advances in asphaltene science and the Yen–Mullins model. *Energy & Fuels, 26*(7), 3986-4003.
Murgich, Juan. (2003). Molecular simulation and the aggregation of the heavy fractions in crude oils. *Molecular Simulation, 29*(6-7), 451-461.
Nassar, Nashaat N, Betancur, Stefania, Acevedo, Sócrates, Franco, Camilo A, & Cortés, Farid B. (2015). Development of a population balance model to describe the influence of shear and nanoparticles on the aggregation and fragmentation of asphaltene aggregates. *Industrial & Engineering Chemistry Research, 54*(33), 8201-8211.
Nassar, Nashaat N, Hassan, Azfar, Carbognani, Lante, Lopez-Linares, Francisco, & Pereira-Almao, Pedro. (2012). Iron oxide nanoparticles for rapid adsorption and enhanced catalytic oxidation of thermally cracked asphaltenes. *Fuel, 95*, 257-262.
Nassar, Nashaat N, Hassan, Azfar, & Pereira-Almao, Pedro. (2011a). Comparative oxidation of adsorbed asphaltenes onto transition metal oxide nanoparticles. *Colloids and Surfaces A: Physicochemical and Engineering Aspects, 384*(1), 145-149.
Nassar, Nashaat N, Hassan, Azfar, & Pereira-Almao, Pedro. (2011b). Effect of surface acidity and basicity of aluminas on asphaltene adsorption and oxidation. *Journal of colloid and interface science, 360*(1), 233-238.
Nassar, Nashaat N, Hassan, Azfar, & Pereira-Almao, Pedro. (2011c). Effect of the particle size on asphaltene adsorption and catalytic oxidation onto alumina particles. *Energy & Fuels, 25*(9), 3961-3965.
Nassar, Nashaat N, Hassan, Azfar, & Pereira-Almao, Pedro. (2011d). Metal oxide nanoparticles for asphaltene adsorption and oxidation. *Energy & Fuels, 25*(3), 1017-1023.
Nassar, Nashaat N, Hassan, Azfar, & Vitale, Gerardo. (2014). Comparing kinetics and mechanism of adsorption and thermo-oxidative decomposition of Athabasca asphaltenes onto TiO_2, ZrO_2, and CeO_2 nanoparticles. *Applied Catalysis A: General, 484*, 161-171.
Nassar, Nashaat N. (2010). Asphaltene Adsorption onto Alumina Nanoparticles: Kinetics and Thermodynamic Studies. *Energy & Fuels, 24*(8), 4116-4122. doi: 10.1021/ef100458g
Nghiem, Long X, & Coombe, Dennis A. (1997). Modelling asphaltene precipitation during primary depletion. *SPE Journal, 2*(02), 170-176.
Nghiem, Long X, Coombe, Dennis A, & Ali, SM. (1998). *Compositional simulation of asphaltene deposition and plugging.* Paper presented at the SPE Annual Technical Conference and Exhibition.
Oskui, Gh, Reza, P, Jumaa, Mohammad A, Folad, Ebtisam G, Rashed, Abeer, & Patil, Shirish. (2011). *Systematic Approach for Prevention and Remediation of Asphaltene Problems During CO2/Hydrocarbon Injection Project.* Paper presented at the The Twenty-first International Offshore and Polar Engineering Conference.
Pak, T, Kharrat, R, Bagheri, M, Khalili, M, & Hematfar, V. (2011). Experimental study of asphaltene deposition during different production mechanisms. *Petroleum science and technology, 29*(17), 1853-1863.
Perman, Roger. (2003). *Natural resource and environmental economics*: Pearson Education.
Rahmani, Nazmul HG, Masliyah, Jacob H, & Dabros, Tadeusz. (2003). Characterization of asphaltenes aggregation and fragmentation in a shear field. *AIChE journal, 49*(7), 1645-1655.

Rana, Mohan S, Samano, Vicente, Ancheyta, Jorge, & Diaz, JAI. (2007). A review of recent advances on process technologies for upgrading of heavy oils and residua. *Fuel, 86*(9), 1216-1231.

Rezvani, Hosein, Khalilnezhad, Ali, Ganji, Parastoo, & Kazemzadeh, Yousef. (2017). How ZrO 2 nanoparticles improve the oil recovery by affecting the interfacial phenomena in the reservoir conditions? *Journal of Molecular Liquids*.

Rogel, E, Leon, O, Espidel, Y, & Gonzalez, Y. (2001). Asphaltene stability in crude oils. *SPE Production & Facilities, 16*(02), 84-88.

Ruiz-Morales, Yosadara. (2009). Aromaticity in pericondensed cyclopenta-fused polycyclic aromatic hydrocarbons determined by density functional theory nucleus-independent chemical shifts and the Y-rule-Implications in oil asphaltene stability. *Canadian Journal of Chemistry, 87*(10), 1280-1295.

Sabbah, Hassan, Morrow, Amy L, Pomerantz, Andrew E, & Zare, Richard N. (2011). Evidence for island structures as the dominant architecture of asphaltenes. *Energy & Fuels, 25*(4), 1597-1604.

Schantz, SS, & Stephenson, WK. (1991). *Asphaltene deposition: development and application of polymeric asphaltene dispersants.* Paper presented at the SPE Annual Technical Conference and Exhibition.

Seifried, Christine. (2016). Asphaltene precipitation and deposition from crude oil with CO2 and hydrocarbons: experimental investigation and numerical simulation.

Setoodeh, Narjes, Darvishi, Parviz, & Lashanizadegan, Asghar. (2018). A comparative study to evaluate the performance of coated Fe3O4 nanoparticles for adsorption of asphaltene from crude oil in bench scale. *Journal of Dispersion Science and Technology, 39*(5), 711-720.

Shen, Ziqi, & Sheng, James J. (2018). Experimental and numerical study of permeability reduction caused by asphaltene precipitation and deposition during CO2 huff and puff injection in Eagle Ford shale. *Fuel, 211*, 432-445.

Shojaati, Faryar, Riazi, Masoud, Mousavi, Seyed Hamed, & Derikvand, Zeinab. (2017). Experimental investigation of the inhibitory behavior of metal oxides nanoparticles on asphaltene precipitation. *Colloids and Surfaces A: Physicochemical and Engineering Aspects, 531*, 99-110.

Sieben, Vincent J, Tharanivasan, Asok Kumar, Andersen, Simon I, & Mostowfi, Farshid. (2016). Microfluidic approach for evaluating the solubility of crude oil asphaltenes. *Energy & Fuels, 30*(3), 1933-1946.

Soroush, Samaneh, Pourafshary, Peyman, & Vafaie-Sefti, Mohsen. (2014). *A comparison of asphaltene deposition in miscible and immiscible carbon dioxide flooding in porous media.* Paper presented at the SPE EOR Conference at Oil and Gas West Asia.

Strausz, Otto P, Peng, Ping'an, & Murgich, Juan. (2002). About the colloidal nature of asphaltenes and the MW of covalent monomeric units. *Energy & fuels, 16*(4), 809-822.

Syunyaev, RZ, Balabin, RM, Akhatov, IS, & Safieva, JO. (2009). Adsorption of petroleum asphaltenes onto reservoir rock sands studied by near-infrared (NIR) spectroscopy. *Energy & Fuels, 23*(3), 1230-1236.

Taborda, Esteban A, Franco, Camilo A, Lopera, Sergio H, Alvarado, Vladimir, & Cortés, Farid B. (2016). Effect of nanoparticles/nanofluids on the rheology of heavy crude oil and its mobility on porous media at reservoir conditions. *Fuel, 184*, 222-232.

Thomas, DC, Becker, HL, & Del Real Soria, RA. (1995). Controlling asphaltene deposition in oil wells. *SPE Production & Facilities, 10*(02), 119-123.

Trimm, DL. (1996). Catalytic deactivation *Studies in Surface Science and Catalysis* (Vol. 100, pp. 65-76): Elsevier.

Uetani, Takaaki. (2014). *Wettability alteration by asphaltene deposition: A field example.* Paper presented at the Abu Dhabi international petroleum exhibition and conference.

Wang, Jianxin, Buckley, Jill S, & Creek, Jefferson L. (2004). Asphaltene deposition on metallic surfaces. *Journal of dispersion science and technology, 25*(3), 287-298.

Wang, Shuhua, Chen, Shengnan, & Li, Zhaomin. (2016). Characterization of produced and residual oils in the CO2 flooding process. *Energy & Fuels, 30*(1), 54-62.

Yen, Teh Fu, Erdman, J Gordon, & Pollack, Sidney S. (1961). Investigation of the structure of petroleum asphaltenes by X-ray diffraction. *Analytical Chemistry, 33*(11), 1587-1594.

You, Zhenjiang, Badalyan, A, Bedrikovetsky, P, Hand, Martin, & Jenson, D. (2013). *Productivity Decline Due to Fines Migration (Modelling and Field Case).* Paper presented at the International Petroleum Technology Conference.

Zabala, R, Mora, E, Botero, OF, Cespedes, C, Guarin, L, & Franco, CA, Cortes, FB, Patino, JE, Ospina, N. (2014). *Nano-technology for asphaltenes inhibition in Cupiagua South Wells.* Paper presented at the IPTC 2014: International Petroleum Technology Conference.

Chapter Three: Size Effects of NiO Nanoparticles on the Competitive Adsorption of Quinolin-65 and Violanthrone-79: Implications for Oil Upgrading and Recovery[2]

Graphical Abstract

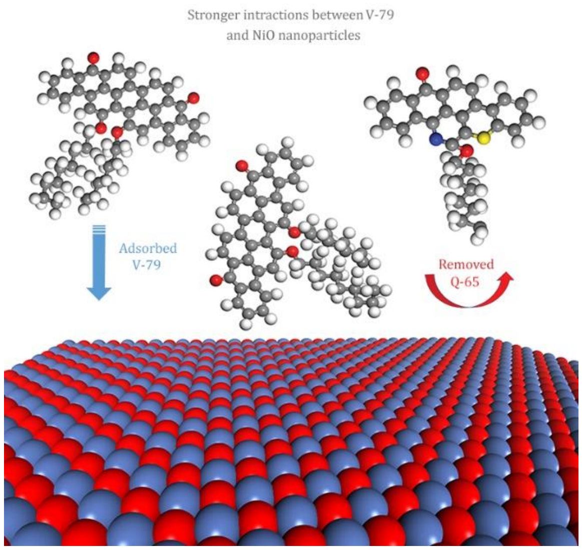

3.1. Abstract

Using Quinolin-65 (Q-65) and Violantrone (V-79) as model molecules for polar heavy hydrocarbons and resins, the nanosize effects of NiO nanoparticles on the competitive molecular adsorption on nanoparticles were conducted using multiwavelength UV-visible derivative spectrophotometry method. This is important for understanding the role of nanoparticles in oil upgrading and recovery processes. Computer simulations were also carried out to validate the experimental findings and provide more insights on the interactions between the Q-65 and/or V79 molecules and the NiO nanoparticle surface. Different-sized NiO nanoparticles (5, 40 and >100

---

[2]This chapter is adapted from the following publication:
Tatiana Montoya, Azadeh Amrollahi, Gerardo Vitale, Negahdar Hosseinpour and Nashaat N. Nassar. **Size Effects of NiO Nanoparticles on the Competitive Adsorption of Quinolin-65 and Violanthrone-79: Implications for Oil Upgrading and Recovery**, Published in ACS applied nano materials journal, 2020: https://doi.org/10.1021/acsanm.0c00697.

nm) were synthesized by controlled thermal dehydroxylation of $Ni(OH)_2$. Nanoparticles were characterized using XRD, BET, FTIR and XPS. Macroscopic adsorption isotherms of Q-65 and V-79 molecules over 5 and 40 nm NiO nanoparticles were evaluated in toluene-based solutions as individual and binary solutions. On a normalized surface area basis, the number of Q-65 and V-79 molecules adsorbed per nm^2 of the NiO surface was the highest for 40 nm NiO nanoparticles and lowest for 5 nm NiO. Results also indicated that NiO nanoparticles were more prone to adsorb V-79 than Q-65. Equilibrium binding constants for V-79 and Q-65, determined by the Langmuir adsorption model, showed the binding affinity for V-79 is size dependent. Simultaneous competitive adsorption between V-79 and Q-65 showed that V-79 concentration is an important factor influencing the uptake of both V-79 and Q-65, whereas the concentration of Q-65 affects only Q-65 uptake. Computational modeling results were consistent with the experimental results, confirming our conclusions about the adsorption process in this binary system.

KEYWORDS: Nanoparticles, Competitive Adsorption, NiO, binary mixture, Q-65, V-79, Computational modeling

3.2. Introduction

Lately, the use of nanoparticles has been presented as alternatives for different sectors such as in-situ heavy oil upgrading (Almao, 2012; Nassar, Hassan, & Pereira-Almao, 2011a), inhibition of the formation damage (S. Betancur, Carmona, Nassar, Franco, & Cortés, 2016; Franco, Nassar, Ruiz, Pereira-Almao, & Cortés, 2013; Romero et al., 2013), wastewater treatment (Hethnawi, Manasrah, Vitale, & Nassar, 2018; Nafie, Vitale, Carbognani Ortega, & Nassar, 2017), drug delivery (Horcajada et al., 2010; Kumari, Yadav, & Yadav, 2010), polymer composites (Balazs, Emrick, & Russell, 2006; Ramanathan et al., 2008), among other applications. In these circumstances, nanotechnology has appeared as an alternative for enhancing crude oil upgrading and recovery. Due to the molecular characteristics of crude oil, conventional porous adsorbents/catalysts have some limitations, therefore, nanoparticles having transition metal components have properties useful for upgrading and/or recovery processes (Nedal Nael Marei, 2016; Nedal N Marei, Nassar, & Vitale, 2016). Some of these attributes are: small particle size, dispersibility, tunable surface functionalities, chemical and thermal stability and high surface area/volume ratio (Nedal N Marei et al., 2016; Rezvani, Khalilnezhad, Ganji, & Kazemzadeh, 2017). These characteristics facilitate their use as catalysts/adsorbents for the capture and removal of heavy fractions such as asphaltenes present in an oil reservoir, having an immediate impact on the oil production improvement, inhibiting formation damage and restoring wettability (Franco et al., 2013; Giraldo, Benjumea, Lopera, Cortés, & Ruiz, 2013; Moradi, Pourafshary, Jalali, Mohammadi, & Emadi, 2015). In addition, nanoparticles have potential application on enhanced oil recovery (EOR) methods showing an important role in terms of wettability alteration and interfacial tension (IFT) reduction (Negin, Ali, & Xie, 2016; Rezvani et al., 2017; Zhang, Shi, Lu, Liu, & Zeng, 2016). In that way, it has been proven that nanoparticles can enhance oil production in EOR processes through different mechanism, such as viscosity/density modification of the injected fluid (Moradi et al., 2015), improvement of emulsification process (Rezvani et al., 2017), enhancement of thermal conductivity and specific heat capacity (Jang & Choi, 2004), improvement of rock-fluid interactions (McElfresh, Holcomb, & Ector, 2012), alteration of heat transfer coefficient (Rezvani et al., 2017), etc.

In addition, the interaction between asphaltenes and solid surfaces has taken the attention of researchers adopting several experimental techniques to study asphaltenes adsorption onto different substrates, including silica (Dudášová, Silset, & Sjöblom, 2008; Zahabi, Gray, & Dabros, 2012), alumina (Dudášová, Silset, et al., 2008; Nassar, 2010; Nassar, Hassan, & Pereira-Almao, 2011b), metal oxides (Amin & Solaimany Nazar, 2016; Hosseinpour, Khodadadi, Bahramian, & Mortazavi, 2013; Kazemzadeh et al., 2015), metals (Rudrake, Karan, & Horton, 2009; Sedghi, Goual, Welch, & Kubelka, 2013; Zahabi et al., 2012), stainless steel (Xie & Karan, 2005), glass (Acevedo, Castillo, Fernández, Goncalves, & Ranaudo, 1998), clay minerals (Dudášová, Simon, Hemmingsen, & Sjöblom, 2008; Pernyeszi, Patzko, Berkesi, & Dékány, 1998; Tu et al., 2006), modified materials (S. a. Betancur, Carrasco-Marín, Franco, & Cortés, 2018; Nassar, Betancur, Acevedo, Franco, & Cortés, 2015; Vargas, Castillo, Ocampo-Torres, Lienemann, & Bouyssiere, 2018), carbonaceous materials (Mansoori Mosleh, Mortazavi, Hosseinpour, & Khodadadi, 2019), among others. Moreover, in the adsorption process it is essential to consider the surface chemistry, porosity, pore size and morphology of the adsorbents (Hassan, Lopez-Linares, Nassar, Carbognani-Arambarri, & Pereira-Almao, 2013; Thommes, 2010). Therefore, asphaltene adsorption has been studied using nonporous materials, since these materials possess macropores and no other pores that increase the external surface area (Montoya, Coral, Franco, Nassar, &

Cortés, 2014). Also, it has been found that the functional groups and charge of the asphaltenes (Adams, 2014; Mullins, 2011) as well as the chemistry and charge of the adsorbent surface play an important role in the nature and the toughness of the interactions occurring between asphaltenes and the surface sites (Nedal Nael Marei, 2016) and the way these molecules are adsorbed (Nedal N Marei et al., 2016), it means, how the asphaltene layers are organized over the adsorbent surface (Montoya et al., 2014).

Accordingly, Dudášová et al. (Dudášová, Flåten, Sjöblom, & Øye, 2009) studied asphaltene adsorption over hydrophilic silica (HS), kaolin and FeS. They found out that asphaltenes were adsorbed by the polar side of the molecule for the HS and kaolin leaving the nonpolar side free, explaining that the adsorption process was guided by steric stabilization as the asphaltenes were adsorbed perpendicularly on the surface. For the FeS particles, they found out that asphaltenes can be adsorbed parallel to the surface leaving the polar and nonpolar sides free resulting in a lower uptake based on the surface area of the adsorbent (Dudášová et al., 2009; Dudášová, Simon, et al., 2008; Montoya et al., 2014). In other study, Betancur et al. (S. Betancur et al., 2016) studied the effect of particle size and surface acidity of synthesized silica gel nanoparticles for asphaltene adsorption and disaggregation. The authors found that the nanoparticles of 11 nm had the highest asphaltene adsorption, and modifying this material with acid, basic and neutral treatments, the aggregate size of asphaltenes in the bulk phase was reduced following the order acid>basic≈neutral≈original materials. Nassar et al. (Nassar et al., 2011b) assessed the effects of porous alumina particles on asphaltene adsorption. Using a normalization based on surface area, they found a higher catalytic activity on the micro alumina particles when compared to alumina nanoparticles; the results showed that a larger quantity of asphaltenes molecules were adsorbed preferentially on the alumina nanoparticles in comparison with the micro alumina. The explanation for this was attributed to the fact that asphaltene adsorption can only occur at particular sites. On a similar study, Hosseinpour et al. (Hosseinpour et al., 2013), determined the asphaltene adsorption onto different acid/base oxides such as WO_3, Fe_2O_3, NiO, MgO, $CaCO_3$, and ZrO_2 , it was found that the predominant forces in the adsorption process were acid-base interactions and electrostatic attraction.

On the other hand, other studies have demonstrated how the presence of nanoparticles such as alumina, silica, magnetite, ZrO_2 and TiO_2 can affect the kinetics of asphaltene aggregation/fragmentation, showing the effects of nanoparticles on the inhibition of asphaltene aggregation (Guzmán et al., 2016; Mohammadi et al., 2011; Nassar et al., 2015). In those studies, the experimental data were obtained using dynamic light scattering (DLS) (Mohammadi et al., 2011) measurements using a fixed asphaltene concentration and then validated by a model based on population balance that accounted for the effects of the nanoparticles on the inhibition of asphaltene aggregate growth (S. Betancur et al., 2016; Nassar et al., 2015). It was demonstrated that the studied nanoparticles could diminish the hydrodynamic ratio of the asphaltene aggregates. Nassar (Nassar, 2010) used γ-Al_2O_3 to study the asphaltene adsorption in batch mode experiments, finding out that alumina nanoparticles adsorbed more asphaltenes, on normalized surface area basis, than porous microalumina particles with similar acidities. Cortés et al. (Cortés, Mejía, Ruiz, Benjumea, & Riffel, 2012) modified silica gel nanoparticles with NiO nanoparticles, they found out that the amount of adsorbed asphaltenes at constant temperature was improved with the amount of NiO but decreased with the temperature, which indicated that the asphaltene adsorption process is exothermic. Guzmán et al. (Guzmán et al., 2016) studied asphaltene adsorption from toluene and/or heptol (n-heptane/toluene) 60/40 v/v onto silica nanoparticles, fumed silica and nanosized magnetite. They found that the adsorption was dependant on the initial concentration of the adsorbent and the adsorbate and not the equilibrium adsorbate concentration. On the other hand, Franco et al. (Franco, Lozano, Acevedo, Nassar, & Cortés, 2015) studied the effects of resin I on the adsorption behaviour of n-C_7 asphaltenes over silica and hematite nanoparticles. They reported that resin I had a solvent-like behavior at the concentrations they used, which suggested that resin I has no big effect on the asphaltene adsorption. Also, the used nanoparticles had more preference to adsorb asphaltenes than resin I.

On the other hand, as asphaltene composition are dependent on the source, the nature of solvent and method employed to extract them (Adams, 2014; Mullins, 2011), some authors have used model molecules to imitate the asphaltenes and try to comprehend the adsorption behavior of these molecules on distinct exposed surfaces (López-Linares et al., 2006; Sjöblom, Simon, & Xu, 2015). López-Linares et al. (López-Linares et al., 2006; Sjöblom et al., 2015) used Q-65 and V-79 as model molecules for Athabasca n-C_7 asphaltenes to study the adsorption over natural microporous silica-alumina. They compared the results of the adsorption of these model molecules with the adsorption of the real Athabasca n-C_7 asphaltenes, concluding that the model molecules resembled the adsorption behaviour of the real asphaltenes. Our research group has recently used V-79 as a model molecule of polar heavy compounds to study the adsorption over pyroxene nanoparticles varying their size from 1 to 100 nm and modifying their surface/structure with Ce, Zr, Ni, Ca and H (Hmoudah, Nassar, Vitale, & El-Qanni, 2016). We found that the adsorption capacity of the nanoparticles between 30 and 60 nm was the highest and the modification with H doubled the adsorption capacity (Hmoudah et al., 2016). We also used Q-65 to study the adsorption over nickel oxide nanoparticles with dimensions between 5 to 80 nm. We found that nanoparticles changed their morphology and texture (shape) with size, this affected the adsorption capacity and interfacial reactivity (Nedal Nael Marei, 2016; Nedal N Marei et al., 2016). In another study we confirmed that n-C_5 asphaltenes were less likely to be adsorbed onto NiO nanoparticles than n-C_7 asphaltenes, due to the presence of resins, since resins affect the colloidal behaviour of asphaltenes and therefore, the interactions between asphaltene and adsorbent (Nassar, Hassan, & Pereira-Almao, 2011c).

Despite of the efforts accomplished up to date, it is still unclear how the nanomaterials in complex mixtures, like crude oils, interact with the heavy components such as asphaltenes and resin during the in-situ upgrading and recovery processes such as catalytic steam cracking, hydroprocessing with ultra-dispersed catalyst, enhanced in situ recovery by nanofluid injection applications or viscosity reduction processes, and how the presence of resins can affect the catalytic performance or adsorption affinity, since other additives or presenting resin may compete with asphaltenes for adsorption sites on the surface of nanoparticles. Hence, it is necessary to question the competitive adsorption process between multiple heavy molecules adsorbing onto the nanoparticle surface. However, due to the fact that asphaltene molecular structure is unknown and it is source dependent, it makes challenging to carry out this competitive adsorption on real crude for laying out the adsorption mechanism. Therefore, in this chapter, and following our previous work, violanthrone-79 (V-79) and Quinolin-65 (Q-65) were used as model heavy compounds to better mimic resin and asphaltenes molecules, respectively, in single and binary model oil solutions to better understand their competitive and individual adsorption behaviors on different NiO nanoparticle sizes (5 and 40 nm). In addition, computational modeling was performed with the model molecules to interact with NiO nanoparticles to have an insight on which parts of these compounds get in contact with the nanoparticle surface and which site has more affinity with each compound. Further, molecular dynamic simulations were performed to have more insights on the mechanism involved in the adsorption process. This is important to know when designing catalyst/adsorbents for in-situ upgrading, oil recovery and viscosity reduction process, since the size can change the surface characteristics of the nanomaterials which play an important role in terms of catalytic performance and adsorption affinity for asphaltenes in presence of other oil component such as resins.

3.3. Materials and Methods

3.3.1. Materials

Nickel (II) nitrate hexahydrate ($Ni(NO_3)_2 \cdot 6H_2O$, Sigma-Aldrich) was the precursor salt of nickel and NaOH pellets (purchased from VWR) were employed as the precipitant to produce $Ni(OH)_2$. Radnor toluene (99.9%, HPLC grade from Sigma Aldrich) was employed to prepare the solutions. Model asphaltene and resin molecules, Quinolin-65 (Q-65) ($C_{30}H_{29}NO_2S$, M_W = 467.62 g/mol, dye content 80%) and Violanthrone (V-79) ($C_{50}H_{48}O_4$, M_W = 712.91 g/mol, dye content 98%) were obtained from Sigma-Aldrich (ON, Canada) and Toronto Research Chemicals (ON, Canada), respectively. All chemicals were used as received. **Figure 3.1**, panels a and b show 3-D ball and stick models as drawn using MolView (Smith, 1995) of the chemical structure of Q-65 and V-79, respectively. From **Figure 3.1**, Panel a, it is observed that the Q-65 resembles the molecular characteristics present in asphaltenes such as alkyl chains, aromatic rings and heteroatoms as oxygen, sulfur and nitrogen. Also, the model molecule Q-65 represents asphaltenes of the continental type, since it meets some general features for asphaltenes such as present of cross-linked poly aromatic hydrocarbons (one large aromatic region per molecule plus side chains), presence of heteroatoms like sulphur, nitrogen and oxygen, which is in agreement with what have been reported on literature (Groenzin & Mullins, 2000; López-Linares et al., 2006). Comparison with asphaltenes shows that resins have a less content of heteroatoms, less aromaticity, and, therefore, longer aliphatic chains, characteristics fairly resemble to the V-79 (Franco et al., 2015).

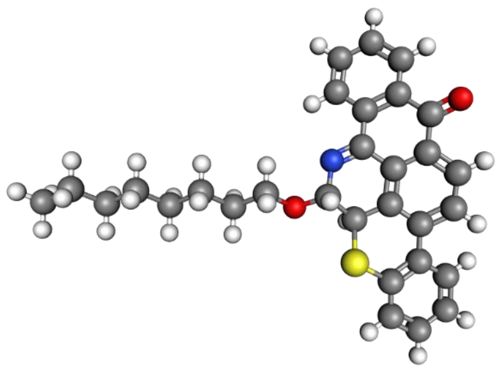

a)

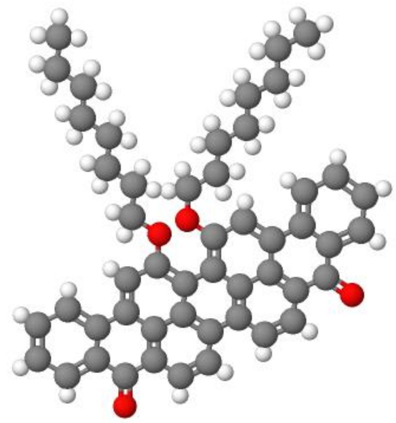

b)

Figure 3.1. 3D ball and stick molecular structure drawn using MolView (Smith, 1995) of the (a) asphaltene model molecule Q-65 and (b) resin model molecule V-79. Nitrogen, oxygen, and sulfur are depicted in blue, red, and yellow, respectively; aromatic and aliphatic carbon are depicted in grey and hydrogen is depicted in white.

3.3.2. Synthesis of NiO Nanoparticles

Preparation on the NiO nanoparticles of 5 and 40 nm (average crystalline domain size) was achieved by dehydroxylation of previously hydrothermally prepared $Ni(OH)_2$ under a well-controlled thermal treatment as reported in previous work (Nedal Nael Marei, 2016; Nedal N Marei et al., 2016). The obtained $Ni(OH)_2$ powder was calcined at a gradient of 5 °C/min for 2 h at two temperatures, 573 and 873 K, to get NiO nanoparticles with average crystalline domain sizes of 5 and 40 nm, respectively. A third sample (used as a reference for characterization) was prepared in a similar fashion, but the calcination temperature was 1073 K (2 h at 5 K/min) to compare the nano-crystalline materials with bulk large crystals of NiO.

3.3.3. Characterization of the Prepared NiO Nanoparticles

3.3.3.1. X-ray Photoelectron Spectroscopy (XPS)

A Physical Electronics PHI VersaProbe 5000-XPS instrument was used to record XPS spectra. Spectra were taken using monochromatic aluminum source, 1486.6 eV, at 50 W of power and with a beam diameter of 200.0 µm. Each sample was pressed on indium foil for XPS analysis. The double neutralization technique, i.e., low energy electron beam and low-energy Ar^+ beam, was used during spectrum acquisition for diminishing the surface charging effect. The binding energies relative to C*1s*, at 284.8 eV, were reported. Peak fitting of the spectra was performed using the Multipack 9.2.0.5 software developed by Physical Electronics and provided with the XPS instrument (Sebakhy, 2017).

3.3.3.2. Fourier Transform Infrared Spectroscopy (FTIR)

An IRAffinity-1S FTIR instrument manufactured by Shimadzu with a smart diffuse reflectance attachment to carry out DRIFTS analysis (Diffuse Reflectance Infrared Fourier Transform Spectroscopy) was used to study the framework mid-infrared region of the prepared samples. 5 mg of sample was mixed with 500 mg of KBr (1 %wt.) after the FTIR background was established. The mixture was spread over the DRIFTS sample holder. FTIR spectra were recorded from 400 to 4000 cm^{-1} with a resolution of 4 cm^{-1}, being these spectra the average output from 50 scans (Nedal Nael Marei, 2016; Sebakhy, 2017).

3.3.3.3. Textural Properties

Nitrogen (N_2) physisorption measurements of the samples were performed at 77 K on a Micromeritics Tristar 3000 surface area analyzer, Norcross, GA, using Brunauer–Emmett–Teller (BET) equation for the surface area calculations. About 200 mg of each sample was used for the analysis. The samples were pretreated overnight on a stream of N_2 at 423 K before the measurements (Nedal Nael Marei, 2016; Nedal N Marei et al., 2016). Additionally, the program SAIEUS, from Micromeritics Corporation was used to study the microporosity observed in the NiO nanoparticles with 5 nm crystalline domain size. In order to do that, the Non-local Density Functional Theory N2-77 Cylindrical model was employed to gain some insights into the microporosity present in the studied material.

3.3.3.4. X-ray Powder Diffraction (XRD)

X-ray analysis of the dry prepared materials was performed using a Rigaku ULTIMA III X-ray diffractometer with Cu Kα radiation as the X-ray source. Each sample was placed in a Rigaku zero background sample holder model 906163 (10 mm × 0.2 mm Well Si510) for the analysis. The sample was evenly distributed on the cavity of the sample holder with the help of a microscope slide. Scans were performed in the range of 20 to120° 2θ degrees using a 0.05° step and a counting time of 0.2° per min at 40 kV and 44 mA (El-Qanni, 2017; Sebakhy, 2017). The crystalline domain sizes were assessed using the Scherrer equation, as found in the commercial software JADE (El-Qanni, 2017; Nedal Nael Marei, 2016; Negin et al., 2016) Rietveld refinements of the three NiO samples were performed by the Reflex Plus Rietveld refinement module within BIOVIA Materials Studio (Balazs et al., 2006) starting with the cubic space group Fm-3m (no. 225) and the initial cell parameters reported for NiO in the BIOVIA Structural database (a = 0.41684 nm).

3.3.4. Macroscopic Adsorption Isotherm Experiments

Macroscopic solution phase adsorption isotherms on different sizes of NiO nanoparticles were performed to quantify surface coverage of V-79 and Q-65 using three approaches, namely: i) individual adsorption, here we investigated the individual adsorption of V-79 and Q-65 on different-sized nanoparticles and used it as a baseline and to benchmark competitive adsorption based on binary solution (as pictured in a simplified cartoon, **Figure 3.2a)**; ii) simultaneous competitive adsorption, here we investigated simultaneous competitive adsorption of the binary solution as depicted in a simplified cartoon, **Figure 3.2b)**; and iii) displacement competitive adsorption, here V-79 was selected as a potential displacing agent, to represent the resin or the inhibitor, for previously adsorbed Q-65 on nanoparticles (simplistically depicted by a cartoon in **Figure 3.2c)**. The latter is equally relevant to the wettability alteration applications, where the displacing molecule "resin" interacts following to the formation of the target asphaltene-surface. Worth noting here that the macroscopic adsorption isotherm experiments for the aforementioned three cases were done by three times, and the standard deviations were determined and showed.

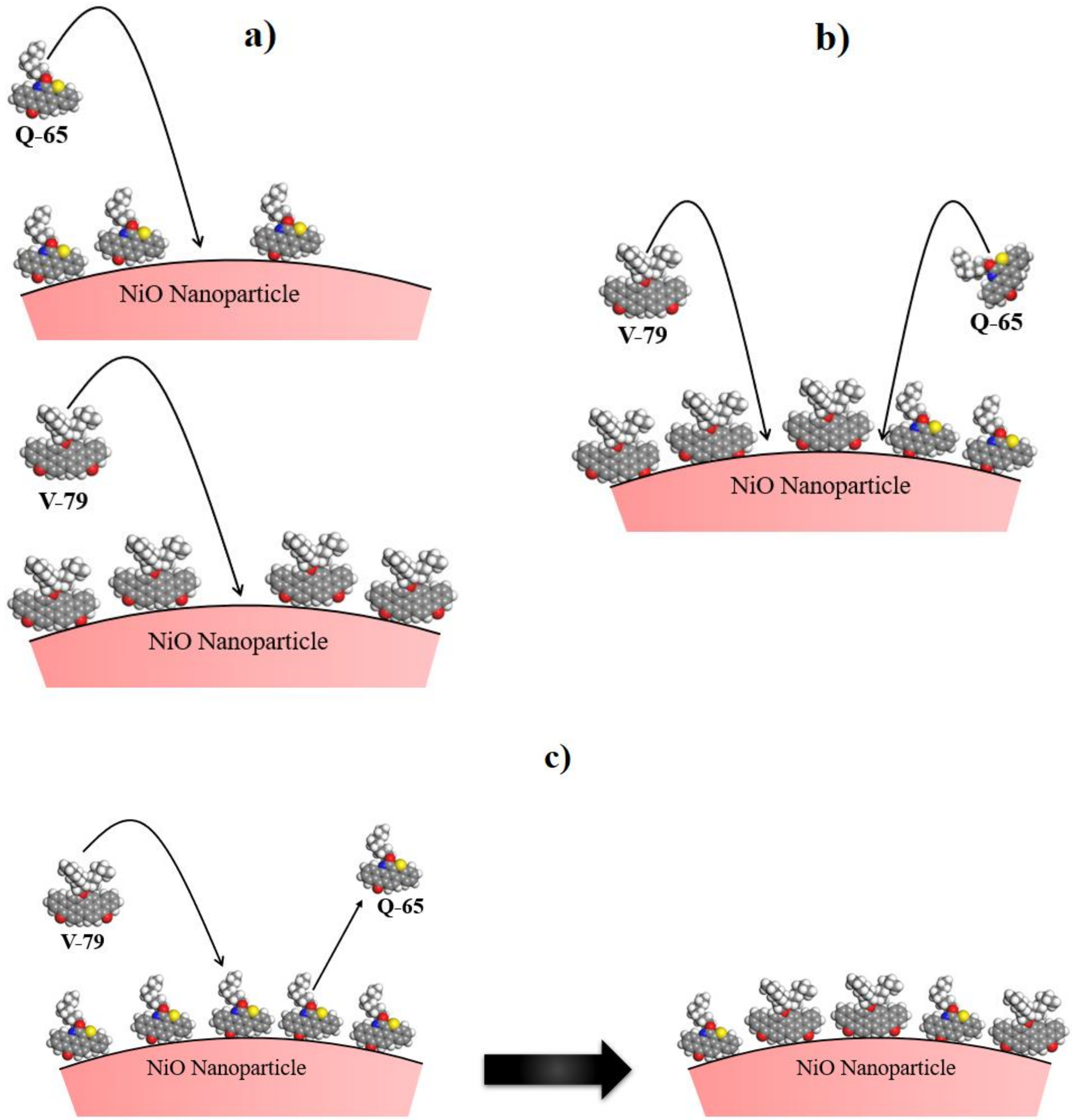

Figure 3.2. Cartoon depictions of a) individual adsorption of Q-65 and V-79 on NiO surface; b) simultaneous competitive adsorption; and c) displacement competitive adsorption.

3.3.5. Individual Adsorption

For the batch adsorption experiments from the individual (Q-65 or V-79) solutions, it was followed the same procedure reported in previous work (Nedal Nael Marei, 2016). 50 mg of the NiO nanoparticles were added into a 25 mL vial containing 5 mL of solution of Q-65 or V-79 mixed with toluene at initial concentrations varying between 0.05 and 1.5 mmol/L at 273 K. The vials well secured to prevent toluene evaporation. Adsorption could occur by shaking the vials for 24 h to be sure the equilibrium was achieved. Then, the samples were left to settle overnight followed by centrifugation during 5 min at 5000 rpm employing an Eppendorf Centrifuge 5804, and the supernatant was decanted. Afterwards, the residual concentration was analyzed with an Evolution 260 Bio UV-Vis spectrophotometer, Thermo Scientific, USA with toluene as a blank. The calibration curves were obtained using standard solutions with known concentrations at wavelength of 345 and 416 nm for V-79 or Q-65 solutions, respectively. Thereby, the adsorption uptake per surface area of the NiO nanoparticles and the equilibrium binding constant were found based on the obtained isotherms.

3.3.6. Simultaneous Competitive Adsorption

The adsorption of Q-65 and V-79 from the binary solutions onto the NiO nanoparticles were conducted following the batch adsorption experiments procedure previously described. 50 mg of the nanoparticles were added to a 25 mL vial that has 5 mL of the binary solutions with equimolar initial concentrations of the Q-65 and V-79 in toluene. The total solute initial concentration in the equimolar binary solutions changed in the range of 0.05-1.5 mmol/L. For these experiments, derivative spectrophotometry based on multi-wavelength linear regression analysis, using the first order derivative was employed to analyze the UV-vis spectra and calibrate the V-79 and Q-65 concentrations in the solution (Blanco, Gene, Iturriaga, Maspoch, & Riba, 1987). This method was applied to the simultaneously determination of substances in a mixture with overlapping spectra without previous separation (Morelli, 1995; Salinas, Nevado, & Mansilla, 1990), as the case for the mixture of Q-65 and V-79. For the analysis, the first order derivative of the spectra of the binary solutions was compared to the derivative spectra of the individual model oils. The first order derivative of the UV-vis spectra for the Q-65 individual model oil solution, exhibited zero values at 250, 288, 331, 340, 416, 437, 566 and 688 nm, indicating the wavelengths of extremum absorption. On the other hand, the zero values for the V-79 individual model oil solutions were found at 287, 345, 396, 462 and 634 nm wavelengths. Hence, the concentrations of the Q-65 and V-79 in the individual model oil solutions were calibrated using the UV-vis absorption values at all the wavelengths of the extremum absorption. Then, it was found that the correlation coefficient of the calibration lines of Q-65 and V-79 concentrations in the individual model solutions against the absorption values is the highest at λ=416 and 345 nm, respectively, reaching almost the unity as depicted in **Figure A4** of the Appendix A. These findings led to analyze the UV-vis spectra of the binary solutions to calibrate the individual concentration of Q-65 and V-79 in the binary solutions. Consequently, the first order derivative of the UV-vis spectra of the binary solutions was plotted against the absorption wavelength, as it was expected, this plot did not show zero values at λ=416 and 345 nm, indicating the overlapping of the absorption of Q-65 and V-79 molecules. This means that, for instance, the first order derivative values at λ=345 nm arise from the absorption by Q-65 molecules since these values are zero in V-79-containing individual solution.

3.3.7. Displacement Competitive Adsorption

In order to evaluate the affinity and strength of the active sites of the NiO nanoparticles for adsorption of Q-65, V-79 was selected here to act as a potential displacing agent for Q-65 conjugated NiO nanoparticle. Here, the vacuum oven-dried solid precipitates obtained from the individual adsorption experiments for Q-65 were added to 5 mL of a fresh individual solution of V-79 at a concentration equal to the original solution of Q-65 (where the used precipitates were obtained from), in a 25 mL vial. Similar procedure was followed for the V-79-containing precipitates obtained from the individual adsorption experiment. The vials were shaken for 24 h, followed by settlement overnight and centrifugation. The supernatant liquids were analyzed by UV-vis spectroscopy to determine the uptake per surface area.

For the aforementioned three cases of adsorption experiments, the adsorbed amount of V-79 or Q-65 (molecules of V-79 or Q-65/nm^2 of NiO nanoparticles) was calculated with Eq 3.1:

$$Q = \frac{(C_0 - C_e)N_A}{SA} V \tag{3.1}$$

where C_0 and C_e are the initial concentration of V-79 or Q-65 in solution (mmol/L) and the equilibrium concentration of V-79 or Q-65 in the supernatant (mmol/L), respectively; N_A is Avogadro's constant; SA is either the external (non-microporous) or the BET (including the microporous) surface areas of NiO nanoparticles (nm^2) and V is the solution volume (L). The solid precipitates, obtained from the adsorption experiments, which contain adsorbed V-79 or Q-65 onto the NiO nanoparticles were dried in a vacuum oven at 338 K and subjected to further analysis. The adsorption experiments were performed using the prepared NiO nanoparticles with 5 and 40 nm crystalline domain sizes to investigate the effects of the size and, thus, surface properties on the adsorption of Q-65 and V-79.

For all cases, the adsorption isotherm curves followed Langmuir-like behaviour (Langmuir, 1916). Hence, the maximum uptake (Q_{max}) and the equilibrium binding constants (K_L) were estimated using the Langmuir model expressed by Eq 3.2 for individual solutions and displacement adsorption, and Eqs 3.3 and 3.4 for binary systems. The selectivity of the nanoparticles to the adsorption of Q-65 and V-79 was defined by Eq 3.5.

$$Q_e = \frac{Q_{max} K_L C_e}{1 + K_L C_e} \tag{3.2}$$

$$Q_{eA} = \frac{Q_{A,max} K_{LA} C_{eA}}{1 + K_{lA} C_{eA} + K_{LB} C_{eB}} \tag{3.3}$$

$$Q_{eB} = \frac{Q_{B,max} K_{LB} C_{eB}}{1 + K_{LA} C_{eA} + K_{LB} C_{eB}} \tag{3.4}$$

$$\alpha_{ij} = \frac{Q_{i,max} K_i}{Q_{j,max} K_j} \tag{3.5}$$

where Q_e is the uptake of molecules of Q-65 or V-79 over the nanoparticles (molecules/m^2); C_e is the equilibrium concentration of Q-65 or V-79 in the solution (mol/L); K_L is the equilibrium binding constant related to the affinity of binding sites (L/mol); Q_{max} is the maximum number of molecules of the solute adsorbed on the surface (molecules/m^2) (Nedal Nael Marei, 2016). A and B correspond to Q-65 and V-79 in Eqs 3.3 and 3.4, respectively, and α_{ij} is the selectivity. The Langmuir model was fitted to the experimental data and the minimization of the absolute average relative error (AARE), shown by Chi-square value on Eq 3.6 was the objective function.

$$\chi^2 = \sum \frac{\left(Q_{e(exp)} - Q_{e(cal)}\right)^2}{Q_{e(cal)}} \tag{3.6}$$

where $Q_{e(exp)}$ and $Q_{e(cal)}$ are the adsorbed amount of the solute obtained from the experiments and predicted by the models, respectively.

3.4. Computational Modeling

Computer simulations were used to have deeper understanding on the adsorption interactions of Q-65 and V-79 molecules on the surface of different-sized NiO nanoparticles. This oxide has the rock salt structure (Nedal N Marei et al., 2016) and it is important for different applications such as adsorbent/catalyst for removal of heavy polar hydrocarbons from crude oil (Hassan et al., 2013; Nedal N Marei et al., 2016; Nassar, Hassan, & Vitale, 2014). A low index surface (100) was created from the BIOVIA Material Studio 2018 (MS2018) database (Balazs et al., 2006; Nedal Nael Marei, 2016), in order to carry out interaction studies. BIOVA Forcite geometrically optimized the Q-65 and V-79 molecules, the NiO unit cell and relaxed the surface atoms prior to its use in the adsorption study (El-Qanni, 2017; Nedal Nael Marei, 2016). In addition, BIOVIA adsorption location module was used, allowing the detection of the potential adsorption configurations by performing Monte Carlo inspections of the configurational space of the chosen nanoparticle surface-model molecule systems while temperature decreases. The process is repeated several times to identify additional local energy minima. More details on the theoretical calculations are given in the subsequent sections.

3.4.1. Q-65 and V-79 Molecules

Q-65 and V-79 molecules were created and optimized with BIOVIA Forcite previous to the adsorption over the picked NiO (100) surface. The quality of the Geometry Optimization in BIOVIA Forcite was stablished to Fine and the Forcefield to BIOVIA COMPASS (Zhao, Liu, & Sun, 2007), as this forcefield is compatible with metal oxides (Zhao et al., 2007), and it is employed to investigate the interactions between Q-65, V-79 and the NiO surface. The optimum Q-65 and

V-79 molecules are displayed in **Figure 3.3**, where a near flat configuration of the molecules is observed.

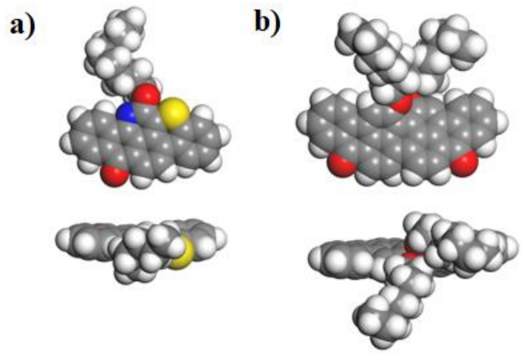

Figure 3.3. Space filling CPK representation of the molecules showing their optimized configuration (top and side views, respectively). a) Q-65 and b) V-79. Grey atoms represent carbon, blue atoms represent nitrogen, white atoms represent hydrogen, yellow atoms represent sulfur, and red atoms represent oxygen.

3.4.2. NiO Nanoparticles

The experimental structural data for NiO reported in BIOVA structural database (Balazs et al., 2006) was transferred to the visualization window and the unit cell was geometrically. The experimental unit cell value for NiO from the MS2018 structural database (Balazs et al., 2006) was 0.41684 nm and the optimized unit cell value obtained was 0.41683 nm for NiO, which is close to the experimental value; confirming the quality of the used forcefield. The optimized unit cell was employed in BIOVIA Builder module to generate the surface (100) (Nedal Nael Marei, 2016). The surface was created with areas of approximately 14.4 nm^2 (∼3.8 nm × ∼3.8 nm) in this way it is possible to avoid any interaction of the molecules in the box with their images in adjacent cells. More details on these types of calculations can be found in previous work (El-Qanni, 2017). **Figure 3.4** shows the optimized (100) surface for NiO.

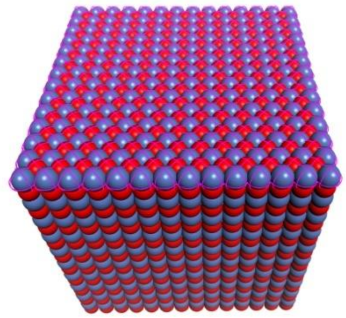

Figure 3.4. 45° perspective of the space filling CPK representation of the optimized (100) surface of NiO used in the calculations. Red atoms represent oxygen and blue atoms represent nickel.

3.4.3. Interactions of Q-65, V-79 and Toluene Molecules with the NiO (100) Surface

BIOVIA Adsorption locator module was used to get more understandings on the interactions of the model molecules with the synthesized NiO surface. The simulating annealing task in BIOVIA Adsorption Locator calculation was set to a quality of Fine with energy cut-off of 1.0×10^{-4} kcal/mol, using the Smart algorithm. The atom-based summation method was used for van der Waals and the group-based method for the electrostatic with a cubic spline truncation and a cut-off distance of 1.55 nm. The force field selected was BIOVIA COMPASS, since it is suitable to study interfaces between organics and inorganics (Balazs et al., 2006; Zhao et al., 2007); the top layer atoms (~0.5 nm) on the surface was selected for the interaction with Q-65, V-79 and toluene molecules.(Nedal Nael Marei, 2016)

3.4.4. Molecular Dynamics Simulations

In order to have more information on the adsorption behavior of V-79 and Q-65 when toluene is present, molecular dynamics (MD) simulations were done using the Forcite module within BIOVIA MS2018 software (Balazs et al., 2006). The interatomic interactions were described by using COMPASS forcefield. The MD simulations were conducted in NVT ensemble at 298 K.

The Andersen method was employed in the thermostat to control the thermodynamic temperature with a Collision ratio of 1.0. The time step in the MD simulation was set to 1.0 fs. The simulation time was set to 1 ns to detect several cycles of thermal vibration, and the full-precision trajectory was recorded. Energies and other statistical data (e.g., coordinates, velocities, etc.) were stored every 5000 steps during the simulations (El-Qanni, 2017).

Here, the system was stablished as a periodic slab with the (100) face, since is the most probable exposed surface on the NiO material. The dimensions of the surface were similar to those used in the Adsorption Locator calculations ~3.8 nm × ~3.8 nm. The thickness of the slab was ~4 nm and the three upper layers of atoms were enabled to evolve without any geometrical constraints during the calculations. A vacuum of 16 nm was added on top of the surface and a slab of about 3 nm containing 200 toluene molecules, 5 V-79 molecules and 5 Q-65 molecules, generated by the BIOVIA Amorphous Cell module and the COMPASS forcefield, was incorporated near to the oxide surface within the periodic cell (El-Qanni, 2017).

3.4.5. Density Functional Theory (DFT) Calculations to Obtain the Calculated Infrared Spectrum of NiO

To obtain further comprehension on the infrared spectrum of the NiO nanoparticles, the unit cell of NiO was optimized at the DFT level using the $DMol^3$ program within BIOVIA MS2018 software (Balazs et al., 2006) and the GGA PBESol (Perdew et al., 2008) functional with the DNP^+ basis set and all electron core treatment with Spin unrestricted. The used tolerances were: Energy = 1.0×10^{-5} Ha; Max. Force = 0.002 Ha/Å; Max. displacement = 0.005 Å; SFC tolerance = 1.0×10^{-6}; and using a smearing of 0.005 Ha and a Global orbital cut-off of 4.5 Å. The generated spectra were obtained with broadenings of the signals (FWHM) of 5, 100, 200 and 300 cm^{-1} for comparison with the experimental spectra.

3.5. Results and Discussions

3.5.1. Characterization Studies

XRD was used to confirm the correct structure of the prepared NiO nanomaterials. For the sample calcined at 300 °C, the obtained average value of the crystalline domain sizes was 4.5 ± 0.5 nm. For the sample calcined at 600 °C, the value was 42 ± 4 nm and for the sample obtained at 900 °C the value was 104 ±3 nm. Hereinafter the sample calcined at 300 °C is denoted as 5nm NiO, the one obtained at 600 °C is denoted as 40nm NiO and the one obtained at 900 °C is denoted as >100nm NiO. The crystalline domain sizes of NiO play an important role in the observed color of the materials; the 5nm NiO is a black powder, the 40nm NiO is a pale grey powder and the >100 NiO is a green powder. Further characterization by XRD was carried out by doing Rietveld refinement of the obtained powder patterns with the BIOVIA Reflex Plus module within the MS2018 software. **Figure 3.5** shows the plots of the refinement performed for the three materials and Table S1 of the supporting information shows details of the refinement. As seen in **Figure 3.5a-c**, as expected, the broadening of the signals decreased with treatment temperature, making them much narrower. The refinements converged to a very low values of R_{wp} and R_p, indicating a good modeling of the experimental patterns with the NiO structure. The cell parameters of the materials 5nm NiO and 40nm NiO are slightly larger than the previously reported value for NiO (0.41684 nm), indicating that the surface defects caused by the nano-size of the particles are important and have a great contribution in expanding the average unit cell, as the surface ratio of hydroxyl defects compared to the bulk is large for these materials.

The BIOVIA Reflex Plus program allows to study the size-strain present in the sample. As seen in **Table 3.1**, the obtained values of crystalline domain sizes by Reflex are larger than the ones calculated by JADE software, assuming that the broadening is only due to crystalline size (obtained by the Scherrer equation). The lattice strains in the prepared nanomaterials (**Table 3.1**) are important and, the lattice strain of the sample 5nm NiO is higher than the other two samples, confirming again the distortion of the cell and aiding in the broadening of the signals. Thus, the contribution of lattice strain to the broadening of the XRD patterns in these samples is important specially for the 5nm NiO and 40nm NiO nanomaterials. These differences should be important in the adsorption process as will be discussed in Section 3.5.3.

Table 3.1. Summary of the Rietveld Refinement of NiO samples.

Parameters/Sample	**5nm NiO**	**40 nm NiO**	**>100nm NiO**
$\mathbf{R_{wp}}$	5.81	4.26	8.72
$\mathbf{R_{p}}$	4.50	3.25	6.37
Cell Parameter "a" (nm)*	0.41854 (2)	0.41789 (4)	0.41676 (4)
Crystalline Size (nm)*	8.8 (2)	72 (8)	442 (7)
Lattice Strain (nm/nm)*	0.47 (2)	0.054 (4)	0.034 (5)

*Values between brackets are estimated by Scherrer equation

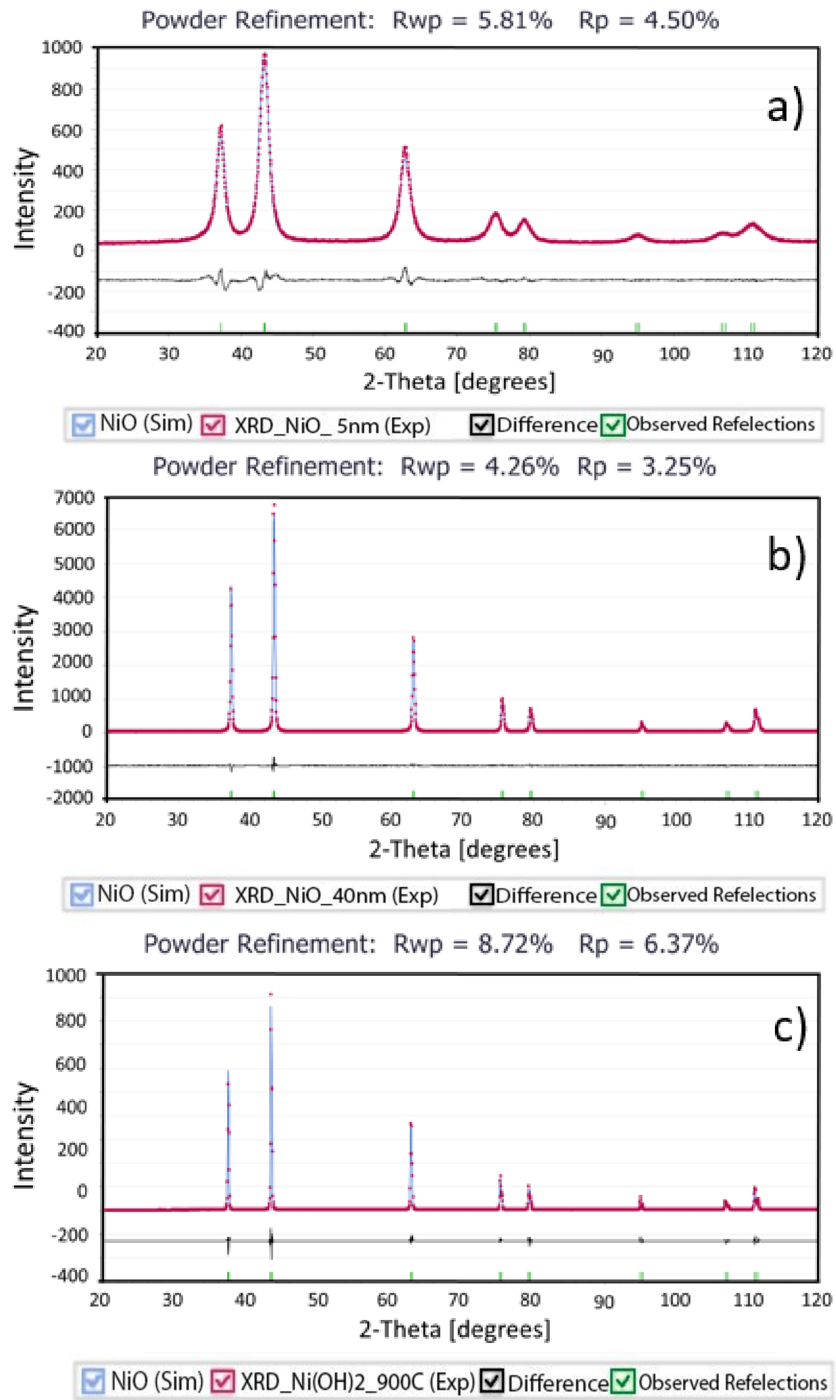

Figure 3.5. XRD analysis of the prepared NiO samples: Reflex Plus Rietveld refinement for the NiO with crystalline domain sizes of a) 5nm, b) 40 nm, and c) >100 nm, respectively.

The FTIR spectra of the three NiO samples are presented in **Figure 3.6a**. As observed, the sample having average crystalline domain sizes of 5 nm has a broad –OH stretching vibration band (3200 – 3700 cm^{-1}), indicating that the surface of these nanoparticles is covered with a high density of hydroxyl groups as would be expected for NiO nanoparticles. For this reason, it is possible to see the bending vibrations modes expanded from 1200 to 1600 cm^{-1}. Also, the vibration modes of the Ni-O can be seen as a broad band from 400 to around 600 cm^{-1}. The higher thermal treatment applied to produce the samples of 40nm and >100nm decreases significantly the intensities of the signals for the stretching and bending of the –OH groups; however, they do not disappear even at the temperature of 900 °C, which means that the produced solids have –OH defects.

To get some information on the vibration modes of the unit cell of NiO, the infrared spectrum was determined using $DMol^3$ and the spectra are shown in **Figure 3.6b**. According to the calculations, three signals are expected to be observed at 267, 398 and 465 cm^{-1} in the spectrum of NiO. The experimental spectra show very broad signals; and thus, artificial broadening of the expected signals was carried out with FWHM of 5, 100, 200 and 300 cm^{-1} as shown together in **Figure 3.6b**. Due to the experimental data was obtained with wavenumbers between 400 and 4000 cm^{-1}, the calculated spectra shown in **Figure 3.6c** are starting from the value of 400 cm^{-1}, and also to compare it with the experimental data as shown in **Figure 3.6d.** In this Figure, the calculated spectrum with FWHM of 300 cm^{-1} was compared with the experimental ones, indicating that there is an important broadening of the signals in the real spectra; also, the calculated one is very close to the experimental NiO 5nm spectrum. The vibration modes of the atoms in the unit cell of NiO are shown in **Figure 3.6e**, and to obtain finer details of the process, a video of the evolution of the system is included in the Supporting Information. The calculated vibrations do not include the hydroxyl region as the calculations were carried out with the NiO unit cell that does not contain hydroxyl groups, as no surface is exposed.

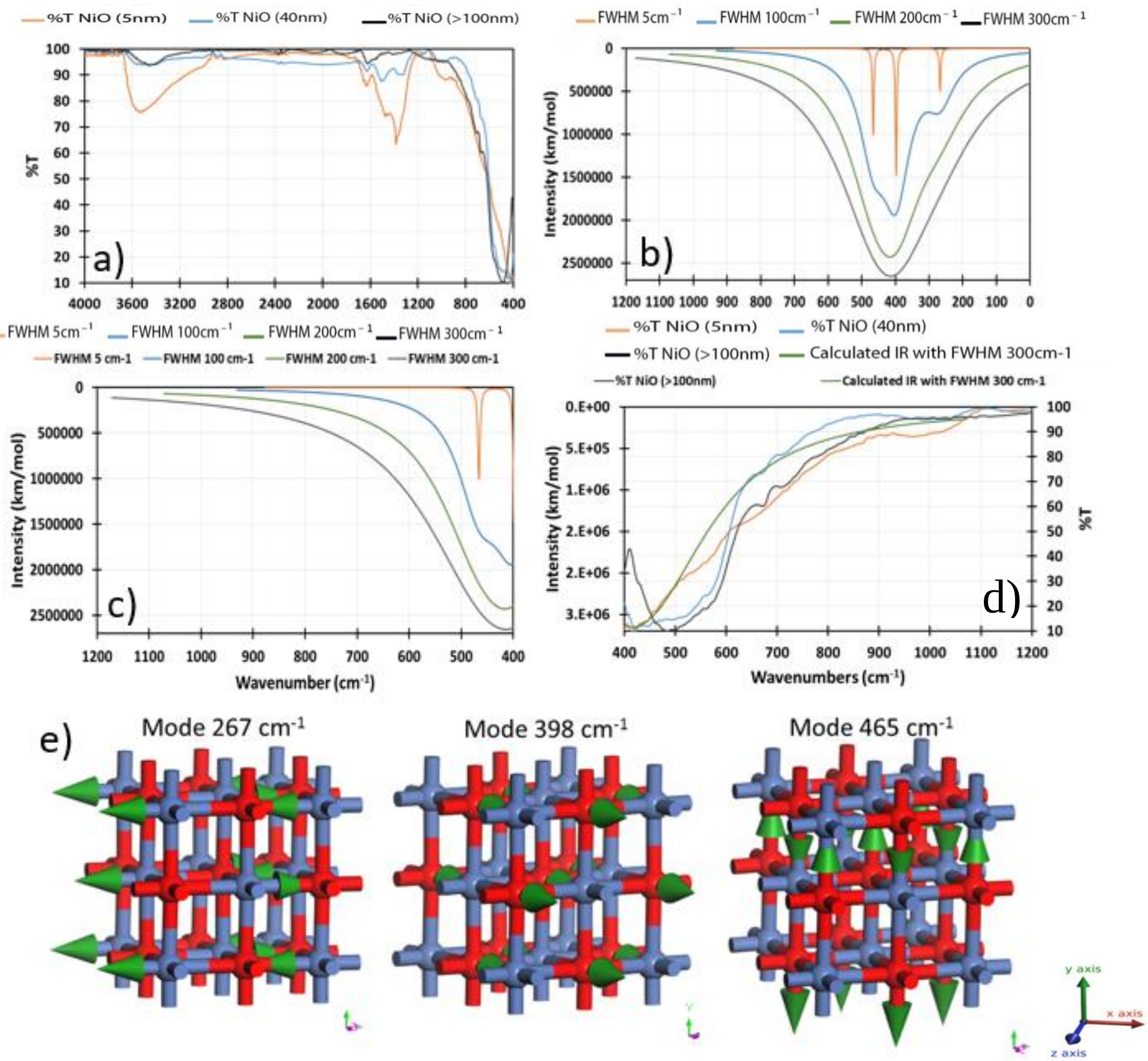

Figure 3.6. Infrared spectra of NiO: a) Experimental Infrared spectra of NiO with different crystalline domain sizes; b) DMol^3 calculated full infrared spectra for NiO with different FWHM; c) DMol^3 calculated infrared spectra in the region 400 – 1200 cm^{-1} for NiO with different FWHM; d) Overlapping of the experimental and calculated infrared spectra in the region 400 – 1200 cm^{-1} and e) Calculated vibration modes of the unit cell of NiO (green arrows indicate the direction of movement).

XPS was also performed to complement the results obtained by XRD and FTIR, gaining further insights on the prepared nanomaterials. In this study, XPS spectra for the prepared NiO nanoparticles and treated at three temperatures are presented in **Figure 3.7**. The fitting of the Ni*2p*$_{3/2}$ regions shown on **Figures 3.7a-c** was done following the procedure presented elsewhere (Biesinger, Payne, Lau, Gerson, & Smart, 2009). The spectra shown on **Figure 3.7a** corresponds to the fitting executed to the spectrum of NiO nanoparticles with average crystalline domain size of 5 nm and **Figure 3.7b** and **Figure 3.7c** to the materials with 40 and >100 nm, respectively. Five signals were used to fit the spectrum and the obtained binding energy values are presented in **Table 3.2**. The obtained binding energies for the three produced nanocrystalline NiO are in agreement with values found in the literature for NiO (Biesinger et al., 2009).

Table 3.2. Binding energies for the signals of the Ni*2p*$_{3/2}$ region of the tested materials.

Sample	**Binding Energy of Signals of Ni*2p*$_{3/2}$ (eV)**				
	#1	**#2**	**#3**	**#4**	**#5**
5nm NiO	853.2	854.8	860.2	863.5	866.0
40nm NiO	853.9	855.6	861.0	864.1	866.5
>100 nm NiO	853.1	854.9	860.3	863.6	865.8

Figures 3.7d-f corresponds to the XPS O*1s* region of the tested materials, 5, 40 and >100 nm, respectively, and in **Table 3.3** are presented the obtained binding energies and the respective quantification of species. It is worth noting that on the spectrum on **Figure 3.7d**, there are 2 oxygen signals, the first one close to 529 eV, which is attributed to lattice oxygen in the NiO; the other signal is around 531 eV and it is attributed to defects in the structure, which leads to a high density of surface hydroxyl groups, which is in line with what is reported in the literature (Payne, Biesinger, & McIntyre, 2012). These results are easily correlated with the intense and broad infrared –OH stretching band displayed in the infrared spectrum on **Figure 3.6a.** As seen in **Table**

3.3, the area of this signal corresponds to 29 % of the total, suggesting the considerable amount of oxygen-type defects for the 5 nm NiO nanoparticles. The O*1s* signals for the other two prepared NiO materials also have two bands one near 531 eV and the other one close to 529 eV. However, in comparison with the 5 nm NiO material, the defect oxygen region (531 eV signal) is less intense and have a lower percentage of contribution. This indicates that the higher thermal treatment decreased the amount of oxygen defects in the structure by inducing dehydroxylation. Nevertheless, even at the treatment carried out at 1073 K, there are still oxygen defects in the structure. Part of these defects can be ascribed to hydroxyl groups as seen in the infrared spectrum of the sample (**Figure 3.6a**).

Table 3.3. Binding energies for the signals of the O*1s* region of the tested materials.

Sample	**O^{2-}**		**O defects**	
	BE (eV)	**Area (%)**	**BE (eV)**	**Area (%)**
5nm NiO	528.8	70.9	530.8	29.1
40nm NiO	529.6	84.9	531.6	15.1
>100nm NiO	528.8	82.7	530.9	17.3

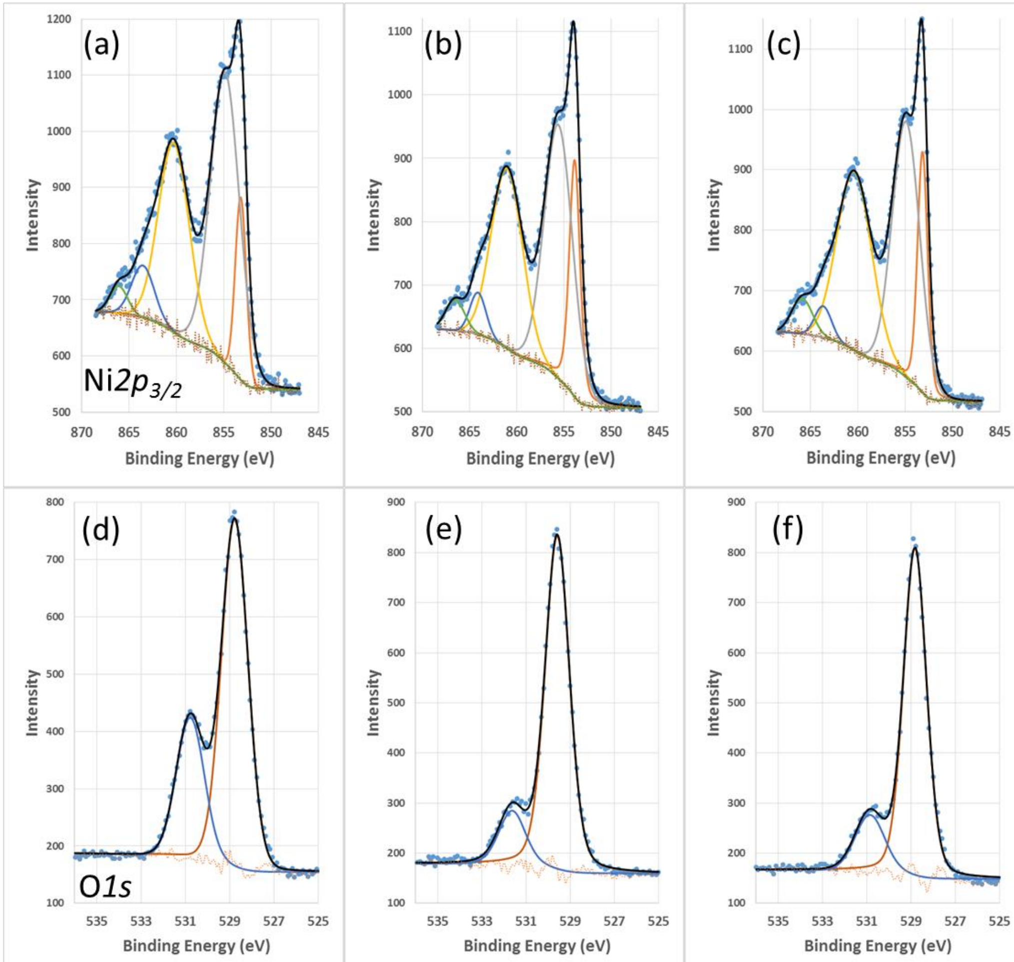

Figure 3.7. XPS spectra for the Ni2p3/2 and O1s regions for: a) and d) 5nm NiO; b) and e) 40nm NiO; and c) and f) >100nm NiO.

Figure 3.8 displays the N_2 adsorption and desorption isotherms for the 5nm NiO and 40nm NiO samples, and in the insets the pore distribution according to BJH can be observed. In accordance with the IUPAC classifications (Thommes et al., 2015), the Type IV(a) isotherm is the most descriptive for both NiO nanomaterials. For both nanomaterials, it is possible to see that the adsorption isotherms at $P/P_o = 0$ do not start from zero but from a slightly higher value of the quantity of adsorbed N_2 (mmol/g), indicating the presence of microporosity in the prepared nanomaterials. Moreover, there is a hysteresis loop that resembles the Type H3 hysteresis loop as indicated by the IUPAC classifications, suggesting the presence of mesopores wider than 4 nm for the 5nm NiO material (Thommes et al., 2015). On the other hand, NiO is a non-porous crystalline material, therefore, the existence of microporosity and mesoporosity in the prepared materials can be attributed to the production of interparticle porosity, due to the aggregation of the particles, generating interparticle cavities of micro and mesoporous dimensions which result in capillary condensation of the N_2 adsorbate. The obtained values of textural properties for the materials are shown in **Table 3.4**. It can be observed in that table, the contribution of the microporosity to the total surface area is important: 34% for the 5nm NiO and 39% for the 40nm NiO. Thereby, it is important to understand the dimensions of the micropores present in the samples as they should not contribute in the adsorption of Q-65 and V-79, since these molecules are large in size.

Table 3.4. Summary of the textural properties for the prepared NiO materials.

Sample	**BET surface area (m^2/g)**	***t-Plot* Micro area (m^2/g)**	***t-Plot* External area (m^2/g)**	**BJH desorption volume (cm^3/g)**	**BJH average desorption pore size (Å)**
NiO (5nm)	153	52	101	0.3271	85
NiO (40nm)	10.1	3.9	6.2	0.0847	466

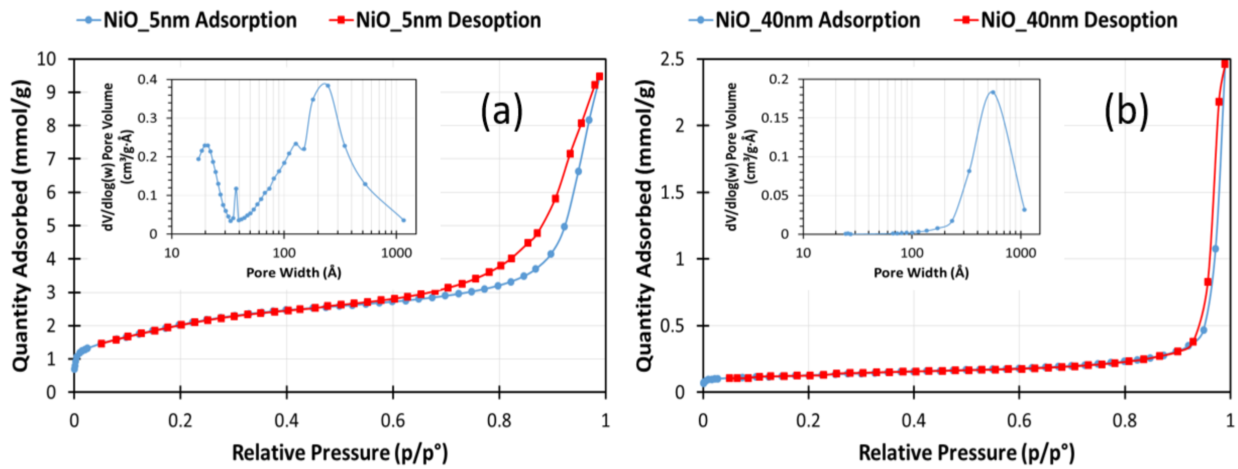

Figure 3.8. N_2 adsorption and desorption isotherms with insets of the pore distributions by BJH: a) 5nm NiO and b) 40nm NiO.

Panel a of **Figure 3.9** displays the pore size distribution obtained with the SAIEUS program for the NiO 5nm material and **Figure 3.9b** shows the NLDFT N2-77 cylindrical model fitting to the experimental N_2-adsorption isotherm obtained for the NiO 5nm material. In **Figure 3.9a** it is possible to notice two main pore sizes in the NiO 5nm material, one around 7 Å and the other one around 26 Å. The latter one is similar to that obtained by the BJH model (**Figure 3.8a**); however, by using the NLDFT cylindrical model it was possible to estimate the size of the micropores present in the NiO 5nm material which are too small (7 Å) to participate in the adsorption of Q-65 and V-79. Thus, that area does not contribute for the adsorption of those bulky molecules.

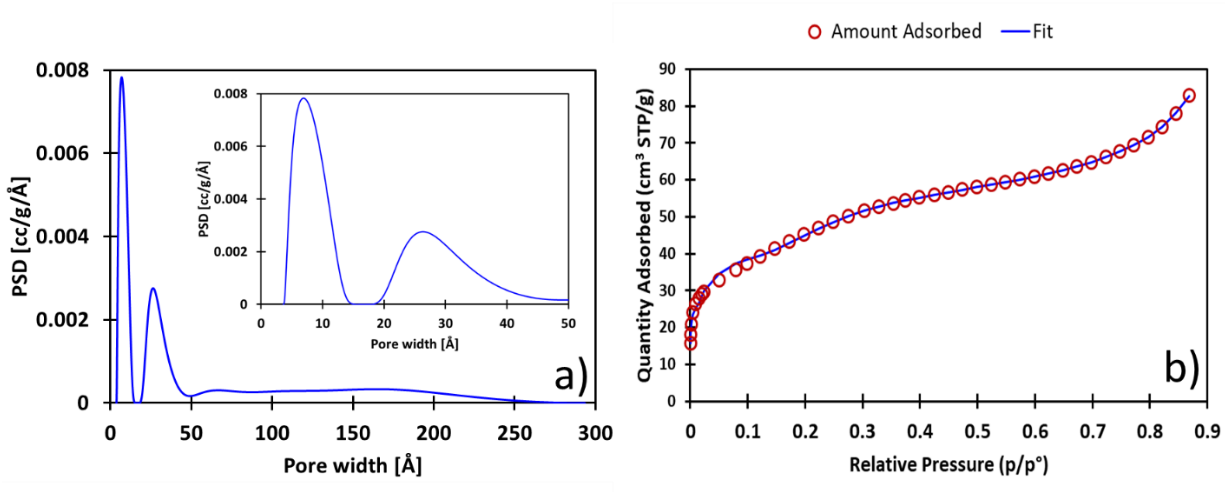

Figure 3.9. a) Pore size distributions of the NiO 5nm obtained by fitting the experimental N_2-Adsorption data to the NLDFT N2-77 Cylindrical model using the SAIEUS program; b) Experimental N_2 adsorbed quantity as a function of the relative pressure together with its fit to the NLDFT N2-77 Cylindrical model.

Particle size can be estimated assuming spherical particles, this can be achieved employing the measured t-plot external surface area as per Eq 3.7:

$$d = \frac{6000}{SA\ \rho_{NiO}} \tag{3.7}$$

where d is the particle size in nm, SA is specific surface area (obtained experimentally) (m^2/g), and ρ_{NiO} is the NiO framework density (6.67 g/cm^3). The calculated values were 8.9 and 145 nm for the 5nm NiO and 40 nm NiO samples, respectively. For the case of the 5nm NiO sample, the obtained value corresponds very good with the crystalline domain sizes attained with the Reflex Rietveld refinement (8.8 nm) indicating the importance of taking into account the lattice strain that affects the broadening of the X-ray diffractions signals, which are not produced just by the nanoparticles size; and thus, the use of the Scherrer equation alone will produce a smaller size of the crystalline domain size than the actual value. For the 40 nm NiO sample, the calculated value is higher than the value obtained by XRD, due to the aggregation of the nanoparticles caused by the higher temperature treatment, then, the assumption of spherical particles is not accurate.

2.12.1. Computational Modeling

Figure 3.10 depicts the results achieved for the adsorption of one Q-65, one V-79 and one toluene molecule on the NiO surface (100) in vacuum. **Figure 3.10a** illustrates in black color the field of adsorption sites with higher density areas (El-Qanni, 2017), pointing the most likely type of places for the Q-65 adsorption on this surface. As it can be seen, the larger areas for adsorption sites fall between nickel and oxygen atoms on the surface (El-Qanni, 2017). The other lower adsorption sites fall over nickel and oxygen atoms but are shifted towards the oxygen and nickel nearest neighbor, respectively. The lowest adsorption energy configuration for the Q-65 molecule is shown in **Figures 3.10b, c**, top and side views, respectively, where the adsorbed molecule tends to be positioned flat on the surface of the NiO material. The resulted adsorption energy in vacuum was -78.1 kcal/mol (-326.8 kJ/mol). **Figure 3.10d** shows the field of adsorption sites with higher density areas, in black color, suggesting the most probable type of locations for the V-79 adsorption on this surface (El-Qanni, 2017). For this case, the nickel atoms are the most likely binding sites for the V-79 molecule. The top and side views of the V-79 adsorbed on the (100) surface of NiO are shown in **Figures 3.10e and 3.10f**, respectively, where a flat configuration of the V-79 molecule is also observed in this case. The acquired adsorption energy in vacuum was -105.7 kcal/mol (442.2 kJ/mol), indicating that V-79 is the molecule having the strongest adsorption interaction with the NiO (100) surface, at least in vacuum, when compared with Q-65, because of the more negative value of the adsorption energy. This result may indicate that NiO may preferentially adsorb V-79 than Q-65 in a mixture as indeed the experiments indicated.

Finally, **Figure 3.10g** shows the preferential binding sites (in black color) for the toluene molecule and **Figure 3.10h and 3.10i** show the top and side view of the adsorbed toluene molecule on the surface. Here, the achieved adsorption energy in vacuum was -66.4 kcal/mol (-227.8 kJ/mol), indicating that toluene can binds on this surface in vacuum, but weakly as compared with Q-65 and V-79 molecules. Thus, to get a more realistic insight about the behavior of these molecules together, a molecular dynamics simulation was performed with 200 toluene molecules as solvent, 5 V-79 and 5 Q-65 molecules as solutes on top of the (100) surface of NiO. **Figure 3.11** display the total energy of the system versus the simulation time with insets of the close-up evolution of the system at the chosen simulation times (El-Qanni, 2017).

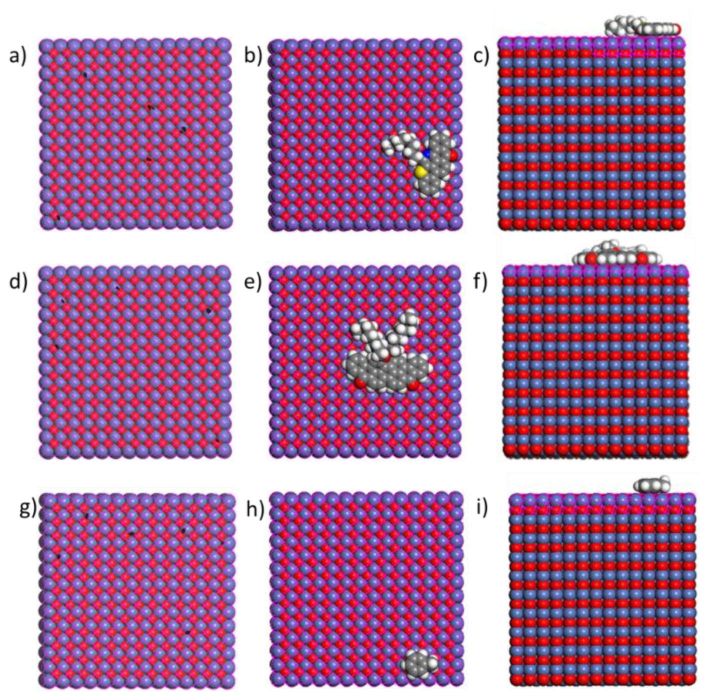

Figure 3.10. Adsorption of Q-65, V-79 and toluene molecules on the (100) surface of NiO indicating: a), d) and g) the field of adsorption sites with higher density areas, in black color, for Q-65, V-79 and toluene, respectively; b), e) and h) top view of the adsorbed Q-65, V-79 and toluene, respectively; and c), f), and i) side view of the adsorbed Q-65, V-79 and toluene, respectively.

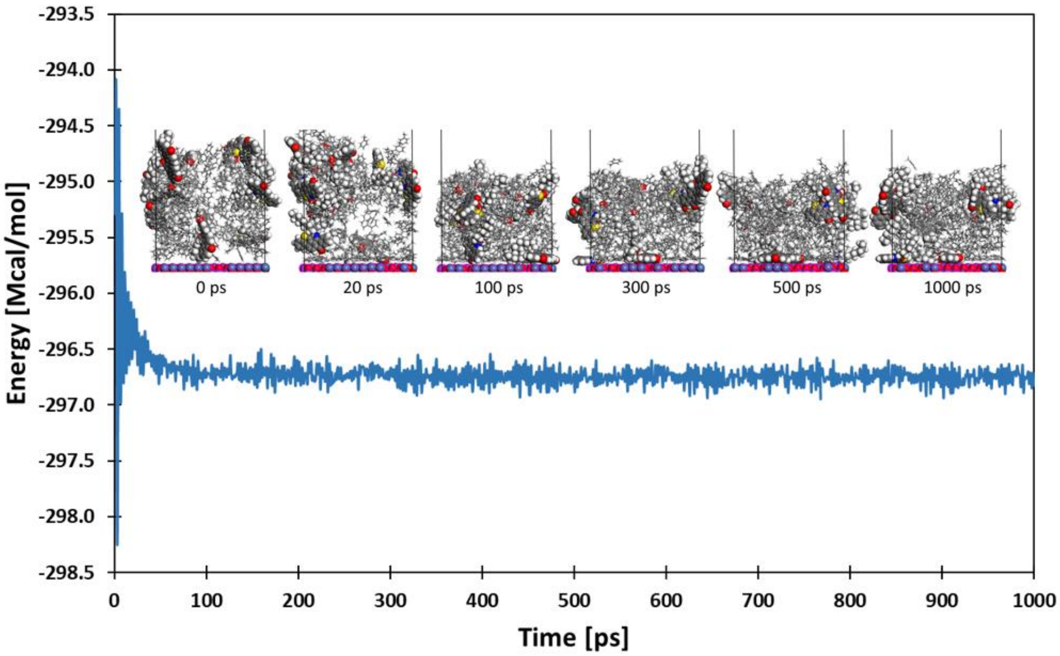

Figure 3.11. Total energy of the system NiO(100) + 200 Toluene + 5 Q-65 + 5 V-79 versus the simulation time with insets of the close-up evolution of the system at chosen simulation times. Yellow atoms depict sulfur; red atoms depict oxygen; grey atoms depict carbon; white atoms depict hydrogen; bright blue atoms depict nitrogen and pale blue atoms depict nickel.

The studied system containing the NiO (100) surface together with 200 toluene molecules, 5 Q-65 molecules and 5 V-79 molecules started with a total energy of -294.2 Mcal/mol; after a few ps one of the V-79 molecules gets very close to the surface while the other V-79, Q-65 and toluene molecules begin to interact among them. After 20 ps the V-79 molecule close to the surface gets adsorbed on the surface in a flat configuration with the alkyl chains aiming to the medium above containing the other organic molecules. Around 100 ps a Q-65 molecule begins to interact with the surface by the oxygen in its structure, but it keeps moving around while the V-79 molecule is firmly adsorbed on the surface. Some toluene molecules share the surface with the V-79 in a flat configuration during the simulation time. Around 300 ps one Q-65 molecule begins to get adsorbed in a flat configuration on the surface, but it is very mobile compare with the adsorbed V-79 that tends to be located very close to the original adsorption site. During the remaining time of the simulation the adsorbed V-79 is less mobile and almost fixed on the adsorption sites while the adsorbed Q-65 together with the adsorbed toluene molecules keep moving around. The total energy of the system keeps an almost constant value of -296.8 Mcal/mol from100 ps up to the end of the simulation time. This seems to indicate that V-79 is the preferred molecule to be strongly adsorbed when compared with the Q-65 even in the presence of toluene molecules as the experimental data corroborated. However, the molecular dynamics calculations seem to also indicate that Q-65 has opportunities to be adsorbed and is not completely replaced by V-79 even though when there are other V-79 molecules in the medium, as it is also going to be shown experimentally. The simulation also indicated that the remaining V-79 and Q-65 tended to interact among themselves in the solution of toluene and that may give the Q-65 some opportunity to be adsorbed on the nanoparticle as the other V-79 molecules are interacting with themselves rather than with the surface.

3.5.2. Adsorption Isotherms

3.5.2.1. Individual Adsorption

The individual adsorption isotherms of Q-65 and V-79 onto 5 nm NiO and 40 nm NiO nanoparticles are shown on **Figure 3.12**. As seen, the adsorption isotherm obeys a Langmuir-like behavior. Applying the Eq 3.2, the equilibrium binding constant, K_L, and the maximum adsorption capacity, Q_{max}, are obtained and listed in **Table 3.5**. It can be observed in **Figure 3.12**, the adsorbed molar density of the adsorbents increases sharply at lower equilibrium concentrations followed by leveling off at relatively higher concentrations. Considering the absolute average relative error, represented by χ^2, the Langmuir adsorption model better reproduced the experimental data for both, Q-65 and V-79 adsorption. It can be interpreted from the good fit of the Langmuir isotherm, that the surface sites of each type of nanoparticles are homogeneous with almost the same adsorption energies. As compared to the 5 nm NiO, the 40 nm NiO exhibits higher adsorption uptakes of both V-79 and Q-65 when expressed per external and BET surface area. It can be noted that the Q_{max} parameter is higher when is per external surface area than when using BET area, this suggests that the microporosity, that is included in the BET area, is not contributing to the adsorption of the model molecules, as should be expected because of the size of the used organic molecules. Therefore, the external surface area was selected here for modeling the adsorption isotherms. In addition, V-79 shows higher and much stronger interactions, represented by the K_L values, with the surface sites of both nanosizes of NiO when compared to Q-65, in agreement with that predicted from the computational modeling discussed previously. This could be attributed to the higher number of peripheral chains of V-79 rather than the Q-65 molecules (**Figure 3.1**). As proposed by Shi et al. (Shi et al., 2010), these alkyl side chains may interact between V-79 molecules rather than with the surface of NiO nanoparticles, producing H-type aggregates arrangements through intermolecular π-π interactions. These nanoaggregates are prone to turn out in small cylinders in toluene, composed by 11 polycyclic aromatic hydrocarbons (PAHs) monomers (Cyran & Krummel, 2015). Also, it has been reported that the H-type aggregates are positioned in a “face to face” stacked structure, promoting more uptake (Liu, Shen, Cao, & Li, 2014; Nedal Nael Marei, 2016). This is in agreement with the findings obtained by the computational modeling as well.

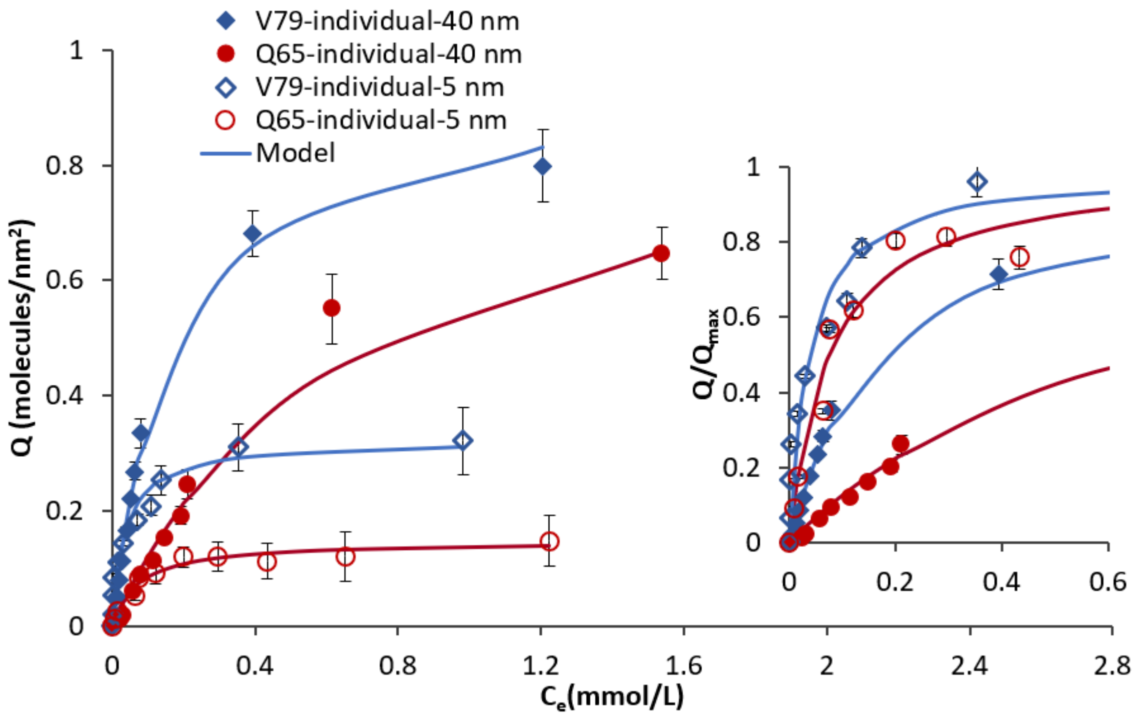

Figure 3.12. Adsorption isotherms of V-79 and Q-65 from individual solutions onto the 5nm NiO and 40 nm NiO nanoparticles with inset graph Ce (mmol/L) vs Q/Qmax. Experimental conditions are nanoparticle dose, 10 g/L; Temperature, 298 K; Experiment time = 24 h.

The Gibbs free energy change of the adsorption of V-79 and Q-65 over both types of the NiO nanoparticles is reported on **Table 3.5**. For additional details on the calculations of $\Delta G°_{ads}$, refer to our previous work (Hosseinpour et al., 2013). The adsorption onto the 40 nm NiO is related with a more negative change in Gibbs free energy. This may be attributed to the stronger interactions of V-79 and Q-65 with the 40 nm NiO nanoparticles surface sites when compared to those with the surface of 5nm NiO. The density of hydroxyl groups on the surface of 5 nm NiO is higher than that on the 40 nm NiO surface, as shown in the FTIR spectra on **Figure 3.6a** and correlated with the O*1s* XPS spectra on **Figure 3.7d, e**. This is an important characteristic that determine the interactions between V-79 and Q-65 molecules and NiO surface. The higher presence of -OH on the nanoparticle surface, the larger the bending and stretching vibrations, which may contributes to the little adsorption of V-79 and Q-65 as the case of 5 nm NiO nanoparticles, since the density of hydroxyl groups changes the interactions of the nanoparticles with the molecules, forcing less V-79 and Q-65 to be -molecules such as V-79 and Q-65 with flat configurations. It is worth nothing that if the model molecules were much smaller, the trend may vary due to the presence of microporosity.

Table 3.5. Langmuir model parameters and Gibbs free energy changes for individual adsorption of V-79 and Q-65 onto the 5 and 40 nm NiO nanoparticles.

Material	**Q_{max} (Molecules/nm^2) (Using external area)**	**Q_{max} (Molecules/nm^2) (Using BET area)**	**K_L ((L/mmol) or (mM)$^{-1}$)**	**χ^2**	**ΔG°_{ads} (Mcal/mol)**
V-79-individual-40nm	0.951	0.566	5.721	1.4×10^{-2}	-6.45×10^{-3}
Q-65-individual-40nm	0.943	0.604	1.439	6.2×10^{-2}	-5.63×10^{-3}
V-79-individual-5nm	0.323	0.213	26.384	4.6×10^{-1}	-7.35×10^{-3}
Q-65-individual-5nm	0.148	0.098	13.360	9.9×10^{-3}	-6.95×10^{-3}

Furthermore, the results obtained by the computational modeling indicated that V-79 is the molecule having the most intense adsorption interaction with the surface, at least in vacuum, when compared with Q-65 and in the presence of toluene and Q-65 molecules, as shown by the Molecular Dynamics simulation. In addition, the results of the experimentally obtained adsorption isotherms supported the characteristic studies and agreed that 40 nm NiO nanoparticles have the more adsorption capacity (molecule per nm^2), for both V-79 and Q-65, than the 5 nm size particles. HRTEM was performed to have more information regarding the morphology and sizes of the synthesized NiO nanoparticles, as reported in our previous work (Nedal N Marei et al., 2016). The

HRTEM images revealed that the 5 nm NiO morphology is flat/rod-like. However, the selected XRD of these samples indicated that they formed by very small crystallites. For the 40 nm size nanoparticles, they appear to be composed of spherical/cylindrical shape particles self-associated with more curvature.

The previous computational modeling was employed to understand the interaction between Q-65/V-79 and NiO nanoparticles assuming of spherical or tablet-like shape nanoparticles (Nedal Nael Marei, 2016). The results indicated that, altering the nanosize between 5 and 40 nm, NiO nanoparticles experiment drastic modifications in surface properties, topology, morphology, and textural properties, which as a result affect their surface site strength and thus, adsorption behavior. The computational results showed that many of the molecules have tendency to be adsorbed in a vertical tilted form onto sphere-like NiO (similar to 5 nm NiO). This configuration suggests that more Q-65/V-79 molecules can be adsorbed on the surface than would be determined by the flat configurations of the Q-65 molecule adsorption. In the case of 40 nm NiO (more flat shape), almost a flat configuration of the Q-65 molecule with the alkyl chains aiming upwards by the interaction of the aromatic rings with the NiO surface is expected (Nedal Nael Marei, 2016). These results confirmed the impact of the nanoparticles topology and morphology on their adsorption capacity of organic-like molecules.

Shifts in the adsorption performance of different-sized NiO nanoparticles are expected, as different forms and topologies are present in the materials, leading to different configurations for adsorbed Q-65 and V-79 molecules on the surface. The smaller the nanoparticles, the more –OH present on their surfaces, resulting in bigger bending vibration, as observed for the 5 nm-sized NiO nanoparticles in our previous work (Nedal Nael Marei, 2016; Nedal N Marei et al., 2016). The FTIR and TGA results showed that the –OH stretching vibration is higher in the 5nm NiO nanoparticle. This elevated –OH density for the 5 nm nanomaterial should impact their surface interactions with the Q-65/V-79 molecules. This feature (–OH density) of the surface leads to the ease of charge transfer, resulting in the presence of weaker sites on the surface. In addition, this may also be promoting the lower adsorption of the Q-65/V-79 molecules on the surface of the 5 nm NiO. Broaden flat surfaces appear to have the needed adsorption sites to better arrange large molecules on their sites. Therefore, bigger nanoparticles with extended flat surfaces can yield higher uptakes. Nevertheless, if the molecules are very small the trend can differ, and thus, it is very important to consider not only the prepared nanoparticles physical characteristics, but also the chosen molecules functional groups and spatial configurations when discussing adsorption data (Nedal Nael Marei, 2016).

3.5.2.2. Simultaneous Competitive Adsorption

In this section, we illustrate the simultaneous competitive adsorption (**Figure 3.2b**) between equimolar V-79 and Q-65 molecules and their interactions with the surface sites of the prepared NiO nanoparticles. The obtained macroscopic adsorption isotherms are shown on **Figure 3.13**; both the equilibrium binding constant, K_L, and the maximum adsorption capacity, Q_{max}, values are different from those obtained by individual adsorption due to competitive uptake. Comparing with the isotherms obtained from the analysis of individual adsorption on the same sizes of NiO nanoparticles (shown in **Figure 3.13**) indicates that V-79 impacts the uptake of Q-65 on NiO nanoparticles under conditions of simultaneous competitive adsorption.

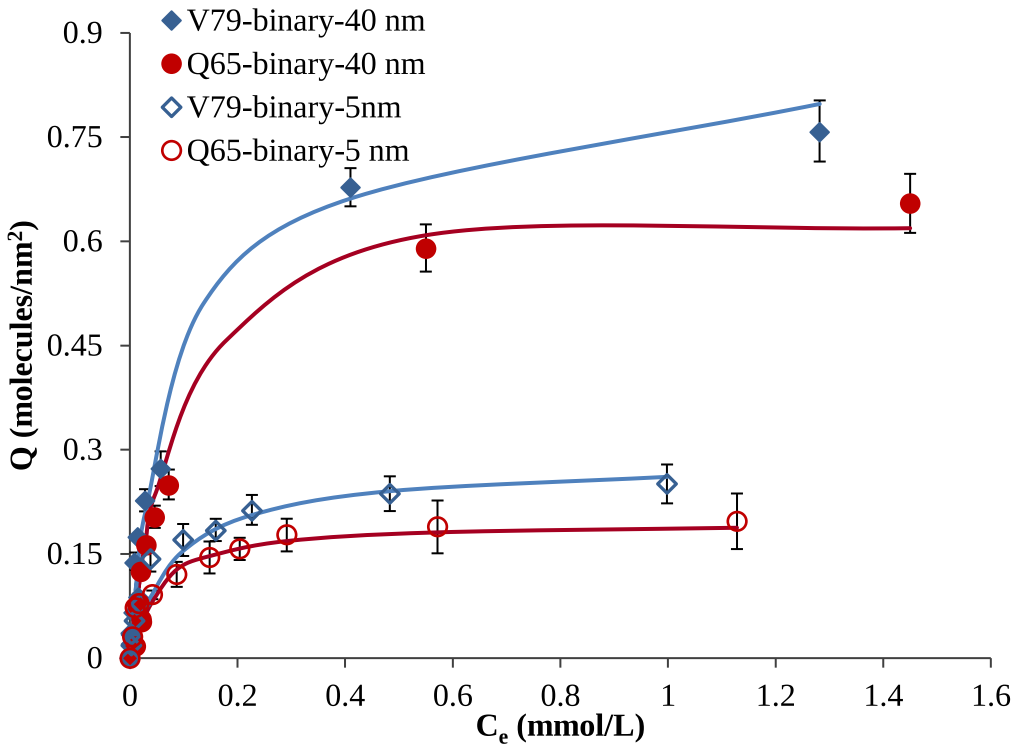

Figure 3.13. Competitive adsorption isotherms of V-79 and Q-65 from the binary solutions onto the 5nm NiO and 40 nm NiO nanoparticles. Nanoparticle dose, 10 g/L; Temperature, 298 K; experiment time = 24 h.

The adsorbed molar density of V-79 is higher than that of Q-65 over both 5 nm NiO and 40 nm NiO nanoparticles, similar to what observed in the individual adsorption. This may be related to the strong interactions of V-79 with the surface sites of the nanoparticles, which is in line with the computational modeling results. In addition, on normalized surface area basis, the adsorption uptake of both V-79 and Q-65, over the 5 nm NiO is lower than that on 40 nm NiO. This may be associated with the lower density of strong adsorption sites over the surface of 5 nm NiO compared to the 40 nm NiO nanoparticles or the lack of a larger surface space. The presence of the other component creates a competition for the adsorption sites on the surface and some sites are filled by the other component, mainly at relatively high concentrations. Furthermore, the adsorbed density leveled off at high concentrations of the adsorbates, indicating monolayer coverage of the surface sites of the nanoparticles.

Table 3.6. Estimated parameters of the extended Langmuir model for the adsorption from the binary solutions.

Material	**$Q_{max\ Q\text{-}65}$ (Molecules/nm^2)**	**$Q_{max\ V\text{-}79}$ (Molecules/nm^2)**	**$K_{V\text{-}79}$ (L/mmol)**	**$K_{Q\text{-}65}$ (L/mmol)**	**$\alpha_{V\text{-}79,\ Q\text{-}65}$**	**χ^2**
40 nm	1.446	1.556	6.736	4.971	1.458	0.231
5 nm	0.382	0.580	7.693	7.433	1.571	0.165

The adsorption data from the binary solutions were described by the extended Langmuir isotherms model, and the results are listed in **Table 3.6**. The adsorption uptake of both V-79 and Q-65 over the nanoparticles in the binary solutions decreases when compared to that in the individual solutions. The decrease in the adsorption uptake is higher for Q-65. In addition, the selectivity (α_{ij}) of the surface sites to V-79 is higher than that to Q-65. It is inferred that not only the strength of the adsorption interactions, but also the orientation of the adsorbing molecules are the deciding factors when dealing with competitive adsorption of V-79 and Q-65. Therefore, V-79 molecules could replace Q-65 and the Q-65 could be the predecessor of V-79.

3.5.2.3. Displacement Competitive Adsorption

For further investigation on the competitive adsorption of V-79 and Q-65 for the surface sites of the nanoparticles, in this section V-79 was selected to act as a prospect displacing agent for Q-65 conjugated NiO nanoparticle (**Figure 3.2c**). Here, the solid precipitates that contains previously adsorbed Q-65 obtained from the individual adsorption experiments were exposed to fresh solutions containing only V-79 in toluene at different initial concentrations. The initial concentrations of the fresh individual V-79 solutions were the same as that of the individual solutions from which the solid precipitates have already been obtained.

For the sake of clarity, the solid precipitate obtained from an individual adsorption test with the initial concentration of 0.05 mmol/L of Q-65 is added to 5 mL of 0.05 mmol/L of V-79. Therefore, the newly added adsorbent needs to be adsorbed on either the vacant surface sites or the sites already occupied by the other adsorbent. **Figure 3.14** illustrates the adsorption isotherms of the newly adsorbent onto the dried Q-65/NiO and the desorption of Q-65 from both materials. The adsorption of V-79 takes place even at low concentration of V-79 on the material 5nm NiO, this indicates that the adsorption over the surface of Q-65-containing 5 nm NiO is associated with higher changes in Gibbs free energy and thus, easier than the 40 nm NiO surface. Furthermore, as expected, the adsorption uptake of 5 nm NiO is lower than the 40 nm NiO nanoparticles. On the other hand, it can be observed some desorption of Q-65, being higher on the 40 nm NiO nanoparticles, this could indicate that V-79 is displacing some Q-65 molecules and occupying their sites plus other active sites present in the nanomaterials. This could be the reason that the uptake of V-79 is higher than the desorption of Q-65.

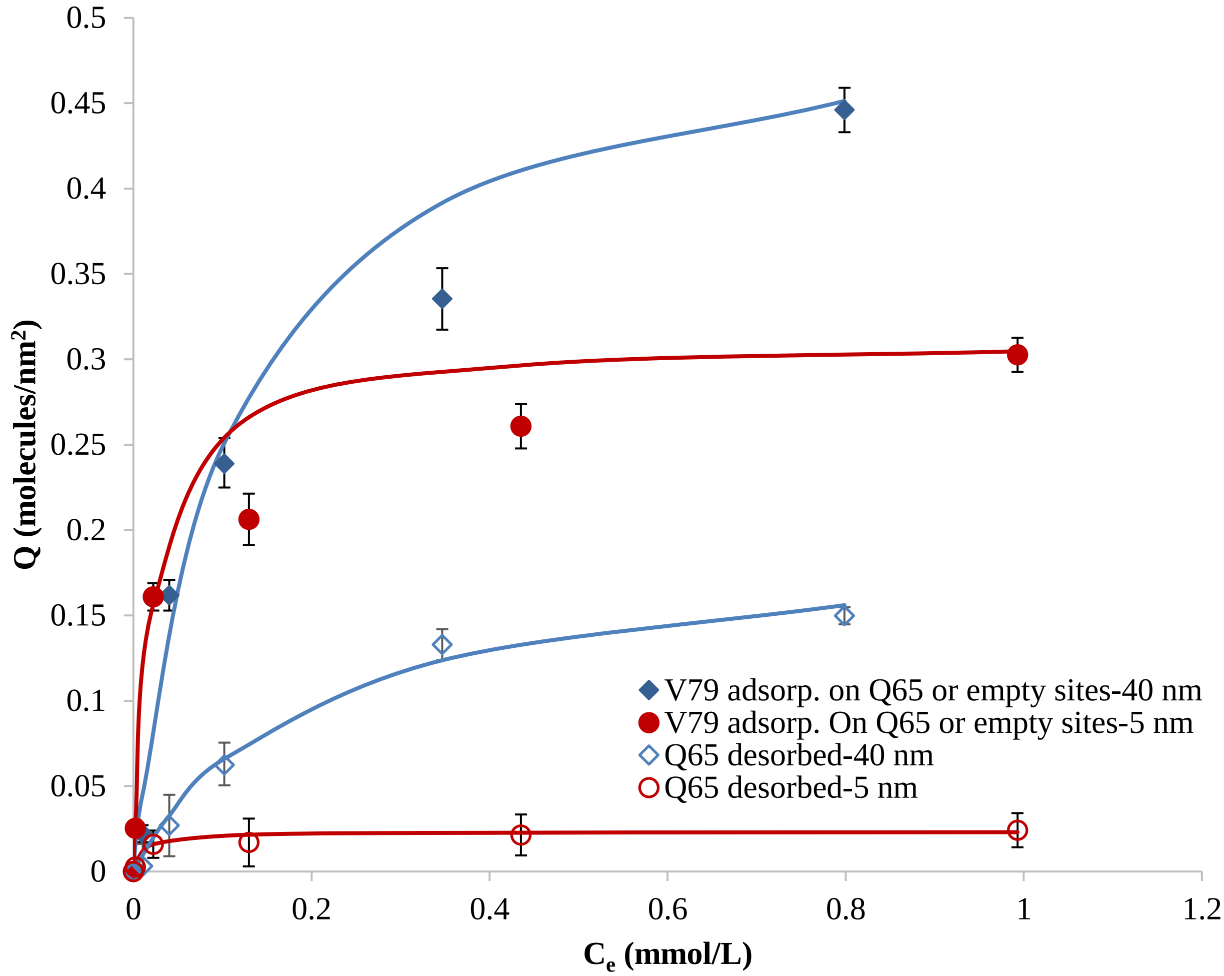

Figure 3.14. Displacement competitive adsorption isotherms of V-79 and desorption of Q-65 onto the 5nm NiO and 40 nm NiO nanoparticles. Nanoparticle dose, 10 g/L; Temperature, 298 K; experiment time = 24 h.

All the adsorption/desorption isotherms followed the Langmuir model (Eq. 3.2) since the adsorption is leveled off at high concentration of the adsorbate. The model parameters are reported in **Table 3.7**. The maximum adsorbed molar density of V-79 over both types of the nanoparticles is higher than Q-65. In addition, based on the values of the Langmuir parameter, K_L, one could observe that the adsorption of V-79 onto the Q-65-containing 5 nm NiO is associated with a high decrease in Gibbs free energy. In general, the adsorption of V-79 could be easily adsorbed over the surface sites of the nanoparticles that was already saturated with Q-65, supporting the statement that the NiO nanoparticles have more preference for V-79 than Q-65. This may be related to the stronger interactions of V-79 with the nanoparticle surface sites when compared to Q-65.

Table 3.7. Estimated Langmuir model parameters for adsorption of V-79 onto NiO with previously adsorbed Q-65 molecules and desorption of Q-65.

Material	**Q_{max} (Molecules/nm^2)**	**K_L(L/mmol)**	**χ^2**
V-79 Adsorption on Q-65-40 nm	0.511	9.443	8.73×10^{-3}
V-79 Adsorption on Q-65 -5nm	0.312	45.115	1.77×10^{-2}
Q-65 Desorption-40 nm	0.195	5.004	6.35×10^{-3}
Q-65 Desorption-5nm	0.023	97.819	1.69×10^{-3}

3.6. Conclusions

This study used Q-65 and V-79 as model molecules for asphaltenes and resins to analyze the nanosize effects of NiO nanoparticles on their competitive adsorption. These model molecules resembled some molecular characteristics of the asphaltenes and resins such as the presence of heteroatoms, cross-linked polyaromatic hydrocarbons and alkyl chains. Nevertheless, these model molecules do not mimic the self-association behaviour of the asphaltenes and how resins prevent this from happening. This study helps in the understanding the interactions and the adsorption behavior over the 5 and 40 nm NiO nanoparticles. NiO nanoparticles were synthesized with different particle sizes using the controlled thermal dehydroxylation method. The adsorption isotherms from the individual and binary solutions were described by the Langmuir model; and the data for the binary solutions were obtained by derivative spectrophotometry method based on multi-wavelength linear regression analysis, using the first order derivative. FTIR analysis identified the hydroxyl density for the nanoparticles, the higher the size the lower the hydroxyl density, which allows the nanoparticles surface to adsorb more Q-65 and/or V-79 molecules. This was supported by the XPS results in terms of the oxygen defects present in the nanoparticles, the higher the size the lower the oxygen defects. Macroscopic adsorption experiments showed that 40 nm NiO nanoparticles have higher adsorption capacity (molecules/nm^2) than 5 nm NiO nanoparticles, which is in agreement with the computational modeling results and characterization studies. From the competitive adsorption experiments, i.e. binary solutions, it can be observed that 5 and 40 nm NiO nanoparticles were more likely to adsorb preferentially V-79 than Q-65 molecules as it was obtained in the individual model oil solutions experiments. Also, the sequential adsorption experiments showed that the adsorption of V-79 over the Q-65-containing solids was higher than the Q-65 desorption, this could suggest that V-79 displaces some Q-65 molecules occupying their sites and other active sites, this could be related with the strong interactions between V-79 and the nanoparticles. Computational modeling was performed to better understand the interactions between the model molecules and NiO nanoparticles. The results agreed with the experimental results, showing that V-79 molecule is preferred to be adsorbed by NiO surface.

The experimental and the computational results help us to understand that different sites over the NiO nanoparticles were active for asphaltene and resin-like molecules. Q-65 and V-79 were prone to be adsorbed more on different sites over the nanoparticles surface, and the presence of oxygen in the Q-65 favors the interactions with the NiO surface and the presence of alkyl chains in the V-79 favors the interactions with the medium where other organic compounds were present during the adsorption process in the binary system. These results are very important in understanding the adsorption performance of the nanomaterials in complex mixtures like crude oils, which can be overestimated in asphaltenes only solution experiments since it is just one molecule competing for the adsorption sites. In addition, the results showed how the size of nanoparticle changed the chemical surface and textural properties affecting the adsorption capacity. Translating these results to an oil system, both NiO nanoparticles (5 and 40 nm) had more affinity for resin-like molecules (V-79) than for asphaltenes; however we need to take into account that asphaltene/resin composition is different in crude oils and their chemical and elemental composition as well; that is necessary to consider when designing a nanomaterial for oil recovery by nanofluid injection or for upgrading processes such as in-situ catalytic upgrading, in order to have a nanomaterial with more affinity for asphaltenes.

ASSOCIATED CONTENT

Supporting Information

Supporting Information associated with this chapter are in Appendix A.

3.7. References

Acevedo, S., Castillo, J., Fernández, A., Goncalves, S., & Ranaudo, M. A. (1998). A study of multilayer adsorption of asphaltenes on glass surfaces by photothermal surface deformation. Relation of this adsorption to aggregate formation in solution. *Energy & Fuels, 12*(2), 386-390.

Adams, J. J. (2014). Asphaltene adsorption, a literature review. *Energy & Fuels, 28*(5), 2831-2856.

Almao, P. P. (2012). In situ upgrading of bitumen and heavy oils via nanocatalysis. *The Canadian Journal of Chemical Engineering, 90*(2), 320-329.

Amin, F., & Solaimany Nazar, A. R. (2016). Assessing the asphaltene adsorption on metal oxide nanoparticles. *Iranian Journal of Oil & Gas Science and Technology, 5*(3), 62-72.

Balazs, A. C., Emrick, T., & Russell, T. P. (2006). Nanoparticle polymer composites: where two small worlds meet. *Science, 314*(5802), 1107-1110.

Betancur, S., Carmona, J. C., Nassar, N. N., Franco, C. A., & Cortés, F. B. (2016). Role of particle size and surface acidity of silica gel nanoparticles in inhibition of formation damage by asphaltene in oil reservoirs. *Industrial & Engineering Chemistry Research, 55*(21), 6122-6132.

Betancur, S. a., Carrasco-Marín, F., Franco, C. A., & Cortés, F. B. (2018). Development of Composite Materials Based on the Interaction between Nanoparticles and Surfactants for

Application in Chemical Enhanced Oil Recovery. *Industrial & Engineering Chemistry Research, 57*(37), 12367-12377.

Biesinger, M. C., Payne, B. P., Lau, L. W., Gerson, A., & Smart, R. S. C. (2009). X-ray photoelectron spectroscopic chemical state quantification of mixed nickel metal, oxide and hydroxide systems. *Surface and Interface Analysis: An International Journal devoted to the development and application of techniques for the analysis of surfaces, interfaces and thin films, 41*(4), 324-332.

Blanco, M., Gene, J., Iturriaga, H., Maspoch, S., & Riba, J. (1987). Diode-array detectors in flow-injection analysis mixture resolution by multi-wavelength analysis. *Talanta, 34*(12), 987-993.

Cortés, F. B., Mejía, J. M., Ruiz, M. A., Benjumea, P., & Riffel, D. B. (2012). Sorption of asphaltenes onto nanoparticles of nickel oxide supported on nanoparticulated silica gel. *Energy & Fuels, 26*(3), 1725-1730.

Cyran, J. D., & Krummel, A. T. (2015). Probing structural features of self-assembled violanthrone-79 using two dimensional infrared spectroscopy. *The Journal of chemical physics, 142*(21), 212435.

Dudášová, D., Flåten, G. R., Sjöblom, J., & Øye, G. (2009). Study of asphaltenes adsorption onto different minerals and clays: Part 2. Particle characterization and suspension stability. *Colloids and Surfaces A: Physicochemical and Engineering Aspects, 335*(1-3), 62-72.

Dudášová, D., Silset, A., & Sjöblom, J. (2008). Quartz crystal microbalance monitoring of asphaltene adsorption/deposition. *Journal of Dispersion Science and Technology, 29*(1), 139-146.

Dudášová, D., Simon, S., Hemmingsen, P. V., & Sjöblom, J. (2008). Study of asphaltenes adsorption onto different minerals and clays: Part 1. Experimental adsorption with UV depletion detection. *Colloids and Surfaces A: Physicochemical and Engineering Aspects, 317*(1-3), 1-9.

El-Qanni, A. (2017). Development of Sustainable Nanosorbcats Based Technology for Hydrocarbons and Organic Pollutants Recovery from Industrial Wastewater.

Franco, C. A., Lozano, M. M., Acevedo, S., Nassar, N. N., & Cortés, F. B. (2015). Effects of resin I on asphaltene adsorption onto nanoparticles: a novel method for obtaining asphaltenes/resin isotherms. *Energy & Fuels, 30*(1), 264-272.

Franco, C. A., Nassar, N. N., Ruiz, M. A., Pereira-Almao, P., & Cortés, F. B. (2013). Nanoparticles for inhibition of asphaltenes damage: adsorption study and displacement test on porous media. *Energy & Fuels, 27*(6), 2899-2907.

Giraldo, J., Benjumea, P., Lopera, S., Cortés, F. B., & Ruiz, M. A. (2013). Wettability alteration of sandstone cores by alumina-based nanofluids. *Energy & Fuels, 27*(7), 3659-3665.

Groenzin, H., & Mullins, O. C. (2000). Molecular size and structure of asphaltenes from various sources. *Energy & Fuels, 14*(3), 677-684.

Guzmán, J. D., Betancur, S., Carrasco-Marín, F., Franco, C. A., Nassar, N. N., & Cortés, F. B. (2016). Importance of the adsorption method used for obtaining the nanoparticle dosage for asphaltene-related treatments. *Energy & Fuels, 30*(3), 2052-2059.

Hassan, A., Lopez-Linares, F., Nassar, N. N., Carbognani-Arambarri, L., & Pereira-Almao, P. (2013). Development of a support for a NiO catalyst for selective adsorption and post-adsorption catalytic steam gasification of thermally converted asphaltenes. *Catalysis today, 207*, 112-118.

Hethnawi, A., Manasrah, A. D., Vitale, G., & Nassar, N. N. (2018). Fixed-bed column studies of total organic carbon removal from industrial wastewater by use of diatomite decorated with polyethylenimine-functionalized pyroxene nanoparticles. *Journal of colloid and interface science, 513*, 28-42.

Hmoudah, M., Nassar, N. N., Vitale, G., & El-Qanni, A. (2016). Effect of nanosized and surface-structural-modified nano-pyroxene on adsorption of violanthrone-79. *RSC advances, 6*(69), 64482-64493.

Horcajada, P., Chalati, T., Serre, C., Gillet, B., Sebrie, C., Baati, T., Eubank, Jarrod F, Heurtaux, Daniela, & Clayette, P., Kreuz, Christine. (2010). Porous metal–organic-framework nanoscale carriers as a potential platform for drug delivery and imaging. *Nature materials, 9*(2), 172.

Hosseinpour, N., Khodadadi, A. A., Bahramian, A., & Mortazavi, Y. (2013). Asphaltene adsorption onto acidic/basic metal oxide nanoparticles toward in situ upgrading of reservoir oils by nanotechnology. *Langmuir, 29*(46), 14135-14146.

Jang, S. P., & Choi, S. U. (2004). Role of Brownian motion in the enhanced thermal conductivity of nanofluids. *Applied Physics Letters, 84*(21), 4316-4318.

Kazemzadeh, Y., Eshraghi, S. E., Kazemi, K., Sourani, S., Mehrabi, M., & Ahmadi, Y. (2015). Behavior of asphaltene adsorption onto the metal oxide nanoparticle surface and its effect on heavy oil recovery. *Industrial & Engineering Chemistry Research, 54*(1), 233-239.

Kumari, A., Yadav, S. K., & Yadav, S. C. (2010). Biodegradable polymeric nanoparticles based drug delivery systems. *Colloids and surfaces B: biointerfaces, 75*(1), 1-18.

Langmuir, I. (1916). The constitution and fundamental properties of solids and liquids. Part I. Solids. *Journal of the American chemical society, 38*(11), 2221-2295.

Liu, H., Shen, L., Cao, Z., & Li, X. (2014). Covalently linked perylenetetracarboxylic diimide dimers and trimers with rigid "J-type" aggregation structure. *Physical Chemistry Chemical Physics, 16*(31), 16399-16406.

López-Linares, F., Carbognani, L., González, M. F., Sosa-Stull, C., Figueras, M., & Pereira-Almao, P. (2006). Quinolin-65 and violanthrone-79 as model molecules for the kinetics of the adsorption of C7 athabasca asphaltene on macroporous solid surfaces. *Energy & Fuels, 20*(6), 2748-2750.

Mansoori Mosleh, F., Mortazavi, Y., Hosseinpour, N., & Khodadadi, A. A. (2019). Asphaltene adsorption onto carbonaceous nanostructures. *Energy & Fuels, 34*(1), 211-224.

Marei, N. N. (2016). *Role of Nanosize Effects on the Adsorptive and Catalytic Properties of NiO Nanoparticles towards Heavy Hydrocarbons.* Graduate Studies.

Marei, N. N., Nassar, N. N., & Vitale, G. (2016). The effect of the nanosize on surface properties of NiO nanoparticles for the adsorption of Quinolin-65. *Physical Chemistry Chemical Physics, 18*(9), 6839-6849.

McElfresh, P. M., Holcomb, D. L., & Ector, D. (2012). *Application of nanofluid technology to improve recovery in oil and gas wells.* Paper presented at the SPE International Oilfield Nanotechnology Conference and Exhibition.

Mohammadi, M., Akbari, M., Fakhroueian, Z., Bahramian, A., Azin, R., & Arya, S. (2011). Inhibition of asphaltene precipitation by TiO2, SiO2, and ZrO2 nanofluids. *Energy & Fuels, 25*(7), 3150-3156.

Montoya, T., Coral, D., Franco, C. A., Nassar, N. N., & Cortés, F. B. (2014). A novel solid–liquid equilibrium model for describing the adsorption of associating asphaltene

molecules onto solid surfaces based on the “chemical theory”. *Energy & Fuels, 28*(8), 4963-4975.
Moradi, B., Pourafshary, P., Jalali, F., Mohammadi, M., & Emadi, M. (2015). Experimental study of water-based nanofluid alternating gas injection as a novel enhanced oil-recovery method in oil-wet carbonate reservoirs. *Journal of Natural Gas Science and Engineering, 27*, 64-73.
Morelli, B. (1995). Determination of ternary mixtures of antibiotics, by ratio-spectra zero-crossing first-and third-derivative spectrophotometry. *Journal of pharmaceutical and biomedical analysis, 13*(3), 219-227.
Mullins, O. C. (2011). The asphaltenes. *Annual Review of Analytical Chemistry, 4*, 393-418.
Nafie, G., Vitale, G., Carbognani Ortega, L., & Nassar, N. N. (2017). Nanopyroxene grafting with β-Cyclodextrin monomer for wastewater applications. *ACS applied materials & interfaces, 9*(48), 42393-42407.
Nassar, N. N. (2010). Asphaltene adsorption onto alumina nanoparticles: kinetics and thermodynamic studies. *Energy & Fuels, 24*(8), 4116-4122.
Nassar, N. N., Betancur, S., Acevedo, S. c., Franco, C. A., & Cortés, F. B. (2015). Development of a population balance model to describe the influence of shear and nanoparticles on the aggregation and fragmentation of asphaltene aggregates. *Industrial & Engineering Chemistry Research, 54*(33), 8201-8211.
Nassar, N. N., Hassan, A., & Pereira-Almao, P. (2011a). Application of nanotechnology for heavy oil upgrading: Catalytic steam gasification/cracking of asphaltenes. *Energy & Fuels, 25*(4), 1566-1570.
Nassar, N. N., Hassan, A., & Pereira-Almao, P. (2011b). Effect of surface acidity and basicity of aluminas on asphaltene adsorption and oxidation. *Journal of colloid and interface science, 360*(1), 233-238.
Nassar, N. N., Hassan, A., & Pereira-Almao, P. (2011c). Metal oxide nanoparticles for asphaltene adsorption and oxidation. *Energy & Fuels, 25*(3), 1017-1023.
Nassar, N. N., Hassan, A., & Vitale, G. (2014). Comparing kinetics and mechanism of adsorption and thermo-oxidative decomposition of Athabasca asphaltenes onto TiO2, ZrO2, and CeO2 nanoparticles. *Applied Catalysis A: General, 484*, 161-171.
Negin, C., Ali, S., & Xie, Q. (2016). Application of nanotechnology for enhancing oil recovery– A review. *Petroleum*, *2*(4), 324-333.
Payne, B., Biesinger, M., & McIntyre, N. (2012). Use of oxygen/nickel ratios in the XPS characterisation of oxide phases on nickel metal and nickel alloy surfaces. *Journal of Electron Spectroscopy and Related Phenomena*, *185*(5-7), 159-166.
Perdew, J. P., Ruzsinszky, A., Csonka, G. I., Vydrov, O. A., Scuseria, G. E., Constantin, Lucian A, Zhou, Xiaolan, & Burke, K. (2008). Restoring the density-gradient expansion for exchange in solids and surfaces. *Physical review letters, 100*(13), 136406.
Pernyeszi, T., Patzko, A., Berkesi, O., & Dékány, I. (1998). Asphaltene adsorption on clays and crude oil reservoir rocks. *Colloids and Surfaces A: Physicochemical and Engineering Aspects, 137*(1-3), 373-384.
Ramanathan, T., Abdala, A., Stankovich, S., Dikin, D., Herrera-Alonso, M., Piner, R., Adamson, DH, Schniepp, HC, & Chen, X., Ruoff, RS. (2008). Functionalized graphene sheets for polymer nanocomposites. *Nature nanotechnology, 3*(6), 327.

Rezvani, H., Khalilnezhad, A., Ganji, P., & Kazemzadeh, Y. (2017). How ZrO 2 nanoparticles improve the oil recovery by affecting the interfacial phenomena in the reservoir conditions? *Journal of Molecular Liquids, 252*, 158-168.

Romero, Z., Disney, R., Acuna, H. M., Cortes, F., Patino, J. E., Cespedes Chavarro, Carolina, Mora, Edgar, & Botero, O. F., Guarin, Liliana. (2013). *Application and evaluation of a nanofluid containing nanoparticles for asphaltenes inhibition in well CPSXL4.* Paper presented at the OTC Brasil.

Rudrake, A., Karan, K., & Horton, J. H. (2009). A combined QCM and XPS investigation of asphaltene adsorption on metal surfaces. *Journal of colloid and interface science, 332*(1), 22-31.

Salinas, F., Nevado, J. B., & Mansilla, A. E. (1990). A new spectrophotometric method for quantitative multicomponent analysis resolution of mixtures of salicylic and salicyluric acids. *Talanta, 37*(3), 347-351.

Sebakhy, K. O. (2017). Developing Novel Heterogeneous Catalysts for the Selective Hydrogenation of Olefins in Light Petroleum Distillates.

Sedghi, M., Goual, L., Welch, W., & Kubelka, J. (2013). Effect of asphaltene structure on association and aggregation using molecular dynamics. *The Journal of Physical Chemistry B, 117*(18), 5765-5776.

Shi, M.-M., Chen, Y., Nan, Y.-X., Ling, J., Zuo, L.-J., Qiu, Wei-Ming, Wang, Mang, & Chen, H.-Z. (2010). $\pi-\pi$ interaction among violanthrone molecules: Observation, enhancement, and resulting charge transport properties. *The Journal of Physical Chemistry B, 115*(4), 618-623.

Sjöblom, J., Simon, S., & Xu, Z. (2015). Model molecules mimicking asphaltenes. *Advances in colloid and interface science, 218*, 1-16.

Smith, T. J. (1995). MolView: a program for analyzing and displaying atomic structures on the Macintosh personal computer. *Journal of molecular graphics, 13*(2), 122-125.

Thommes, M. (2010). Physical adsorption characterization of nanoporous materials. *Chemie Ingenieur Technik, 82*(7), 1059-1073.

Thommes, M., Kaneko, K., Neimark, A. V., Olivier, J. P., Rodriguez-Reinoso, F., Rouquerol, J., & Sing, K. S. (2015). Physisorption of gases, with special reference to the evaluation of surface area and pore size distribution (IUPAC Technical Report). *Pure and Applied Chemistry, 87*(9-10), 1051-1069.

Tu, Y., Woods, J., Kung, J., McCracken, T., Kotlyar, L., Sparks, B., & Dong, M. (2006). Adsorption of SARA Fractions from Heavy Oil and Bitumen on Kaolinite. *Clay Science, 12*(Supplement2), 183-187.

Vargas, V., Castillo, J., Ocampo-Torres, R., Lienemann, C.-P., & Bouyssiere, B. (2018). Surface modification of SiO2 nanoparticles to increase asphaltene adsorption. *Petroleum Science and Technology, 36*(8), 618-624.

Xie, K., & Karan, K. (2005). Kinetics and thermodynamics of asphaltene adsorption on metal surfaces: A preliminary study. *Energy & Fuels, 19*(4), 1252-1260.

Zahabi, A., Gray, M. R., & Dabros, T. (2012). Kinetics and properties of asphaltene adsorption on surfaces. *Energy & Fuels, 26*(2), 1009-1018.

Zhang, L., Shi, C., Lu, Q., Liu, Q., & Zeng, H. (2016). Probing Molecular Interactions of Asphaltenes in Heptol Using a Surface Forces Apparatus: Implications on Stability of Water-in-Oil Emulsions. *Langmuir, 32*(19), 4886-4895.

Zhao, L., Liu, L., & Sun, H. (2007). Semi-ionic model for metal oxides and their interfaces with organic molecules. *The Journal of Physical Chemistry C, 111*(28), 10610-10617.

Chapter Four: Investigation of the Interaction between Nanoparticles, Asphaltenes, and Silica Surfaces by Real-Time Quartz Crystal Microbalance with Dissipation[3]

Graphical Abstract

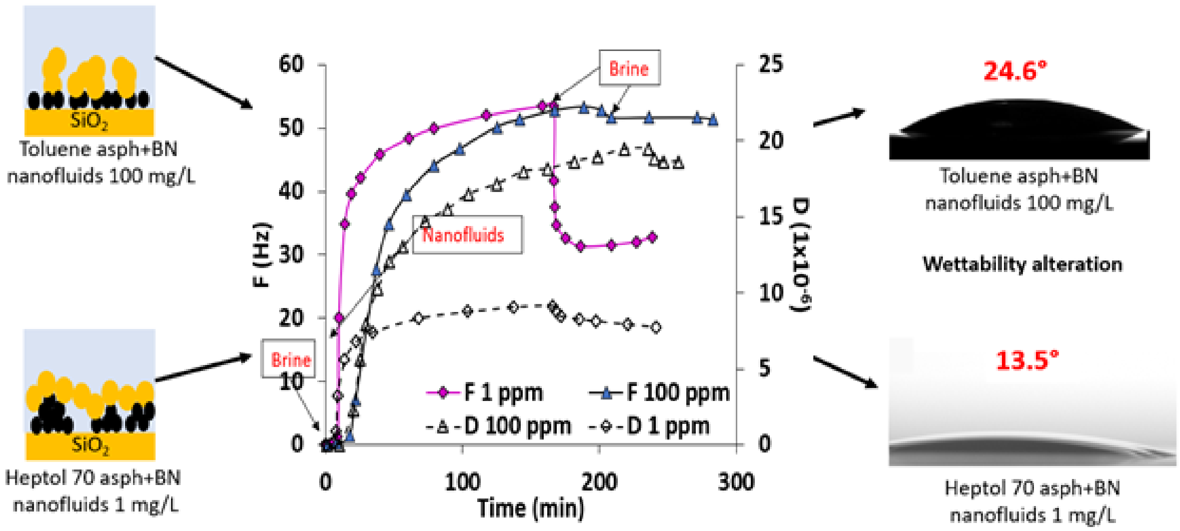

4.1. Abstract

The effects of nanofluids as wettability alternators and inhibitors of asphaltene precipitation and formation damage were studied in this work. Silicate-based nanoparticles with different chemical surfaces, named neutral (NN), basic (BN), and acidic (AN), dispersed in NaCl brine were tested to observe their interactions with n-C_7 asphaltenes and silica surfaces using the quartz crystal microbalance with dissipation (QCM-D). The properties of nanoparticles were characterized using XRD, BET, TPD, and HRTEM. Heptol 70 asphaltenes, pre-adsorbed/deposited on SiO_2 sensors were used for studying the concentration effect of 10 nm-sized BN-based nanofluids, which exhibited a decreasing trend in frequency shift in the following order 1>10 > 25 mg/L. For toluene asphaltenes, the frequency shifts in BN nanofluids changed with the following order of concentration 100 >150 > 50 > 25 mg/L. The effect of particle size on frequency shift, tested for

[3]This chapter is adapted from the following publication:
Tatiana Montoya, Archana Jaiswal, Nashaat N. Nassar. *Investigation of the Interaction between Nanoparticles, Asphaltenes, and Silica Surfaces by Real-Time Quartz Crystal Microbalance with Dissipation*, Accepted for publication in The Canadian Journal of Chemical Engineering, 2021.

toluene asphaltenes demonstrated the following order 10 > 99 > 45 > 20 nm BN. A cycle injection test between asphaltenes and a nanofluid solution was performed to evaluate the effect of the nanoparticles in a sequence injection. Wettability alteration was assessed before and after nanofluid injection using contact angle measurements, which resulted in a decrease after nanofluid injection. In addition, atomic force microscopy (AFM) measurements were performed on some of the samples to support the findings. The QSense data analysis software Q-Tools was used to determine the thickness of the layer before and after the injection of nanofluids; the trend was similar to the change in frequency for all parameters. Finally, brine-based nanofluids with 10 nm-sized BN at 1 and 100 mg/L were more effective in treating the deposited asphaltenes in heptol 70 and toluene, respectively.
Keywords: Asphaltenes, nanofluids, QCM-D, wettability alteration, formation damage

4.2. Introduction

Asphaltenes is the heaviest, most aromatic and surface-active fraction of crude oil (Acevedo et al., 2007; Adams, 2014; Andersen, 1995). Asphaltenes exhibit polarizability, amphiphilic behaviour, and complex chemical structures. These structures are composed mainly of cores of polycyclic aromatic hydrocarbons (PAH); naphthenic groups; heteroatoms, such as nitrogen, oxygen, and sulfur; and metals, such as vanadium, nickel, and iron (Qiao et al., 2017; Schuler, Meyer, Peña, Mullins, & Gross, 2015), and they display a self–associating feature that provokes aggregation.(Yarranton, 2005) This aggregation is augmented by reducing the aromaticity of the solvent (Qiao et al., 2017; Zhang, Shi, Lu, Liu, & Zeng, 2016). Moreover, aggregation leads to an increase in crude oil viscosity (Mullins, 2011). Due to these characteristics, asphaltenes can cause several problems at different stages of crude oil production, any of which entail a loss of productivity (Tavakkoli et al., 2013). Changes in reservoir conditions, including temperature, pressure, and oil composition, are parameters that can lead to high asphaltene precipitation in a reservoir (Nasrabadi, Moortgat, & Firoozabadi, 2016). Asphaltene deposition is significant in many domains of the oil industry, for example alteration of reservoir rock wettability, from water-wet to oil-wet, due to its potential to be adsorbed on reservoir rock(Al-Maamari & Buckley, 2003; Majid Mohammadi, Dadvar, & Dabir, 2017); plugging flow lines (Creek, 2005); and refinery catalyst deactivation (Trimm, 1996).

For these reasons, the interaction of asphaltenes with solid surfaces is considered by researchers, who have implemented several experimental techniques to study the adsorption of asphaltenes onto different substrates, including silica (Dudášová, Silset, & Sjöblom, 2008; Zahabi, Gray, & Dabros, 2012), alumina (Dudášová, Silset, et al., 2008; González, Stull, López-Linares, & Pereira-

Almao, 2007), iron oxide (Carbognani, 2000), gold (Goual & Abudu, 2009; Harbottle et al., 2014; Rudrake, Karan, & Horton, 2009; Sedghi, Goual, Welch, & Kubelka, 2013; Zahabi et al., 2012), stainless steel (Xie & Karan, 2005), glass (Acevedo, Castillo, Fernández, Goncalves, & Ranaudo, 1998), and clay minerals (Dudášová, Simon, Hemmingsen, & Sjöblom, 2008; Jada & Debih, 2009; Jada, Debih, & Khodja, 2006; Klein, Kim, Rodgers, Marshall, & Yen, 2006; Pernyeszi, Patzko, Berkesi, & Dékány, 1998; Tu, Woods, et al., 2006). Using QCM-D, researchers have studied asphaltene adsorption and film formation in real time (Dudášová, Silset, et al., 2008; Harbottle et al., 2014; Rudrake et al., 2009; Xie & Karan, 2005; Zahabi et al., 2012). In addition, they have characterized surface modification caused by asphaltene adsorption/deposition using X-ray photoelectron spectroscopy (XPS) (Rudrake et al., 2009; Tu, Kung, et al., 2006), X-ray diffraction (XRD) (Jada & Debih, 2009; Pernyeszi et al., 1998; Tu, Kung, et al., 2006), small-angle X-ray scattering (SAXS) (Pernyeszi et al., 1998), Fourier transform infrared spectroscopy (FTIR) (Jada & Debih, 2009; Jada et al., 2006), and Fourier transform ion cyclotron resonance mass spectrometry (FT-ICR MS) (Klein et al., 2006). However, it is not possible to compare the results from various adsorption studies, since asphaltene adsorption is a complex process that is influenced by different parameters, including crude oil source, type of solvents used for extraction, temperature, etc (Qiao et al., 2017).

There have been several suggested methods to prevent the deposition of asphaltenes, mainly in areas near wells (Leontaritis, Amaefule, & Charles, 1994). Among these methods is the periodic intervention by solvent soaking or constant chemical injection (Betancur, Carmona, Nassar, Franco, & Cortés, 2016; Mansoori, 2010). Also, other methods include incorporation of dispersants, anti-flocculants, coagulants, flocculants, and nonpolar solvents, which are mainly employed to manage asphaltene precipitation and deposition (Ghloum, Al-Qahtani, & Al-Rashid, 2010; Mansoori, 2010). Nonetheless, conventional methods can be expensive because, in most cases, they need complex equipment and more staff on location (Betancur et al., 2016; Mansoori, 2010). Also, they have low durability and can produce changes in fluid composition (Betancur et al., 2016; Mansoori, 2010).

Therefore, in the recent years, nanoparticles and nanofluids have been introduced as options to reduce the damage produced by asphaltene precipitation, and for in-situ enhancement of reservoir productivity (Li et al., 2016; Mohsen Mohammadi et al., 2011; Rezvani, Khalilnezhad, Ganji, & Kazemzadeh, 2017). Nanoparticles portray unique properties, such as high surface area/volume ratios, specific chemical reactivity, active surfaces, and excellent dispersibility (Rezvani et al., 2017). These characteristics facilitate the capture and removal of the asphaltenes present in a reservoir, which improves oil production, reduces damage, and restores wettability (Franco, Nassar, Ruiz, Pereira-Almao, & Cortés, 2013; Giraldo, Benjumea, Lopera, Cortés, & Ruiz, 2013; Moradi, Pourafshary, Jalali, Mohammadi, & Emadi, 2015). Nanoparticles improve oil production in EOR processes by various mechanisms, like viscosity/density alteration of the injected fluid (Moradi et al., 2015), enhancement of the emulsification process, amelioration of thermal conductivity and specific heat capacity (Jang & Choi, 2004; Patel et al., 2003), improvement of rock-fluid interactions (McElfresh, Holcomb, & Ector, 2012), and alteration of heat transfer coefficients (Rezvani et al., 2017).

Accordingly, several nanoparticles have been tested along with different types of surfactant and polymer solutions to increase the effectiveness of the EOR processes (Cheraghian & Khalilinezhad, 2015; Nezhad & Cheraghian, 2016; Sedaghat, Mohammadi, & Razmi, 2016), water-alternating gas injections (WAG) (Moradi et al., 2015), water flooding (Dehghan Monfared, Ghazanfari, Jamialahmadi, & Helalizadeh, 2016; Joonaki & Ghanaatian, 2014), and CO_2 flooding

(Worthen, Bryant, Huh, & Johnston, 2013). Nanoparticle performance in these processes has been investigated in the laboratory using different techniques, such as sessile-drop wettability tests, micromodel experiments, and core flooding experiments (Giraldo et al., 2013; Li et al., 2016; Rezvani et al., 2017). As a result, researchers have determined that the main mechanism attributed to the presence of nanoparticles in the EOR processes is disjoining pressure (Li et al., 2016; Moradi et al., 2015; Rezvani et al., 2017). In this mechanism, nanoparticles form a self-assembled wedge-shaped film with the discontinuous fluid at the interface (Moradi et al., 2015; Rezvani et al., 2017). In other words, a wedge film forms between the oil, the solid surface, and the nanoparticles (Rezvani et al., 2017). This wedge film can divide formation fluids, such as oil, paraffin, water, and/or gas, from the formation surface, consequently improves the recovery of the fluids more effectively compared with conventional fluids or additives used (Moradi et al., 2015).

However, there is still a need to understand the interaction of the coupled asphaltene-nanoparticles and how their chemical nature affects the adsorption and asphaltene growth process over silica surfaces or in reservoirs. In the current chapter, QCM-D was employed to establish the interaction of silicate-based nanofluids on asphaltene pre-adsorbed/deposited silica surfaces. Silica oxide (SiO_2) sensors were selected as the solid surface to be studied as they represent the basic components of sandstones reservoirs. Asphaltenes were employed as the organic material for adsorption/deposition over the solid surfaces because they are the heaviest components in oil. Asphaltene deposition was performed in two different solvents: heptol 70 (heptane 70% and toluene 30%) and 100% toluene. For nanoparticle solution, first, the 10 nm neutral nanoparticles (NN) were chemically modified on the surface to obtain basic nanoparticles (BN) and acid nanoparticles (AN); then, these materials were used to prepare nanofluids in NaCl brine. The nanoparticle concentrations of 1, 10, and 25 mg/L were tested for asphaltenes in heptol 70, and 25, 50, 100, and 150 mg/L were tested for asphaltenes in toluene. Particle sizes, 10, 20, 45, and 99 nm of asphaltenes were evaluated in toluene. Finally, a cycle injection experiment was carried out with asphaltenes in heptol 70 to study the effect of cycle injection of the nanofluid solutions in wettability alteration as it occurs in a real reservoir during the treatment of asphaltene precipitation. The QSense data analysis software Q-Tools was used to analyse the QCM-D data and obtain the thickness of the layer before and after nanofluid injection. The contact angle of a water droplet on the treated sensor surfaces was measured to study the change in wettability, and AFM images were taken for some sensors to see the effect of nanofluids. All experiments were conducted to explore the potential of different nanofluids and determine the parameters that increased water-wettability of the contaminated sensors; the experiments were focused on the nanofluid-induced structural effect on the sensor surface and the asphaltenes, and nanofluids as an alternative treatment to reduce damage without the use of additional chemicals.

4.3. Experimental Procedure

4.3.1. Materials and Methods

Toluene and n-heptane HPLC grade obtained from Sigma-Aldrich (ON, Canada) were used to prepare the asphaltene solutions and to extract the asphaltenes from an oil matrix, respectively. NaCl from sigma Aldrich (ON, Canada) was employed to prepare brine solutions in deionized water. For typical silicate-based nanoparticles preparation, sulfuric acid (H_2SO_4 97%) was purchased from Fisher Scientific (ON, Canada); sodium silicate (SiO_2 26.5%, Na_2O 10.6%) from Sigma-Aldrich (ON, Canada); iron(III) chloride hexahydrate ($FeCl_3.6H_2O$ 99%) from Merck (ON, Canada); and sodium hydroxide (NaOH 99%) from Merk (ON, Canada). The silicate-based nanoparticles were then modified using calcium nitrate ($Ca(NO_3)_2$ 100%) and sulfuric acid (H_2SO_4 97%) from Sigma Aldrich (ON, Canada). An industrial partner provided the oil used for asphaltene extraction and the other experiments, and the oil had 28.5 API gravity and a viscosity of 7.5 cP @ 60 °C. All chemicals were employed as received.

4.3.2. Nanoparticles Preparation

Silicate-based nanoparticles were synthesized by a hydrothermal route that controlled time and maintained a low temperature as reported in other studies (Vitale, 2013; Vitale, Nafie, Hethnawi, & Nassar, 2020). The 20 nm-sized silicate-based nanoparticles were prepared following the same procedure, but varying the Fe/Na ratio; for the 45 nm-sized nanoparticles, 10 nm-sized nanoparticles were employed as seeds and added to gel to generate conditions for nucleation of the crystals to form larger crystals. For the 99 nm-sized nanoparticles, 10 nm-sized nanoparticles were treated at 450 °C for 1 h.

4.3.3. Nanoparticle Surface Modification

The surfaces of the silicate-based nanoparticles were functionalized with hydronium ions and calcium by superficial ion exchange to substitute the sodium cation present in the original structure (Vitale, 2013). The prepared nanoparticles were dispersed in an aqueous solution of diluted sulfuric acid at room temperature for 25 min in the case of the hydronium ions, and in the case of calcium, the nanoparticles were dispersed in an aqueous solution of $Ca(NO_3)_2.4H_2O$ and mixed for 1 h. The solid was filtered and washed with distilled water, and then dried at room temperature overnight and stored in a sealed container. The modified nanoparticles were named BN (basic nanoparticles), AN (acidic nanoparticles), and NN (neutral nanoparticles). Neutral nanoparticles were those prepared without any further modification to the surface.

4.3.4. Asphaltene Extraction

n-C_7 asphaltenes were extracted from oil following a modified ASTM D-6560 method (Ovalles, Rogel, Moir, & Morazan, 2015). This method consisted of heating the oil sample with heptane at a ratio of 1:40 in a 1 L round-bottomed flask until boiling. After that, the mixture was refluxed for 35 min and then left to cool to room temperature. The precipitate was washed with n-heptane until the filtrate was pale orange in color; this step was necessary to remove the sticky residue that covered the surface (Ortega et al., 2015). The solid was dried overnight in a vacuum oven. Element analyzer 2400 series II (Perkin Elmer, Canada) was used to determine the content of carbon (C), hydrogen (H), and nitrogen (N) in the extracted n-C_7 asphaltenes. The amount of sulphur and metal were determined using ICP-AES (IRIS Intrepid II XDL, Thermo-Instruments Canada, Inc., Mississauga, ON, Canada), and the oxygen content was obtained by balance. The results are shown in **Table 4.1**.

Table 4.1. The chemical composition of n-C_7 asphaltenes from the obtained oil sample.

Element	wt.%
Mo	0.0033
Ni	0.0233
W	0.0032
Fe	0.0038
V	0.1087
K	0.0017
C	82.25
H	7.35
N	1.13
S	4.42
O	4.73

4.3.5. Nanofluids and Asphaltene Solutions Preparation

Two solutions were used to prepare the oil with asphaltenes. One solution was prepared using only toluene, and for the second solution, the asphaltenes were dissolved in a solution of 70 heptol (70% n-heptane and 30% toluene). To ensure the presence of asphaltenes in aggregate forms, the concentration of asphaltenes was 180 mg/L in toluene and 500 mg/L in heptol. Then, these solutions were sonicated for 45 min. The nanofluid solutions were prepared by adding different masses of the prepared silicate-based nanoparticles to a brine solution (1000 mg/L of NaCl). These solutions were sonicated for 20 minutes.

4.3.6. DLS and Zeta Potential (ζ) Measurements

To measure the particle size distribution for heptol 70 asphaltenes solution, zeta sizer ZS90, Malvern Instruments, Southborough, UK. was used. A solution of 500 ppm heptol 70 asphaltenes was prepared, and sonicated for about 30-45 min. Then, an aliquot of 1.5 mL was placed into a quartz cuvette cell to measure the particle size distribution in the zeta sizer ZS90 using dispersion light scattering (DLS) technique. All measurements were taken at 25 °C. The measurements were taken every 5 min for 70 min until the equilibrium was achieved.

For nanofluid samples at different concentrations of nanoparticles 1, 10, 25, 50, 100 and 150 mg/L, a dynamic light scattering (DLS) and ζ potential analyses were performed to determine the average hydrodynamic size distribution and stability of the particles in the brine solution, respectively. To start the tests, the NaCl brine was prepared at 1000 ppm. Then, nanoparticles were added to achieve each concentration; after that it was sonicated for about 30-40 min. Then, an aliquot of 2 mL was put into a cuvette plastic cell to measure the particle size distribution in the zeta sizer ZS90, Malvern Instruments, Southborough, UK. Through the technique of dispersion light scattering (DLS), the measurements were taken at 25° C. The measurements were taken 3 times every 80 min until reaching 240 min (time QCM-D experiments).

4.3.7. Characterization of the Prepared Nanoparticles

4.3.7.1. Powder X-ray Diffraction (XRD)

The crystalline phases and physicochemical properties of the powder materials were characterized using XRD Ultima III Multi Purpose Diffraction System (Rigaku Corp., The Woodlands, TX) with Cu Kα radiation operating at 40 kV and 44 mA with a θ-2θ goniometer. (Vitale, 2013; Vitale et al., 2020).

4.3.7.2. Textural Properties

The surface areas for the prepared and modified nanoparticles were measured by performing nitrogen physisorption at 77 K using a surface area and porosity analyzer (TriStar II 3020, Micromeritics Corporate, Norcross, GA). All the samples were pretreated at 150 ° C under N_2 flow overnight before analysis. The surface area was determined from the BET equation (Vitale et al., 2020).

4.3.7.3. Temperature Programmed Desorption (TPD) Analysis

The total acidity and the strength distribution of components for the surface chemistry-modified nanoparticles (acidic, basic and neutral) were performed on a CHEMBET 3000 (Quantachrome Inc.). Ammonia (TPD-NH_3) were used for this analysis. The amount of NH_3 desorbed is therefore an indication of the total acidity of the nanoparticles studied. Therefore, about 100 mg of sample was introduced in a U-shaped quartz micro reactor (2 mm internal diameter). The sample was then dried at 200 °C for 2 h under helium (He) flow at atmospheric pressure. The sample was then cooled to 100 °C. A flow of 10% NH_3(g) in Ar was then introduced to be adsorbed and saturate the nanoparticle surface at 100 °C for 1 h. The flow rate of NH_3 was kept at 25 cm^3/min. Then, He was passed at a flow rate of 15 cm^3 /min for 1 h at 100 °C to desorb physisorbed NH_3. The solid was then heated up to 900 °C at a heating rate of 10 °C/min to release chemisorbed NH_3. The amount of NH_3 was determined from the area under the peak using a calibration curve made for this purpose (Nassar, Franco, Montoya, Cortés, & Hassan, 2015; Vitale et al., 2020).

4.3.7.4. High Resolution Transmission Electron Microscopy (HRTEM) Analysis

Transmission electron microscopy images for different 10 nm-sized modified nanoparticles were obtained using FEI Tecnai F20 FEG TEM at an accelerating voltage of 200 kV to analyse the sizes and morphology of the nanoparticles.

4.3.8. Quartz Crystal Microbalance with Dissipation (QCM-D) Analysis

Quartz crystal microbalance with dissipation (QCM-D) technology based QSense Analyzer instrument (Biolin scientific, Sweden) was used to measure the adsorption/deposition of asphaltenes and nanofluids on silica (SiO_2) coated sensors. The sensors used in this study were 14 mm in diameter and composed of AT-cut crystals (5 MHz) coated with silica (QSX 303). The frequency and dissipation shifts for each sample were recorded at the fundamental frequency (5 MHz) and for 6 overtones (3, 5, 7, 9, 11, and 13). All experiments were conducted at 25 °C and with a solution flow rate of 150 µL/min. The resonance frequency of the crystal relates to total mass adsorbed on the sensor surface (including the solvent) coupled with the oscillations (Mason & Baerwald, 1951; Reviakine, Johannsmann, & Richter, 2011). A decrease in oscillation frequency indicates mass adsorption, while an increase in oscillation frequency occurs if the mass is removed from the sensor (Reviakine et al., 2011). Before placing the sensors in QCM-D, they were cleaned in a UV/ozone cleaner for 10 min and then blown with clean nitrogen gas. The sample flow modules were equipped with highly resistant Kalrez O-rings and gaskets, and the pump tubing that was used was made of GORE (100 CR) to ensure solvent (toluene/heptol 70) compatibility with the flow path. The experiment included two steps: formation of an asphaltene layer on the surface of the silica sensor and treatment of this layer with nanofluids.

Each experiment started with baseline stabilization in a blank solvent.(Domack, Prucker, Rühe, & Johannsmann, 1997) The baseline of a pristine sensor was first recorded in brine solution, and the data was saved. For this experiment, a clean sensor was carefully mounted in the flow module with the active surface facing the testing solutions. The brine solution was pumped through the flow module at a flow rate of 150 μL/min for 5 min. Then, the sensors were removed from the modules and dried with nitrogen prior to asphaltene adsorption. For the formation of the asphaltene layer, the sensors were put back into the modules, and the baseline in pure toluene/heptol 70 was recorded for 10 min. Next, the asphaltene solution was flowed over the sensor, and mass adsorption was monitored by recording the frequency and dissipation shifts until equilibrium was reached, i.e., until the frequency and dissipation data stabilized. Finally, pure toluene/heptol 70 was flowed over the adsorbed asphaltene layer to remove the excess asphaltenes. The sensor was then dried over night at room temperature. A schematic representation of the process is depicted in **Figure 4.1.**

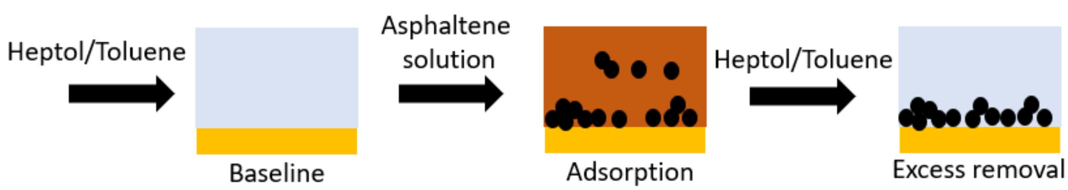

Figure 4.1. Schematic representation of asphaltene coating over the sensors.

A similar procedure was followed for the nanofluids. After drying for 24 h, the sensors with the adsorbed asphaltenes were placed into the QSense flow modules, and brine was allowed to flow for 10 min. Then, the brine was switched by the nanofluids, and nanofluids were allowed to flow until no further changes in frequency and dissipation were recorded. Finally, the brine flowed again to remove excess nanoparticles. A schematic representation of the process is shown in **Figure 4.2**.

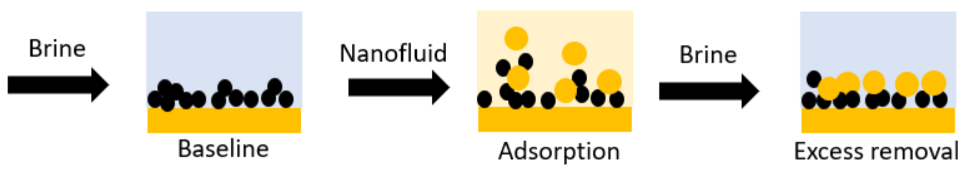

Figure 4.2. Schematic representation of nanofluid flow over the sensors.

4.3.9. Contact Angle Analysis

Contact angle measurements of bare sensors, sensors coated with asphaltene (both heptol 70 and toluene media), and after treatment with different nanofluids were determined. These measurements were performed on an Attension (formerly KSV Instruments) CAM200 Optical tensiometer, Biolin Scientific, USA using the sessile drop method with water in air, and with an accuracy of ±2°and an equilibrium time of 2 min.

4.3.10. Atomic Force Microscopy (AFM) Analysis

Surface topography of the asphaltenes adsorbed on the sensors' surfaces and the change in surface topography after the nanofluid flow was measured using the contact mode of the Agilent 5500 AFM system (Agilent Technologies, USA) and PicoView software. AFM measurements were determined at 0° scan angle on a 5 μm × 5 μm area at a speed 0.49 μm/s.

4.4. Results and Discussion

4.4.1. Characterization of the Material

4.4.1.1. X-ray Diffraction Analysis for Different Surface Chemistry of 10 nm-Sized Nanoparticles

X-ray diffraction analysis for the modified 10 nm-sized silicate-based nanoparticles is shown in **Figure 4.3**. The sharp peaks in the X-ray pattern suggest crystallinity of the nanoparticles. The pattern confirms that the nanoparticles are silicate-based. This confirmation was carried out by comparing the experimental patterns with reported signals included in the pdf card #01-076-2564 of the 2005 ICDD (International Centre for Diffraction Data) database in the program JADE V.7.5.1 (Materials Data XRD Pattern Processing Identification and Quantification) (Vitale, 2013). The broad pattern also indicates that these nanoparticles have a small crystalline domain size, which is expected as the 10 nm-sized silicate-based material was modified chemically on the surface, but not structurally, and that is why all three present the same pattern.

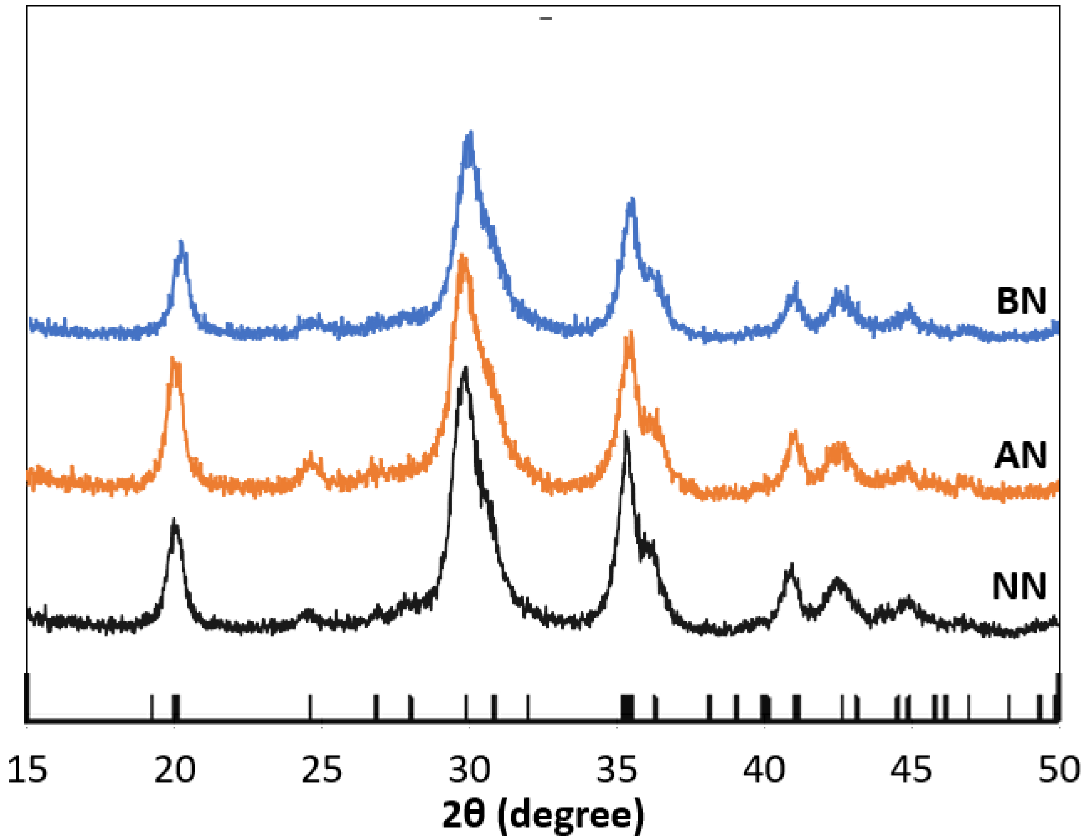

Figure 4.3. X-ray diffraction patterns of the modified surfaces of the nanoparticles for (a) basic nanoparticles (BN), (b) acidic nanoparticles (AN), and (c) neutral nanoparticles (NN). The vertical lines are the reference data (pdf card #01-076-2564) for iron-silicate pyroxene from Materials Data XRD Pattern Processing Identification & Quantification.

4.4.1.2. Textural Properties

From the BET analysis for the modified and unmodified 10 nm-sized nanoparticles, there is not a significant difference between the surface area obtained by BET and that obtained by the *t*-plot method; this agrees with the results reported in the literature for silicate-based materials (Vitale, 2013; Vitale et al., 2020). This means that the studied nanoparticles do not have significant porosity and maintain large surface areas (Nassar, Hassan, & Pereira-Almao, 2011; Vitale et al., 2020). An estimation of the particle size was made assuming spherical particles and using the following equation:

$$d = \frac{6000}{SA * \rho_{SBN}} \tag{4.1}$$

where d is the particle size in nm, SA is the experimentally measured specific surface area by BET (m^2/g), and ρ_{SBN} is the iron silicate density (3.577 g/cm^3). As shown in **Table 4.2**, the values obtained for 10 nm-sized neutral, basic, and acid nanoparticles agree with the values obtained by X-ray. Hence, the assumption of spherical nanoparticles is correct.

Table 4.2. BET surface area, particle size, and XRD crystalline domain size for the 10 nm unmodified and modified nanoparticles.

Nanoparticle	**BET surface area (m^2/g)**	**Particle size by BET (nm)**	**Crystalline domain size by XRD (nm)**
Neutral	171	9.8±0.07	10 ± 2
Basic	181	9.2±0.09	10 ± 3
Acid	203	8.2±0.07	10 ± 2

4.4.1.3. TPD Analysis

A surface acidity analysis of the modified nanoparticles was performed using the NH_3-TPD method to quantify the total acid sites (Brønsted+Lewis) (Vitale, 2013), and the results are shown in **Table 4.3**. The proton ion exchange with H_2SO_4 on the surface increased the number of acid sites from 609.4 μmol/g to 1004.8 μmol/g. For the ion exchange with $Ca(NO_3)_2.4H_2O$, the number of acid sites also increased from 609.4 μmol/g to 857.8 μmol/g. Dividing the amount of NH_3 adsorbed per nanoparticle by the surface area of NH_3, 3.6 μmol/ m^2 is obtained for a neutral material (without modification), 4.7 μmol/ m^2 for basic nanoparticles, and 4.9 μmol/ m^2 for acid nanoparticles. Compared with the original material, the acid sites increased with modification, but for the acid and basic nanoparticles, there was no noticeable difference.

Table 4.3. TPD results for the 10 nm-sized nanoparticles with and without modification.

Material	NH_3 µmol/g
Neutral	609.4
Basic	857.8
Acid	1004.8

4.4.1.4. High Resolution Transmission Electron Microscopy (HRTEM) Analysis

As shown in **Figure 4.4a-c**, HRTEM images confirm the presence of silicate-based nanoparticles. Both the unmodified and modified nanoparticles are spherical in shape. **Figure 4.4a-c** show that all nanoparticles tend to form large particles composed of small particles, which explains the large surface area for the small-sized (less than12 nm) silicate-based nanoparticles (Vitale et al., 2020).

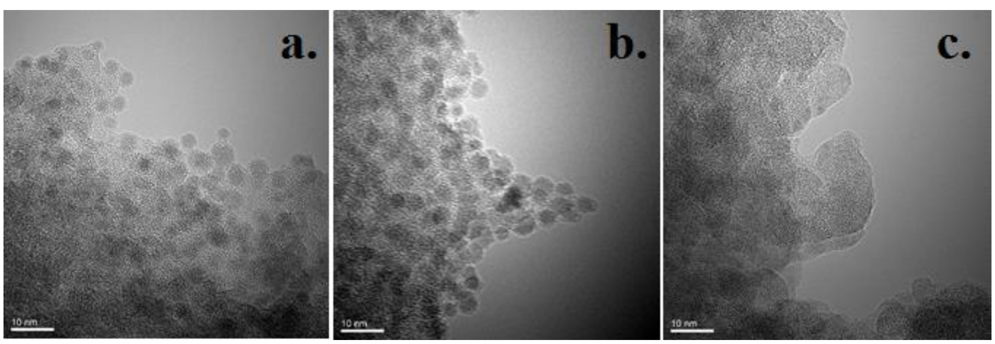

Figure 4.4. HRTEM images for the 10 nm-sized silicate-based nanoparticles: (a) acidic nanoparticles (AN), (b) basic nanoparticles (BN), and (c) neutral nanoparticles (NN). Line marks in the images correspond to 10 nm scale.

4.4.2. QCM-D Asphaltene Coating

Figure 4.5a-b shows the results for the asphaltene depositions on SiO_2 coated surfaces in heptol 70 and toluene, respectively, at overtone 9. The frequency of all four sensors (two repeats for each deposition) shifted in a negative direction, which indicated asphaltene adsorption on the sensor surface in both, the heptol 70 and toluene solvent media. Equilibrium was reached at about 55 min, and the duplicate measurements for each solvent exhibited reproducible frequency shifts, indicating that the experiments were performed under very close conditions in the different QCM-D modules. Consequently, small particles adsorbed on the surfaces of the sensors, and these particles had lower resonance frequencies compared with the resonance frequency of the sensor alone (before adsorption) (Reviakine et al., 2011; Wang, Segin, Wang, Masliyah, & Xu, 2011).

Since QCM-D measures total mass, the mass calculated from the data includes the mass of asphaltenes and the mass of heptol 70 or toluene (Johannsmann, Reviakine, Rojas, & Gallego, 2008). As shown in **Figure 4.5a-b**, dissipation values of heptol 70 asphaltenes was higher than the dissipation for the toluene asphaltenes; this could indicate that the layer formed by the toluene asphaltenes was more rigid than the one formed by the heptol 70 asphaltenes. This result agrees with reports that state that the size of the toluene asphaltene molecules are smaller than those of heptol 70 (Dudášová, Silset, et al., 2008; F. Liu, Hickman, Maqbool, Pauchard, & Banerjee, 2020). The adsorption/deposition of the first asphaltene layer in both cases occurred due to the interaction between π-electrons and the SiO_2 active sites (Keiluweit & Kleber, 2009); following this, the asphaltenes formed multilayers due to their amphiphilic nature and weaker interactions between alkyl chains of the aggregates/molecules in the solution and the nonpolar part exposed from the first layer of adsorbed/deposited asphaltenes (F. Liu et al., 2020; Vuillaume & Giasson, 2009). This result agrees with other QCM-D studies in the literature (Dudášová, Silset, et al., 2008; F. Liu et al., 2020; Zahabi et al., 2012) where asphaltenes at different stages of aggregation have been studied. One explanation for a softer heptol 70 layer could be that the heptol 70 asphaltenes formed larger aggregates that entrapped more solvent molecules compared to the toluene asphaltenes, resulting in a less rigid layer as indicated by higher dissipation (F. Liu et al., 2020). Aggregate size distribution for heptol 70 asphaltenes is shown in **Figure 4.6**. It is worth mentioning that toluene asphaltenes aggregates size was not detected by the DLS equipment, therefore it was not included, but it is expected to be much smaller than heptol 70 asphaltenes as toluene is a well-known solvent.

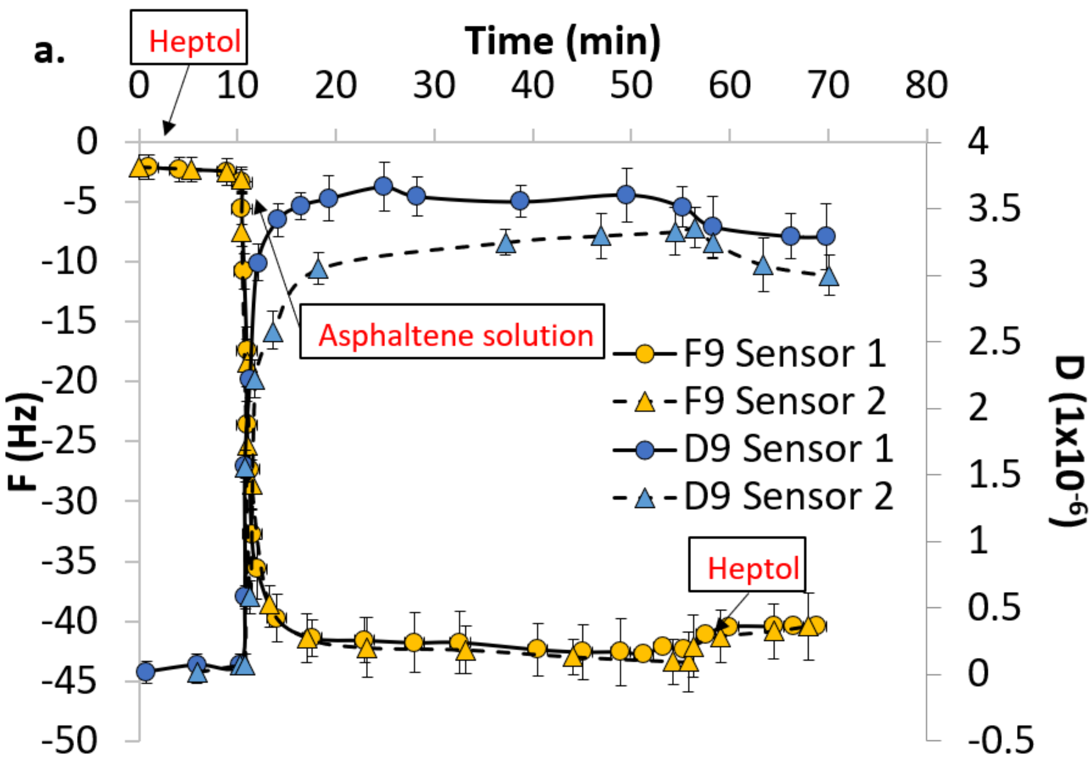

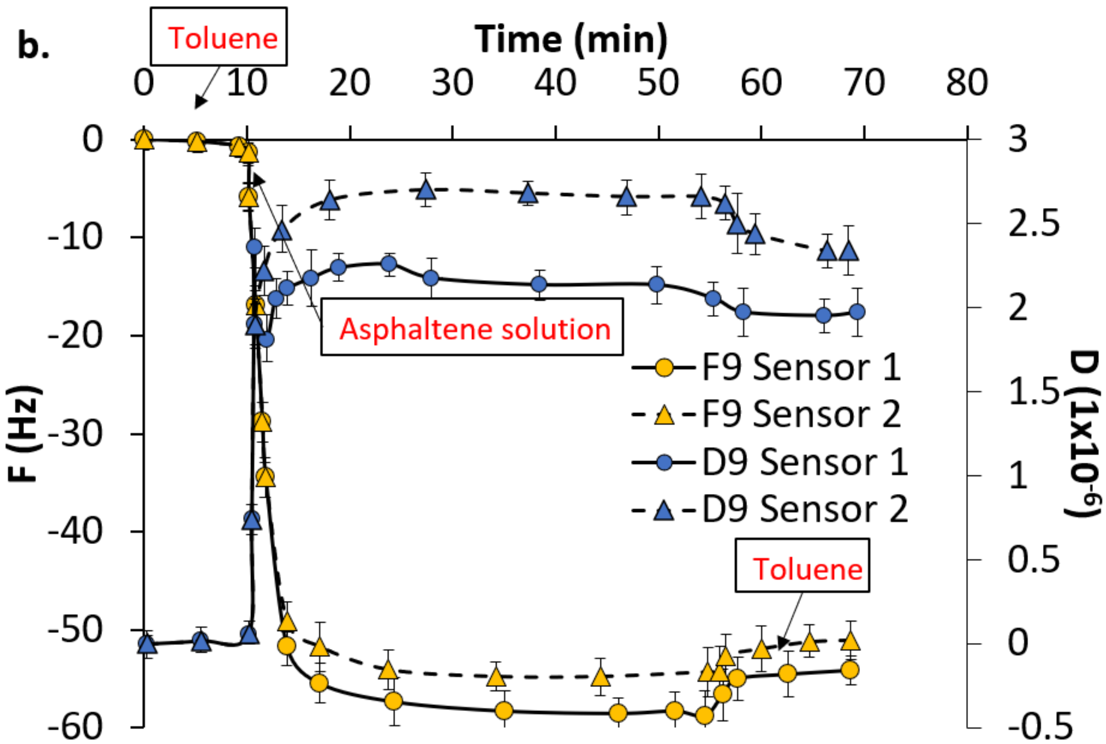

Figure 4.5. Frequency and dissipation shifts for asphaltene coatings on SiO_2 sensors for two asphaltene solutions a) heptol 70 and b) toluene. Experimental conditions: flow rate 150 µL/min, temperature 25 °C, experiment time 1 hr and 20 min. Concentrations of heptol 70 and toluene in the asphaltene solution are 500 and 180 mg/L, respectively.

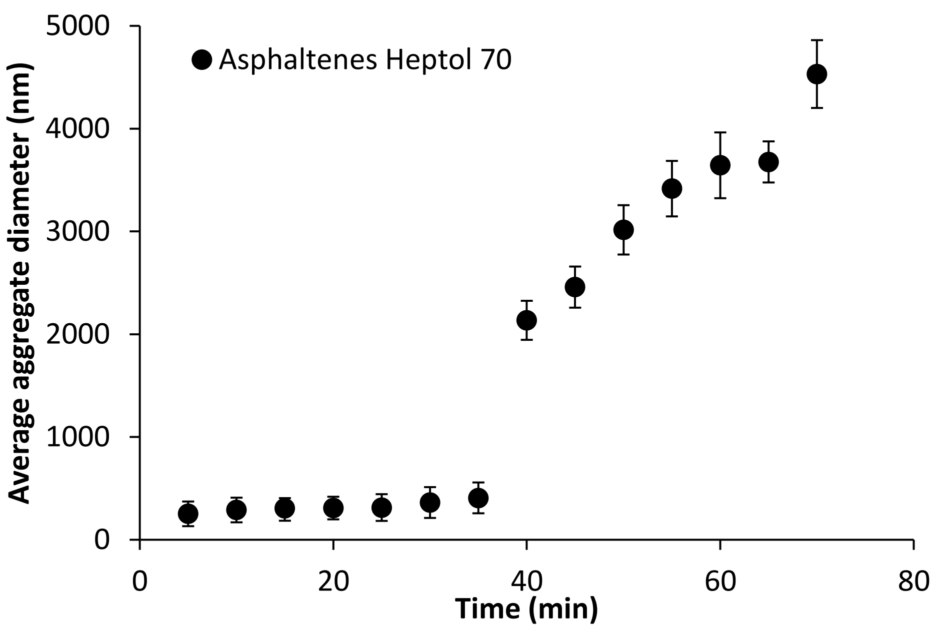

Figure 4.6. Heptol 70 asphaltenes average aggregates diameter with time measured in DLS using a quartz cell at 25 °C.

The negatively charged SiO_2 (Farooq, Asif, Tweheyo, Sjöblom, & Øye, 2011; Richards, 2006) may behave as a Bronsted acid (Farooq et al., 2011), whereas the asphaltenes can have basic components in their structure (Chen & Akbulut, 2012) that may lead to the formation of strong acid-base electrostatic interactions between the two. In addition, the interaction between aromatic groups present in the asphaltenes and the sensor surface may occur (Chen & Akbulut, 2012; Farooq et al., 2011; J. Liu, Zhang, Xu, & Masliyah, 2006).

The thicknesses of the adsorbed/deposited asphaltenes from heptol 70 and toluene solutions were calculated from QCM-D data as ~54 nm and ~28.3 nm, respectively. This calculation agreed with what has been reported in the literature (F. Liu et al., 2020; Vuillaume & Giasson, 2009); as the solubility of the asphaltenes decreased, i.e., as they formed aggregates in heptol 70, the adsorbed/deposited layer was thicker than the layer for asphaltenes in smaller molecules (toluene); consequently, a concentration of 70% heptane-30% toluene experienced more asphaltene adsorption/deposition in this QCM-D studies.

As shown in **Figure 4.7a-c**, the contact angle increased after the adsorption/deposition of asphaltenes compared with the bare SiO_2 sensor, indicating that there was a change in the wettability of the SiO_2 surface after asphaltene adsorption, making it less compatible with water. Also, the contact angle for the sensor with toluene asphaltenes was lower than that for the sensor with heptol 70 asphaltenes. This result agreed with the findings from the QCM-D measurements discussed above; heptol 70 asphaltenes formed larger aggregates that had room for larger amount of heptol 70 therefore they entrapped more solvent. The non-polar properties of heptol 70 made the surface more hydrophobic compared to toluene asphaltenes, where less amount of solvent (toluene) was entrapped due to the small size of adsorbed particles.

Figure 4.7. Contact angle measurements at 25 °C for a) water drop/air/SiO_2 original sensor, b) water drop/air/SiO_2 with adsorbed/deposited asphaltenes from heptol 70 solution and c) water drop/air/SiO_2 with adsorbed/deposited asphaltenes from toluene solution.

4.4.3. Effect of Surface Chemistry

Figure 4.8a-b represent frequency shift and dissipation shift, respectively, for the sensors coated with toluene asphaltenes after the flow of the BN, AN, and NN nanofluids in brine at a nanoparticle concentration of 100 ppm. Data for only 9 overtone are shown for clarity. As shown in **Figure 4.8a**, the frequency increased for each nanofluid tested in the order BN >AN >NN. An increase in frequency associated with a decrease in or a constant dissipation usually represents a loss of mass. In these experiments, however, the frequency and associated dissipation both increased (**Figure 4.8b**). These results demonstrated the flow of the different nanofluids on adsorbed asphaltene softens the layer, making it more viscoelastic (Pomorska et al., 2010). Notably, the BN nanofluid presented a higher shift, which indicated a stronger interaction with the pre-adsorbed/deposited asphaltenes compared with the other two nanofluids. The acid sites created on the surface of the modified BN and AN seemed to improve the interaction between the exposed parts of the asphaltenes (that could be alkyl chains or heteroatoms) (F. Liu et al., 2020; Vuillaume & Giasson, 2009). There was a possibility that the nanoparticles partially removed the pre-adsorbed/deposited asphaltene layer and reorganised of the adsorbed/deposited layer at the asphaltene-SiO_2 sensor interface as suggested in the literature when studying the effect of an asphaltene inhibitor (F. Liu et al., 2020).

Table 4.4 presents the results for the layer thickness obtained from analysing the QCM-D data using the extended viscoelastic model in QTools. After flowing nanofluids, the layer is called asph+nanoparticles in **Table 4.4**; for all three cases the layer thicknesses increased after the injection of nanofluids. These results could prove to be very important when formulating a nanofluid to treat reservoirs that have formation damage caused by asphaltene precipitation. The surface chemistry plays a role in the wettability alteration and interaction with asphaltenes.

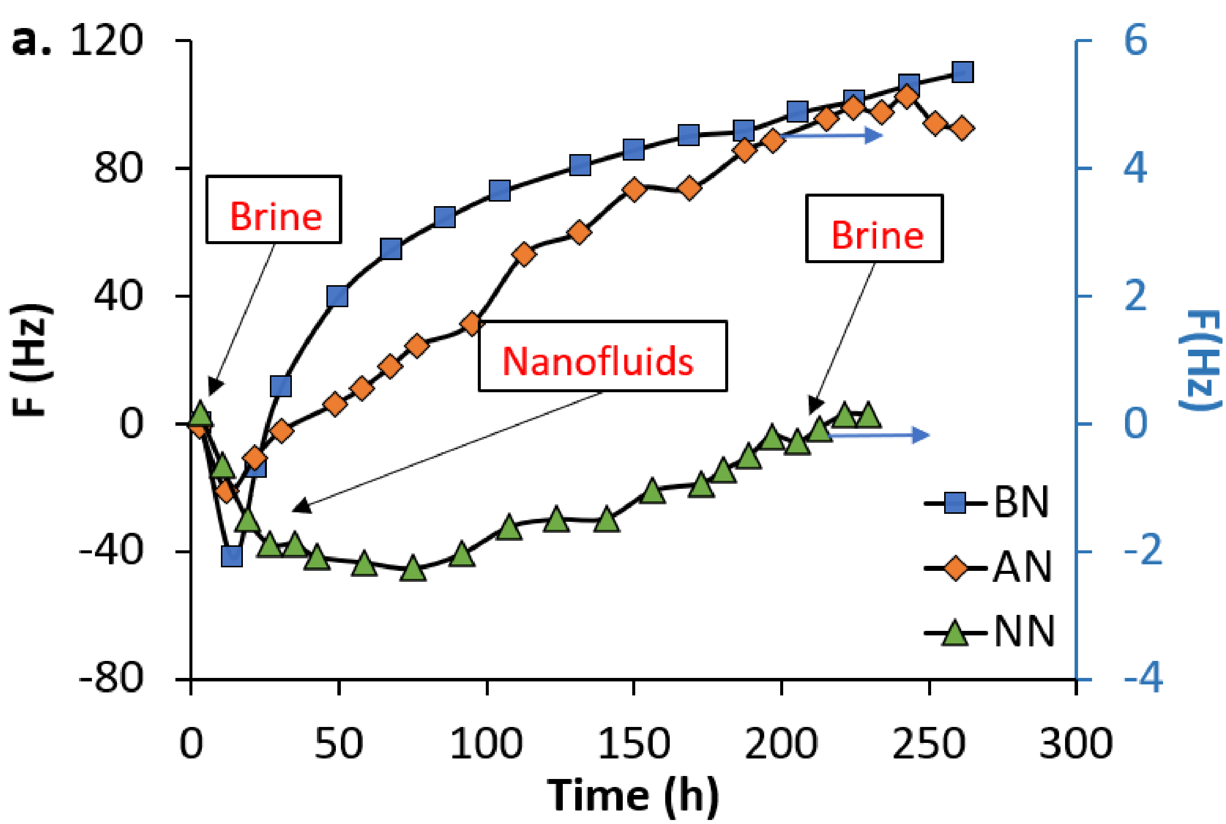

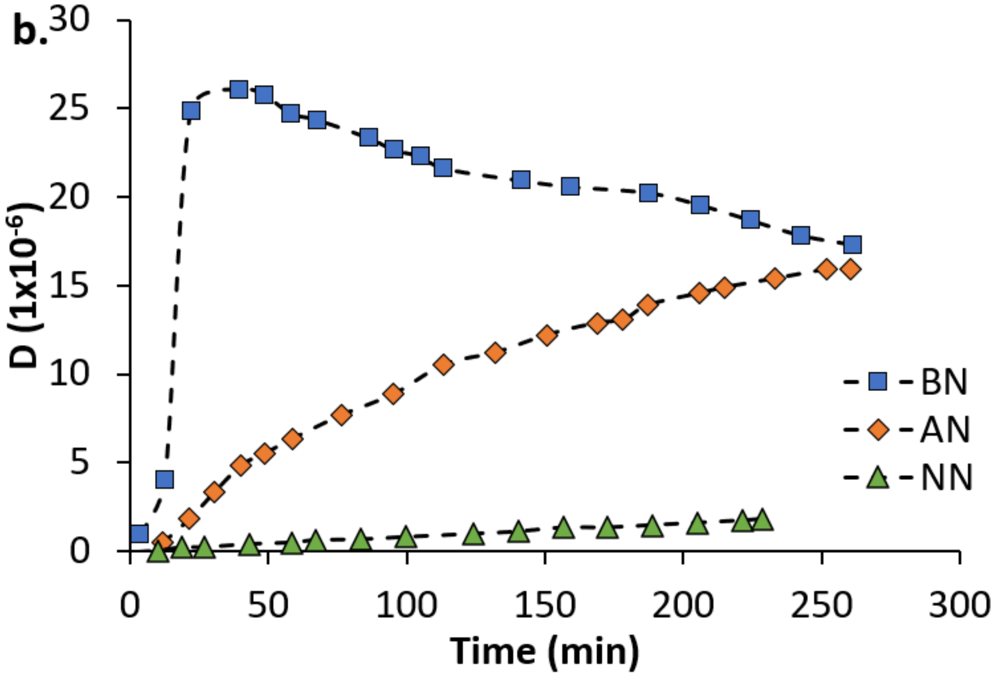

Figure 4.8. Effect of nanoparticles that have different surface chemistries on SiO_2 sensors with pre-adsorbed/deposited asphaltenes from toluene solutions a) Frequency shift and b) Dissipation shift. Experimental conditions are flow rate 150 µL/min, temperature 25 °C, experiment time 260 min. For the nanofluids: concentration of the10 nm BN, AN, and NN 100 in 1000 mg/L NaCl brine.

Table 4.4. Layer thicknesses obtained from QTools for nanofluids that have different surface chemistry.

Nanofluid	**Asphaltene layer (nm)**	**Asph+Nanoparticle layer (nm)**
NN	36±0.14	53
AN	20±0.14	35
BN	28±0.14	46

Figure 4.9a-d show the water contact angle for the sensor with adsorbed/deposited toluene asphaltenes after injection of the BN, AN, and NN nanofluids. As shown, the contact angle is reduced after the injection of the nanofluids in the following order BN<AN<NN. These results agree with the results obtained for the frequency shifts and layer thickness. The BN nanofluid had

the highest reduction, making the surface more water-wet (hydrophilic), which could indicate that the nanoparticles were removing some of the asphaltenes, and the adsorbed/deposited layer was being reorganised. Similar behaviour was observed for the AN nanofluid. In the case of the NN nanofluid, the reduction in the contact angle was not significant possibly because the interaction between the unmodified silicate-based nanoparticles and the pre-adsorbed asphaltenes was insignificant. It seems that the active sites of the NN nanoparticles did not have high affinity with the exposed functional groups of the pre-adsorbed/deposited asphaltenes. However, as noted in the literature (F. Liu et al., 2020), there is a possibility that the nanoparticles aggregated over the pre-adsorbed/deposited asphaltene layer, resulting in increased layer thickness after the nanofluid injection. If this were the case, some of the brine could have been trapped between adsorbed nanoparticles, resulting in a high dissipation shift as shown in **Figure 4.8b**. Since BN nanofluids caused more interaction and the highest reduction in the contact angle, these nanoparticles were chosen for the subsequent sections.

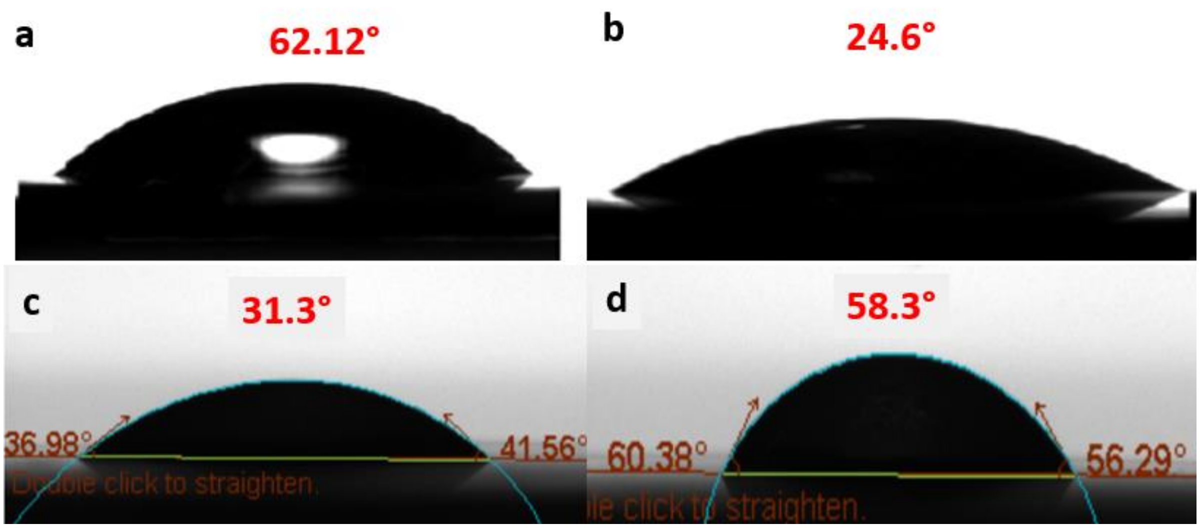

Figure 4.9. Contact angle measurements at 25 °C for a) water drop/air/SiO_2 with adsorbed/deposited asphaltenes from toluene solution, b) water drop/air/SiO_2 with adsorbed/deposited asphaltenes from toluene solution after brine nanofluid with BN, c) water

drop/air/SiO_2 with adsorbed/deposited asphaltenes from toluene solution after brine nanofluid with AN and d) water drop/air/SiO_2 with adsorbed/deposited asphaltenes from toluene solution after brine nanofluid with NN. Nanoparticle concentration is 100 and 1000 mg/L concentration of NaCl brine.

4.4.4. Effect of Nanoparticle Concentration

Figure 4.10a-b show the frequency and dissipation shifts, at overtone 9, for the sensors with asphaltene coating from heptol 70 and toluene solutions after the flow of 10 nm BN nanofluids in brine at nanoparticle concentrations of 1, 10, and 25 mg/L, and at 25, 50, 100, and 150 mg/L, respectively. **Figures 4.11 and 4.12** show the zeta potential (ζ) and DLS measurements of these nanofluids; As seen, for all the concentrations considered in this set of experiments, ζ values were < -30. The value of ζ of the nanofluids indicates their stability, higher ζ absolute values (i.e., >30 or < -30 indicate more stable nanofluids with low tendency to flocculate and precipitate (Hwang et al., 2008; Standard, 1985). For all nanofluids concentration ζ value were < -30, this means the nanofluids are stable (Hwang et al., 2008; Standard, 1985). This is also confirmed by the DLS analyses as shown on **Figure 4.12**. The average particle size does not change considerably during the QCM-D experiments time (240 min on average). The results show that the resonance frequency of the heptol 70 asphaltene coated sensor increased with exposure to BN nanofluids at all concentrations in the order 1>10>25 mg/L. The associated dissipation also increased following a similar trend. Exposing BN nanofluids to the toluene asphaltene coated sensor, as shown in **Figure 4.10b**, caused an increase in frequency in the following trend 100 >150 >50>25 mg/L.

As shown in **Figure 4.10a-b**, the frequency and dissipation shifts are positive for all nanofluids and concentrations. In the literature (Pomorska et al., 2010), this phenomena is explained within the framework of the QCM-D as a force balance in terms of the stiffness of the sphere/crystal contact. Sensitivity to the particle-surface contact stiffness arises because the particles are attached to surfaces via narrow linkers or contact zones (Pomorska et al., 2010; Reviakine et al., 2011) that act as a spring, the frequency of which adds to the sensor oscillation frequency leading to a positive shift in frequency (Pomorska et al., 2010). In this case, the nanoparticles essentially act as lever arms pivoted around the linkers as they are moved through the liquid by the oscillating crystal.

When comparing the change in dissipation, the sensor with heptol 70 asphaltenes showed lower dissipation than the sensors with toluene asphaltenes after nanofluid injection. There are two factors that could have influenced these results; first, the adsorbed heptol 70 asphaltenes aggregated and were adsorbed/deposited as larger aggregates, and when the nanofluids were injected, the nanoparticles occupied spaces between asphaltene molecules and interacted not only with the exposed functional groups of the asphaltenes but laterally as well. These interactions resulted in a less viscoelastic layer (compared to those injected into the toluene-asphaltene sensors). Secondly, in the case of the asphaltenes on the toluene sensors, the concentrations of the nanofluids were higher and, as discussed above, the asphaltene layer was less viscoelastic. Hence, the nanoparticles formed another layer on top of the pre-adsorbed/deposited asphaltenes and formed aggregates that trapped some of the brine in between aggregates of nanoparticles, which resulted in a higher dissipation. These results agreed with the study performed by Lui, F. et al.,(F. Liu et al., 2020) where an asphaltene inhibitor was used in different concentrations in QCM-D experiments; at higher concentrations the effect was the opposite, and the inhibitor did not remove asphaltenes from the sensor surface, but instead, the inhibitor was being adsorbed on the sensor surface because it was forming aggregates over the asphaltenes, which resulted in an increase in the adsorbed mass.

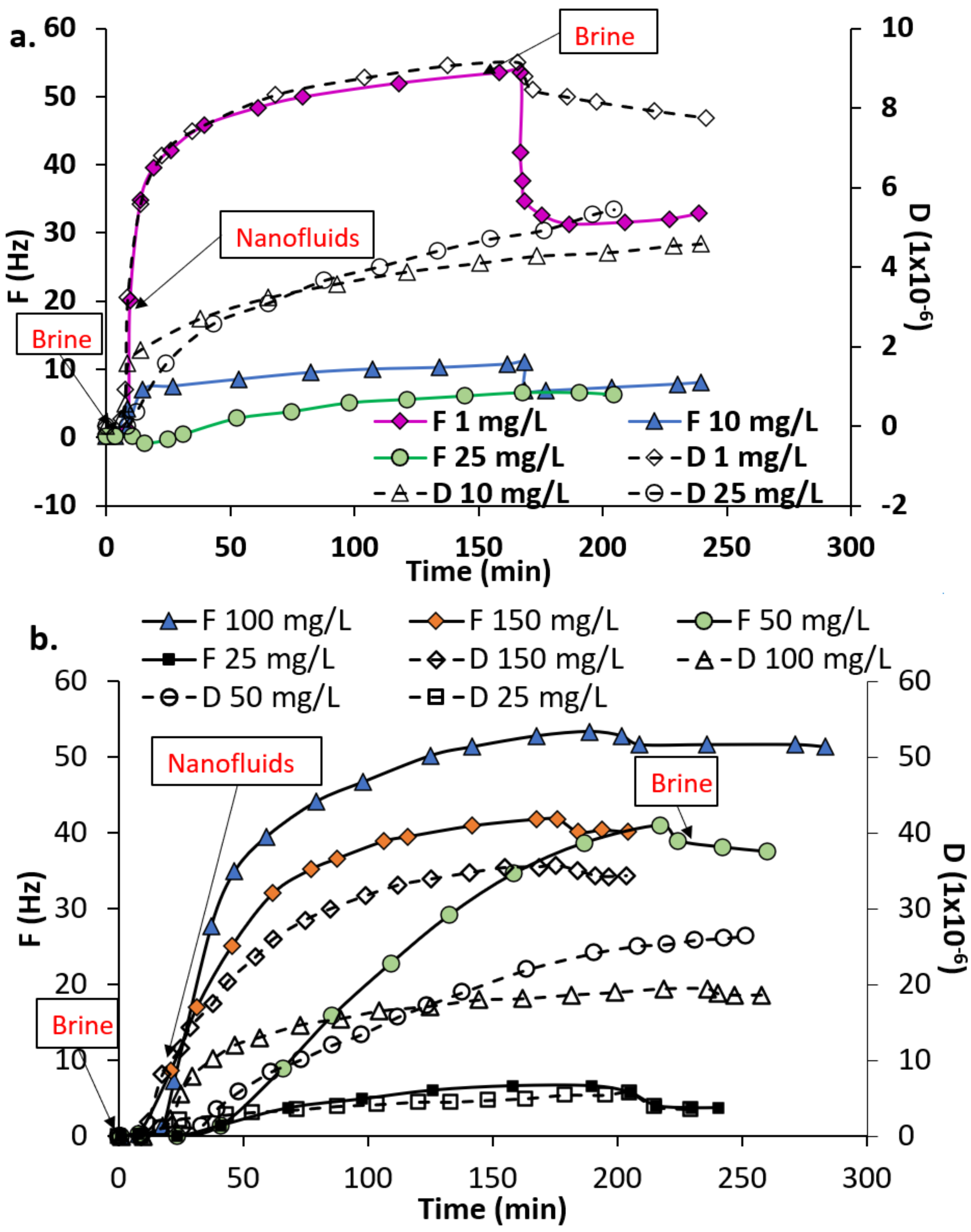

Figure 4.10. Effect of nanoparticle concentrations on pre-coated asphaltene SiO_2 sensors for a) asphaltenes from heptol 70 concentrations of 1, 10, and 25 mg/L and b) asphaltenes from toluene concentrations of 25, 50, 100, and 150 mg/L. Experimental conditions are flow rate 150 µL/min, temperature 25 °C, experiment time 260 min. For the nanofluids: 10 nm BN in 1000 mg/L NaCl brine.

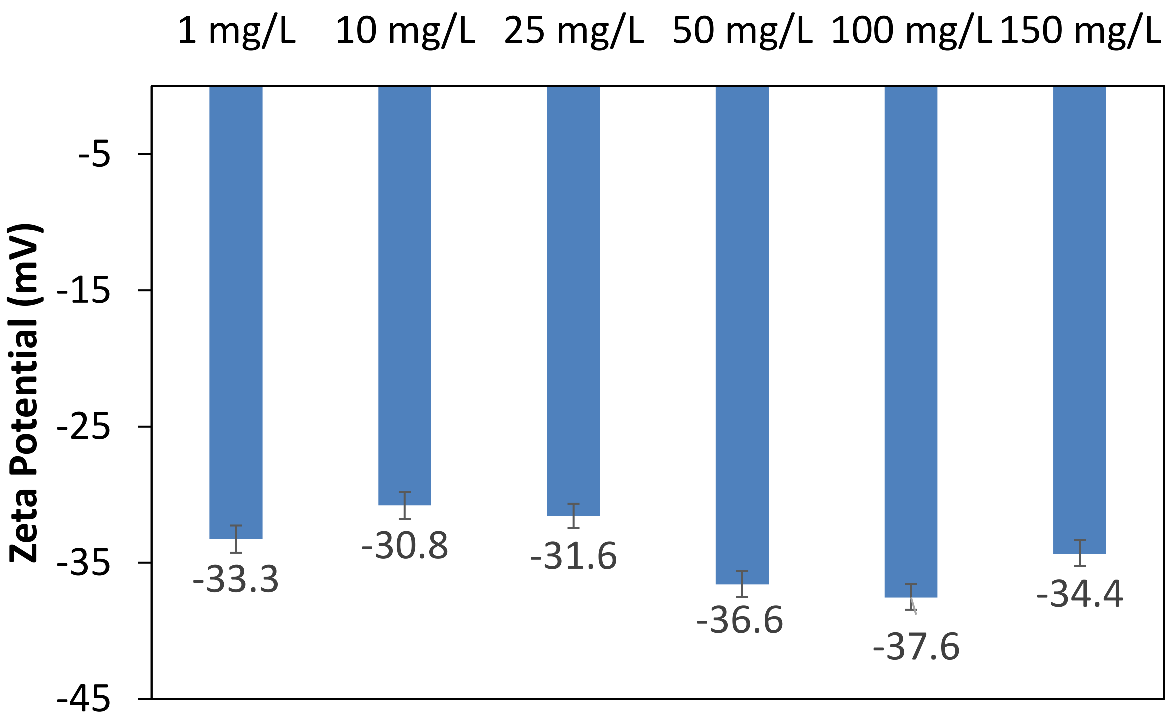

Figure 4.11. ζ potential of silicate-based nanofluids at different nanoparticles concentrations.

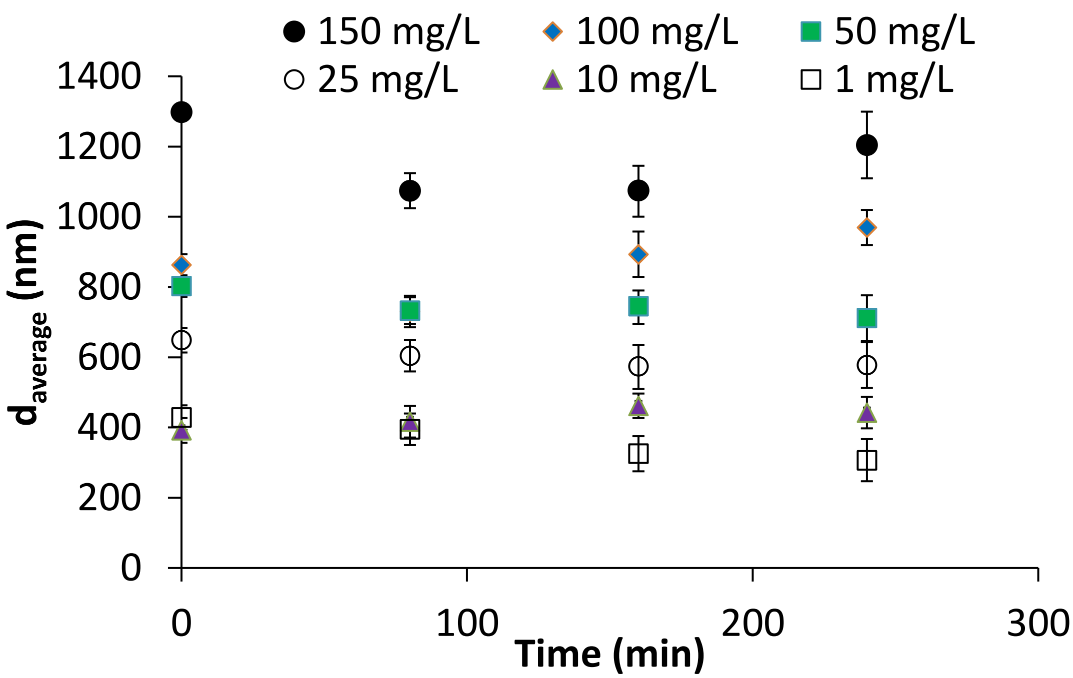

Figure 4.12. Average particle size measured in the DLS each 80 min for the silicate-based nanofluids at different concentrations.

Table 4.5 presents the results for the thicknesses of the layer before and after the different nanofluid injection concentrations for the sensors with heptol 70 and toluene asphaltenes. As shown, in both cases, the layer thickness increased after the nanofluid injection. In the case of the sensors with heptol 70 asphaltenes, the layer thickness is higher at lower concentrations of nanofluids. Since there are fewer nanoparticles in solution, they interact less with each other and more with the high energy sites of the pre-adsorbed/deposited asphaltenes, which possibly increases the aggregation of the nanoparticles over the surface, allowing the formation of a bigger adsorbed layer, because more particles will interact with the pre-adsorbed/deposited asphaltene layer. In the case of the sensor with toluene asphaltenes, a different trend was observed. For 25 and 50 mg/L, the final layer thickness increased as the concentration increased, while for 100 and 150 mg/L, the layer thickness decreased possibly because the nanoparticles in the lower nanofluid concentrations were adsorbed over the high energy sites of the pre-adsorbed/deposited asphaltenes and were aggregating more over the surface than the nanoparticles from higher concentrations. Also, the aggregates of nanoparticles in the higher nanofluid concentrations possibly removed some of the asphaltenes and were not linked to the asphaltenes strongly enough on the surface, and consequently, the layer thickness was not that high. QCM-D does not record this as suggested by Dudášová, D. et al. (Dudášová, Silset, et al., 2008) because the shear rate of the brine is not high enough to remove the excess nanoparticles, and they are trapped on the sensor (Dudášová, Silset, et al., 2008).

Table 4.5. Layer thicknesses obtained from Q-tools for different nanofluid concentrations.

Asphaltenes	**Concentration (mg/L)**	**Asphaltene layer (nm)**	**Asph+Nanoparticle layer (nm)**
Heptol 70	1	68±0.14	118

	10	64±0.14	77
	25	36±0.14	49
Toluene	25	12±0.14	35
	50	35±0.14	90
	100	28±0.14	46
	150	14±0.14	32

Figures 4.13a-d and 4.14a-e present the results for the contact angle after the nanofluid injection at different concentrations for the sensors with pre-adsorbed/deposited asphaltenes from heptol 70 and toluene, respectively. In both cases, the contact angle decreased, which indicated the nanofluids were acting as wettability alternators. For the sensors with pre-adsorbed heptol 70 asphaltenes, the order was 1<10<25 mg/L, and for the toluene sensors, the order was 100<150< 50<25 mg/L. The greater reduction was after 1 mg/L BN nanofluid injection close to the original contact angle of the SiO_2 sensor (7°). This result could be due to the nanoparticles in the nanofluid being more homogeneously distributed and adsorbed onto the asphaltene layer; this conclusion was supported by the QCM-D results because the frequency was the highest. In the case of the heptol 70 sensors, the contact angle increased as the nanofluid concentration increased possibly because the nanoparticles formed larger aggregates on the high energy sites, leaving some of the surface with exposed asphaltenes. In the case of the toluene sensors, it seemed that higher nanofluid concentrations were more effective in the wettability alteration because the surface became more water-wet (decreased contact angle); however, for the highest concentration (150 mg/L), an opposite trend was observed, and the contact angle started to increase compared to that for the concentration of 100 mg/L. This experiment is very important for the oil and gas industry because it determines the optimum nanoparticle concentration to prepare the nanofluid, which can

help reverse formation damage without compromising other reservoir characteristics such as permeability and wettability.

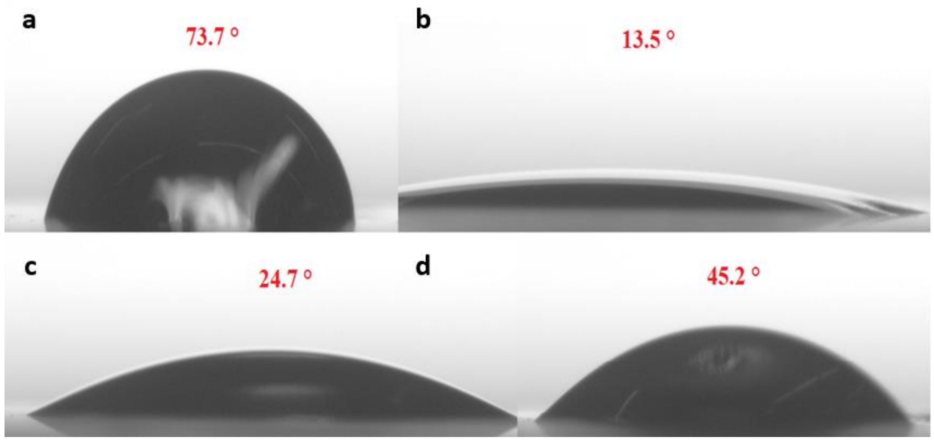

Figure 4.13. Contact angle at 25 °C for a) water drop/air/SiO_2 with adsorbed/deposited asphaltenes from heptol 70 solution, b) water drop/air/SiO_2 with adsorbed/deposited asphaltenes from heptol 70 solution after flooding with 1 mg/L BN nanofluid, c) water drop/air/SiO_2 with adsorbed/deposited asphaltenes from heptol 70 solution after flooding with 10 mg/L BN nanofluid, and d) water drop/air/SiO_2 with adsorbed/deposited asphaltenes from heptol 70 solution after flooding with 25 mg/L BN nanofluid. For the nanofluids: 10 nm BN in 1000 mg/L NaCl brine.

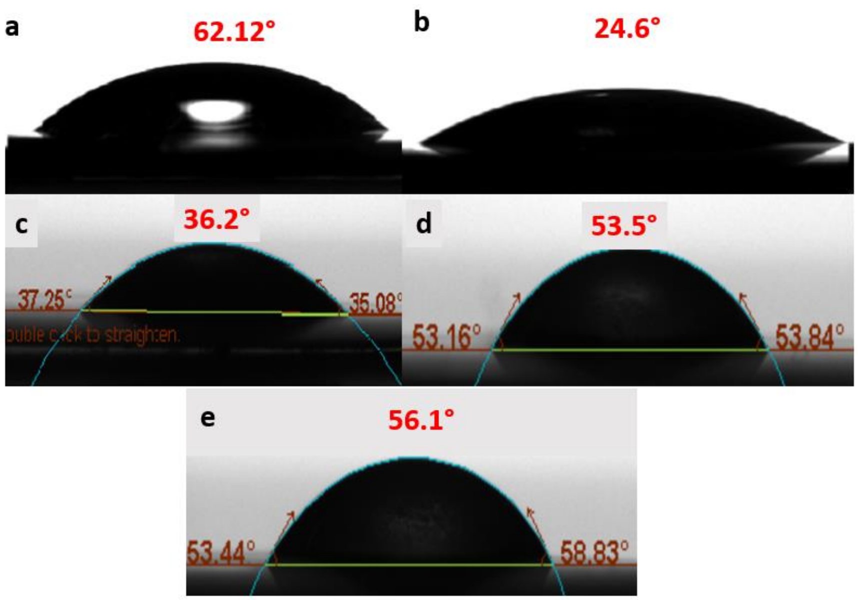

Figure 4.14. Contact angle at 25 °C for a) water drop/air/SiO_2 with adsorbed/deposited asphaltenes from toluene solution, b) water drop/air/SiO_2 with adsorbed/deposited asphaltenes from toluene solution after flooding with 10 mg/L BN nanofluid, c) water drop/air/SiO_2 with adsorbed/deposited asphaltenes from toluene solution after flooding with 150 mg/L BN nanofluid, d) water

drop/air/SiO_2 with adsorbed/deposited asphaltenes from toluene solution after flooding with 50 mg/L BN nanofluid and d) water drop/air/SiO_2 with adsorbed/deposited asphaltenes from toluene solution after flooding with 25 mg/L BN nanofluid. For the nanofluids: 10 nm BN in 1000 mg/L NaCl brine.

Figure 4.15a-d show the AFM images for the SiO_2 sensors coated with heptol 70 asphaltenes before and after flooding with different concentrations of nanofluids. As shown, increasing the concentration of the nanoparticles in the nanofluid causes particle aggregation over the pre-adsorbed/deposited asphaltene layer; molecules with larger sizes can be observed in **Figure 4.15c-d.** This result could be due to the tendency of nanoparticles to form multiple layers over high energy sites, and when the concentration is low, the nanoparticles are distributed more homogeneously over the asphaltene layer and interact less with each other, as discussed above.

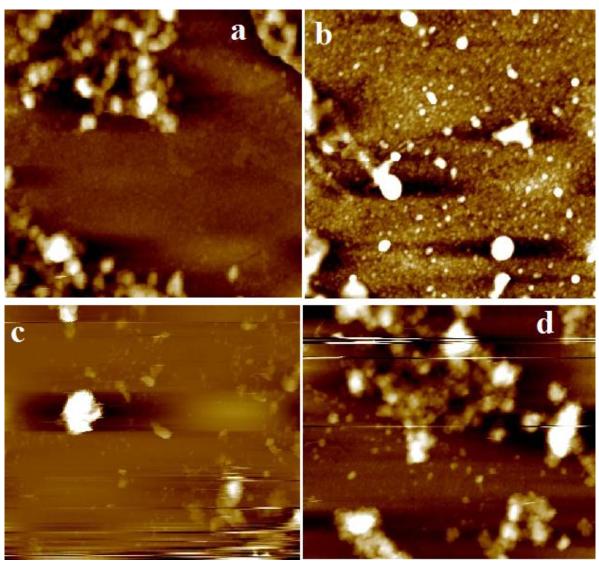

Figure 4.15. AFM retrace contact mode topographic images for a) SiO_2 sensor after asphaltenes in heptol 70 adsorption/deposition, b) SiO_2 sensor after asphaltenes in heptol 70 adsorption/deposition after 1 mg/L BN nanofluids injection, c) SiO_2 sensor after asphaltenes in heptol 70 adsorption/deposition after 10 mg/L BN nanofluids injection and d) SiO_2 sensor after asphaltenes in heptol 70 adsorption/deposition after 25 mg/L BN nanofluids injection. The dimension for the images is 5 μm × 5 μm.

4.4.5. Effect of Nanoparticle Size

Figure 4.16a-b present the QCM-D frequency and dissipation changes, respectively, over the sensors with pre-adsorbed/deposited toluene asphaltenes after the flow of nanofluids with different particle sizes of 10, 20, 45, and 99 nm of BN. As shown, the dissipation increases as the frequency increases for the 10 and 99 nm nanofluids. As previously mentioned, the adsorbed particles bond to the asphaltene layer via sufficiently weak bridges, which causes a positive frequency shift. In contrast, for the 20 and 45 nm nanoparticles, there is a negative shift in the frequency associated with positive dissipation shift, which indicates adsorption of these particles (without any bridges) over the pre-adsorbed asphaltenes on the sensor surface. These results suggest that the interactions of the nanoparticles with the pre-adsorbed/deposited asphaltenes is size dependant and perhaps related to the preparation of the nanomaterials. The different preparation methods also affect the shape of the nanoparticles, which, in turn, can affect their interaction with the asphaltenes. The positive changes in dissipation values observed in **Figure 4.16b** suggest that the layers formed after the nanofluid injection with different particle sizes are soft in all cases.

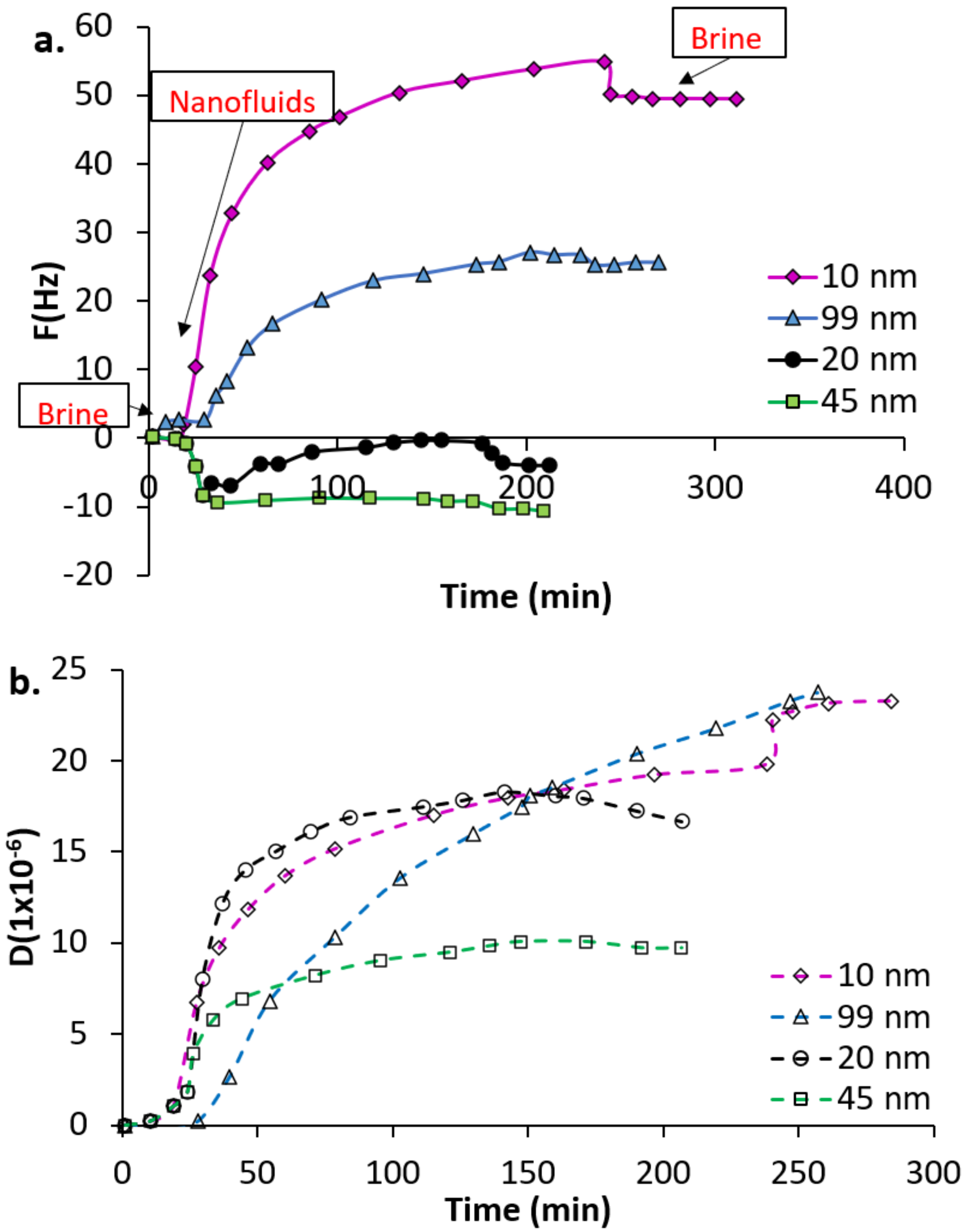

Figure 4.16. Effect of different nanoparticle sizes, 10, 20, 45, and 99 nm, on SiO_2 sensors with pre-adsorbed/deposited asphaltenes from toluene solutions a) Frequency (Hz) and b) Dissipation. Experimental conditions are flow rate 150 µL/min, temperature 25 °C, experiment time 260 min. For the nanofluids: concentrations of different BN nanoparticle sizes 100 mg/L in 1000 mg/L NaCl brine.

Table 4.6 presents the results for the layer thicknesses obtained from QTools. As shown, the layer was thicker after the nanofluid injection. The 20 nm BN nanofluids seemed to have the thickest layer compared with the other nanofluids possibly because the sensor had the thickest asphaltene layer before the nanofluid injection. For the other sizes, there were no significant differences, which suggested that the interaction between the asphaltenes and the 10 nm, 45 nm, and 99 nm nanoparticles were similar.

Table 4.6. Layer thicknesses obtained from QTools for different BN nanoparticles sizes in nanofluids.

Size (nm)	Asphaltene layer (nm)	Asph+Nanoparticle layer (nm)
10	28±0.14	46
20	54±0.14	82
45	34±0.14	46
99	27±0.14	51

Figure 4.17a-e show the contact angle results before and after the injection of different particle sizes in nanofluids; the order of contact angle was observed as follows:10 nm<99nm< 45 nm< 20 nm. The 20 nm BN nanofluids had the least contact angle reduction from the untreated asphaltene surface because of the lack of affinity between these nanoparticles and the pre-adsorbed asphaltenes. The fact that the layer of the nanofluid had the thickest layer and was linked to the contact angle could mean that the nanoparticles were being adsorbed/deposited at a few active sites and were forming agglomerates on these sites. A similar observation was seen for the 45 nm nanofluids. However, for the larger 99 nm nanoparticles, the adsorption/deposition was not as homogeneous as in the case of the 10 nm nanofluid, resulting in less reduction in the contact angle. From these results, it can be concluded that the 10 nm BN nanofluids performed the best in terms of wettability alteration, and there was more interaction with the asphaltenes as discussed in the QCM-D results.

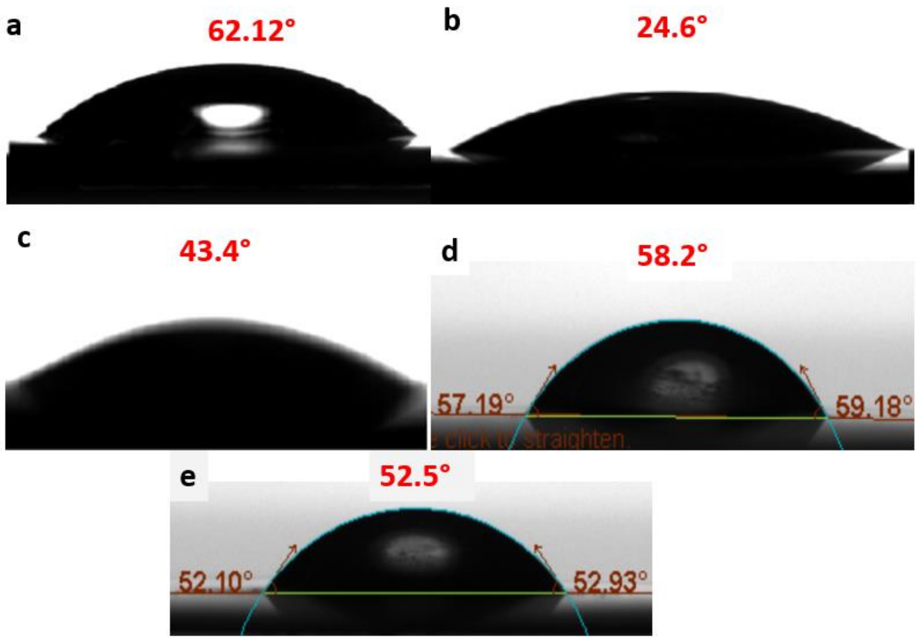

Figure 4.17. Contact angle at 25 °C for a) water drop/air/SiO_2 with adsorbed/deposited asphaltenes from toluene solution, b) water drop/air/SiO_2 with adsorbed/deposited asphaltenes from toluene solution after flooding with 10 nm BN nanofluid, c) water drop/air/SiO_2 with adsorbed/deposited asphaltenes from toluene solution after flooding with 99 nm BN nanofluid, d) water drop/air/SiO_2 with adsorbed/deposited asphaltenes from toluene solution after flooding with 20 nm BN nanofluid and e) water drop/air/SiO_2 with adsorbed/deposited asphaltenes from toluene solution after flooding with 45 nm BN nanofluid. For the nanofluids: 100 mg/L BN in 1000 mg/L NaCl brine.

4.4.6. Cycle Injection Sequence

For this part of the experiments, a sensor with pre-adsorbed heptol 70 asphaltenes on the surface was used. Then, the brine-based nanofluid at 1 mg/L concentration of of 10 nm BN was injected until the system reached equilibrium (no further change in resonance frequency and dissipation). Then, the heptol 70 asphaltene solution was injected again for 1 hour until resonance frequency and dissipation data stabilized. This sequence of injections, i.e., nanofluid and asphaltene solution, was repeated. As seen in **Figure 4.18**, the first injection of the nanofluid followed the same behaviour presented in the previous test for different concentrations of nanoparticles in the nanofluid, i.e., both parameters, the resonance frequency and dissipation, increased. This result meant the nanoparticles were adsorbed over the asphaltene layer and formed a laterally heterogeneous film as previously explained.

However, for the second injection of asphaltene solution, the frequency shift became negative, and dissipation increased. The asphaltene molecules in this step may have reorganised the previously adsorbed layer and displaced the trapped brine solution before being deposited over them. The oscillation in the sensor coupled well with the adsorbed particle layer, leading to a decrease in frequency and increase in dissipation (Sauerbrey, 1959). This response is also known as inertial loading and can be observed in the subsequent layer formed by the nanoparticles after the nanofluid injection and for the last injection that corresponds to the asphaltene solution. At the end of the experiment, some nanofluid was injected again and the frequency no longer changed, which meant that the active sites were saturated, and no more adsorptions could take place.

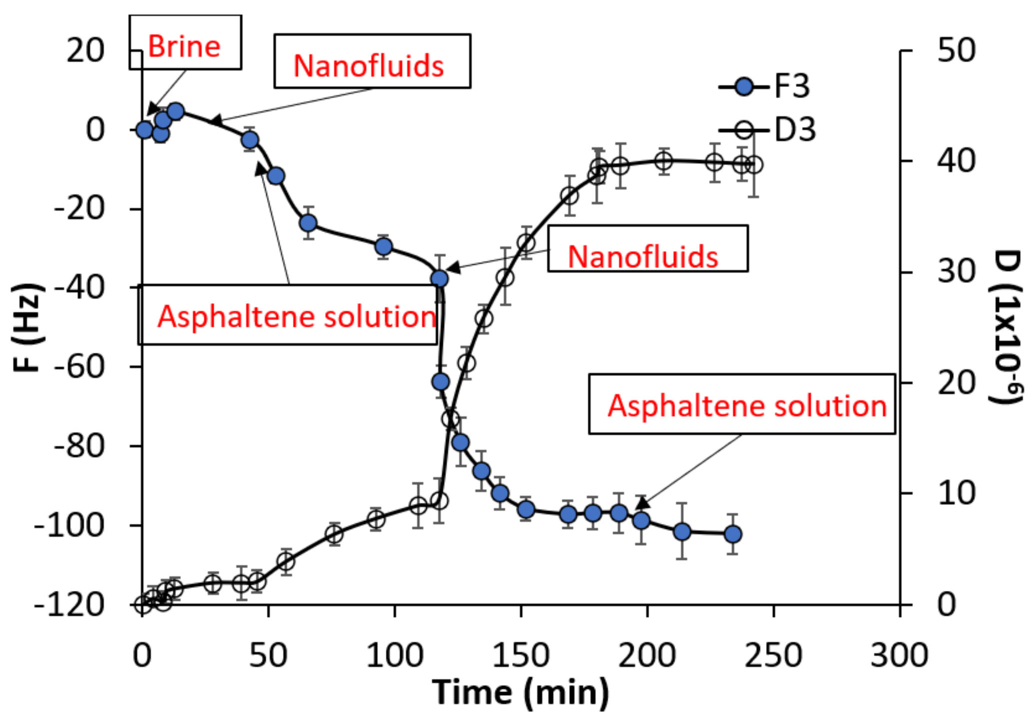

Figure 4.18. QCM-D results for a 1 mg/L concentration of 10 nm BN nanofluid in a cycle injection with heptol 70 asphaltene solution. Experimental conditions are flow rate 150 μL/min, temperature 25 °C, experiment time 250 min. For the nanofluids: 1000 mg/L NaCl brine.

Table 4.7 presents the results for the layer thicknesses obtained from QTools. As shown, after each switch of solution, the layer thickness increased, which agreed with the results obtained for the change in resonance frequency. The layer thickness did not change considerably during the last injection of the heptol 70 asphaltene solution possibly because the energy of the active sites was not strong enough and there were fewer available adsorption sites compared to the previous injections.

Table 4.7. Layer thicknesses obtained from Q-tools for the cycle injection experiment.

Test	**Asph. layer (nm)**	**Asph+NP layer (nm)**	**Asph+NP+Asph layer (nm)**	**Asph+NP+Asph+NP layer (nm)**	**Asph+NP+Asph+NP+Asph layer (nm)**
cycle	68±0.14	73	88	108	110

Figure 4.19a-b show the contact angle for the sensor coated with heptol 70 asphaltenes and the sensor after a sequence injection of 1 mg/L BN nanofluid and heptol 70 asphaltene solutions. As shown, the nanoparticles acted as a wettability modifier even after the formation of several layers of asphaltenes and nanoparticles over the initially adsorbed layer of asphaltenes during the first injection cycle, and the contact angle decreased compared to that for the sensor only with asphaltenes. This result could be because the nanoparticles occupied spaces between the adsorbed/deposited asphaltene molecules, as previously discussed. Also, it agreed with the QCM-D results that showed that after each cycle there was adsorption/deposition, and even with high dissipation, the formed layers presented laterally homogeneous behaviour evidenced by a negative

change in frequency. In addition, the change in the contact angle was not high compared with the that of the sensor after one injection of the 1 mg/L nanofluid (**Figure 4.13b**), because the interaction between the asphaltenes and nanoparticles changed with each cycle due to decrease in the number of active sites with each injection.

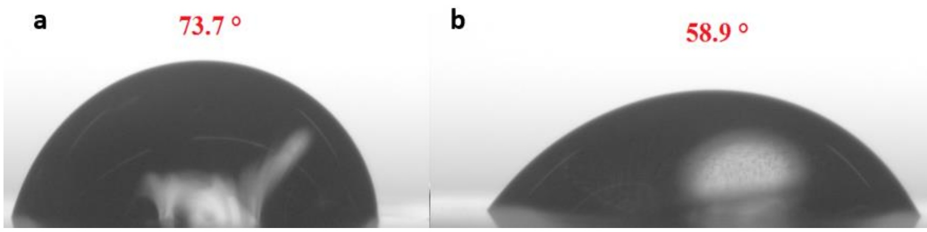

Figure 4.19. Contact angle at 25 °C for water drop/air/SiO_2 sensors a) after coating with asphaltenes from heptol 70 and b) after a cycle injection of 10 nm BN nanofluid → heptol 70 asphaltenes→ 10 nm BN nanofluid →heptol 70 asphaltenes. For the nanofluids: 1 mg/L BN in 1000 mg/L NaCl brine.

Figure 4.20a-b show AFM images for two different positions of the sensor after the sequence injection of 1 mg/L BN nanofluid and heptol 70 asphaltenes. As shown, the size of the aggregates that formed on the surface was larger compared with those shown in **Figure 4.15b**, which corresponds to the sensor with heptol 70 asphaltenes after the injection of the 1 mg/L BN nanofluid. These findings supported the results from the QCM-D and the layer thickness since it was shown that the frequency decreased because adsorption/deposition over the surface took place during each injection cycle; consequently, multilayer adsorption occurred, and the number of available active sites decreased, which resulted in different interactions between asphaltenes and nanoparticles. The AFM results were helpful in clarifying the reason why there was a decrease in the contact angle but not as much as the one obtained with just one injection of nanofluid.

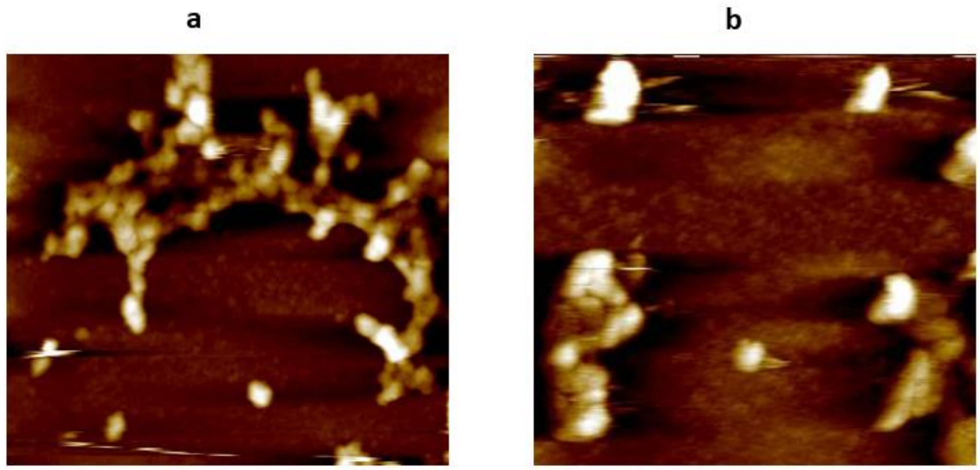

Figure 4.20. AFM retrace contact mode topographic images for after a cycle injection of 10 nm BN nanofluid → heptol 70 asphaltenes→ 10 nm BN nanofluid →heptol 70 asphaltenes. For the nanofluids: 1 mg/L BN in 1000 mg/L NaCl brine, a) one position of the sensor and b) other position of the sensor. The dimension for the images is 5 µm × 5 µm.

4.5. Conclusions

The effect of asphaltene solubility in two different solvents; toluene and heptane, on asphaltene deposition was found to favour the adsorption/deposition on the silica sensors, which resulted in a soft layer indicated by an increase in dissipation and contact angle, making the SiO_2 surface less hydrophilic. The contact angels and QCM-D results of different asphaltene layers suggested that the asphaltenes adsorbed/deposited differently depending on their current aggregation stage in solution. This characteristic is an important factor to consider when designing treatments to inhibit formation damage by asphaltene precipitation in reservoirs. The experiments showed that the BN nanofluid had the best results in terms of wettability alteration. Further, BN were used to evaluate the effect of different concentrations on wettability alteration. For the sensors with asphaltenes from heptol 70, it was found that 1 mg/L BN nanofluid interacted more with the pre-adsorbed/deposited asphaltene layer. Considering the contact angle, 1 mg/L BN nanofluid had the highest reduction, which suggested that when the nanoparticle concentration increased, the nanoparticles started to agglomerate over high energy sites. For the sensors with asphaltenes from toluene, the trend was the opposite; at higher concentrations of nanoparticles the contact angle was lower, except for 150 mg/L nanofluid. These results are important for the oil and gas industry because it is necessary to find an optimal concentration for treatments to reduce preparation costs and maximize production.

In addition, the results suggested that nanoparticle size influenced the interaction of nanoparticles with the asphaltenes. The nanoparticles in 10 and 90 nm nanofluids, were found to interacted more with the asphaltenes compared with the other two sizes i.e., 20 and 45 nm. Finally, the results of the cycle injection experiment indicated that the previously adsorbed layer was reorganised and multiple layers of asphaltenes and nanoparticles formed after each change in solution injection until the adsorption sites were completely occupied.

Finally, the results showed how chemical modification changed the properties of the chemical surfaces of the nanoparticles, which affected the interaction with the asphaltenes. Also, the nanoparticle concentration, when formulating a nanofluid for asphaltene inhibition, and the asphaltene characteristics were found to be important in improving nanofluid performance. Applying these results to an oil system, 1 mg/L and 100 mg/L of 10 nm-sized BN nanofluids performed the best when asphaltenes were precipitated in larger and smaller aggregates, respectively. It is important to consider that asphaltenes are not the only component in oil; their chemical and elemental compositions are different in crude oils, and the performance of the nanoparticles is affected by the temperature and pressure of a reservoir. Therefore, these parameters need to be considered when designing a nanofluid to inhibit or remediate formation damage caused by asphaltene precipitation or upgrading processes, such as in situ catalytic upgrading, so that a nanomaterial can be developed that has more affinity for asphaltenes at reservoir conditions.

4.6. References

Acevedo, S., Castillo, J., Fernández, A., Goncalves, S., & Ranaudo, M. A. (1998). A study of multilayer adsorption of asphaltenes on glass surfaces by photothermal surface deformation. Relation of this adsorption to aggregate formation in solution. *Energy & Fuels, 12*(2), 386-390.

Acevedo, S., Castro, A., Negrin, J. G., Fernández, A., Escobar, G., Piscitelli, V., Delolme, Frederic, & Dessalces, G. (2007). Relations between asphaltene structures and their physical and chemical properties: The rosary-type structure. *Energy & Fuels, 21*(4), 2165-2175.

Adams, J. J. (2014). Asphaltene adsorption, a literature review. *Energy & Fuels, 28*(5), 2831-2856.

Al-Maamari, R. S., & Buckley, J. S. (2003). Asphaltene precipitation and alteration of wetting: the potential for wettability changes during oil production. *SPE Reservoir Evaluation & Engineering, 6*(04), 210-214.

Andersen, S. I. (1995). Effect of precipitation temperature on the composition of n-heptane asphaltenes part 2. *Fuel science & technology international, 13*(5), 579-604.

Betancur, S., Carmona, J. C., Nassar, N. N., Franco, C. A., & Cortés, F. B. (2016). Role of particle size and surface acidity of silica gel nanoparticles in inhibition of formation damage by asphaltene in oil reservoirs. *Industrial & Engineering Chemistry Research, 55*(21), 6122-6132.

Carbognani, L. (2000). Effects of iron compounds on the retention of oil polar hydrocarbons over solid sorbents. *Petroleum science and technology, 18*(3-4), 335-360.

Chen, I.-C., & Akbulut, M. (2012). Nanoscale dynamics of heavy oil recovery using surfactant floods. *Energy & Fuels, 26*(12), 7176-7182.

Cheraghian, G., & Khalilinezhad, S. (2015). Effect of nanoclay on heavy oil recovery during polymer flooding. *Petroleum science and technology, 33*(9), 999-1007.

Creek, J. L. (2005). Freedom of action in the state of asphaltenes: Escape from conventional wisdom. *Energy & Fuels, 19*(4), 1212-1224.

Dehghan Monfared, A., Ghazanfari, M. H., Jamialahmadi, M., & Helalizadeh, A. (2016). Potential Application of Silica Nanoparticles for Wettability Alteration of Oil–Wet Calcite: A Mechanistic Study. *Energy & fuels, 30*(5), 3947-3961.

Domack, A., Prucker, O., Rühe, J., & Johannsmann, D. (1997). Swelling of a polymer brush probed with a quartz crystal resonator. *Physical Review E, 56*(1), 680.

Dudášová, D., Silset, A., & Sjöblom, J. (2008). Quartz crystal microbalance monitoring of asphaltene adsorption/deposition. *Journal of Dispersion Science and Technology, 29*(1), 139-146.

Dudášová, D., Simon, S., Hemmingsen, P. V., & Sjöblom, J. (2008). Study of asphaltenes adsorption onto different minerals and clays: Part 1. Experimental adsorption with UV depletion detection. *Colloids and Surfaces A: Physicochemical and Engineering Aspects, 317*(1-3), 1-9.

Farooq, U., Asif, N., Tweheyo, M. T., Sjöblom, J., & Øye, G. (2011). Effect of low-saline aqueous solutions and pH on the desorption of crude oil fractions from silica surfaces. *Energy & Fuels, 25*(5), 2058-2064.

Franco, C. A., Nassar, N. N., Ruiz, M. A., Pereira-Almao, P., & Cortés, F. B. (2013). Nanoparticles for inhibition of asphaltenes damage: adsorption study and displacement test on porous media. *Energy & Fuels, 27*(6), 2899-2907.

Ghloum, E. F., Al-Qahtani, M., & Al-Rashid, A. (2010). Effect of inhibitors on asphaltene precipitation for Marrat Kuwaiti reservoirs. *Journal of Petroleum Science and Engineering, 70*(1-2), 99-106.

Giraldo, J., Benjumea, P., Lopera, S., Cortés, F. B., & Ruiz, M. A. (2013). Wettability alteration of sandstone cores by alumina-based nanofluids. *Energy & Fuels, 27*(7), 3659-3665.

González, M. F., Stull, C. S., López-Linares, F., & Pereira-Almao, P. (2007). Comparing asphaltene adsorption with model heavy molecules over macroporous solid surfaces. *Energy & Fuels, 21*(1), 234-241.

Goual, L., & Abudu, A. (2009). Predicting the adsorption of asphaltenes from their electrical conductivity. *Energy & Fuels, 24*(1), 469-474.

Harbottle, D., Chen, Q., Moorthy, K., Wang, L., Xu, S., Liu, Q., Sjoblom, Johan, & Xu, Z. (2014). Problematic stabilizing films in petroleum emulsions: Shear rheological response of viscoelastic asphaltene films and the effect on drop coalescence. *Langmuir, 30*(23), 6730-6738.

Hwang, Y., Lee, J.-K., Lee, J.-K., Jeong, Y.-M., Cheong, S.-i., Ahn, Y.-C., & Kim, S. H. (2008). Production and dispersion stability of nanoparticles in nanofluids. *Powder Technology, 186*(2), 145-153.

Jada, A., & Debih, H. (2009). Hydrophobation of clay particles by asphaltenes adsorption. *Composite Interfaces, 16*(2-3), 219-235.

Jada, A., Debih, H., & Khodja, M. (2006). Montmorillonite surface properties modifications by asphaltenes adsorption. *Journal of Petroleum Science and Engineering, 52*(1-4), 305-316.

Jang, S. P., & Choi, S. U. (2004). Role of Brownian motion in the enhanced thermal conductivity of nanofluids. *Applied Physics Letters, 84*(21), 4316-4318.

Johannsmann, D., Reviakine, I., Rojas, E., & Gallego, M. (2008). Effect of sample heterogeneity on the interpretation of QCM (-D) data: comparison of combined quartz crystal microbalance/atomic force microscopy measurements with finite element method modeling. *Analytical chemistry, 80*(23), 8891-8899.

Joonaki, E., & Ghanaatian, S. (2014). The application of nanofluids for enhanced oil recovery: effects on interfacial tension and coreflooding process. *Petroleum science and technology, 32*(21), 2599-2607.

Keiluweit, M., & Kleber, M. (2009). Molecular-level interactions in soils and sediments: the role of aromatic π-systems. *Environmental science & technology, 43*(10), 3421-3429.

Klein, G. C., Kim, S., Rodgers, R. P., Marshall, A. G., & Yen, A. (2006). Mass spectral analysis of asphaltenes. II. Detailed compositional comparison of asphaltenes deposit to its crude oil counterpart for two geographically different crude oils by ESI FT-ICR MS. *Energy & Fuels, 20*(5), 1973-1979.

Leontaritis, K., Amaefule, J., & Charles, R. (1994). A systematic approach for the prevention and treatment of formation damage caused by asphaltene deposition. *SPE Production & Facilities, 9*(03), 157-164.
Li, R., Jiang, P., Gao, C., Huang, F., Xu, R., & Chen, X. (2016). Experimental investigation of silica-based nanofluid enhanced oil recovery: The effect of wettability alteration. *Energy & Fuels, 31*(1), 188-197.
Liu, F., Hickman, S., Maqbool, T., Pauchard, V., & Banerjee, S. (2020). Study of Asphaltene Deposition onto Stainless-Steel Surfaces Using Quartz Crystal Microbalance with Dissipation. *Energy & Fuels, 34*(8), 9283-9295.
Liu, J., Zhang, L., Xu, Z., & Masliyah, J. (2006). Colloidal interactions between asphaltene surfaces in aqueous solutions. *Langmuir, 22*(4), 1485-1492.
Mansoori, G. A. (2010). Remediation of asphaltene and other heavy organic deposits in oil wells and in pipelines. *Socar proceedings, 2010*(4), 12-23.
Mason, W. P., & Baerwald, H. (1951). Piezoelectric crystals and their applications to ultrasonics. *Physics Today, 4*, 23.
McElfresh, P. M., Holcomb, D. L., & Ector, D. (2012). *Application of nanofluid technology to improve recovery in oil and gas wells.* Paper presented at the SPE International Oilfield Nanotechnology Conference and Exhibition.
Mohammadi, M., Akbari, M., Fakhroueian, Z., Bahramian, A., Azin, R., & Arya, S. (2011). Inhibition of asphaltene precipitation by TiO2, SiO2, and ZrO2 nanofluids. *Energy & Fuels, 25*(7), 3150-3156.
Mohammadi, M., Dadvar, M., & Dabir, B. (2017). TiO2/SiO2 nanofluids as novel inhibitors for the stability of asphaltene particles in crude oil: Mechanistic understanding, screening, modeling, and optimization. *Journal of Molecular Liquids, 238*, 326-340.
Moradi, B., Pourafshary, P., Jalali, F., Mohammadi, M., & Emadi, M. (2015). Experimental study of water-based nanofluid alternating gas injection as a novel enhanced oil-recovery method in oil-wet carbonate reservoirs. *Journal of Natural Gas Science and Engineering, 27*, 64-73.
Mullins, O. C. (2011). The asphaltenes. *Annual Review of Analytical Chemistry, 4*, 393-418.
Nasrabadi, H., Moortgat, J., & Firoozabadi, A. (2016). New three-phase multicomponent compositional model for asphaltene precipitation during CO2 injection using CPA-EOS. *Energy & fuels, 30*(4), 3306-3319.
Nassar, N. N., Franco, C. A., Montoya, T., Cortés, F. B., & Hassan, A. (2015). Effect of oxide support on Ni–Pd bimetallic nanocatalysts for steam gasification of nC 7 asphaltenes. *Fuel, 156*, 110-120.
Nassar, N. N., Hassan, A., & Pereira-Almao, P. (2011). Metal oxide nanoparticles for asphaltene adsorption and oxidation. *Energy & Fuels, 25*(3), 1017-1023.
Nezhad, S. S. K., & Cheraghian, G. (2016). Mechanisms behind injecting the combination of nano-clay particles and polymer solution for enhanced oil recovery. *Applied Nanoscience, 6*(6), 923-931.
Ortega, L. C., Rogel, E., Vien, J., Ovalles, C., Guzman, H., Lopez-Linares, F., & Pereira-Almao, P. (2015). Effect of precipitating conditions on asphaltene properties and aggregation. *Energy & Fuels, 29*(6), 3664-3674.
Ovalles, C., Rogel, E., Moir, M. E., & Morazan, H. (2015). Effect of temperature on the analysis of asphaltenes by the on-column filtration/redissolution method. *Fuel, 146*, 20-27.

Patel, H. E., Das, S. K., Sundararajan, T., Sreekumaran Nair, A., George, B., & Pradeep, T. (2003). Thermal conductivities of naked and monolayer protected metal nanoparticle based nanofluids: Manifestation of anomalous enhancement and chemical effects. *Applied Physics Letters, 83*(14), 2931-2933.

Pernyeszi, T., Patzko, A., Berkesi, O., & Dékány, I. (1998). Asphaltene adsorption on clays and crude oil reservoir rocks. *Colloids and Surfaces A: Physicochemical and Engineering Aspects, 137*(1-3), 373-384.

Pomorska, A., Shchukin, D., Hammond, R., Cooper, M. A., Grundmeier, G., & Johannsmann, D. (2010). Positive frequency shifts observed upon adsorbing micron-sized solid objects to a quartz crystal microbalance from the liquid phase. *Analytical chemistry, 82*(6), 2237-2242.

Qiao, P., Harbottle, D., Tchoukov, P., Masliyah, J., Sjoblom, J., Liu, Q., & Xu, Z. (2017). Fractionation of asphaltenes in understanding their role in petroleum emulsion stability and fouling. *Energy & Fuels, 31*(4), 3330-3337.

Reviakine, I., Johannsmann, D., & Richter, R. P. (2011). Hearing what you cannot see and visualizing what you hear: interpreting quartz crystal microbalance data from solvated interfaces: American Chemical Society.

Rezvani, H., Khalilnezhad, A., Ganji, P., & Kazemzadeh, Y. (2017). How ZrO 2 nanoparticles improve the oil recovery by affecting the interfacial phenomena in the reservoir conditions? *Journal of Molecular Liquids*.

Richards, R. (2006). *Surface and nanomolecular catalysis*: CRC Press.

Rudrake, A., Karan, K., & Horton, J. H. (2009). A combined QCM and XPS investigation of asphaltene adsorption on metal surfaces. *Journal of colloid and interface science, 332*(1), 22-31.

Sauerbrey, G. (1959). Use of quartz crystal units for weighing thin films and microweighing. *Magzine for Physics, 155*(2), 206-222.

Schuler, B., Meyer, G., Peña, D., Mullins, O. C., & Gross, L. (2015). Unraveling the molecular structures of asphaltenes by atomic force microscopy. *Journal of the American Chemical Society, 137*(31), 9870-9876.

Sedaghat, M., Mohammadi, H., & Razmi, R. (2016). Application of SiO2 and TiO2 nano particles to enhance the efficiency of polymer-surfactant floods. *Energy Sources, Part A: Recovery, Utilization, and Environmental Effects, 38*(1), 22-28.

Sedghi, M., Goual, L., Welch, W., & Kubelka, J. (2013). Effect of asphaltene structure on association and aggregation using molecular dynamics. *The Journal of Physical Chemistry B, 117*(18), 5765-5776.

Standard, A. (1985). Zeta potential of colloids in water and waste water. *ASTM Standard D*, 4187-4182.

Tavakkoli, M., Panuganti, S. R., Vargas, F. M., Taghikhani, V., Pishvaie, M. R., & Chapman, W. G. (2013). Asphaltene deposition in different depositing environments: part 1. Model oil. *Energy & fuels, 28*(3), 1617-1628.

Trimm, D. (1996). Catalytic deactivation *Studies in Surface Science and Catalysis* (Vol. 100, pp. 65-76): Elsevier.

Tu, Y., Kung, J., McCracken, T., Kotlyar, L., Kingston, D., & Sparks, B. (2006). Effect of Clay Particle Size on the Adsorption of a Pentane Insoluble Bitumen Fraction. *Clay Science, 12*(Supplement2), 194-198.

Tu, Y., Woods, J., Kung, J., McCracken, T., Kotlyar, L., Sparks, B., & Dong, M. (2006). Adsorption of SARA Fractions from Heavy Oil and Bitumen on Kaolinite. *Clay Science, 12*(Supplement2), 183-187.

Vitale, G. (2013). Iron Silicate Nano-Crystals as Potential Catalysts or Adsorbents for Heavy Hydrocarbons Upgrading. *"Iron Silicate Nano-Crystals as Potential Catalysts or Adsorbents for Heavy Hydrocarbons Upgrading". PhD thesis, University of Calgary*.

Vitale, G., Nafie, G., Hethnawi, A., & Nassar, N. N. (2020). Naturally derived pyroxene nanomaterials: an ore for wide applications *Handbook of Functionalized Nanomaterials for Industrial Applications* (pp. 731-774): Elsevier.

Vuillaume, K., & Giasson, S. (2009). Interactions between mica surfaces across crude oil and asphaltene solutions. *The Journal of Physical Chemistry C, 113*(9), 3660-3665.

Wang, S., Segin, N., Wang, K., Masliyah, J. H., & Xu, Z. (2011). Wettability control mechanism of highly contaminated hydrophilic silica/alumina surfaces by ethyl cellulose. *The Journal of Physical Chemistry C, 115*(21), 10576-10587.

Worthen, A. J., Bryant, S. L., Huh, C., & Johnston, K. P. (2013). Carbon dioxide-in-water foams stabilized with nanoparticles and surfactant acting in synergy. *AIChE Journal, 59*(9), 3490-3501.

Xie, K., & Karan, K. (2005). Kinetics and thermodynamics of asphaltene adsorption on metal surfaces: A preliminary study. *Energy & Fuels, 19*(4), 1252-1260.

Yarranton, H. W. (2005). Asphaltene self-association. *Journal of dispersion science and technology, 26*(1), 5-8.

Zahabi, A., Gray, M. R., & Dabros, T. (2012). Kinetics and properties of asphaltene adsorption on surfaces. *Energy & Fuels, 26*(2), 1009-1018.

Zhang, L., Shi, C., Lu, Q., Liu, Q., & Zeng, H. (2016). Probing Molecular Interactions of Asphaltenes in Heptol Using a Surface Forces Apparatus: Implications on Stability of Water-in-Oil Emulsions. *Langmuir, 32*(19), 4886-4895.

Chapter Five: Investigating the Role of Silicate-Based Nanofluids in Inhibiting Formation Damage by Asphaltenes in Oil Reservoirs[4]

5.1. Abstract

In this study, naturally derived basic modified silicate-based nanoparticles (BN) were tested as an option for inhibiting formation damage caused by asphaltene precipitation/deposition. These nanoparticles were characterized using XRD, BET, TPD, and HRTEM, and nanofluid stability was determined using zeta potential measurements. A QCM-D experiment using oil and 50 mg/L BN nanofluid was performed to determine the effect of BN on wettability alteration. BN showed a reduction in the contact angle from 56.4° to 17.3°. In addition, displacement tests were performed at a confining pressure of 500 psi and 60°C to determine the effect and performance of BN nanofluids under flow conditions of different concentrations of BN (50, 250, and 500 mg/L), different NaCl brine concentrations (1000, 10000, and 30000 mg/L), and different pH levels (7 and 9). The results showed that BN increased the effective permeability of oil in the order 50>250>500 mg/L for different BN concentrations, 1000>10000>30000 mg/L for different NaCl concentrations, and pH9>pH7. The recovery factor also increased after the injection of nanofluids to inhibit/remediate the induced damage, and the highest increase was 14.4 % for the nanofluid that had 50 mg/L BN in 1000 mg/L NaCl brine. The nanoparticle treatment was also effective in altering the wettability of the sand pack after the formation damage; the treatment reduced the residual water saturation and shifted the crossover point to the right in the relative permeability curves. It was found that BN stability was more affected by the NaCl concentration compared to BN concentration and pH. Therefore, silicate-based nanoparticles represent a promising solution for inhibiting and remediating asphaltene precipitation/deposition under reservoir conditions.

Keywords: Asphaltenes, formation damage, relative permeability, wettability alteration

---

[4] This chapter is adapted from the following publication:
Tatiana Montoya, Camilo A. Franco, Farid Cortes and Nashaat N. Nassar. *Investigating the Role of Silicate-Based Nanofluids in Inhibiting Formation Damage by Asphaltenes in Oil Reservoirs,* Submitted for publication in Energy and Fuels, 2021

5.2. Introduction

Reservoir production can be limited due to formation damage that diminishes oil and gas recovery and causes inefficient operation (Betancur, Carmona, Nassar, Franco, & Cortés, 2016; Civan, 2015; Maqbool, Balgoa, & Fogler, 2009). Formation damage may be the result of different interactions, such as chemical, biological, physicochemical, and thermal, between reservoir fluids and a porous medium (Betancur, Carmona, et al., 2016). The interactions between reservoir fluids and rock can cause fines migration (Sharma & Yortsos, 1987; You, Badalyan, Bedrikovetsky, Hand, & Jenson, 2013), asphaltene adsorption/deposition, (Adams, 2014; Mullins, 2011), and condensate banks (Alzate et al., 2006). Of the types of formation damage, asphaltene precipitation/deposition in reservoirs and production equipment is the most difficult to address (Hoepfner, Limsakoune, Chuenmeechao, Maqbool, & Fogler, 2013; Leontaritis, Amaefule, & Charles, 1994; Maqbool et al., 2009). Asphaltenes are the most surface active, polar, and heaviest compounds in crude oil (Acevedo et al., 2007; Adams, 2014; Andersen, 1995), and they are insoluble in light paraffins, such as n-heptane and n-pentane (Adams, 2014; Groenzin & Mullins, 2000; Montoya, Coral, Franco, Nassar, & Cortés, 2014) and soluble in light aromatic solvents like toluene, benzene, and pyridine (Mullins, 2011; Mullins et al., 2012). Their complex chemical structures exhibit high polarizability and amphiphilic behavior, and they are composed of heteroatoms, such as nitrogen, oxygen, and sulfur, and metals, such as nickel, vanadium, and iron; in addition, asphaltene cores consist of polycyclic aromatic hydrocarbons (PAH) and naphthenic groups (Qiao et al., 2017; Schuler, Meyer, Peña, Mullins, & Gross, 2015).

Asphaltenes cause several problems that occur in the oil and gas industry, mainly when light conventional oils are being produced and heavy or unconventional oils are being refined (Adams, 2014; Chopra & Lines, 2008). In addition, asphaltene stability can impact different stages of the oil production process; it can reduce oil recovery due to wettability changes (Adams, 2014) and cause rock pore plugging (Drummond & Israelachvili, 2004; Mendoza de la Cruz, Arguelles-Vivas, Matias-Perez, Durán-Valencia, & Lopez-Ramirez, 2009; Syunyaev, Balabin, Akhatov, & Safieva, 2009) and asphaltene deposition in rock (Adams, 2014; Vafaie-Sefti & Mousavi-Dehghani, 2006). Asphaltene deposition can cause clogging within pipelines and wellbores (Akbarzadeh et al., 2007; Cosultchi, Rossbach, & Hernández-Calderon, 2003), which limits crude oil flow (Maqbool et al., 2009) and causes the formation of oil and water emulsions (Kokal, 2005). It can also cause adsorption onto refining equipment (Gawel, Bociarska, & Biskupski, 2005) and plugging during crude oil storage (Adams, 2014). Further, asphaltene deposition corrodes and poisons production equipment and catalysts (Gawel et al., 2005; Masuda & Hashimoto, 1996; Rana, Samano, Ancheyta, & Diaz, 2007) and causes coke formation (Absi-Halabi, Stanislaus, & Trimm, 1991; Gawel et al., 2005; Marchal, Abdessalem, Tayakout-Fayolle, & Uzio, 2010).

Therefore, various methods have been proposed to inhibit asphaltene deposition. These methods include intervention via solvent soaking (Mansoori & Elmi, 2010) and chemical injection of flocculants, dispersants, coagulants, and non-polar solvents (Barcenas, Orea, Buenrostro-González, Zamudio-Rivera, & Duda, 2008; Chang & Scott Fogler, 1996). In addition to the environmental impact, conventional methods to treat asphaltene precipitation/deposition may require additional staff and equipment on location, which increases cost (Betancur, Carmona, et al., 2016; Mansoori, 2010). Further, asphaltene treatments can have low durability, can change fluid composition, and do not prevent asphaltene re-deposition (Betancur, Carmona, et al., 2016; Mansoori, 2010).

To address these issues, nanoparticles and nanofluids have been proposed as alternatives to inhibit formation damage caused by asphaltene precipitation and for in-situ enhancement of oil recovery

(Li et al., 2016; Mohammadi et al., 2011; Rezvani, Khalilnezhad, Ganji, & Kazemzadeh, 2017). Nanoparticles' specific chemical reactivity, active surfaces, and dispersibility (Rezvani et al., 2017) facilitate the capture and removal of asphaltenes present in a reservoir, and these characteristics enhance oil production, inhibit formation damage, and restore wettability (Franco, Nassar, Ruiz, Pereira-Almao, & Cortés, 2013; Giraldo, Benjumea, Lopera, Cortés, & Ruiz, 2013; Moradi, Pourafshary, Jalali, Mohammadi, & Emadi, 2015). In addition, using nanoparticles in enhanced oil recovery (EOR) processes plays and important role in terms of wettability alteration and interfacial tension (IFT) reduction (Li et al., 2016; Negin, Ali, & Xie, 2016; Rezvani et al., 2017).

Therefore, researchers have studied the interactions between asphaltenes and solid surfaces, and several experimental techniques have been developed to study the adsorption of asphaltenes onto different surfaces, including silica (Dudášová, Silset, & Sjöblom, 2008; Zahabi, Gray, & Dabros, 2012), alumina (Dudášová, Silset, et al., 2008; González, Stull, López-Linares, & Pereira-Almao, 2007), iron oxide (Carbognani, 2000), gold (Goual & Abudu, 2009; Harbottle et al., 2014; Rudrake, Karan, & Horton, 2009; Sedghi, Goual, Welch, & Kubelka, 2013; Zahabi et al., 2012), stainless steel (Xie & Karan, 2005), glass (Acevedo, Castillo, Fernández, Goncalves, & Ranaudo, 1998), and clay minerals (Dudášová, Simon, Hemmingsen, & Sjöblom, 2008; Jada & Debih, 2009; Jada, Debih, & Khodja, 2006; Klein, Kim, Rodgers, Marshall, & Yen, 2006; Pernyeszi, Patzko, Berkesi, & Dékány, 1998; TU et al., 2006).

Mohammadi et al. (Mohammadi et al., 2011) used nanoparticles, TiO_2, ZrO_2, and SiO_2, to improve asphaltene stability by Mohammadi et al. (Mohammadi et al., 2011). They found that because hydrogen bonds formed in acidic conditions, TiO_2 nanofluids enhanced asphaltene stability. However, in the absence of hydrogen bonds, asphaltene stability decreased. The authors concluded that the surface acidity of adsorbents affects asphaltene stability. Lu et al. (Lu, Li, Fan, Zhang, & Lv, 2016) evaluated the adsorption of asphaltenes onto Al_2O_3 nanoparticles during CO_2 flooding. The influence of Al_2O_3 nanoparticles on asphaltene precipitation was investigated using the interfacial tension (IFT) behavior of the oil−CO_2 system. Coreflood tests were conducted to study the potential of nanoparticles to inhibit asphaltene damage during CO_2 flooding; their results showed reduced asphaltene precipitation. Kazemzadeh et al. (Kazemzadeh et al., 2015) investigated asphaltene adsorption onto SiO_2, NiO, and Fe_3O_4 nanoparticles on a micro-glass module to prevent asphaltene precipitation. The authors concluded that increasing n-heptane in the presence of nanoparticles resulted in more adsorption regardless of the type of nanomaterial used. They found that silica nanoparticles had more affinity to asphaltenes than NiO or Fe_3O_4 nanoparticles had.

Franco et al. (Franco et al., 2013) evaluated the effect of the chemical nature of 12 types of nanoparticles on asphaltene adsorption on a porous medium at reservoir temperature and pressure. The displacement tests showed that damage from asphaltenes can be inhibited by adding nanoparticles, and oil recovery increased by 7% after the damage was inhibited. Betancur et al. (Betancur, Carmona, et al., 2016) studied the role of nanoparticle size and surface acidity in inhibiting formation damage. They found that materials with the highest adsorptive capacity, higher total surface acidity, and lower mean particle size were the best at inhibiting asphaltene aggregate growth. In the coreflood experiments (Betancur, Carmona, et al., 2016), the authors found that nanofluid treatment using silica nanoparticles increased the effective permeability of oil and enhanced oil recovery by 11% under the reported conditions. Also, Betancur et al. (Betancur, Franco, & Cortés, 2016) determined that core shell-type nanoparticles composed of a magnetite core and a silica shell can inhibit asphaltene formation damage, and the nanoparticles can be recovered and regenerated using their magnetic properties.

In contrast, a Colombian field was treated with alumina-based nanofluids to inhibit formation damage by asphaltene precipitation, and (Zabala et al., 2014) found that the treated wells increased production by 120000 bbl, and the nanofluids had a perdurability greater than 10 months. Also, Guzman et al. (Guzmán et al., 2016) reported a methodology to design asphaltene-related treatments using batch adsorption experiments. They evaluated nanoparticles that had different chemical natures and different physicochemical properties in adsorption tests by exposing a certain mass of nanoparticles in a fixed volume of liquid to varying initial concentrations of asphaltenes, and by exposing a given amount of asphaltenes in a fixed volume of liquid to varying amounts of nanoparticles. Guzman et al. (Guzmán et al., 2016) concluded that both methods led to different results in several applications. Shojaati et al. (Shojaati, Riazi, Mousavi, & Derikvand, 2017) evaluated the inhibition capacity of metal oxide nanoparticles, such as Fe_3O_4, NiO, and Al_2O_3, to delay of the onset of asphaltene precipitation for a synthetic oil sample. They concluded that the nanoparticles were effective in containing the onset point and reducing the amount of precipitated asphaltenes. Recently, López et al. (Lopez et al., 2020) investigated the effects of Cardanol/SiO_2 nanocomposites on formation damage caused by asphaltene precipitation using an asphaltene model solution. They found that adsorption of n-C_7 asphaltenes onto the surfaces of the Cardanol/SiO_2 nanocomposites decreased the amount of asphaltenes in the bulk solution and reduced the aggregation process. Mahmoudi Alemi et al. (Mahmoudi Alemi, Mousavi Dehghani, Rashidi, Hosseinpour, & Mohammadi, 2021) synthesized Fe_2O_3 and functionalized SiO_2 nanoparticles to study their effect on asphaltene precipitation and aggregation in a light live oil that had a high asphaltene deposition risk during an isothermal depressurization process. The authors found that compared to the F-SiO_2 nanoparticles, the Fe_2O_3 nanoparticles reduced asphaltene precipitation and aggregation.

However, there are only a few reported studies that use nanoparticles under reservoir conditions and study their role in formation damage inhibition. Therefore, continuing the study performed in the previous chapter, naturally derived basic modified silicate-based nanoparticles (BN) are tested for the first time by varying their concentration (50, 250, 500 mg/L), pH (7,9), and NaCl brine concentration (1000, 10000, 30000 mg/L) and investigating the inhibition/remediation of n-C_7 asphaltene formation damage on a sand pack under reservoir conditions. Also, a QCM-D test that uses oil is presented to show the interactions between oil, SiO_2 sensors, and BN. Also, the wettability alteration was determined using contact angle measurements and AFM images before and after BN nanofluid injection are presented. This study describes the use of nanoparticles in inhibiting/remediating formation damage, the effect of nanoparticles on oil recovery enhancement, and the parameters that can affect nanofluid formulation in these processes under reservoir conditions.

5.3. Experimental Procedure

5.3.1. Materials and Methods

Toluene and n-heptane HPLC grade obtained from Sigma-Aldrich (ON, Canada) were used to prepare the oil solution and to precipitate asphaltenes on the sand pack, respectively. NaCl from Sigma Aldrich (ON, Canada) was used to prepare the brine solutions in deionized water. For typical silicate-based nanoparticle preparation, sulfuric acid (H_2SO_4 97%) was purchased from Fisher Scientific (ON, Canada); sodium silicate (SiO_2 26.5%, Na_2O 10.6%) from Sigma-Aldrich (ON, Canada); and iron(III) chloride hexahydrate ($FeCl_3.6H_2O$ 99%) and sodium hydroxide

(NaOH 99%) from Merck (ON, Canada). The silicate-based nanoparticles were then modified using calcium nitrate ($Ca(NO_3)_2$ 100%) from Sigma Aldrich (ON, Canada). An industrial partner provided the oil used for the quartz crystal microbalance with dissipation (QCM-D) and displacement test experiments; the characteristics of this oil are listed in Table 5.1. The oil had a viscosity of 2.5 cP @ 60 °C. The sand used for the displacement tests was provided by a local company and consisted of crystalline silica sand of 140-270 mesh. All chemicals were used as received.

Table 5.1. Oil sample properties

Sample	**Saturates (wt.%)**	**Aromatics (wt.%)**	**Resins (wt.%)**	**Asphaltenes (wt. %)**	**API°**	**Density (g/mL)**
oil	65.4	19.4	13.9	1.4	32.8	0.86

5.3.2. Nanoparticle Preparation

Silicate-based nanoparticles were synthesized using a hydrothermal route that controlled time and a low temperature was maintained, as reported in other studies (Vitale, 2013; Vitale, Nafie, Hethnawi, & Nassar, 2020) Then, the prepared nanoparticles were dispersed in an aqueous solution of $Ca(NO_3)_2.4H_2O$ and mixed for 1 h. The solid was filtered and washed with distilled water and dried at room temperature overnight as reported in the previous chapter. These nanoparticles were called basic nanoparticles (BN).

5.3.3. Nanofluids and Oil Solutions Preparation

The oil solution was prepared by adding enough oil to reach 2000 mg/L concentration in toluene, and this solution was used to perform the QCM-D experiment. The oil was mixed with toluene to obtain a solvent baseline to subtract in the QTools software to calculate the oil layer thickness that covered the SiO_2 sensor. To determine the nanoparticles concentration effect, the nanofluid solutions were prepared by adding different masses of the prepared BN to a 10000 mg/L NaCl brine solution; 50 mg/L of BN was added to different concentrations of NaCl brine for the brine effect. For the displacement tests at different pH, 50 mg/L of BN was added to 10000 mg/L of NaCl brine at pH 9. Lastly, for the QCM-D experiment, 50 mg/L of BN was added to 1000 mg/L of NaCl brine. These solutions were sonicated for 20 minutes.

5.3.4. Nanoparticle and Nanofluid Characterization

Nanoparticles were characterized by XRD using an X-ray Ultima III Multi-Purpose Diffraction System (Rigaku Corp., The Woodlands, TX) that had Cu Kα radiation operating at 40 kV and 44 mA with a θ–2θ goniometer (Vitale et al., 2020). Surface area was estimated using the Brunauer-Emmet-Teller method and a surface area and porosity analyzer (TriStar II 3020, Micromeritics Corporate, Norcross, GA); total acidity using NH_3-TPD titration was determined using a CHEMBET 3000 (Quantachrome Inc.); size and morphology of the BN were measured using a transmission electron microscopy (HRTEM) by FEI Tecnai F20 FEG TEM at an accelerating voltage of 200 kV; the detailed procedures for each technique can be found in previous studies (Nassar, Franco, Montoya, Cortés, & Hassan, 2015; Vitale et al., 2020)

For the nanofluid samples at different BN concentrations (50, 250, 500 mg/L) in10000 mg/L of NaCl brine, for the nanofluids at different concentrations of NaCl brine (1000, 10000, 30000 mg/L) with 50 mg/L BN, and 50 mg/L BN in10000 NaCl brine at pH 9, ζ (zeta) potential analyses were performed to determine the stability of the nanoparticles in the brine solutions, respectively. All nanofluids were prepared to sonicate them for about 30-40 min. Then, a sample of each nanofluid was put on a zeta potential cell to measure it in the zeta sizer ZS90, Malvern Instruments, Southborough, UK at 25° C. The measurements were taken 3 times.

5.3.5. Oil QCM-D Tests

Quartz crystal microbalance with dissipation (QCM-D) was used to measure the adsorption/deposition of 2000 mg/L of oil in toluene onto SiO_2 sensors and the effect of BN injection over the pre-adsorbed oil SiO_2 sensors. The frequency and dissipation shifts were recorded for 6 overtones (3, 5, 7, 9, 11, and 13) at a fundamental frequency of 5 MHz. The sensors, 14 mm in diameter, used in this study were AT-cut crystals coated with silica (QSX 303). The experiments were carried out at 25 °C and 150 µL/min. The sensors were cleaned in a UV/ozone cleaner for 10 min and then blown with clean nitrogen gas before the experiments. The experiments were composed of two steps: formation of an oil layer on the surface of the silica sensor and treatment of this layer using BN nanofluid. The detailed procedure can be found in the previous chapter.

5.3.6. Contact Angle and AFM Analysis

Contact angles were measured for the sensors that had oil over their surfaces and for the sensors that had oil over their surfaces after the nanofluid flow. These measurements were performed an Attension (formerly KSV Instruments) CAM200 Optical tensiometer (Biolin Scientific, USA) Biolin Scientific, USA to determine changes in wettability. The sessile drop method was used with brine in air, with an accuracy of ±2°, and an equilibrium time of 2 min. The surface topography of the oil deposited over the sensor surfaces and changes in the surface topography after the nanofluid flow was measured via AFM in contact mode using an Agilent 5500 AFM system (Agilent

Technologies, USA) and PicoView software. AFM measurements were performed at 0° scan angle on a 5 µm X 5 µm area at a speed 0.49 µm/s.

5.3.7. Displacement Tests Setup

A schematic representation of the displacement test setup is shown in **Figure 5.1**. The setup consisted of a pump, tubing, three transfer vessels, two pressure transducers, a sand-pack holder, graduated cylinders for sample collection, a back-pressure regulator, and heating tapes that were used reach the operation temperature. The sand pack characteristics and operating conditions for the displacement tests are listed in **Table 5.2**. Before packing the column, the sand was washed with deionized water to remove impurities, and it was then placed in a vacuum oven at 60 °C for 12 hr to dry (Betancur, Carmona, et al., 2016). Each sand pack was fully saturated with brine and the porosity and pore volume were determined. The absolute permeability of each sand pack was obtained using Darcy's Law and injecting 10000 mg/L NaCl brine at different flow rates and recording the corresponding pressure drops. The properties of each of the six sand packs used for the displacement tests are listed in **Table 5.3**.

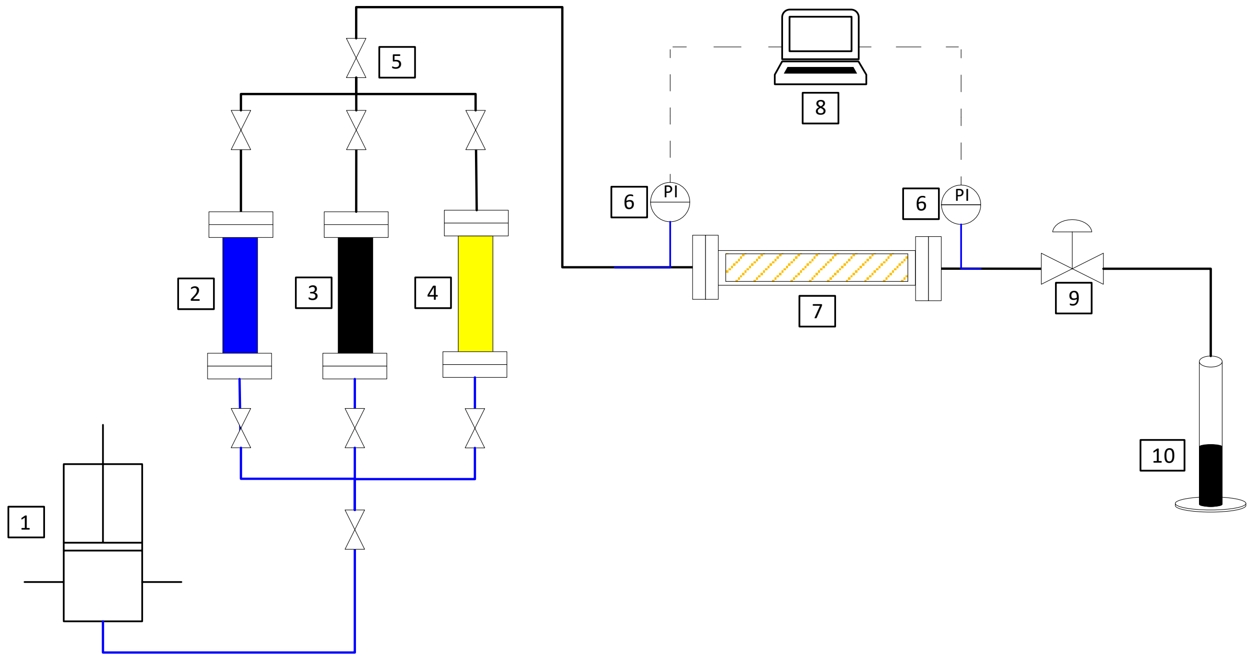

Figure 5.1. Displacement test setup: 1 is the Isco Pump; 2, 3, and 4 are the transfer vessels for water, oil and nanofluids, respectively; 5 is the valve; 6 are the pressure transducers; 7 is the sand pack holder; 8 is the computer for data collection; 9 is the back pressure regulator; and 10 is the sample collector.

Table 5.2. Sand pack holder specifications and experimental conditions

Properties	**Value**
Absolute permeability (D)	1.5±0.2
Confining pressure (psi)	500
Flow rate (cm^3/min)	0.5
Temperature (°C)	60
Crystalline silica sand (mesh)	140-270
Sand pack length (cm)	19.5
Internal sand pack diameter (cm)	2.4

Table 5.3. Displacement test sand pack properties

Property	**50 mg/L sand pack**	**250 mg/L sand pack**	**500 mg/L sand pack**	**1000 mg/L sand pack**	**30000 mg/L sand pack**	**pH9 sand pack**
Pore volume(cm^3)	24.2	24.7	23.8	24.7	25.8	25.6
Porosity (%)	24.5	24.3	23.4	24.3	25.31	26.1

5.3.8. Displacement Test Procedure

These tests were conducted to study the performance of BN in terms of inhibiting/remediating the damage caused by n-C_7 asphaltene precipitation and the role that nanoparticles played in the wettability alteration in the sand packs. The displacement tests consisted of three steps: (1) fluid displacement in clean, porous media, (2) assessment of the damage caused by n-C_7 asphaltene precipitation/deposition, and (3) evaluation of the BN nanofluids in terms of their ability to inhibit/remediate the damage. The first step was called the base scenario, and for this step, brine was injected until the pressure drop was stable. Then, the core was saturated with oil until no change in pressure occurred (K_{ro} at S_{wr}). Then, approximately 15 PV of brine was injected (K_{rw} at S_{or}) to construct the relative permeability and recovery curves as a function of water saturation. The second step, for the same sand pack, oil was injected simultaneously with 0.5 PV of n-heptane to induce formation damage; the system soaked for 12 hr, and after, 15 PV of brine was injected to measure the relative permeability and recovery curves for the damage. For the third step, oil was injected simultaneously with 0.5 PV of BN nanofluids, and the system soaked for 12 hr. Then, 15 PV of brine was injected, and the relative permeability and recovery curves were obtained for the nanofluid system. For all cases, effective permeability to oil (K_o) and water (K_w) were obtained under residual water saturation (S_{wr}) and residual oil saturation (S_{ro}) conditions, respectively. The relative permeability curves were obtained using JBN method.

5.4. Results and Discussion

5.4.1. Nanoparticle Characterization

XRD analysis confirmed the formation of silicate-based nanoparticles and suggested a small crystalline domain size of 10±3 nm. BET analysis showed a surface area of 181 m^2/g, which agreed with the results reported in the literature for silicate-based materials (Vitale, 2013; Vitale et al., 2020). From the NH_3-TPD analysis, it was found that the acid was 4.7 μmol/ m^2. HRTEM images in **Figure 5.2** showed spherical shapes for BN and confirmed the nanoscale size.

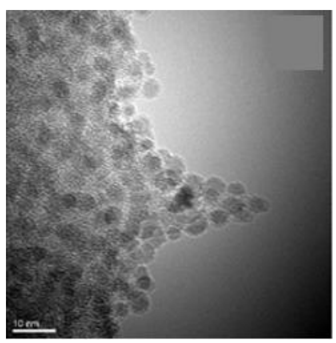

Figure 5.2. HRTEM images for 10 nm-sized basic modified silicate-based nanoparticles. The line mark in the image indicates to 10 nm.

5.4.2. QCM-D Adsorption Experiment

This experiment is a small-scale displacement test under room conditions used to evaluate wettability changes, interactions of oil and SiO_2 surfaces, and the effect of BN. **Figure 5.3**, panel a, shows the results for the oil deposition on SiO_2 coated surfaces in toluene at overtone 9. This experiment was repeated two times, and as shown, the frequency shifted in a negative direction, indicating oil adsorption on the sensors surface. Equilibrium was reached after approximately 45 min, and then toluene was injected to remove the excess of oil until the experiment reached almost 60 min. This behavior agreed with the results obtained in the previous chapter for asphaltene adsorption, in terms of the equilibrium time of the adsorption experiment. The particles adsorbed on the surface of the sensors lowered the resonance frequencies of the sensors compared to the resonance frequency of the sensors before adsorption, which resulted in a negative shift (Reviakine, Johannsmann, & Richter, 2011; Wang, Segin, Wang, Masliyah, & Xu, 2011). **Figure 5.3**, panel b, shows the frequency and dissipation shifts for BN over SiO_2 pre-coated with oil. The frequency shift followed the same behavior of the pre-coated asphaltenes after nanofluid injection; the frequency and dissipation shifts were positive, which meant that 50 mg/L BN nanofluid in 1000 mg/L NaCl was deposited over the oil layer. Also, the oil layer that formed over the SiO_2 sensor was rigid compared to the BN layer that had viscoelastic properties (Pomorska et al., 2010). Since the dissipation shift was greater, this shift agreed with the results obtained in the previous chapter. The rigid layer formed by the organic components of the oil agreed with results obtained in QCM-D studies on asphaltenes (Dudášová, Silset, et al., 2008; F. Liu, Hickman, Maqbool, Pauchard, & Banerjee, 2020; Zahabi et al., 2012). It is possible that the adsorption/deposition of the organic components of the oil occurred due to the interactions between π-electrons and the SiO_2 active sites (Keiluweit & Kleber, 2009). Also, the interactions between aromatic groups present in the oil and the sensors surface may occur (Chen & Akbulut, 2012; Farooq, Asif, Tweheyo, Sjöblom, & Øye, 2011; J. Liu, Zhang, Xu, & Masliyah, 2006).

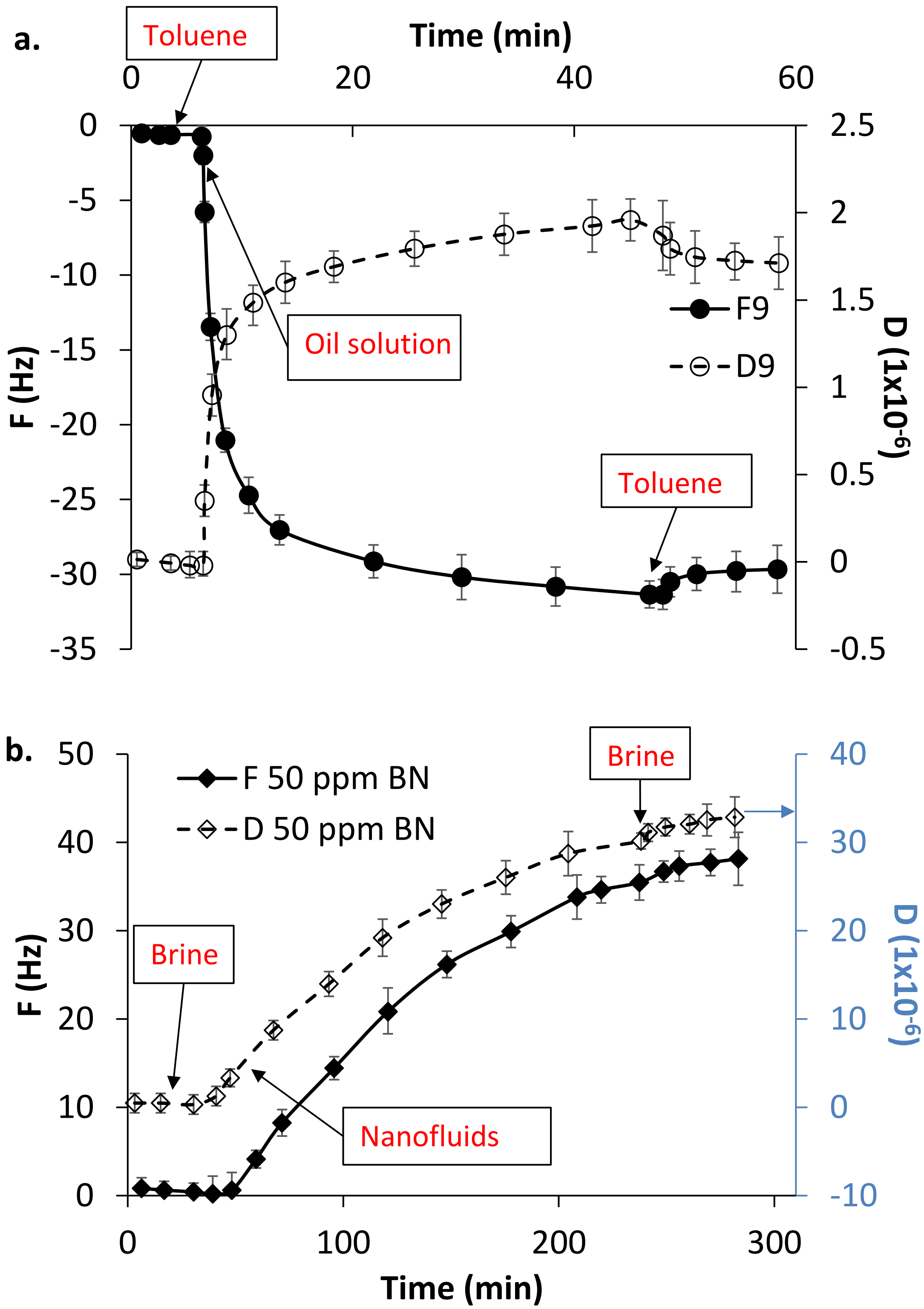

Figure 5.3. Frequency and dissipation shifts for asphaltene coatings on SiO_2 sensors for a) oil in toluene coating and b) BN on pre-coated oil SiO_2 sensors. Experimental conditions: flow rate 150

μL/min; temperature 25 °C; experiment time 58 and 283 min, respectively; oil concentration in toluene 2000 mg/L; nanofluid concentration 10 nm BN in 1000 mg/L NaCl brine.

From the QTools software, it was found that the adsorbed/deposited oil layer thickness was 30 nm, and after BN nanofluid injection, it was 300 nm. The increased thickness after nanofluid flow confirmed that the nanoparticles were adsorbed/deposited over the oil layer. The brine contact angle for the sensor that was covered by adsorbed/deposited oil in toluene after injecting BN nanofluids is depicted in **Figure 5.4**. As shown, the contact angle decreased from 56.4° to 17.3° after the injection of the BN nanofluid. The BN nanofluid made the surface more water-wet (hydrophilic), which could indicate that the nanoparticles removed some of the deposited oil components, and the adsorbed/deposited layer was rearranged. Also, it was possible that the nanoparticles aggregated on the SiO_2 sensors pre-coated with oil, increasing the layer thickness (F. Liu et al., 2020).

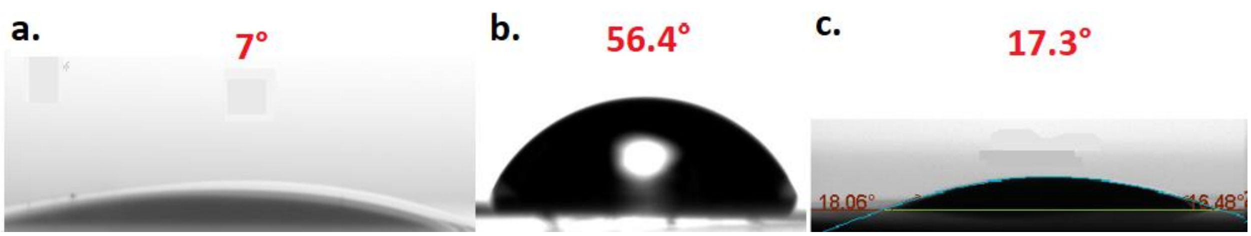

Figure 5.4. Contact angle measurements at 25 °C for a) brine drop/air/SiO_2 original sensor b) brine drop/air/SiO_2 with adsorbed/deposited 2000 mg/L oil in toluene solution, c) water drop/air/SiO_2 with adsorbed/deposited oil dissolved in toluene solution after flowing 1000 mg/L NaCl brine nanofluid with 10 mg/L BN.

Figure 5.5, panels a-b, show AFM images for oil adsorption/deposition and after injecting BN nanofluid, respectively. As shown, after injecting BN nanofluid, the deposited particles were larger compared to the sensor covered in oil. This result agreed with the QCM-D results from BN adsorption/deposition over the pre-adsorbed oil layer and the increased layer thickness.

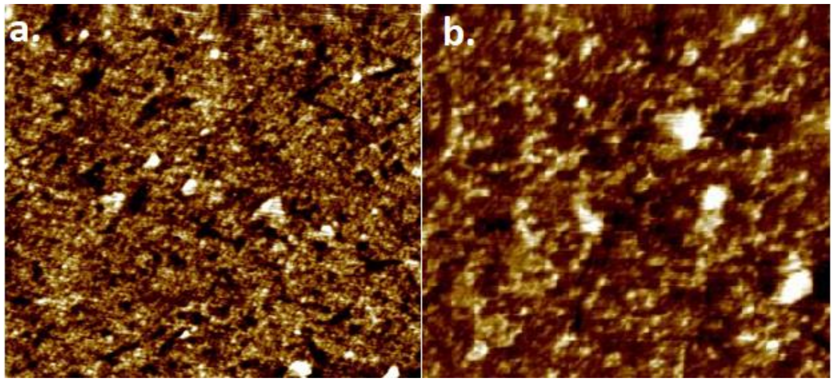

Figure 5.5. AFM retrace contact mode topographic images for a) SiO_2 sensor after oil in toluene adsorption/deposition, b) SiO_2 sensor after oil in toluene adsorption/deposition after 50 mg/L BN nanofluid injection in 1000 mg/L NaCl brine. The dimensions for the images are 5 μm x 5 μm.

5.4.3. Effect of Nanoparticle Concentration in Displacement Tests

Figure 5.6, panels a-b, shows the relative permeability curves for the base scenario and damage systems, and after concentrations of 50, 250, and 500 mg/L BN nanofluids in 10000 mg/L NaCl brine treatment, respectively. As shown in **Figure 5.6**, panel a (the relative permeability curves for the base and damage scenarios), the reproducibility of the experiment was achieved. Comparing both panels in **Figure 5.6**, the oil relative permeability (K_{ro}) followed the order 50mg/L>250 mg/L>500 mg/L>base>damage. The reduction in K_{ro} from the base to the damage system was caused by n-C_7 asphaltene precipitation/deposition on the sand pack; however, after the injection of BN nanofluids, K_{ro} increased when the BN concentration decreased; this difference in K_{ro} could be due to the nanoparticles being less stable and aggregating and adsorbing in multilayers and probably causing some pore clogging when BN concentration increased. Nanoparticle aggregation over the asphaltenes was observed in the experiments presented in the previous chapter, and the results agreed with the results obtained in the oil QCM-D test. From the AFM images in **Figure 5.5**, panel b, larger particles were observed over the sensor surface. Also, the increase in K_{ro} agreed with the results reported in the literature (Betancur, Franco, et al., 2016; Franco et al., 2013; Giraldo et al., 2013). Therefore, using porous media, after injecting nanofluids, the effective permeability to oil increased, which showed that silicate-based nanoparticles inhibited/remediated the damage caused by asphaltene precipitation/deposition in a porous medium.

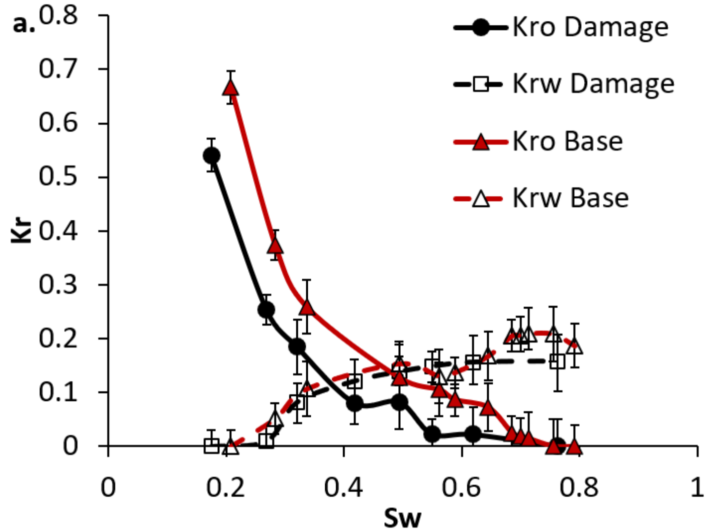

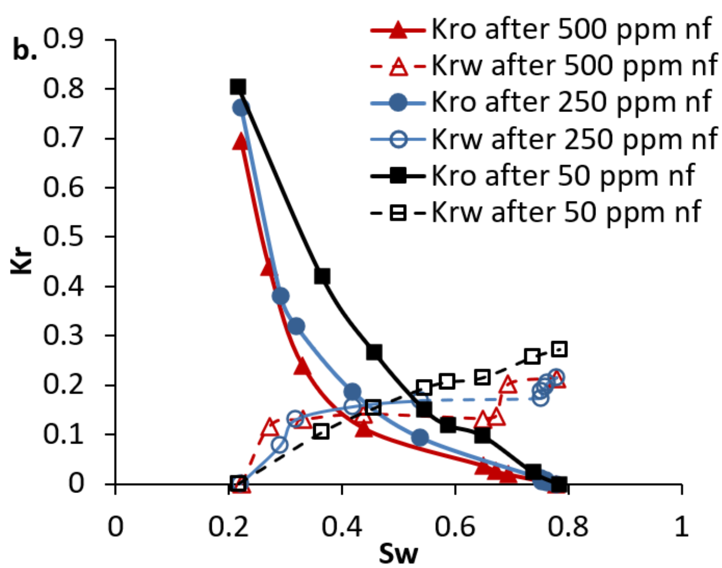

Figure 5.6. Relative permeability curves for a) base and damage scenarios and b) after injecting BN nanofluids of different concentrations. Experiment conditions: confining pressure 500 psi, temperature 60 °C, flow rate 0.5 cm^3/min, and NaCl brine concentration 10000 mg/L.

Table 5.4 presents the obtained values of residual water saturation (S_{wr}) and residual oil (S_{wo}) saturation for the base, damage, and different BN nanofluid concentration systems. There is a decrease in S_{ro} after nanofluid injection following the order 50 mg/L<250 mg/L<500 mg/L<damage, and an increase in S_{wr} in the order 500mg/L>250 mg/L>50 mg/L. These trends indicate that inhibiting/remediating formation damage is not the only mechanism associated with an increase in K_{ro}; there is also a change in sand pack wettability, which is confirmed by the shift in the crossover point. For the base system, the point where k_{rw} is equal to k_{ro} is 0.46, and for the damage system, this point is 0.38. After the treatment with 50 mg/L BN nanofluid, the crossover point shifted to the right at 0.52, followed by 0.44 for 250 mg/L BN nanofluid and 0.4 for 500 mg/L BN nanofluid. The 50 mg/L BN nanofluid caused the greatest shift in the crossover point, which meant that this nanofluid changed the sand pack wettability from oil-wet to a more water-wet system (Giraldo et al., 2013) compared to the other two BN concentrations. The change to a more water-wet system with decreasing BN concentrations coincides with the obtained results for the heptol 70 asphaltenes presented in the previous chapter.

Table 5.4. Estimated residual water saturation and residual oil saturation for BN nanofluid concentrations.

System	**S_{wr} (±0.2%)**	**S_{or} (±0.2%)**
Base	20.8	24.3
Damage	17.5	33.1
After 50 mg/L nf	21.6	21.0
After 250 mg/L nf	22.1	22.6
After 500 mg/L nf	22.2	25.4

Figure 5.7, panels a-b, shows the oil recovery and zeta potential for the BN concentrations, respectively. The oil recovery curves were determined based on the oil at the starting point of each scenario or system (base, damage, nanofluid), i.e., 1-S_{wr} of each system. Oil recovery decreased in the damage scenario to 64.7% compared to the base system (69.4 %); this reduction was expected because n-C_7 asphaltenes precipitated/deposited on the sand pack. In contrast, for different BN concentrations, oil recovery was higher than the induced damage scenario, indicating inhibition/remediation of the damage. The highest recovery, 73.4%, was obtained after the treatment using 50 mg/L BN nanofluid. For 250 mg/L BN nanofluid and for 500 mg/L BN nanofluid, the recovery was 71% and 67.3%, respectively. The increased oil recovery after nanofluid treatment agreed with the results obtained by several researchers (Betancur, Franco, et al., 2016; Giraldo et al., 2013). It is worth noting that even though the 500 mg/L BN nanofluid inhibited/remediated the damage and increased oil recovery compared with the damage system, oil recovery was less than the value for the base system; this difference in oil recovery agreed with the relative permeability curves crossover point trend previously obtained and with the S_{wr} and S_{ro} values for both systems. Table B1 in Appendix B presents the viscosities for the different nanofluids. As seen, nanofluids have a lower viscosity in comparison with the oil, which supports that the main mechanism related with the change in relative permeability curves and oil recovery is wettability alteration. The mobility ratio is not calculated as the intention of the nanofluids is not to recover more oil but to inhibit asphaltene precipitation.

In contrast, as shown in **Figure 5.7**, panel b, ζ potential decreases as BN concentration increases. ζ indicates nanofluid stability, and usually, nanoparticle dispersion that has ζ potential values lower than −30 mV or larger than +30 mV are stable (Hwang et al., 2008; Standard, 1985). For all BN concentrations, ζ potential values are higher than -30 mV and less than +30 mV, indicating that all nanofluids are unstable and tend to aggregate/flocculate. In addition, the electrostatic attractive forces are higher that the repulsion forces (Kaufui V & Omar, 2010; Sagala, Montoya, Hethnawi, Vitale, & Nassar, 2019) These ζ potential results confirm the differences in the wettability alteration given by the crossover point; at higher BN concentrations, the nanoparticles tend to aggregate more and, therefore, can clog the sand pack pores. This clogging can eventually reduce oil recovery, as observed in the trend of the different BN concentrations. The results show that the optimum nanoparticle concentration is 50 mg/L BN nanofluid for inhibiting/remediating formation damage caused by asphaltene precipitation/deposition; therefore, this concentration is used for the other experiments.

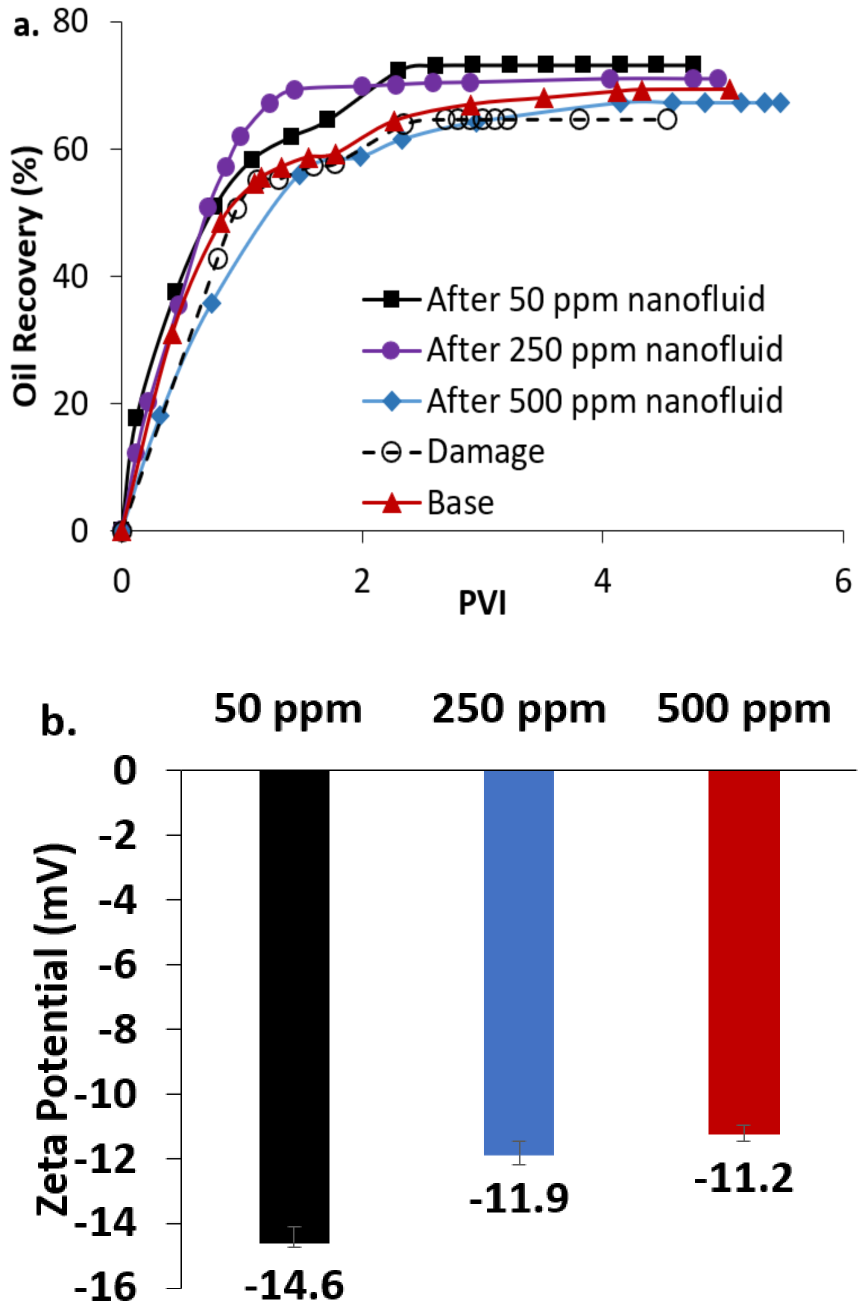

Figure 5.7. a) Oil recovery curves for base, damage, and different concentrations of BN in 10000 mg/L NaCl brine and b) zeta potential of different concentrations of BN nanofluids in 10000 mg/L NaCl brine. Displacement test conditions: confining pressure 500 psi, temperature 60 °C, and flow rate 0.5 cm^3/min. Zeta potential conditions: temperature 25 °C.

5.4.4. Effect of Brine Concentration in the Displacement Tests

Figure 5.7 shows the relative permeability curves after treatment with concentrations of 1000, 10000, and 30000 mg/L NaCl brine and 50 mg/L BN. Comparing **Figure 5.6,** panel a, and **Figure 5.7**, the relative oil permeability (K_{ro}) followed the order 1000 mg/L>10000 mg/L>30000 mg/L> base> damage. After the injection of BN nanofluids, K_{ro} increased as NaCl concentration decreased; this difference in K_{ro} might have occurred because when NaCl concentration increased, BN nanoparticles were less stable and tended to aggregate and probably plugged pores in the sand pack. This difference in K_{ro} indicated that the concentration of NaCl affected the inhibition/remediation of formation damage caused by asphaltene deposition/precipitation, even more so than different concentrations of BN did. In contrast, as shown in **Table 5.5**, S_{ro} decreased after different salinities of BN nanofluid were injected following the order in decrement 1000 mg/L<10000 mg/L<base<30000 mg/L<damage. An increase in S_{wr} was obtained after different salinities nanofluids injection in the order 30000mg/L>10000 mg/L> 1000 mg/L. In the case of different BN concentrations, differences in S_{wr} and S_{ro} indicated that the inhibition/remediation of the formation damage was also caused by a change in the sand pack wettability, which was confirmed by the shift in the crossover point. As previously mentioned, the crossover points for the base and damage systems were 0.46 and 0.38, respectively. After treatment with different salinities of BN nanofluids, the crossover point shifted to the right to 0.61 for 1000 mg/L NaCl brine, to 0.52 for 10000 mg/L NaCl brine, and to 0.415 for 30000 mg/L NaCl brine. For 1000 and 10000 mg/L NaCl nanofluids, the crossover points were higher than 0.5, and according to Craig's rule of thumb, these values correspond to strongly water-wet systems (Anderson, 1987; Giraldo et al., 2013); in contrast, the crossover point for 30000 mg/L NaCl brine nanofluid shifted to the right, but the shift was less than 0.5. The change to a more water-wet system as NaCl concentration decreases coincides with the results from the QCM-D oil tests; the contact angle in **Figure 5.4**, panel c, significantly reduced after injecting 50 mg/L BN nanofluid at low salinity (1000 mg/L NaCl). Ions present in the nanofluids can also affect the charge of the sand as reported in the literature (Fjelde, Polanska, Taghiyev, & Asen, 2013).

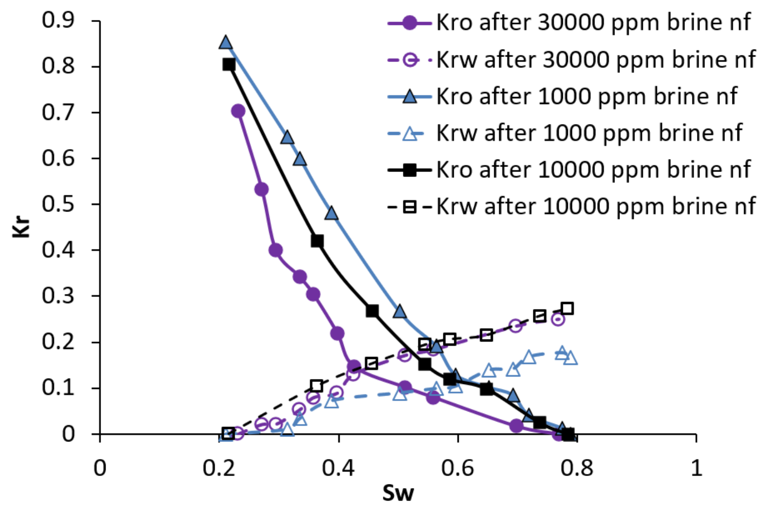

Figure 5.8. Relative permeability curves after injecting BN nanofluids at different NaCl brine concentrations. Experiment conditions: confining pressure 500 psi, temperature 60 °C, and flow rate 0.5 cm^3/min, BN concentration 50 mg/L.

Table 5.5. Estimated residual water saturation and residual oil saturation for BN nanofluids at different NaCl brine concentrations.

System	**S_{wr} (±0.2%)**	**S_{or} (±0.2%)**
Base	20.8	24.3
Damage	17.5	33.1
After 10000 mg/L NaCl brine nf	21.6	21.0
After 1000 mg/L NaCl brine nf	21.1	16.5
After 30000 mg/L NaCl brine nf	23.2	25.9

Figure 5.9, panels a-b, depicts oil recovery and ζ potential for different NaCl brine concentrations, respectively. The highest oil recovery was obtained for 1000 mg/L NaCl brine nanofluid, which was expected because of the relative permeability curve results for wettability alteration and the increased K_{ro} for this particular NaCl concentration. The increase in oil recovery for the 1000 mg/L nanofluid was from 64.7 % (damage) to 79.1%, which agreed with the values presented in the literature where were used nanoparticles dispersed in water (Betancur, Carmona, et al., 2016; Gawel et al., 2005). Also, for the 30000 mg/L NaCl brine nanofluid, the oil recovery was 66.2% less than the base system (69.4%) and slightly higher than the damage system (64.7%). This result agreed with the results obtained by the relative permeability curves. In addition, as shown in **Figure 5.9**, panel b, ζ potential increased when NaCl concentration decreased. As the ζ potential value for 1000 mg/L NaCl nanofluid was the only value less than -30 mV, this nanofluid was considered the most stable (Hwang et al., 2008; Standard, 1985). According to Sagala et al. (Sagala, Hethnawi, & Nassar, 2020), adding nanoparticles to a low salinity brine considerably affected the expansion of the electrical double layer and changed the interactions between organic compounds and sandstone. The ζ potential results supported the findings of the relative permeability curves and oil recovery in terms of wettability alteration; higher NaCl concentrations did not improve wettability and K_{ro} since ζ potential values confirmed the fact that higher NaCl concentrations facilitated BN aggregation/flocculation and possibly produced clogs in the sand pack pores.

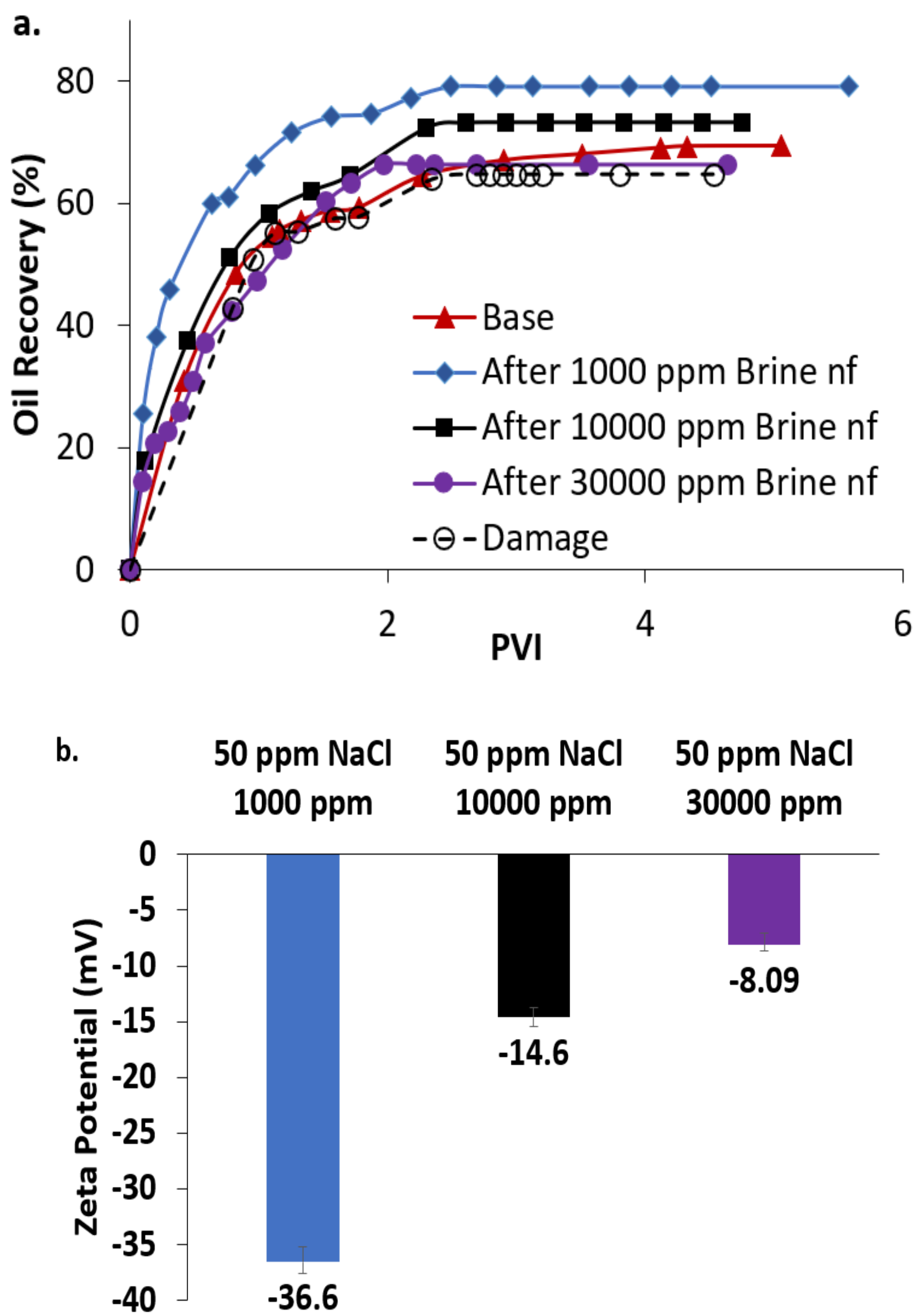

Figure 5.9. a) Oil recovery curves for base, damage systems, and different concentrations of BN in 10000 mg/L NaCl brine and b) zeta potential different concentrations of BN nanofluids in 10000 mg/L NaCl brine. Displacement test conditions: confining pressure 500 psi, temperature 60 °C, and flow rate 0.5 cm^3/min; zeta potential conditions: temperature 25 °C.

5.4.5. Effect of pH in the Displacement Tests

Figure 5.10 shows the relative permeability curves after treatment with pH 7 and pH 9 with 50 mg/L BN in 10000 mg/L NaCl brine nanofluids. Comparing **Figure 5.6,** panel a, and Figure 5.10, the relative oil permeability (K_{ro}) followed the order pH9> pH7> base> damage. After injecting BN nanofluids, K_{ro} increased from 0.8 for the damage step to 1.7 and 1.8 for pH 7 and pH 9 nanofluids, respectively. The similar K_{ro} values for different pH values could be because pH had only a slight effect on BN nanoparticle stability, and BN tended to aggregate and probably plug pores to the same extent in the sand pack. These results suggested that pH affected the inhibition/remediation of formation damage caused by asphaltene deposition/precipitation less than BN concentration and NaCl concentration. In addition, it has been reported in the literature that nanoparticle stability in divalent brines and low salinity NaCl brine can be considerably affected (Fjelde et al., 2013; Sagala et al., 2020). However, neither divalent brines nor low salinity occurred in this experiment. In contrast, as shown in **Table 5.6**, a decrease in S_{ro} occurred after BN nanofluids that had different pH levels were injected; the decrease followed the order pH9<pH7<base<damage. An increase in S_{wr} was also obtained in the order pH9>pH7. Differences in S_{wr} and S_{ro} suggested that the inhibition/remediation of formation damage was also caused by wettability changes, which was confirmed by the shift to the right in the crossover point compared to the crossover point that occurred in the damage system (0.38). After the treatment with BN nanofluids that had different pH levels, the crossover point shifted to the right to 0.52 and 0.53 for pH7 and pH9 nanofluids, respectively. This shift meant that both nanofluids shifted the wettability of the sand pack to strongly water-wet since the crossover point was higher than 50 (Anderson, 1987; Giraldo et al., 2013).

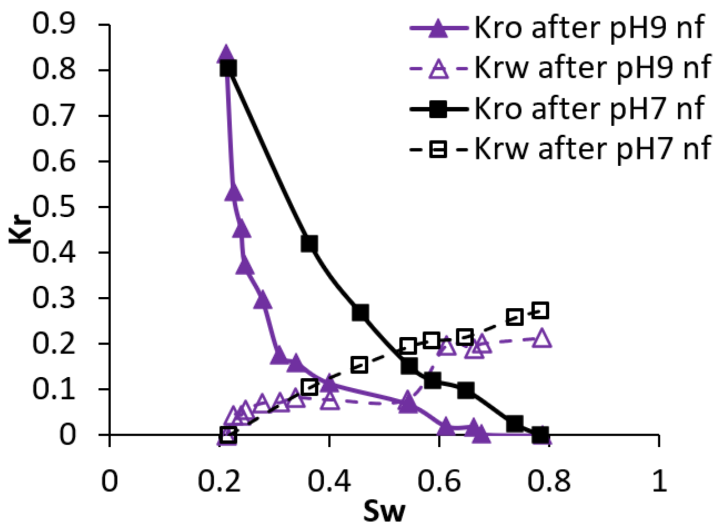

Figure 5.10. Relative permeability curves after injecting BN nanofluids that had different pH values. Experiment conditions: confining pressure 500 psi, temperature 60 °C, flow rate 0.5 cm^3/min, BN concentration 50 mg/L, and NaCl concentration 10000 mg/L.

Table 5.6. Estimated residual water saturation and residual oil saturation for BN of different pH values.

System	**S_{wr} (±0.2%)**	**S_{or} (±0.2%)**
Base	20.8	24.3
Damage	17.5	33.1
After pH7 nf	21.6	21.0
After pH9 nf	21.3	18.3

Figure 5.11, panels a-b, shows oil recovery and ζ potential for BN nanofluids that had different pH levels, respectively. For the recovery oil curves, recovery increased from 64.7 % for the damage system to 73.4 % for pH 7 and to 76.8% for pH 9. The differences in oil recovery agreed

with the relative permeability curve results. For both pH values, ζ potential values were higher than -30 mV and less than +30 mV, indicating that these nanofluids were unstable and tended to aggregate/flocculate since the electrostatic attractive forces were higher that the repulsion forces (Kaufui V & Omar, 2010; Sagala et al., 2019). These ζ potential results confirm the similarities in wettability alteration given by the crossover point. For both pH values, BN tended to aggregate in a similar way. However, the nanofluids increased recovery, which suggested that under the experimental conditions, the nanofluids inhibited/remediated the damage, but they might not perform well in terms of remediating asphaltene redeposition due to their instability. In this case, further modifications to BN should be considered to increase stability.

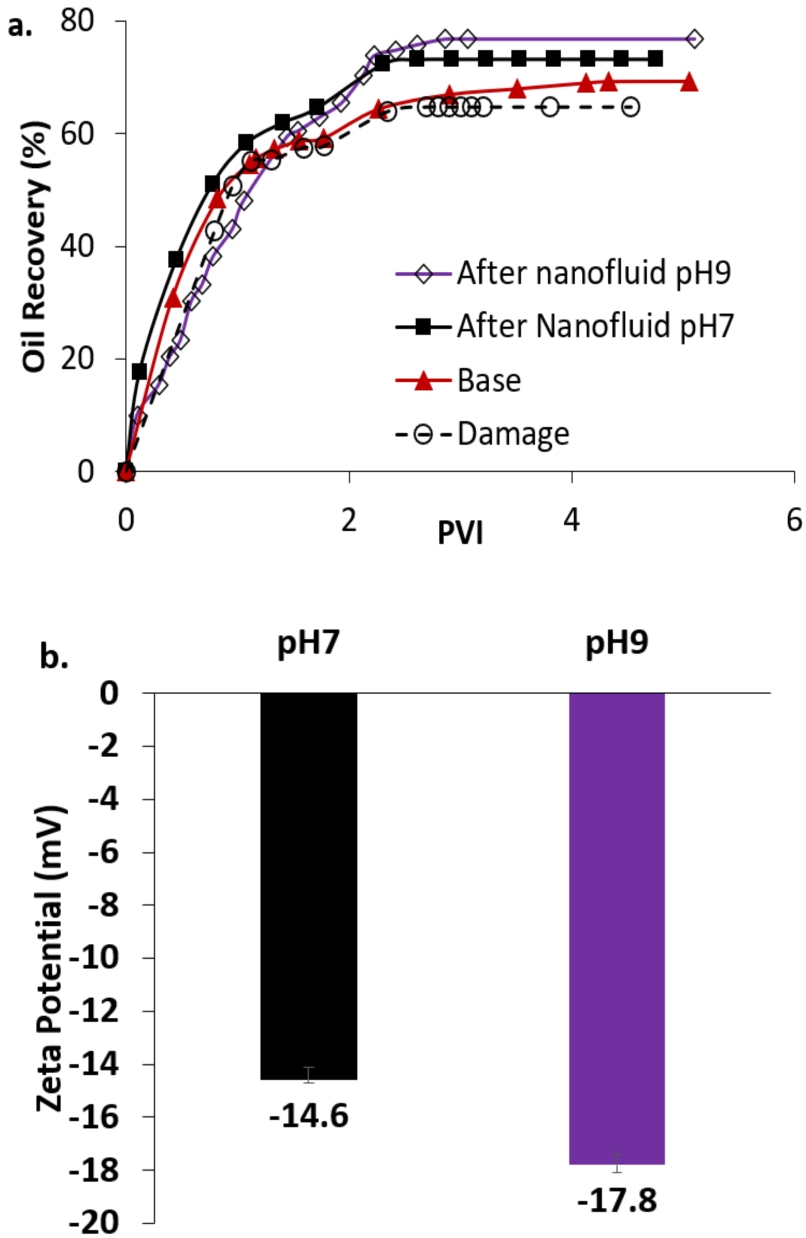

Figure 5.11. a) Oil recovery curves for base, damage systems, and different pH values of 50 mg/L BN in 10000 mg/L NaCl brine nanofluids and b) zeta potential different pH values of 50 mg/L BN nanofluids in 10000 mg/L NaCl brine. Displacement test conditions: confining pressure 500 psi, temperature 60 °C, and flow rate 0.5 cm^3/min. Zeta potential conditions: temperature 25 °C.

5.5. Conclusions

Oil interactions with SiO_2 sensors were successfully tested using QCM-D under atmospheric conditions. Injecting 50 mg/L BN nanofluid displayed strong interactions with the organic compounds adsorbed over the SiO_2 surface. These interactions changed the wettability considerably by reducing the contact angle. AFM images showed that larger molecules formed over the sensor pre-coated with oil. QCM-D was a fast way to evaluate nanofluid performance in terms of reducing formation damage caused by asphaltene precipitation/deposition under atmospheric conditions.

Nanofluid treatments of varying concentrations of BN and NaCl and at different pH levels increased the effective permeability to oil and increased oil recovery (%). The highest increase in oil recovery was by 14.4% in 1000 mg/L NaCl concentration and 50 mg/L BN nanofluid. This increase is a promising result because it indicates that nanofluids could be used on a larger scale, for example, in producing fields. It is important to account for nanoparticle concentration, brine concentration, and pH when designing nanofluids for remediating asphaltene precipitation/deposition in porous media; these parameters influence wettability alteration and oil recovery by changing the interactions between asphaltenes and nanoparticles. In terms of stability, the nanofluids prepared in this work can be improved by modifying the nanoparticles using other compounds. Using naturally derived silicate-based nanoparticles can inhibit/remediate formation damage caused by asphaltene precipitation/deposition in light oil reservoirs because the inhibition/remediation of the damage can result in a higher oil recovery.

5.6.References

Absi-Halabi, M, Stanislaus, A, & Trimm, DL. (1991). Coke formation on catalysts during the hydroprocessing of heavy oils. *Applied catalysis, 72*(2), 193-215.

Acevedo, Sócrates, Castillo, Jimmy, Fernández, Alberto, Goncalves, Sonia, & Ranaudo, María A. (1998). A study of multilayer adsorption of asphaltenes on glass surfaces by photothermal surface deformation. Relation of this adsorption to aggregate formation in solution. *Energy & Fuels, 12*(2), 386-390.

Acevedo, Sócrates, Castro, Alexandra, Negrin, Juan Gabriel, Fernández, Alberto, & Escobar, Gastón, Piscitelli, Vincent, Delolme, Frederic, Dessalces, Guy. (2007). Relations between asphaltene structures and their physical and chemical properties: The rosary-type structure. *Energy & fuels, 21*(4), 2165-2175.

Adams, Jeramie J. (2014). Asphaltene adsorption, a literature review. *Energy & Fuels, 28*(5), 2831-2856.

Akbarzadeh, Kamran, Hammami, Ahmed, Kharrat, Abdel, Zhang, Dan, Allenson, Stephan, Creek, Jefferson, Kabir, Shah, Jamaluddin, A, & Marshall, Alan G, Rodgers, Ryan P. (2007). Asphaltenes—problematic but rich in potential. *Oilfield Review, 19*(2), 22-43.

Alzate, Guillermo A, Franco, Carlos Alberto, Restrepo, Alejandro, Del Pino Castrillon, Jessica J, Barreto Alvares, Diogenes Laureano, & Escobar Murillo, Alfaro Alberti. (2006). *Evaluation of alcohol-based treatments for condensate banking removal.* Paper presented at the SPE International Symposium and Exhibition on Formation Damage Control.

Andersen, Simon Ivar. (1995). Effect of precipitation temperature on the composition of n-heptane asphaltenes part 2. *Fuel science & technology international, 13*(5), 579-604.

Anderson, William G. (1987). Wettability literature survey part 5: The effects of wettability on relative permeability. *Journal of Petroleum Technology, 39*(11), 1453-1468.

Barcenas, Mariana, Orea, Pedro, Buenrostro-González, Eduardo, Zamudio-Rivera, Luis S, & Duda, Yurko. (2008). Study of medium effect on asphaltene agglomeration inhibitor efficiency. *Energy & Fuels, 22*(3), 1917-1922.

Betancur, Stefanía, Carmona, Juan C, Nassar, Nashaat N, Franco, Camilo A, & Cortés, Farid B. (2016). Role of particle size and surface acidity of silica gel nanoparticles in inhibition of formation damage by asphaltene in oil reservoirs. *Industrial & Engineering Chemistry Research, 55*(21), 6122-6132.

Betancur, Stefanía, Franco, Camilo A, & Cortés, Farid B. (2016). Magnetite-silica nanoparticles with a core-shell structure for inhibiting the formation damage caused by the precipitation/deposition of asphaltene. *Journal of Magnetohydrodynamics and Plasma Research, 21*(3), 289-322.

Carbognani, Lante. (2000). Effects of iron compounds on the retention of oil polar hydrocarbons over solid sorbents. *Petroleum science and technology, 18*(3-4), 335-360.

Chang, Chia-Lu, & Scott Fogler, H. (1996). Peptization and coagulation of asphaltenes in apolar media using oil-soluble polymers. *Fuel Science and Technology International, 14*(1-2), 75-100.

Chen, I-Cheng, & Akbulut, Mustafa. (2012). Nanoscale dynamics of heavy oil recovery using surfactant floods. *Energy & Fuels, 26*(12), 7176-7182.

Chopra, Satinder, & Lines, Larry. (2008). Introduction to this special section: heavy oil. *The Leading Edge, 27*(9), 1104-1106.

Civan, Faruk. (2015). *Reservoir formation damage: fundamentals, modeling, assessment, and mitigation*: Gulf Professional Publishing.

Cosultchi, A, Rossbach, P, & Hernández-Calderon, I. (2003). XPS analysis of petroleum well tubing adherence. *Surface and Interface analysis, 35*(3), 239-245.

Drummond, Carlos, & Israelachvili, Jacob. (2004). Fundamental studies of crude oil–surface water interactions and its relationship to reservoir wettability. *Journal of Petroleum Science and Engineering, 45*(1-2), 61-81.

Dudášová, Dorota, Silset, Anne, & Sjöblom, Johan. (2008). Quartz crystal microbalance monitoring of asphaltene adsorption/deposition. *Journal of Dispersion Science and Technology, 29*(1), 139-146.

Dudášová, Dorota, Simon, Sébastien, Hemmingsen, Pål V, & Sjöblom, Johan. (2008). Study of asphaltenes adsorption onto different minerals and clays: Part 1. Experimental adsorption with UV depletion detection. *Colloids and Surfaces A: Physicochemical and Engineering Aspects, 317*(1-3), 1-9.

Farooq, Umer, Asif, Naveed, Tweheyo, Medad T, Sjöblom, Johan, & Øye, Gisle. (2011). Effect of low-saline aqueous solutions and pH on the desorption of crude oil fractions from silica surfaces. *Energy & Fuels, 25*(5), 2058-2064.

Fjelde, IF, Polanska, AP, Taghiyev, FT, & Asen, SMA. (2013). *Low salinity water flooding: retention of polar oil components in sandstone reservoirs.* Paper presented at the IOR 2013-17th European Symposium on Improved Oil Recovery.

Franco, Camilo A, Nassar, Nashaat N, Ruiz, Marco A, Pereira-Almao, Pedro, & Cortés, Farid B. (2013). Nanoparticles for inhibition of asphaltenes damage: adsorption study and displacement test on porous media. *Energy & Fuels*, *27*(6), 2899-2907.

Gawel, Irena, Bociarska, Dagmara, & Biskupski, Piotr. (2005). Effect of asphaltenes on hydroprocessing of heavy oils and residua. *Applied Catalysis A: General, 295*(1), 89-94.

Giraldo, Juliana, Benjumea, Pedro, Lopera, Sergio, Cortés, Farid B, & Ruiz, Marco A. (2013). Wettability alteration of sandstone cores by alumina-based nanofluids. *Energy & Fuels, 27*(7), 3659-3665.

González, Manuel F, Stull, Clementina Sosa, López-Linares, Francisco, & Pereira-Almao, Pedro. (2007). Comparing asphaltene adsorption with model heavy molecules over macroporous solid surfaces. *Energy & fuels, 21*(1), 234-241.

Goual, Lamia, & Abudu, Adewunmi. (2009). Predicting the adsorption of asphaltenes from their electrical conductivity. *Energy & Fuels, 24*(1), 469-474.

Groenzin, Henning, & Mullins, Oliver C. (2000). Molecular size and structure of asphaltenes from various sources. *Energy & Fuels, 14*(3), 677-684.

Guzmán, Juan D, Betancur, Stefania, Carrasco-Marín, Francisco, Franco, Camilo A, Nassar, Nashaat N, & Cortés, Farid B. (2016). Importance of the adsorption method used for obtaining the nanoparticle dosage for asphaltene-related treatments. *Energy & Fuels, 30*(3), 2052-2059.

H Harbottle, David, Chen, Qian, Moorthy, Krishna, Wang, Louxiang, Xu, Shengming, Liu, Qingxia, & Sjoblom, Johan, Xu, Zhenghe. (2014). Problematic stabilizing films in petroleum emulsions: Shear rheological response of viscoelastic asphaltene films and the effect on drop coalescence. *Langmuir, 30*(23), 6730-6738.

Hoepfner, Michael P, Limsakoune, Vipawee, Chuenmeechao, Varun, Maqbool, Tabish, & Fogler, H Scott. (2013). A fundamental study of asphaltene deposition. *Energy & fuels, 27*(2), 725-735.

Hwang, Yujin, Lee, Jae-Keun, Lee, Jong-Ku, Jeong, Young-Man, Cheong, Seong-ir, Ahn, Young-Chull, & Kim, Soo H. (2008). Production and dispersion stability of nanoparticles in nanofluids. *Powder Technology, 186*(2), 145-153.

Jada, A, & Debih, H. (2009). Hydrophobation of clay particles by asphaltenes adsorption. *Composite Interfaces, 16*(2-3), 219-235.

Jada, A, Debih, H, & Khodja, M. (2006). Montmorillonite surface properties modifications by asphaltenes adsorption. *Journal of Petroleum Science and Engineering, 52*(1-4), 305-316.

Kaufui V, Wong, & Omar, De Leon. (2010). Applications of nanofluids: current and future. *Advances in Mechanical Engineering, 2010*.

Kazemzadeh, Yousef, Eshraghi, S Ehsan, Kazemi, Keyvan, Sourani, Saeed, Mehrabi, Mehran, & Ahmadi, Yaser. (2015). Behavior of asphaltene adsorption onto the metal oxide nanoparticle surface and its effect on heavy oil recovery. *Industrial & Engineering Chemistry Research, 54*(1), 233-239.

Keiluweit, Marco, & Kleber, Markus. (2009). Molecular-level interactions in soils and sediments: the role of aromatic π-systems. *Environmental science & technology, 43*(10), 3421-3429.

Klein, Geoffrey C, Kim, Sunghwan, Rodgers, Ryan P, Marshall, Alan G, & Yen, Andrew. (2006). Mass spectral analysis of asphaltenes. II. Detailed compositional comparison of asphaltenes deposit to its crude oil counterpart for two geographically different crude oils by ESI FT-ICR MS. *Energy & fuels, 20*(5), 1973-1979.

Kokal, Sunil Lalchand. (2005). Crude oil emulsions: A state-of-the-art review. *SPE Production & facilities, 20*(01), 5-13.

Leontaritis, KJ, Amaefule, JO, & Charles, RE. (1994). A systematic approach for the prevention and treatment of formation damage caused by asphaltene deposition. *SPE Production & Facilities, 9*(03), 157-164.

Li, Rong, Jiang, Peixue, Gao, Cheng, Huang, Feng, Xu, Ruina, & Chen, Xue. (2016). Experimental investigation of silica-based nanofluid enhanced oil recovery: The effect of wettability alteration. *Energy & Fuels, 31*(1), 188-197.

Liu, Fang, Hickman, Scott, Maqbool, Tabish, Pauchard, Vincent, & Banerjee, Sanjoy. (2020). Study of Asphaltene Deposition onto Stainless-Steel Surfaces Using Quartz Crystal Microbalance with Dissipation. *Energy & Fuels, 34*(8), 9283-9295.

Liu, Jianjun, Zhang, Liyan, Xu, Zhenghe, & Masliyah, Jacob. (2006). Colloidal interactions between asphaltene surfaces in aqueous solutions. *Langmuir, 22*(4), 1485-1492.

Lopez, Daniel, Giraldo, Lady J, Lucas, Elizabete F, Riazi, Masoud, Franco, Camilo A, & Cortes, Farid B. (2020). Cardanol/SiO2 Nanocomposites for Inhibition of Formation Damage by Asphaltene Precipitation/Deposition in Light Crude Oil Reservoirs. Part I: Novel Nanocomposite Design Based on SiO2–Cardanol Interactions. *Energy & Fuels, 34*(6), 7048-7057.

Lu, Teng, Li, Zhaomin, Fan, Weiyu, Zhang, Xinglu, & Lv, Qichao. (2016). Nanoparticles for Inhibition of Asphaltenes Deposition during CO2 Flooding. *Industrial & Engineering Chemistry Research*.

Mahmoudi Alemi, Fatemeh, Mousavi Dehghani, Seyed Ali, Rashidi, Ali, Hosseinpour, Negahdar, & Mohammadi, Saber. (2021). Potential Application of Fe2O3 and Functionalized SiO2 Nanoparticles for Inhibiting Asphaltene Precipitation in Live Oil at Reservoir Conditions. *Energy & Fuels, 35*(7), 5908-5924.

Mansoori, G Ali. (2010). Remediation of asphaltene and other heavy organic deposits in oil wells and in pipelines. *Socar proceedings, 2010*(4), 12-23.

Maqbool, Tabish, Balgoa, Arjames T, & Fogler, H Scott. (2009). Revisiting asphaltene precipitation from crude oils: A case of neglected kinetic effects. *Energy & Fuels, 23*(7), 3681-3686.

Marchal, Charles, Abdessalem, Eswar, Tayakout-Fayolle, Melaz, & Uzio, Denis. (2010). Asphaltene diffusion and adsorption in modified NiMo alumina catalysts followed by ultraviolet (UV) spectroscopy. *Energy & fuels, 24*(8), 4290-4300.

Masuda, T, & Hashimoto, K. (1996). Deactivation of zeolite catalysts by coke: ACS Publications.

Mendoza de la Cruz, Jose L, Arguelles-Vivas, Francisco J, Matias-Perez, Victor, Durán-Valencia, Cecilia de los A, & Lopez-Ramirez, Simon. (2009). Asphaltene-induced precipitation and deposition during pressure depletion on a porous medium: an experimental investigation and modeling approach. *Energy & fuels, 23*(11), 5611-5625.

Mohammadi, Mohsen, Akbari, Mahdi, Fakhroueian, Zahra, Bahramian, Alireza, Azin, Reza, & Arya, Sharareh. (2011). Inhibition of asphaltene precipitation by TiO2, SiO2, and ZrO2 nanofluids. *Energy & Fuels, 25*(7), 3150-3156.

Montoya, Tatiana, Coral, Diana, Franco, Camilo A, Nassar, Nashaat N, & Cortés, Farid B. (2014). A novel solid–liquid equilibrium model for describing the adsorption of associating asphaltene molecules onto solid surfaces based on the "chemical theory". *Energy & Fuels, 28*(8), 4963-4975.

Moradi, B, Pourafshary, P, Jalali, F, Mohammadi, M, & Emadi, MA. (2015). Experimental study of water-based nanofluid alternating gas injection as a novel enhanced oil-recovery method in oil-wet carbonate reservoirs. *Journal of Natural Gas Science and Engineering, 27*, 64-73.

Mullins, Oliver C. (2011). The asphaltenes. *Annual Review of Analytical Chemistry, 4*, 393-418.

Mullins, Oliver C, Sabbah, Hassan, Eyssautier, Joëlle, Pomerantz, Andrew E, Barré, Loïc, & Andrews, A Ballard, Ruiz-Morales, Yosadara, Mostowfi, Farshid, McFarlane, Richard, Goual, Lamia. (2012). Advances in asphaltene science and the Yen–Mullins model. *Energy & Fuels, 26*(7), 3986-4003.

Nassar, Nashaat N, Franco, Camilo A, Montoya, Tatiana, Cortés, Farid B, & Hassan, Azfar. (2015). Effect of oxide support on Ni–Pd bimetallic nanocatalysts for steam gasification of n-C7 asphaltenes. *Fuel, 156*, 110-120.

Negin, Chegenizadeh, Ali, Saeedi, & Xie, Quan. (2016). Application of nanotechnology for enhancing oil recovery–A review. *Petroleum, 2*(4), 324-333.

Pernyeszi, Tímea, Patzko, Agnes, Berkesi, Ottó, & Dékány, Imre. (1998). Asphaltene adsorption on clays and crude oil reservoir rocks. *Colloids and Surfaces A: Physicochemical and Engineering Aspects, 137*(1-3), 373-384.

Pomorska, Agata, Shchukin, Dmitry, Hammond, Richard, Cooper, Matthew A, Grundmeier, Guido, & Johannsmann, Diethelm. (2010). Positive frequency shifts observed upon

adsorbing micron-sized solid objects to a quartz crystal microbalance from the liquid phase. *Analytical chemistry, 82*(6), 2237-2242.
Qiao, Peiqi, Harbottle, David, Tchoukov, Plamen, Masliyah, Jacob, Sjoblom, Johan, Liu, Qingxia, & Xu, Zhenghe. (2017). Fractionation of asphaltenes in understanding their role in petroleum emulsion stability and fouling. *Energy & Fuels, 31*(4), 3330-3337.
Rana, Mohan S, Samano, Vicente, Ancheyta, Jorge, & Diaz, JAI. (2007). A review of recent advances on process technologies for upgrading of heavy oils and residua. *Fuel, 86*(9), 1216-1231.
Reviakine, Ilya, Johannsmann, Diethelm, & Richter, Ralf P. (2011). Hearing what you cannot see and visualizing what you hear: interpreting quartz crystal microbalance data from solvated interfaces: American Chemical Society.
Rezvani, Hosein, Khalilnezhad, Ali, Ganji, Parastoo, & Kazemzadeh, Yousef. (2017). How ZrO 2 nanoparticles improve the oil recovery by affecting the interfacial phenomena in the reservoir conditions? *Journal of Molecular Liquids*.
Rudrake, Amit, Karan, Kunal, & Horton, J Hugh. (2009). A combined QCM and XPS investigation of asphaltene adsorption on metal surfaces. *Journal of colloid and interface science, 332*(1), 22-31.
Sagala, Farad, Hethnawi, Afif, & Nassar, Nashaat N. (2020). Integrating Silicate-Based Nanoparticles with Low-Salinity Water Flooding for Enhanced Oil Recovery in Sandstone Reservoirs. *Industrial & Engineering Chemistry Research, 59*(37), 16225-16239.
Sagala, Farad, Montoya, Tatiana, Hethnawi, Afif, Vitale, Gerardo, & Nassar, Nashaat N. (2019). Nanopyroxene-based nanofluids for enhanced oil recovery in sandstone cores at reservoir temperature. *Energy & Fuels, 33*(2), 877-890.
Schuler, Bruno, Meyer, Gerhard, Peña, Diego, Mullins, Oliver C, & Gross, Leo. (2015). Unraveling the molecular structures of asphaltenes by atomic force microscopy. *Journal of the American Chemical Society, 137*(31), 9870-9876.
Sedghi, Mohammad, Goual, Lamia, Welch, William, & Kubelka, Jan. (2013). Effect of asphaltene structure on association and aggregation using molecular dynamics. *The Journal of Physical Chemistry B, 117*(18), 5765-5776.
Sharma, MM, & Yortsos, YC. (1987). Fines migration in porous media. *AIChE Journal, 33*(10), 1654-1662.
Shojaati, Faryar, Riazi, Masoud, Mousavi, Seyed Hamed, & Derikvand, Zeinab. (2017). Experimental investigation of the inhibitory behavior of metal oxides nanoparticles on asphaltene precipitation. *Colloids and Surfaces A: Physicochemical and Engineering Aspects, 531*, 99-110.
Standard, ASTM. (1985). Zeta potential of colloids in water and waste water. *ASTM Standard D*, 4187-4182.
Syunyaev, RZ, Balabin, RM, Akhatov, IS, & Safieva, JO. (2009). Adsorption of petroleum asphaltenes onto reservoir rock sands studied by near-infrared (NIR) spectroscopy. *Energy & Fuels, 23*(3), 1230-1236.
Tu, Yun, Kung, Judy, McCracken, Thom, Kotlyar, Luba, Kingston, David, & Sparks, Bryan. (2006). Effect of Clay Particle Size on the Adsorption of a Pentane Insoluble Bitumen Fraction. *Clay Science, 12*(Supplement2), 194-198.

Vafaie-Sefti, M, & Mousavi-Dehghani, SA. (2006). Application of association theory to the prediction of asphaltene deposition: Deposition due to natural depletion and miscible gas injection processes in petroleum reservoirs. *Fluid phase equilibria, 247*(1-2), 182-189.

Vitale, Gerardo. (2013). Iron Silicate Nano-Crystals as Potential Catalysts or Adsorbents for Heavy Hydrocarbons Upgrading. *"Iron Silicate Nano-Crystals as Potential Catalysts or Adsorbents for Heavy Hydrocarbons Upgrading". PhD thesis, University of Calgary*.

Vitale, Gerardo, Nafie, Ghada, Hethnawi, Afif, & Nassar, Nashaat N. (2020). Naturally derived pyroxene nanomaterials: an ore for wide applications *Handbook of Functionalized Nanomaterials for Industrial Applications* (pp. 731-774): Elsevier.

Wang, Shengqun, Segin, Nataliya, Wang, Ke, Masliyah, Jacob H, & Xu, Zhenghe. (2011). Wettability control mechanism of highly contaminated hydrophilic silica/alumina surfaces by ethyl cellulose. *The Journal of Physical Chemistry C, 115*(21), 10576-10587.

Xie, Kui, & Karan, Kunal. (2005). Kinetics and thermodynamics of asphaltene adsorption on metal surfaces: A preliminary study. *Energy & fuels, 19*(4), 1252-1260.

You, Z, Badalyan, A, Bedrikovetsky, P, Hand, M, & Jenson, D. (2013). *Productivity decline due to fines migration (modelling and field case study).* Paper presented at the IPTC 2013: International Petroleum Technology Conference.

Zabala, R, Mora, E, Botero, OF, Cespedes, C, Guarin, L, & Franco, CA, Cortes, FB, Patino, JE, Ospina, N. (2014). *Nano-technology for asphaltenes inhibition in Cupiagua South Wells.* Paper presented at the IPTC 2014: International Petroleum Technology Conference.

Zahabi, Atoosa, Gray, Murray R, & Dabros, Tadeusz. (2012). Kinetics and properties of asphaltene adsorption on surfaces. *Energy & fuels, 26*(2), 1009-1018.

Chapter Six: Conclusions and Future Work

This final chapter includes the main findings that were obtained through the discussions included in previous chapters, since conclusions were included for each chapter. Also, this chapter present some recommendations for future research on inhibition of formation damage by asphaltene precipitation.

6.1. Conclusions

Problems related with asphaltene instability in the oil industry are severe and costly, therefore, it is important to understand the interactions between asphaltenes, oil and the rock surface. For this reason, known nanoparticles such as NiO were used to evaluate their performance in competitive adsorption of model molecules that resembled characteristics of asphaltenes (V-Q-65) and resins (Q-V79). Nanoparticle size (5 and 40 nm) resulted a parameter that affected the adsorption of Q-65 and V-79, since the nanoparticles had different properties; 40 nm NiO nanoparticles showed higher adsorption capacity compared to 5 nm NiO nanoparticles. For the binary system, NiO nanoparticles of both sizes were more prone to adsorb V-79 molecules than Q-65 molecules. This trend was supported by the obtained results from individual adsorption. When V-79 molecules were in contact with NiO nanoparticles with pre-adsorbed Q-65, V-79 adsorption was higher than Q-65 desorption, this indicated that NiO nanoparticles had more affinity for resin-like components and the V-79 molecules were able to displace Q-65 molecules from the NiO nanoparticles surface. In addition, computational modeling helped to understand the interactions between model molecules and NiO surface, showing that V-79 were interacting with the nanoparticles through the alkyl chains and Q-65 was interacting with the NiO surface because of the presence of oxygen.

These results are very important because they revealed that NiO nanoparticles had different adsorption sites available for each model molecule, but V-79 was the preferred molecule to be adsorbed. These findings support the fact that the use of certain nanoparticles for asphaltene inhibition/remediation depends on the composition of the asphaltenes or to be more specific the oil, as asphaltenes are not the only component in the oil. It is necessary to account for the presence of different components in the oil to improve the nanoparticle formulation.

In addition, the of QCM-D as a tool to investigate the use of silicate-based nanoparticles, showed that silicate-based nanoparticles are a very promising alternative for the inhibition/remediation of formation damage caused by asphaltene precipitation/deposition. The use of two different asphaltene solutions, one with toluene and the other with heptol 70, showed that asphaltenes interact differently with SiO_2 surfaces, because they form different layers. The size of the asphaltene molecules in contact with SiO_2 surfaces (which resembled sandstone reservoirs) was important to consider, since the layer of asphaltenes formed over the SiO_2 sensors surface, influenced the interaction with different silicate-based nanoparticles. Surface chemistry, nanoparticle concentration and nanoparticle size were evaluated. All the tested nanofluids showed an effect in wettability alteration because contact angle measurements after nanofluid injection decreased in comparison to the SiO_2 sensor with pre-adsorbed asphaltenes. However, the best results were for 10 nm BN, at a concentration of 100 ppm for toluene asphaltenes and 1 ppm for heptol 70 asphaltenes. AFM images confirmed that nanoparticles interacted differently with the pre-adsorbed asphaltene layer, forming smaller particles and distributing more homogeneously over the surface at lower concentration. The results from this study helped to understand how the silicate-based nanoparticles acted as inhibitors of asphaltene precipitation/deposition at atmospheric conditions, they serve as a baseline to understand the parameters necessary to consider when formulating a nanofluid. Wettability alteration seemed to be the main mechanism involved in the contact of nanoparticles and pre-adsorbed asphaltenes.

Finally, basic silicate-based nanoparticles were used at reservoir conditions to study their effect in inhibition of formation damage by asphaltene precipitation/deposition in sandstone reservoirs. Nanofluid concentration, NaCl brine concentration and pH were the parameters considered in the study. The results showed that the use of nanoparticles changed the wettability of the sand pack when injected to the system after the induced damage, since the relative permeability curves were shifted to the right. However, the best results were for 50 mg/L BN in 1000 mg/L NaCl brine nanofluid, because the oil recovery increased by 14.4% and the residual oil saturation was decreased the most. This was in agreement with the results obtained for the QCM-D experiment. In addition, oil recovery was improved and increased after the injection of nanofluids for inhibition/remediation of the formation damage. According to the results, this improvement can be caused by the wettability change in the sand pack. Moreover, it is still necessary to optimize the nanofluid formulation, more nanoparticles not necessarily meant more improvement, because the stability of the nanofluids solutions changed as showed by zeta potential measurements.

6.2.Recommendations and Future Work

Experimentally, silicate-based nanoparticles showed good performance in homogeneous porous media. It is necessary to perform tests with different sands to achieve different permeabilities, since the induced damage will be different and the effect of nanoparticles too. Also, different types of cores will be helpful to use to study silicate-based nanoparticles in different porous media chemistry.

BN nanofluids at low salinity brine presented the best results in inhibiting/ remediating the formation damage at reservoir conditions. However, it is still necessary to consider other pressures and temperatures, in order to find optimal conditions for the use of these type of nanofluids. The use of silicate-based nanofluids at higher salinities can be improved considering other ions to modify the nanoparticles surface as well as natural components that can enhance nanoparticles stability in brine.

BN nanofluids showed an effect in wettability alteration. In porous media and at reservoir conditions, it is necessary to determine distribution or an estimation of the asphaltene precipitated along the sand pack, also, after the treatment with nanofluids, it is important to determine nanoparticles distribution along the sand pack too, this will help in the understanding of the mechanisms involved on inhibition/remediation of the formation damage. For this it is recommended the use of a tracer to identify the nanoparticles.

Despite the laboratory experiments, it is the paramount importance to perform tests at field scale, because in this way nanofluids formulation can be improved and the study of nanoparticle performance and scalability of the process can be more accurately achieved.

This work was performed for asphaltene formation damage from light oils; therefore, it can have some limitations. If it is intended to use with other oil, it is necessary to characterize the oil because the acidity and composition of the oil can affect the performance of the asphaltenes. The presented nanoparticle concentrations worked for an oil with less than 5 wt% asphaltenes. If it is intended to use in heavy oils or with higher asphaltene content, it needs further experiments to find an optimal concentration for asphaltene precipitation. The nanofluids presented here are intended to work at temperatures below of 120 °C. The optimal brine concentration for the nanoparticle dispersion was 1000 ppm NaCl, if it is intended to use a production brine, further experiments on nanoparticle stability must be performed as the present of other ions in solution may affect nanoparticle performance.

APPENDIX A: SUPPORTING INFORMATION FOR CHAPTER THREE

Supplementary figures for the derivative spectrophotometry based on multi-wavelength linear regression analysis, using the first order derivative method

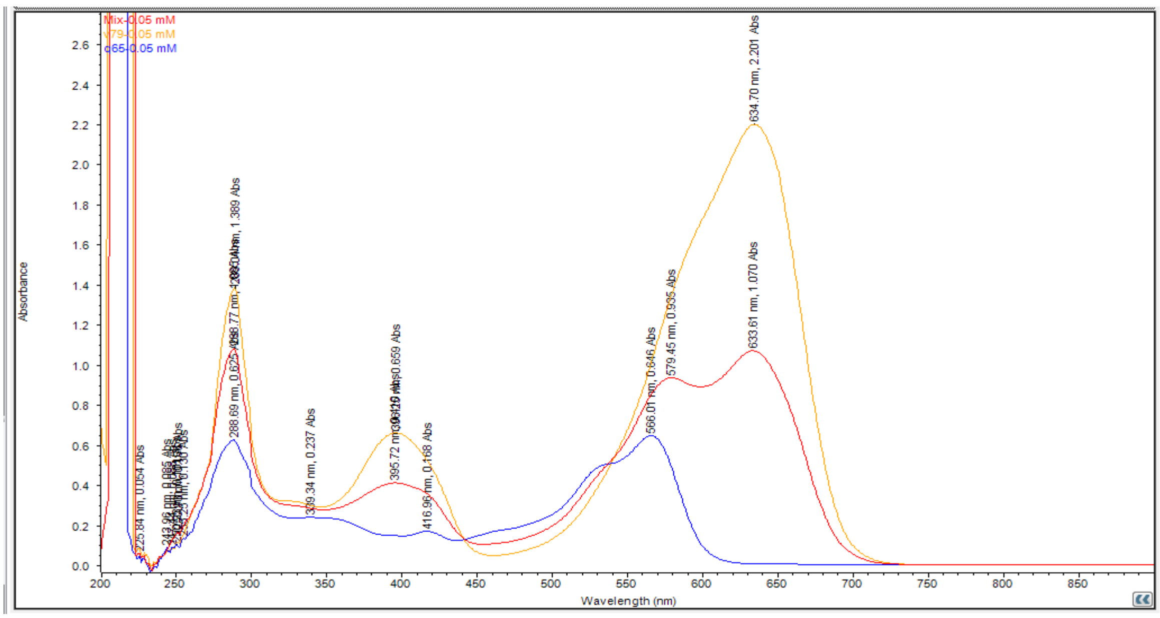

Figure A1. UV absorption spectrum of Q-65- or V-79-containing individual solution and a binary solution. Total solute concentration is 0.05 mM.

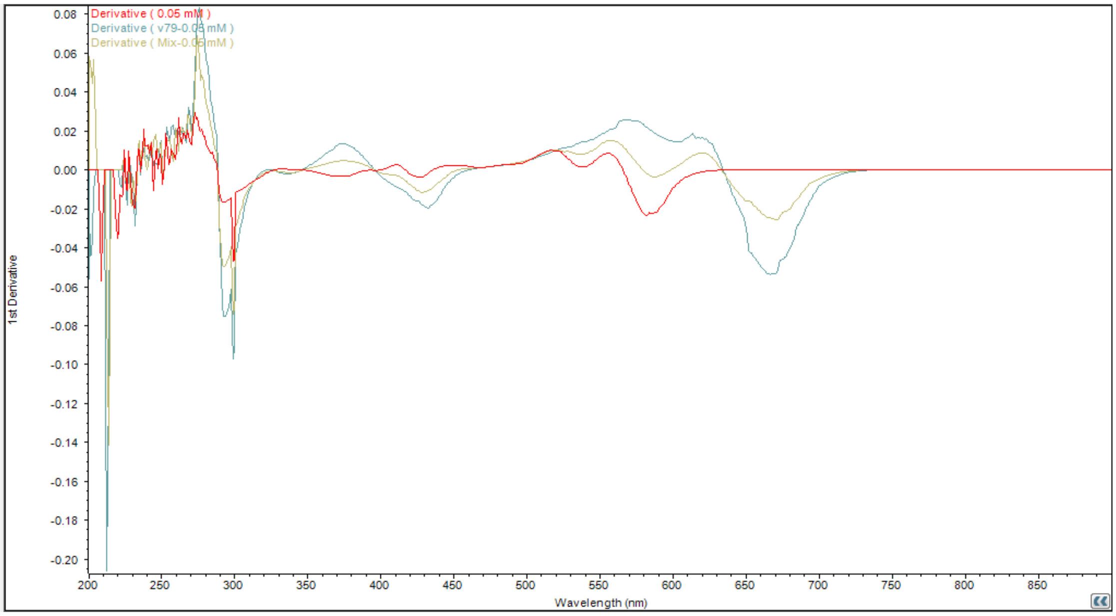

Figure A2. First order derivative of the spectrum of the V-79- and Q-65-containing individual solutions and the binary solution after smoothing by Savitzky-Golay method. Total solute concentration is 0.05 mM.

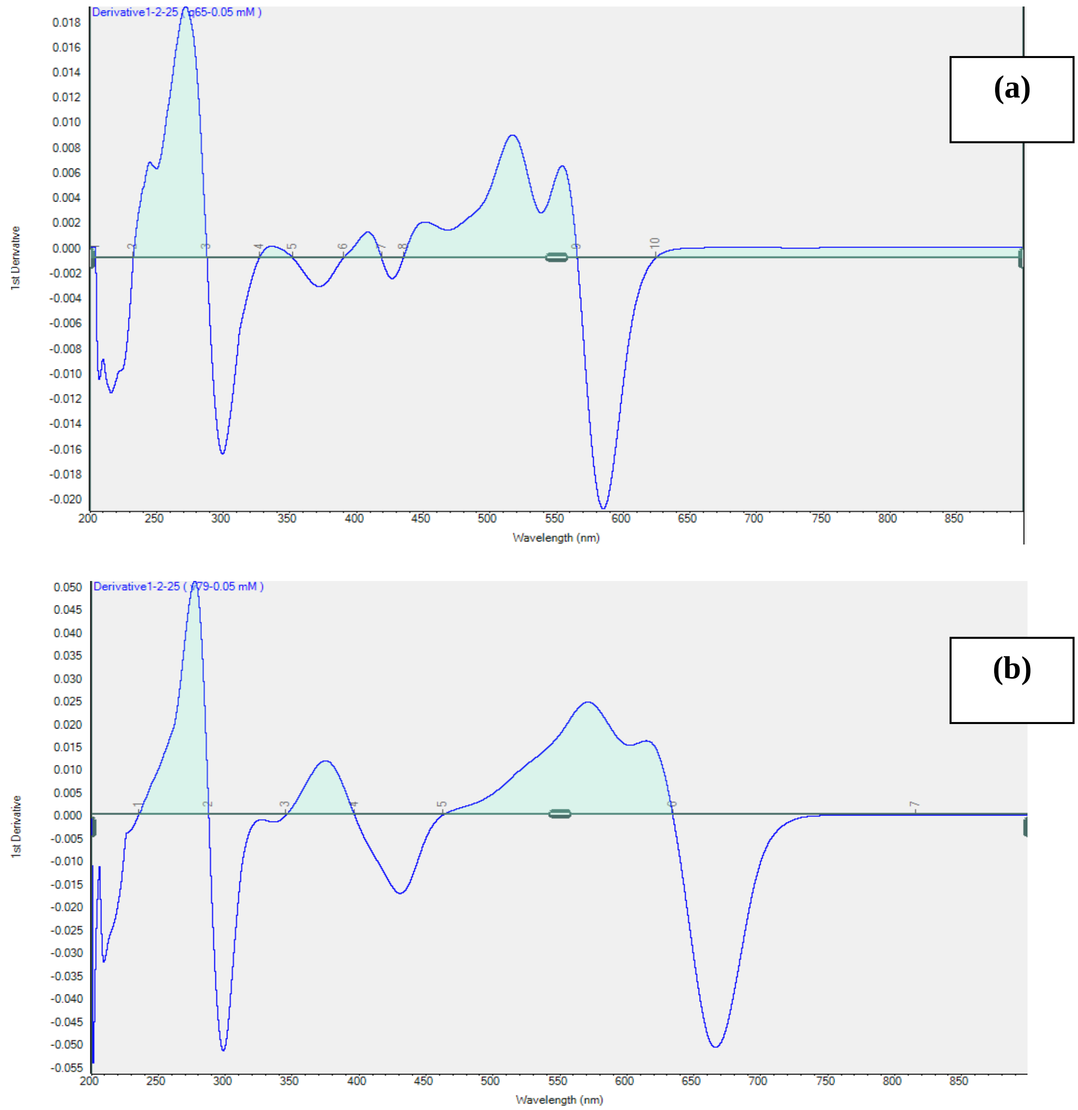

Figure A3. The wavelengths corresponding to the zero value of the first order derivative of the spectrum of (a) the Q-65-containing and (b) V-79-containing individual solutions.

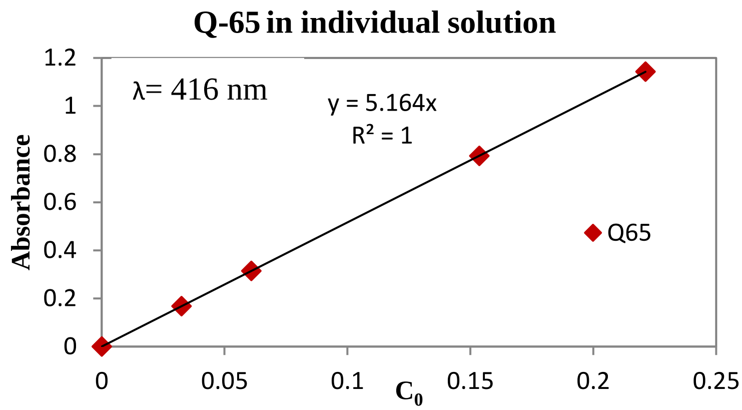
Q-65 in individual solution
λ= 416 nm
y = 5.164x
R² = 1
Q65
Absorbance
C0
1.2
1
0.8
0.6
0.4
0.2
0
0
0.05
0.1
0.15
0.2
0.25

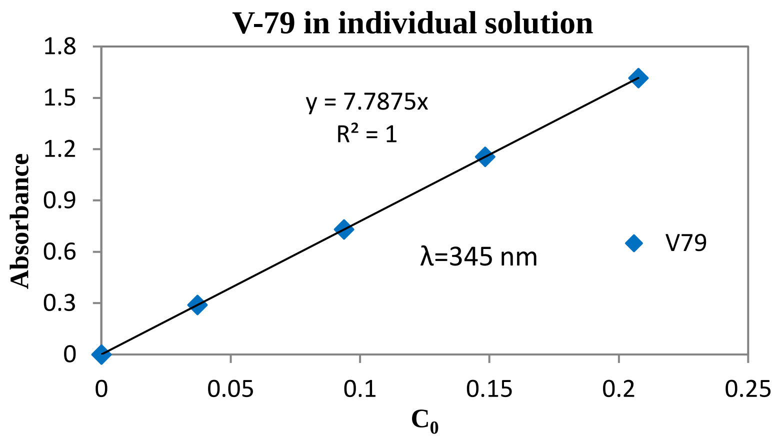
V-79 in individual solution
y = 7.7875x
R² = 1
λ=345 nm
V79
Absorbance
C0
1.8
1.5
1.2
0.9
0.6
0.3
0
0
0.05
0.1
0.15
0.2
0.25

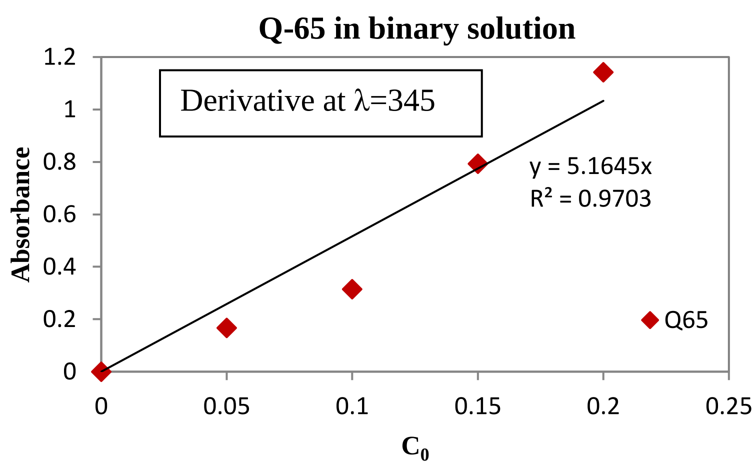
Q-65 in binary solution
Derivative at λ=345
y = 5.1645x
R² = 0.9703
Q65
Absorbance
C0
1.2
1
0.8
0.6
0.4
0.2
0
0
0.05
0.1
0.15
0.2
0.25

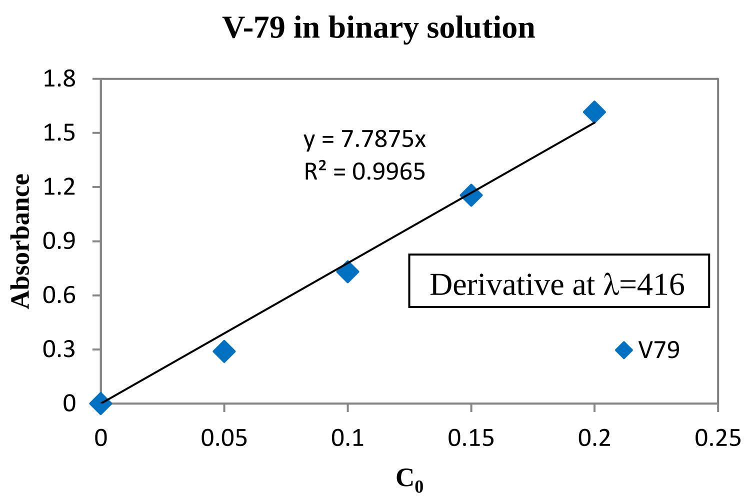

Figure A4. Calibration lines for the concentration of Q-65 and V-79 in individual and binary solutions.

APPENDIX B: SUPPORTING INFORMATION FOR CHAPTER FIVE

The viscosity was measured by using a Brookfield viscometer model DV-II+ Pro provided with a water recirculation bath model TC-502 which allows to measure the viscosity in a range of temperatures between 0 to 100 °C. The viscosity of the nanofluids was measured at 25 and 60 °C. The procedure for the viscosity determination initializes by setting the desired temperature. Then, the spindle is screwed to the bottom of the rotatory shaft and the viscometer and the distance between the spindle and the bottom of the cell is adjusted. The sample placed in the cell ensures that the surface of the spindle is covered. The rotation engine is started, and the velocity was adjusted. The viscosity value is reported in cP by the equipment. Table B1 shows the results for the viscosities of the used nanofluids.

Table B1. Viscosities for the used nanofluids at 25 and 60 °C.

Fluid	**Viscosities (cP ±0.16)**	
	25 °C	**60 °C**
50 ppm	1.44	0.92
250 ppm	1.46	0.93
500 ppm	1.49	0.96
1000 ppm NaCl	1.42	0.9
30000 ppm NaCl	1.47	0.95
pH 9	1.45	0.91
NaCl Brine (10000 ppm)	1.05	0.52

APPENDIX C: COPY RIGHTS CLEARENCE

ACS Publications
Most Trusted. Most Cited. Most Read.

Size Effects of NiO Nanoparticles on the Competitive Adsorption of Quinolin-65 and Violanthrone-79: Implications for Oil Upgrading and Recovery

Author: Tatiana Montoya, Azadeh Amrollahi, Gerardo Vitale, et al

Publication: ACS Applied Nano Materials

Publisher: American Chemical Society

Date: Jun 1, 2020

PERMISSION/LICENSE IS GRANTED FOR YOUR ORDER AT NO CHARGE

This type of permission/license, instead of the standard Terms and Conditions, is sent to you because no fee is being charged for your order. Please note the following:

- Permission is granted for your request in both print and electronic formats, and translations.
- If figures and/or tables were requested, they may be adapted or used in part.
- Please print this page for your records and send a copy of it to your publisher/graduate school.
- Appropriate credit for the requested material should be given as follows: "Reprinted (adapted) with permission from {COMPLETE REFERENCE CITATION}. Copyright {YEAR} American Chemical Society." Insert appropriate information in place of the capitalized words.
- One-time permission is granted only for the use specified in your RightsLink request. No additional uses are granted (such as derivative works or other editions). For any uses, please submit a new request.

If credit is given to another source for the material you requested from RightsLink, permission must be obtained from that source.

BACK

CLOSE WINDOW